NASA 22 C.
Pt. A

N66 28899 N66 28904

FACILITY FORM 602

(ACCESSION NUMBER) 139219 (PAGES)

(THRU) 1

(CODE) 11

CR-64952 (NASA CR OR TMX OR AD NUMBER)

(CATEGORY)

GPO PRICE $ _____

CFSTI PRICE(S) $ _____

Hard copy (HC) 4.00

Microfiche (MF) 1.00

ff 653 July 65

HE ROLE OF SIMULATION

VIRGINIA POLYTECHNIC INSTITUTE

ENGINEERING EXTENSION SERIES CIRCULAR No. 4
(In four parts: A,B,C,D)

PART A

PROCEEDINGS OF THE CONFERENCE ON

The Role of Simulation in Space Technology

AUGUST 17-21, 1964

Supported by grants from the National Aeronautics and Space Administration and the National Science Foundation; assisted in planning and presentation by the NASA Langley Research Center.

ACKNOWLEDGMENTS

VPI is indebted to the National Science Foundation for providing funds for travel and expenses for educational personnel attending the conference and to the National Aeronautics and Space Administration (through the Virginia Associated Research Center) for providing funds for speakers and incidental expenses.

VPI is particularly indebted to the Langley Research Center of NASA for assistance in planning the conference and to the NASA in general for providing many of the speakers and session chairmen.

The helpful co-operation of Poly-Scientific Division, Litton Precision Products, Inc. of Blacksburg, for arranging a plant tour showing their facilities for manufacturing slip rings and torque motors and for sponsoring the reception before the banquet is also acknowledged.

The conference committee wishes also to express its gratitude to the conference speakers, session chairmen and local personnel who have contributed to the success of the meeting.

The Conference Committee

M. L. Collier, Jr., Professor, Engineering Mechanics
J. B. Eades, Jr., Head, Aerospace Engineering
T. E. Gilmer, Jr., Professor, Physics
J. A. Jacobs, Head, Physics
F. J. Maher, Professor, Engineering Mechanics, and Chairman

TABLE OF CONTENTS

PART A

List of Conference Attendees

SPACE ENVIRONMENT

Vacuum Technology - Donald Santeler I

Electromagnetic Radiation in Space - Francis J. Clauss II

Ionizing Particle Radiations Effects and Simulation Consideration - J. E. Duberg and W. C. Hulten III

Meteoroids: Needs for Penetration Scaling Laws and the Potentials of Simulation Techniques - E. T. Kruszewski IV

Magnetic Fields: Reasons for Simulation and Methods Available - Normal F. Ness V

INTRODUCTION

The complexity of space exploration, manned or unmanned, dictates the need for prior knowledge of the interaction of operations, materials and humans with the hostile environment of space. Ground simulation of these problems is a highly challenging area of the entire space effort.

This conference represents an attempt to outline the principles governing simulation in general, to explore its limits in design, fabrication and operation and to correlate early studies with information gained from actual flights to date.

A large fraction of the total investment of manpower, materials and money in the space effort will continue to be devoted toward ground simulation of space environment and operations. Many scientists (from all branches of physical and life sciences) and engineers are engaged in this effort.

It was the purpose of the conference to present to educational personnel and to representatives from industry and government agencies the most recent efforts and results in the field of ground simulation. The benefits of such a conference to educational personnel are twofold; to acquaint them with the type of activity in which many of their present students will be engaged and to open new directions for their own investigations.

The participation of scientists from industry and government agencies was welcomed and it is hoped that by discussion they contributed to the general understanding and it is further hoped that they profited by association with others in their field.

CONFERENCE ATTENDEES

LIST OF SPEAKERS

GEORGE A. ALBRIGHT
Chief, Life Science & Space Environment
Republic Aviation Corporation
Farmingdale, Long Island,
New York

JOHN M. BOZAJIAN
Manager, Engineering Mechanics Department
Hughes Aircraft Company
El Segundo, California

GEORGE W. BROOKS
Head, Vibration & Dynamics Branch
NASA - Langley Research Center
Hampton, Virginia

WILLIAM A. BROOKS, JR.
Aerospace Technologist
NASA - Langley Research Center
Hampton, Virginia

JOHN LOTT BROWN
Department of Physiology
School of Medicine
University of Pennsylvania
Philadelphia, Pennsylvania

THOMAS N. CANNING
Chief, Hypersonic Free Flight
Ames Research Center - NASA
Moffett Field, California

RANDALL M. CHAMBERS
Head, Human Factors
U. S. Naval Air Development Center
Johnsville, Pennsylvania

FRANCIS J. CLAUSS
Senior Staff Scientist
Lockheed Missiles & Space Company
Palo Alto, California

JOHN E. DUBERG
Assistant Director,
Langley Research Center
NASA
Hampton, Virginia

SIEGFRIED J. GERATHEWOHL
Life Science Manager
NASA Headquarters
Washington, D. C.

R. M. HOWE
Chairman, Instrumentation Engineering
The University of Michigan
Ann Arbor, Michigan

E. T. KRUSZEWSKI
Head, Protective Structures Section
NASA - Langley Research Center
Hampton, Virginia

S. C. LIN
Principal Research Scientist
Everett Research Laboratory
AVCO Corporation
Everett, Massachusetts

NORMAN F. NESS
Physicist, Space Science Div.
Goddard Space Flight Center
NASA
Greenbelt, Maryland

J. LEITH POTTER
Manager, Research Branch
Von Karman Facility
ARO, Inc.
Arnold Air Force Station,
Tennessee

WILMER H. REED
Assistant Head,
Aeroelasticity Branch
NASA - Langley Research Center
Hampton, Virginia

HARRY L. RUNYAN
Head, Structural Dynamics Branch
NASA - Langley Research Center
Hampton, Virginia

DONALD J. SANTELER
Vice-President - Technical Director
Aero Vac Corporation
Troy, New York

G. ALLAN SMITH
Chief, Guidance & Controls Systems Branch
Ames Research Center - NASA
Moffett Field, California

SIDNEY WEINSTEIN
Director, Neuropsychological Laboratory Albert Einstein College of Medicine
New York, New York

CHARLES B. WESTBROOK
Chief, Control Criteria Branch
Flight Control Division
Wright-Patterson AFB,
Ohio

HERBERT A. WILSON, JR.
Chief, Applied Materials and Physics Division
NASA - Langley Research Center
Hampton, Virginia

ARTHUR W. VOGELEY
Head, Guidance and Control Branch
NASA - Langley Research Center
Hampton, Virginia

BANQUET SPEAKER

RAYMOND L. BISPLINGHOFF
Associate Administrator for Advanced Research and Technology
National Aeronautics and Space Administration
Washington, D. C.

LIST OF PARTICIPANTS AND GUESTS

ROBERT L. ARMSTRONG
University of Michigan

J. EARL BAILEY
University of Alabama

WILLIAM J. BARCLAY
North Carolina State University

JEWEL B. BARLOW
Auburn University

CHARLES E. BELL, JR.
Old Dominion College

U. H. BENTS
University of Missouri

E. F. BLICK
Oklahoma State University

A. E. BOCK
U. S. Naval Academy

JOHNNY E. BURKHALTER
Auburn University

JOSEPH W. BURSIK
Rensselaer Polytechnic Institute

WILLIAM J. BYATT
University of New Mexico

CHARLES E. CARVER, JR.
University of Massachusetts

ANSEL CHALLENNER
University of Oklahoma

MING M. CHEN
Boston University

D. H. CHENG
The City College of New York

E. H. CHERRINGTON, JR.
The University of Akron

H. D. CHRISTENSEN
University of Arizona

S. J. CITRON
Purdue University

ALLEN K. CLARK
Old Dominion College

FORREST P. CLAY, JR.
Old Dominion College

EUSTACE R. CONWAY
University of South Carolina

MERL D. CREECH
New Mexico State University

HERBERT L. DURST
Broome Technical Community College

LESTER T. EARLS
Iowa State University

FREDERICK H. EDWARDS
University of Massachusetts

N. F. ERASLAN
Louisiana State University

C. W. F. EVERITT
Stanford University

WILLIAM R. FERRANTE
University of Rhode Island

MARION A. FORBES
Broome Technical College

E. I. FREY
Mass. Inst. of Technology

JOSEPH H. GIBBONS
University of South Carolina

ANTHONY B. GIORDANO
Poly. Inst. of Brooklyn

WARD J. HAAS
University of Missouri

CHARLES E. HARP
University of Oklahoma

DONALD R. HAWORTH
Oklahoma State University

H. S. HAYRE
Kansas State University

ARTHUR HEBARD
Stanford University

R. M. HELMS
East Carolina College

PAUL J. HERMANN
Iowa State University

LESLIE R. HESTER
Mississippi State University

THOMAS J. HIGGINS
University of Wisconsin

A. N. HOSNY
University of South Carolina

ARTHUR V. HOUGHTON
University of New Mexico

JOHN L. IMHOFF
University of Arkansas

JOSEPH JAFFE
Columbia University

R. L. JENNINGS
University of Virginia

M. R. JOHNSON, JR.
Louisiana Poly. Institute

S. W. JOHNSON
Air Force Inst. of Technology

A. ROLAND JONES
Virginia Military Institute

LOUIS A. JONES
North Carolina State University

M. J. KAPRAL, JR.
Broome Technical College

CHARLES KILLGORE
Louisiana Poly. Institute

THOMAS J. KOZIK
Texas A & M University

ROBERT J. KROLL
University of Cincinnati

ROBERT A. KROMHOUT
The Florida State University

ALFRED A. KUEBLER
Rutgers University

IRWIN I. LAWN
Broome Technical College

RICHARD J. LEITE
University of Michigan

RALPH A. LOWRY
University of Virginia

C. S. MARTIN
Georgia Inst. of Technology

GEORGE B. MATTHEWS
University of Virginia

LEONARD MEIROVITCH
Arizona State University

ARTHUR T. MURPHY
Pennsylvania Military College

A. RONALD McKAY
Utah State University

LAWRENCE C. NEALE
Worcester Poly. Institute

ROY J. NICHOLS
University of Michigan

JAMES R. NICHOLSON
The Ohio State University

JOSEPH M. O'BYRNE
University of Massachusetts

AUBREY E. PALMER
Duke University

WILLIAM B. PARDO
University of Miami

EDWIN K. PARKS
University of Arizona

THOMAS A. PARNELL
University of North Carolina

PHILIPS PIKE
University of South Carolina

J. D. PINSON
Oklahoma State University

SOL D. PRENSKY
Fairleigh Dickinson University

MILTON RAVILLE
Georgia Inst. of Technology

GEORGE M. RESCH
Florida State University

TURGUT SARPKAYA
University of Nebraska

R. H. SCANLAN
Case Inst. of Technology

R. J. SENTER
University of Cincinnati

M. SEVIK
Pennsylvania State University

URI SHAFRIR
University of California

M. G. SHARMA
Pennsylvania State University

A. WILEY SHERWOOD
University of Maryland

LOWELL Z. SHUCK
West Virginia Inst. of Technology

J. J. SINGH
College of William and Mary

FRED W. SMITH
University of Cincinnati

ROBERT G. STERN
Massachusetts Inst. of Technology

WILLIAM B. STREETT
U. S. Military Academy

RALPH A. TROUPE
Northeastern University

JOHN J. TURIN
University of Toledo

V. UTGOFF
U. S. Naval Academy

GARVIN L. VON ESCHEN
Ohio State University

JOHN C. WESTKAEMPER
University of Texas

ROBERT A. WHEASLER
University of Wyoming

THOMAS H. WILSON
University of South Carolina

CHARLES C. WUNDER
State University of Iowa

TSUTE YANG
Villanova University

CHING H. YEW
University of Texas

PHILLIP M. ARONSON
U. S. Naval Ordnance Lab.

OAKIE ASBURY
Roanoke Times & World News

J. S. ATTINELLO
Institute for Defense Analyses

BEN BEAGLE
The Roanoke Times

WILLIAM BELLER
Missiles and Rockets

RICHARD BEAM
Ames Research Center - NASA

H. L. BOHON
Langley Research Center - NASA

MARY BUBB
Electronics News

BILL BURLESON
Roanoke World News

DONALD R. BURROWBRIDGE
Goddard Space Flight Center - NASA

E. W. CAIRNS
ACF Electronics Division

JOHN B. CARPENTER
Electro-Tech Corporation

GERHARDT C. CLEMENTSON
Space & Infor. Systems Division

T. CORNILLON
Sud-Aviation

WALTER C. COX
Oak Ridge National Laboratory

B. H. CRANE
Bellcomm, Inc.

·AN CURTIS
Litton Systems, Inc.

PAUL CZYSZ
McDonnell Aircraft Corporation

H. K. DOETSCH
Arnold Air Force Station

V. J. ESPOSITO, JR.
Army Map Service

BILL FERGUSON
Arlington, Virginia

W. F. FLITTER
Naval Training Device Center

PETER J. FOLIO
Grumman Aircraft

GILBERT A. GAGNE
Cornell Aeronautical Lab.

I. E. GARRICK
Langley Research Center - NASA

CLYDE GIORDANO
Franklin Pierce Arrow

FLOYD HARLIN
General Electric Company

GEORGE M. HIEBER
RCA - Astroelectronics Div.

S. WALTER HIXON, JR.
Langley Research Center - NASA

ROBERT E. HOLZMAN
Jet Propulsion Laboratory

P. J. KELLY
ACF Electronics Division

MARSHALL K. KINGERY
Arnold Eng. Development Center

FRANKLIN D. KIZER
Va. Dept. of Education

JOHN L. LANKFORD
Naval Ordnance Laboratory

M. SEVIK
Pennsylvania State University

URI SHAFRIR
University of California

M. G. SHARMA
Pennsylvania State University

A. WILEY SHERWOOD
University of Maryland

LOWELL Z. SHUCK
West Virginia Inst. of Technology

J. J. SINGH
College of William and Mary

FRED W. SMITH
University of Cincinnati

ROBERT G. STERN
Massachusetts Inst. of Technology

WILLIAM B. STREETT
U. S. Military Academy

RALPH A. TROUPE
Northeastern University

JOHN J. TURIN
University of Toledo

V. UTGOFF
U. S. Naval Academy

GARVIN L. VON ESCHEN
Ohio State University

JOHN C. WESTKAEMPER
University of Texas

ROBERT A. WHEASLER
University of Wyoming

THOMAS H. WILSON
University of South Carolina

CHARLES C. WUNDER
State University of Iowa

TSUTE YANG
Villanova University

CHING H. YEW
University of Texas

CHARLES A. LEIST
IBM Corporation

LESTER CARL LEMKE, JR.
General Dynamics/Astronautics

DOUG LESTER
WSLS TV - Roanoke

JOHN LO
Electro-Tech Corporation

EDWARD G. MARKOW
Grumman Aircraft Corporation

W. L. MITCHELL
North American Aviation

HEBER G. MOORE
NASA Headquarters

ROBERT MORRISON
Sperry Gyroscope Company

WALTER MYLES
ACF Electronics Division

ARTHUR T. McCLINTON, JR.
Naval Research Laboratory

FRANKLIN J. NIEDZ
General Electric Company

E. H. NORMAN
Hagerstown, Maryland

E. H. NORMAN, JR.
Hagerstown, Maryland

KEN NORTH
Electro-Tech Corporation

WALTER F. O'BRIEN
Aerospace Research Corporation

BEVERLY ORNDORFF
Richmond,Times-Dispatch

JOSEPH OTTERMAN
General Electric Company

B. PAIEWONSKY
Institute for Defense Analyses

WILLIAM H. PHILLIPS
Langley Research Center - NASA

LEONARD M. PICK
Friden, Inc.

ARTHUR REETZ
NASA Headquarters

A. W. REGER
Sandia Corporation

THOMAS REYNOLDS, JR.
Boeing Aircraft

F. W. RHODE
Army Map Service

FRANK S. ROOP
East Lansing, Michigan

L. C. ROSE
Aerospace Research Corporation

L. J. RUNCHEY
Naval Ordnance Test Station

G. R. SOWTER
ACF Electronics Division

CAROL SPENCER
US Naval Training Dev. Center

JAMES H. STILTNER
State Dept. of Education

H. F. STOKES, JR.
ACF Electronics Division

WARREN H. STRALEY
The Marquardt Corporation

G. C. SZEGO
Institute for Defense Analysis

JEROME G. THEISEN
Lockheed-Georgia Company

DAVID G. THOMPSON
U.S. Naval Ordnance Laboratory

EDWIN A. ULBRICH
North American Aviation

RUSSELL UTTKE
AC Spark Plugs

GEORGE H. WADE
Marshall Space Flight Center NASA

IVAN T. WALTERS
ACIC, St. Louis

WALTER W. WIERWILLE
Cornell Aeronautical Laboratory

W. F. YOUNG, JR.
Va. State Dept. of Education

ART ZOREF
Electro-Tech Corporation

VPI

WILLIAM BARKER
Engineering Mechanics

ERNEST BRANCH
Engineering Mechanics

W. W. BRANDT
Vice-President

W. J. BREEDLOVE, JR.
Aerospace Engineering

H. R. BUNGAY
Civil Engineering

LEONARD CLARK
Engineering Mechanics

M. L. COLLIER, JR.
Engineering Mechanics

J. COUNTS
Engineering Mechanics

J. B. EADES, JR.
Aerospace Engineering

LEONARD ERMOLD
Engineering Mechanics

D. FREDERICK
Engineering Mechanics

T. E. GILMER, JR.
Physics Department

J. L. HAMMER
Civil Engineering

J. A. JACOBS
Physics Department

P. R. KURZHALS
Aerospace Engineering

GEORGE LEA
Engineering Mechanics

VICTOR MADERSPACH
Engineering Mechanics

HERB MAHAN
Aerospace Engineering

F. J. MAHER
Engineering Mechanics

VIRGINIA MASON
Geology Department

LEWIS NEWMIRE
Physics Department

D. H. PLETTA
Engineering Mechanics

DAVID PURDY
Engineering Mechanics

CARL RENFROE
Chemical Engineering

J. F. RYMAN
Physics Department

C. W. SMITH
Engineering Mechanics

HOWARD SWORD
Engineering Mechanics

J. E. VIA
Public Relations Officer

JOE WALTERS
Engineering Mechanics

M. J. WERLE
Aerospace Engineering

R. W. WERLWAS
Aerospace Engineering

W. G. WORCESTER
Dean of Engineering

N66 28900

VACUUM TECHNOLOGY

by

Donald Santeler

Aero Vac Corporation

Originally Printed In
International Science and Technology
January 1963, No. 13
Reprinted by Permission

Only a few years ago, vacuum was an art, a cookbook type of black magic. Little was known about the limitations of pumping and measureing equipment, or the nature of gas evolution from surfaces. Much of the vacuum hardware which we use today didn't exist. Then a series of difficult problems arose, each requiring vacuum conditions beyond the normal range, which provided the impetus for a more sophisticated vacuum technology.

Typical of these developments were the isotope separations of the Second World War, the advent of vacuum metallurgy, the need for more and better quality vacuum tubes for the expending communications industry, and the need for ultrahigh vacuum in nuclear fusion projects. Today many new applications exist, all making their contribution to improved understanding of vacuum technique. Two of these, space simulation and the production of electronic thin films, will be discussed in some detail. But first, we need to define some of the more important parameters of vacuum.

The Limits of Vacuum

By popular usage, atmospheric pressure is the upper limit of vacuum. Any pressure less than standard atmospheric pressure is some form of vacuum. Originally, the vacuum level was measured in inches of mercury below atmosphere, and a vacuum of 28 or 29 in. Hg was considered pretty good. As vacuum improved, and in order to have meaning to engineering equations, it became necessary to switch to an absolute scale in the same fashion that an absolute scale is required for temperature measurement. Temperature, in fact, represents a surprising similarity to vacuum in range, in nomenclature, and in equations.

Figure 1 gives a comparison of the more popular pressure, or vacuum, scales in existence today. These are self-explanatory, with the possible exception of the difference between the torr and the mm of Hg. The mm of mercury is a unit of pressure corresponding to a column of mercury exactly 1 mm high at 0° C and under standard gravitational acceleration. The torr is defined as 1/760 of a standard atmosphere. Since the standard atmosphere is not quite equal to the normal atmosphere of 760 mm, a discrepancy of approximately 1 ppm exists between the mm of Hg and the torr.

At standard atmospheric pressure and temperature, there are approximately 2.5×10^{19} molecules/cc and, on the average, a molecule will travel 2.6×10^{-6} in. between each collision. As the pressure decreases, the density decreases and the mean free path increases as

shown on Fig. 1. At a pressure of 10^{-10} torr, within the region of *ultrahigh* vacuum, we have this rather startling condition: there are over three million molecules/cc, yet, on the average, a molecule will travel over 300 miles between collisions. In outer space, the pressure is estimated at around 10^{-16} torr, the density is about 3 molecules/cc, but the mean free path is in the order of the distance between the earth and the sun.

The concept of the mean free path is extremely important to anyone interested in evacuating a confined space to very low pressure. This is because a tremendous variation in gas properties exists, depending on whether the mean free path of the molecules in the gas is small or large relative to the confining vessel. The mean free path is defined as the average distance that a molecule will travel between collisions with another molecule. It is an inverse linear function of the pressure.

At atmospheric pressure (or *low* vacuum) conditions, the mean free path is exceedingly small and the molecules are in a constant state of intercollision. Energy or momentum is transferred through the gas by means of this constant intercollision process. This region is known as the region of *viscous* flow.

As the pressure is reduced, the mean free path increases. Eventually, the point is reached where the mean free path is equal to or greater than the dimensions of the confining chamber. Under this condition, the molecules will collide more frequently with the walls of the chamber than with each other, and the gas is said to be in *molecular* flow. At this point, the gas flow is governed by the

statistical motion of the individual molecules. An important characteristic of this flow regime is that the molecules are diffusely reflected from the wall according to a cosine distribution; i.e., most probable direction is perpendicular to the surface. As a result, the directional momentum of a molecule is lost at each collision. The relationship between pressure, chamber dimension, and flow regimes is illustrated for N_2 gas at 25° C in Fig. 2.

High Vacuum Means Molecular Flow

Since molecular flow is the prevailing condition for high and ultrahigh vacuum, let us look at some of its more important ramifications. We will first consider an idealized situation of a large chamber containing a gas of molecular weight M, at temperature T, and pressure P, low enough so that molecular flow conditions exist. The thermal velocity of the molecules in this nonflowing gas results in a constant rate of collision with the walls. From kinetic theory, the collision frequency per unit area in molecules/cm^2-sec is found to be

$$\nu = 3.513 \times 10^{22} P/(MT)^{0.5}$$

where P is the pressure in torr, M is the molecular weight, and T the temperature in °K.

Now, suppose we induce flow by connecting our chamber full of gas at rest to a second chamber containing a perfect vacuum. The rate of flow of molecules through the orifice between them will be simply the

product q of the collision frequency ν and the area A (in cm^2) of the connecting orifice. If the two chambers are at two different pressures, the net rate of molecular flow, one to the other, is simply the difference between the two separate gas flows calculated as though each were flowing to a perfect vacuum:

$$q = 3.513 \times 10^{22} \times A \times \Delta P/(MT)^{0.5}$$

This is true because of the absence of interactions between molecules under molecular flow conditions.

Expressing flow rate in terms of molecules is cumbersome to engineers accustomed to volume or mass flow rates.

To convert into the vacuum engineer's units of pressure-volume flow, we divide the molecular rate q by the molecular density, $n = 9.656 \times 10^{21}/T$, in molecules per liter at 1 torr and at reference temperature T °K. Then, the gas flow-rate, or through-put is

$$Q = 3.638\ A \times \Delta P\ (T/M)^{0.5}$$

This is the customary expression for gas flow through an orifice and is in the units of torr liters/sec. The advantage of this nomenclature is that the gas flow at any point is then simply the product of the pressure and the speed, where the speed is taken as the volumetric flow past the point in liters/sec.

From Orifices to Long Pipes

Few pieces of vacuum equipment are connected by orifices. Thus, we can ask what is the effect on gas flow if the orifice is extended into

a long tube of length L with ΔP as the difference in pressure at either end. Knudsen deduced a fundamental equation for such flow,

$$Q = \frac{4}{3} v_a \Delta P / \int_0^L (H/A^2)\, dL$$

where v_a is the statistically determined average molecular velocity, H is the perimeter of the tube, and A is its area at any point. For a tube of uniform circular area, this integrates (with appropriate gas constants inserted) to

$$Q = 30.48\ (a^3/L)\ (T/M)^{0.5}\ \Delta P$$

There are serious limitations to this equation that are revealed only if we consider the probability aspects of molecular flow down the tube. Since each molecule entering the tube is reflected from the surface according to a cosine distribution, it may continue down the tube, or it may rebound in the opposite direction. The statistical probability that it will pass through the tube was first calculated by Clausing - the solid line in Fig. 3.

We see that this curve is a function of the ratio of the length L and the radius a and is bounded by two different curves of probability θ depending on this ratio. For short pipes θ is given by $1/(1 + L/2a)$. This expression, which derives from the assumption of random gas motion, only applies for $L/a < 1.5$. For long pipes $(L/a > 40)$, θ is practically $8a/3L$, and the flow is this fraction of ordinary orifice flow.

$$Q = 3.638 \times A \times \Delta P\ (T/M)^{0.5} \times 8a/3L$$

This, for the circular pipe of area πa^2, is

$$Q = 30.48\ a^3/L\ (T/M)^{0.5}\ \Delta P$$

which is precisely the equation cited earlier.

But it is important to note that this identity holds only if probability $\theta = 8a/3L$; that is, only when L/a in Fig. 3 is 40 or above. This means that flow through shorter tubes must be computed on the basis of the short tube probability. Otherwise, errors will result.

Flow Through Restrictions

Probabilities can be of considerable help in estimating the flow through complex geometries, much as pressure drop coefficients are used in hydraulic systems to take into account valves, elbows, etc. For example, if the separate probability of transmission is known for each of two restrictions A and B in series, the new probability of going through both is,

$$\theta_T = \theta_A \theta_B / (\theta_A + \theta_B - \theta_A \theta_B)$$

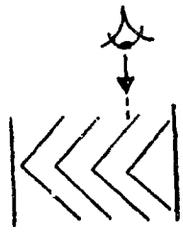

chevron baffle

Levenson, Milleron, and Davis have measured the probability of molecular transfer of gas through a variety of complex geometries. Among these was a 45° angled-fin array for which they obtained a value of 0.4. Suppose we combine two sets of fins, resulting in an "optically tight" chevron as sketched in the margin. If we assume that the probability of going through the second set of fins is also 0.4, then the net probability of going through both would be 0.25 from the above expression. The same result can be obtained from Fig. 3

by noting the "equivalent" value of L/a which gives a probability of 0.4 The resulting L/a value of 3 is then doubled, and the probability at an L/a of 6 is observed to be 0.25.

Reaching For Zero Pressure

Since molecules are constantly being removed during the pumping process, it would seem that eventually a pressure of absolute zero would be obtained. This would be true if the only molecules to be removed were those in the gas space. However, other gas sources do exist and must be considered. The predominant gas sources are leakage and outgassing. Leakage is the direct transmission of gas molecules, driven by the higher external pressure, through holes or porosities in the vacuum chamber wall or in the various seals used in the system. Outgassing refers to all forms of gas coming from the materials *in* the vacuum system. It includes gases which are adsorbed on the surface, dissolved in the material, and occluded in gas pockets, as well as that due to evaporation or decomposition.

The continual addition of gas from these sources represents the major limitation on the ultimate pressure which can be obtained in a given system. Mathematically, we may state that the ultimate pressure P_u is given by the influx of gas divided by the system pumping speed, $P_u = Q/S$. Because the pump *itself* is one source of outgassing, its effect is frequently included in the equation, so that $P_u = Q/S + P_p$, where Q now refers to gas from all sources except the pump.

Even though the pump may be operating at a particular limiting pressure for one gas type, because of a leak or outgassing, it still is capable of pumping other gas types to extremely low pressures. This is true because in molecular flow, all gases are flowing independent of each other. Typically, a gas analysis of an ultra-high vacuum system operating at a total pressure of 10^{-10} torr will show hydrogen and carbon monoxide as the residual gas still coming from the walls of the system, yet the partial pressure of the original nitrogen and oxygen is too low to be measured. A more realistic equation to express this phenomena of independent molecular flows is to write the ultimate pressure as a summation,

$$P_u = \Sigma \, (Q_m/S_m) + P_p$$

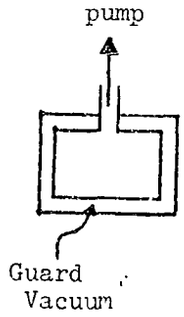

To obtain low ultimate pressures, we must reduce the various sources of gas previously discussed. Leakage can be eliminated by first locating the leak and then properly repairing it, or by placing a guard vacuum (see sketch) around the points of potential leakage.

Outgassing is best eliminated by proper selection of materials, reduction of surface area, and most importantly, by temperature control. At ambient temperature, the outgassing rate of organic materials and polymers is generally between 10^{-4} and 10^{-6} torr liters/sec-cm^2 after a few hours of pumping. The short-term outgassing rate of most metals is between 10^{-7} and 10^{-8} torr liters/sec-cm^2. Most of this is water vapor, which can be condensed easily and rapidly by cryogenic cooling.

To obtain even better ultimate vacuums, system bakeout is the

answer. When heat is applied, the outgassing increases sharply from both the surface and the interior of the materials in the system. The surfaces are soon stripped clean of contamination and most of the gases within the materials are removed. When the system is subsequently cooled to ambient temperature, outgassing is reduced by a considerable factor (typically 10^6). Operation of the vacuum system at cryogenic temperatures, if that can be tolerated, will reduce the ultimate pressure even lower. The combination of bakeout, cryogenic cooling, and a guard vacuum has been used to produce extremely low pressures, less than 10^{-15} torr. A more practical limit for industrial ultrahigh vacuum systems is 10^{-10} torr. It is important to realize that the pressures obtainable under good laboratory conditions in an empty chamber are far different from those possible in a factory operation.

Pumps and Pumping Problems

The many different applications of vacuum in use today require a variety of operating pressures. Consequently there are a number of different types of pumps, as shown in Fig. 4, each with its own particular advantages and limitations. For pressures down to 10^{-2} torr, the mechanical oil-sealed rotary pump is the workhorse of the industry. For lower pressures, the other pump types are used, including oil- and mercury-vapor diffusion pumps, getters, ion pumps, getter-ion pumps and cryogenic pumps.

The most common of these is the *oil-vapor diffusion pump*, which operates on the principle of the free diffusion of gas molecules into

a dense, high-velocity vapor stream. Once in the stream, the molecules are accelerated by successive collisions with the vapor toward the exhaust. Here they are removed by means of a mechanical backing pump.

The major limitation of the oil-diffusion pump is that the oil may backstream or evaporate into the vacuum system. The presence of a cold surface such as a liquid nitrogen trap will considerably reduce this problem by condensing most of the oil. However, unless the trap is properly designed to stop the migrating oil, a certain amount will still creep back.

Even with a well-designed trap, gas problems remain. Decomposition of hydrocarbons in the pump oil may produce hydrogen and carbon monoxide, contaminants which are not condensed by the trap. It helps to add a second diffusion pump to the line between the diffusion pump and the backing pump. This prevents mechanical pump oil from migrating into the boiler region of the main diffusion pump, and maintains a low partial pressure for the removal of hydrogen.

To minimize hydrocarbon decomposition problems, so that lower pressures can be generated, mercury vapor is substituted for the oil. Mercury diffusion pumps have been used on systems operating at 10^{-15} torr. However, they do not have as high a pumping speed, which makes oil diffusion pumps preferable for most industrial applications.

Chemical and electronic pumping can also produce high and ultrahigh vacuums. In chemical pumping, the gas molecules react with a metal like titanium (call a getter) and are absorbed. Or, gas molecules can be trapped in a porous material such as silica gel which can adsorb large quantities of gas when cooled to cryogenic temperatures. In electronic

pumping, the gas molecules are bombarded with electrons, form positive ions, and are trapped on the negatively charged walls of the collector.

So far, these two pumping methods have been generally limited to continuous pumping of radio tubes, though gels have been widely applied to help hold vacuum in larger volumes such as vacuum-insulated LOX tanks. However, a combination method known as *getter-ion pumping* has been commercially developed into a practical pumping mechanism for vacuum systems. It has several advantages over the diffusion pump. It does not need a liquid nitrogen trap, does not require a warmup time, and may be mounted in any position. However, it has a higher initial cost, a variable pumping speed for different gases, and cannot be operated at as high a pressure.

Cryogenic pumping is the newest technique. At 20° K, all gases except H_2, He, and Ne are condensed to low ultimate pressures. Thus, surfaces maintained at this temperature can be used as pumps. Because of the high cost of generating such a low temperature, the heat loading on the pumping panels must be minimized. This is done by hiding them behind liquid N_2 panels, which cost much less to operate. Some diffusion pumping may be needed to remove noncondensible gases.

How Do You Measure "Nothingness?"

Surprisingly enough, vacuum measuring equipment was for a long time a major obstacle in the production of ultrahigh vacuums. For many years, the main vacuum gage was the conventional hot cathode ionization gage

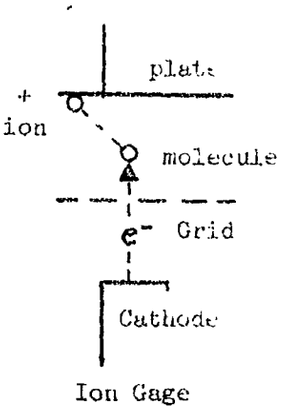

Ion Gage

— simply a triode which produces ions by means of accelerated electrons, as sketched in the margin. The ratio of the collected ion current to the electron current is a linear function of pressure over a wide pressure region.

Nottingham pointed out that this gage has a lower pressure limit of about 2×10^{-8} torr because of the emission of secondary electrons (which the collector "sees" as positive ions) from the collector. This electron emission is caused by soft-x-rays produced when electrons are collected on the grid. Measurement of pressures below the limiting value required special techniques, thus seriously impairing the development of ultrahigh vacuum techniques. The invention of the Bayard-Alpert gage lowered the x-ray limit of the ion gage by a factor of about 200, opening the way for accurate measurement of much lower pressures. This was shortly followed by Redhead's magnatron gage, which has no x-ray limit and has been used to measure down to 10^{-15} torr.

None of these gages measure true pressure, but rather they respond to a complex mixture of gas properties including ionization efficiency, mobility, and mass. The gages are normally calibrated for nitrogen gas. The calibration constant for helium gas is 0.16 relative to nitrogen. Hydrocarbons are in the reverse direction with calibration constants ranging well over 10. It is apparent then that considerable errors may exist when measuring the ultimate pressure of a vacuum system where the predominant residual gas may be as diverse as water vapor, carbon monoxide, or hydrogen. The only sure way to overcome this difficulty is to use some form of gas analysis equipment

such as the mass spectrometer. Mass spectrometers have been designed which are capable of reading partial pressures as low as 10^{-16} torr. Most commercial instruments of this sort have sensitivities around 10^{-12} torr.

Other problems exist in the measurement of high and ultrahigh vacuum - including outgassing from the gage elements, pumping action of the gage, cracking of large molecules on hot surfaces, and location of the gage. These have all been treated in detail in the literature. Just keep in mind two important points; first, there is much more to measuring low pressure than simply connecting a vacuum gage to a test chamber; secondly, calibration of a vacuum gage does not insure accuracy.

A Typical Vacuum System

Vacuum systems currently being used in industry may be classified in a number of ways: by the type of pump being used, by the material of construction (either glass or metal), by the ultimate pressure, or by the size or usage of the system. The most common system in use today is the metal system pumped by means of an oil diffusion pump. Because of its popularity, we will consider this type of system in further detail in order to develop the total system concept. This does not imply, however, that this system is recommended over others such as the getter-ion pump type.

The simplest form of diffusion pump system consists of a diffusion pump, a backing pump, interconnecting lines, necessary

gaging, and a chamber or component to be exhausted, as shown in the margin. The size of the diffusion pump is normally chosen on the basis of the gas load Q to be handled at the desired operating pressure P. This is governed by the basic vacuum equation $S = Q/P$. Figure 5 gives a graphical summary of the speed required at the chamber for different ultimate pressures and outgassing rates.

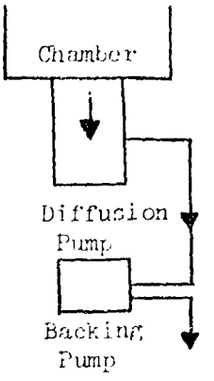

The size of the backing pump is usually recommended by the vendor of the diffusion pump. In general its speed is about 1/100 of the speed of the diffusion pump. The size of the interconnecting line must be large enough so as not to limit the performance of the mechanical pump, which operates at a much higher pressure of the diffusion pump and is thus often in the viscous-flow region. However, the line is usually so short that ordinary viscous-flow equations do not apply. Rather, nozzle equations are used.

A number of additional features may be added to the basic system, as shown in the next marginal sketch. First, there is the liquid nitrogen trap which has already been discussed. The trap is a further restriction in the line, but it produces a high pumping speed for condensible gases. If the trap is connected directly to the diffusion pump, it will receive direct thermal radiation from the pump and will also condense the hot oil molecules

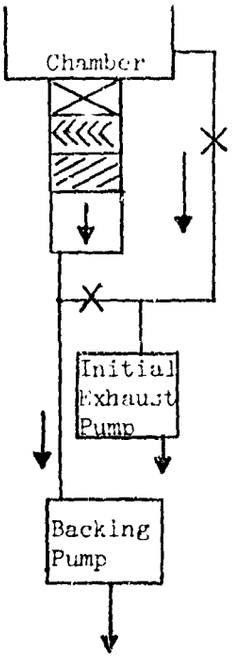

back-streaming from it. This high heat load consumes a considerable amount of liquid nitrogen, so water baffes are often added between the pump and the trap to reduce this effect, though this adds further restriction to the flow of gas.

Sometimes, a high-vacuum valve is added between the pumping system and the test area in order to keep the diffusion pump hot while the test section is opened to atmosphere. For a system that must be pumped down often, an additional mechanical pump and shutoff valve bypassing the diffusion pump is required. This allows for the initial exhaust of the system while still maintaining the diffusion pump at operating temperature. In the absence of the valves, initial exhaust is accomplished by "roughing" through the cold diffusion pump.

The Question of Cost

In addition to pumps, traps, baffes, and valves, a vacuum system contains many other components. These include electrical lead-throughs, vacuum gages, mechanical seals, furnaces and bakeout ovens, refrigerated shrouds, and all manner of mechanical hardware for special purpose testing. All of these items, as well as the system itself, represent dollar investment to the user.

As a first approximation, the cost of each component in a pumping system can be related to the diffusion pump size at a rate of $100/in. diameter. On this basis, the cost of the components in a 10 in. pumping system, for example, would average $1000 for each of

the following components: diffusion pump, backing pump, liquid nitrogen trap, water baffle, roughing and bypass lines and valves, and high-vacuum valve. From this list, it is apparent that a pumping system may range from 3 to 6 components. These prices do not include the cost of assembly, testing, cabinet, instrumentation, or chamber. For estimating purposes, the first three of these - assembly, testing, and cabinet (with controls and plumbing) - may be considered as one additional component each. Hence, a complete vacuum pumping system will vary from 6 to 9 components at $100/in. of diffusion pump diameter.

This cost information is illustrated on Fig. 6 in terms of pumping speed. Note that the speed scale refers to the net speed of the system rather than that of the diffusion pump. The curve illustrates an interesting point: that the cost of the system goes up as a linear function of the diameter, yet the speed increases as the square of the diameter. As a result the cost per unit pumping speed is a square-root relationship (slope = 1/2) as illustrated. However, when additional pumps are added to a system, the cost increases linearly with the speed, as indicated by the 45° lines indicating the average cost of a multiple pumped system. This comparison shows that it is far cheaper to obtain a given system pumping speed by using the largest possible pump rather than by using a multiplicity of smaller vacuum pumps.

Further, allowance must be made for instrumentation, extra mechanical pumps, and the system chamber. Instrumentation can generally

be estimated at a total cost of $1000 unless special situations are involved requiring multiple gage locations. As for extra pumps, single-stage, oil-sealed mechanical types are approximately $10/cfm; large-size mechanical blowers run about $4/cfm. The cost of the chamber will obviously vary with the number of penetrations the type of finish, and so on, but for rough estimating, a figure of $100/ft.^{2} of surface may be used.

The cost of special features such as electrical or mechanical lead-throughs, bakeout ovens, refrigerated shrouds, automatic control equipment, or various special fixtures must still be added in. Finally, there is the cost of special design and drafting, a factor when a special vacuum pumping system is required.

Simulating the Void of Space

The reliability requirements for manned spacecraft have emphasized the need for both component- and systems-testing in vacuum. As we move further out into space, the pressure level drops steadily until it reaches a value of about 10^{-16} torr, the presently accepted value of free space vacuum. To duplicate this environment, we would have to obtain such a pressure and maintain it in the presence of a high outgassing load from the test vehicle sitting inside the chamber. But is this necessary?

Space simulation refers to the duplication of the effects of the environment rather than to the duplication of the environment itself. A vacuum level of only 10 torr, for example, will adequately simulate

the mechanical distortion effects of outer space. Yet at this level, the heat transfer characteristics are essentially the same as on the earth. To simulate the thermal properties of space vacuum, it is necessary to decrease the pressure to around 10^{-6} to 10^{-5} torr. At this level, gas conduction is very small relative to thermal radiation. In addition, the problem of arc and glow discharge is eliminated for most voltages used in vacuum space simulators. Note that the pressure requirements stated above apply when the test item is present. Many test items have phenomenally high outgassing rates and hence a lower empty system pressure is required as well as a very high pumping speed.

Outgassing is sometimes cited as a justification for further reduction in the pressure level for simulation. This is true in certain extreme cases where surface phenomena are being studied and where the pressure level can be reduced well into the ultrahigh vacuum region, in the order of 10^{-10} torr. However, in most situations, a reduction in operating pressure below 10^{-6} torr does not have a measureable effect on the outgassing rate.

An example will illustrate the outgassing problem and the complexities of simulating space vacuum in general. Suppose we wish to measure the evaporation rate of a hydrocarbon lubricant to be used in a space vehicle. A sample might be placed in an ultrahigh vacuum chamber which has been baked out and would have an ultimate pressure in the range of 10^{-10} torr in the absence of the lubricant. Initially, the lubricant would evaporate at its full rate and condense on the walls of the test chamber. Soon, the chamber walls would become covered

with a layer of the oil, which would feed back to the sample, thus reducing the observed evaporation rate.

The results would be much different if the test was run in much poorer vacuum (still in the molecular flow region), *but* with a low-temperature surface in line with the evaporating molecules from the lubricant. In this event, the cold surface would continue to condense the evaporating molecules, preventing their return to the lubricant sample, As a result, full evaporation would continue and a valid measurement of the evaporation rate could be made despite the fact that the total pressure may be considerably higher than the equilibrium vapor pressure of the lubricant.

The approach of supplying large-area condensing surfaces surrounding the test item is typical of the present trend in space simulation. Black, liquid-nitrogen cooled panels are used to provide a sink for both thermal radiation and condensible gas molecules such as water vapor. These panels also act as thermal radiation barriers when 20° K pumping panels are used. The 20° K panels, in turn, reduce the number of diffusion pumps required for most applications, but some are still required to handle the non-condensible gases H_2, He, and Ne.

Thin Film Deposition is Different

In space simulation, we noted the deliberate use of several methods of pumping. When thin films are deposited, several pumping methods are also present, but not intentionally. Let's see why.

The thin films that are presently used for computer elements and for microminiaturized electronic components are produced by evaporating a material and collecting a deposit on a substrate such as glass. The surface of the freshly deposited film has a high affinity for the gas molecules that are constantly bombarding it, from the vacuum environment. This gettering action of the film itself adds impurities to the film, and in many instances, affects its properties. The magnitude of the pumping action can be considerable: at an evaporation rate of 10 A/sec and a gas pressure of 10^{-5} torr, there are as many impurity molecules bombarding the surface as there are molecules being deposited. If all gas impurities were to stick, the film would contain 50% impurity, some of which, ironically, were dissolved in the original solid evaporant.

In thin-film deposition, as in many high-vacuum phenomena, it is not just the total pressure which is important, but rather the partial pressure of particular gas types. Film properties are affected more by such impurities as water vapor and hydrocarbons than by inert gases such as nitrogen or argon. As a result, it is sometimes necessary to use the best of the modern ultrahigh vacuum techniques. In these cases, bakeable systems with ultimate pressures as low as 10^{-10} torr are used to produce films with relatively low contamination. For other film types, contaminated atmospheres and total pressures as high as 10^{-4} torr are adequate.

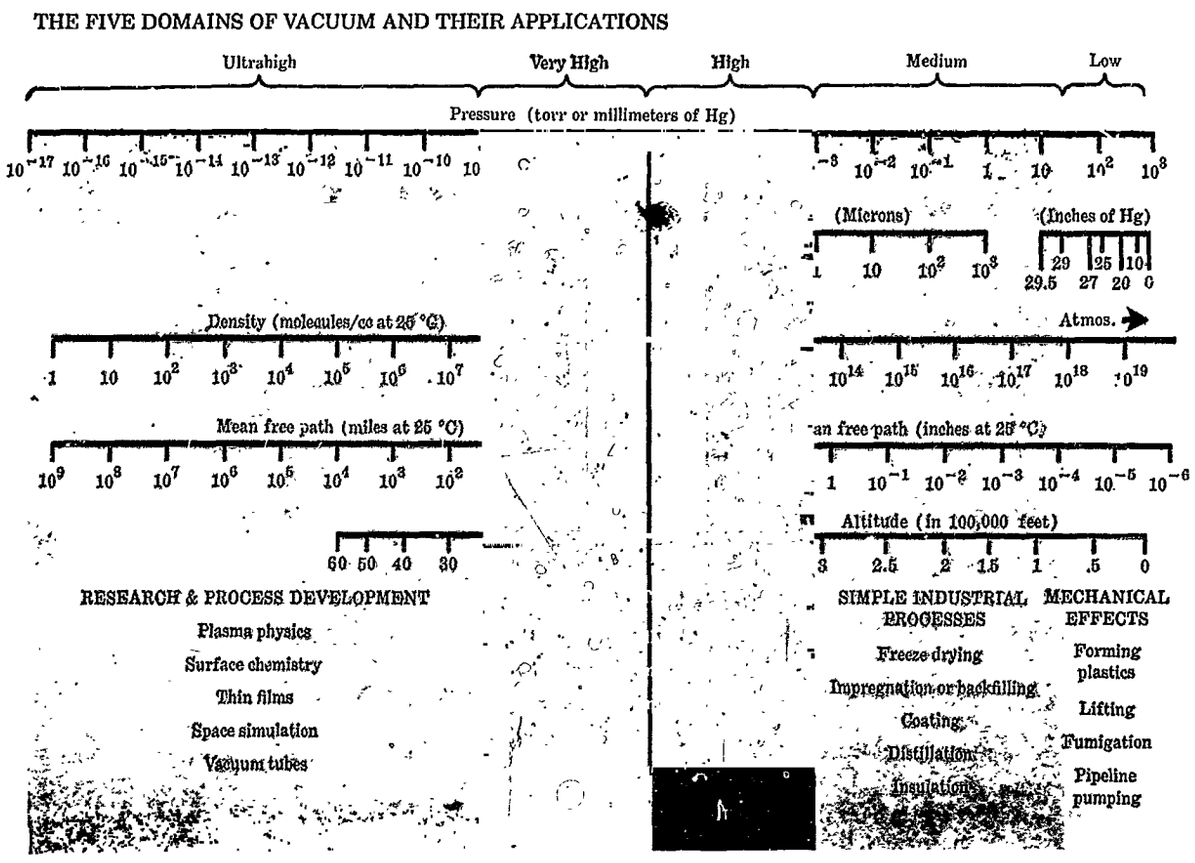

Fig. 1. The five domains of vacuum, as defined by modern low-pressure parlance, actually turn out to be four in terms of application areas. Most of the applications cluster in high- and very-high-vacuum domains, from 10^{-3} down to 10^{-9} torr. And most of these currently concentrate in the 10^{-4} to 10^{-7} torr range, the densest tone above.

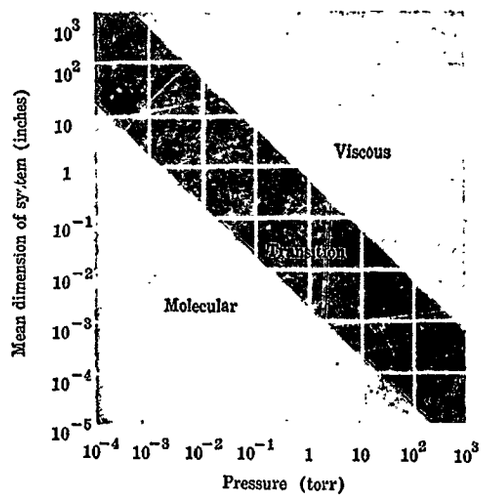

Fig. 2. Regimes of flow. At high pressure (low vacuum), flow may be viscous—molecules are close and can interact. At low pressure (high vacuum), they are far apart—flow is governed by statistics of interaction with the system walls.

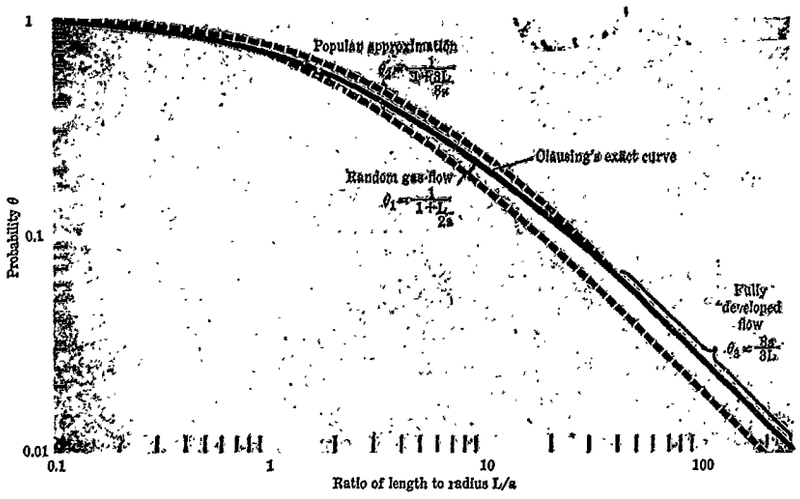

Fig. 3 Probability of gas molecules moving through a pipe once they enter it depends on pipe geometry. Solid line is exact probability curve whose equation is complex. Curve Θ_2 has simple equation, matches exact curve when $L/a > 4C$. Curve Θ_1 assumes random molecular flow down the pipe, matches exact curve only when $L/a < 1.5$.

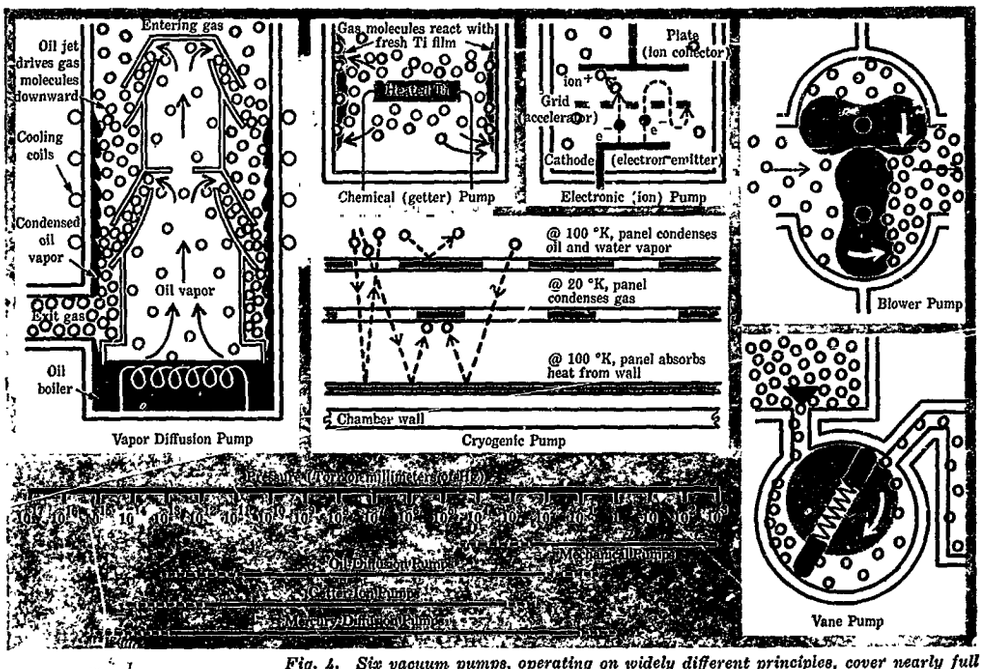

Fig. 4. Six vacuum pumps, operating on widely different principles, cover nearly full spectrum of vacuum domains, as shown by bars at bottom. Dashes are possible extensions of normal usage. The low-pressure limits shown can only be achieved by using bake out techniques. Note how simple diffusion pump easily reaches to 10^{-9} torr. one reason many industrial processes can operate at this low a pressure.

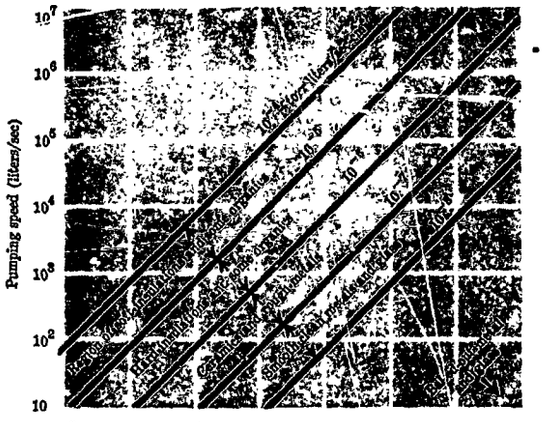

Fig. 5. From this nomograph you can estimate pumping speeds required to keep up with outgassing of various materials under nonbaked conditions. For example, a vacuum of 10^{-6} torr around 100 in.² of ceramic would need a pumping speed of from 70 to 700 liters/sec, depending on precise kind of ceramic. Outgassing rates shown are aft[illegible]

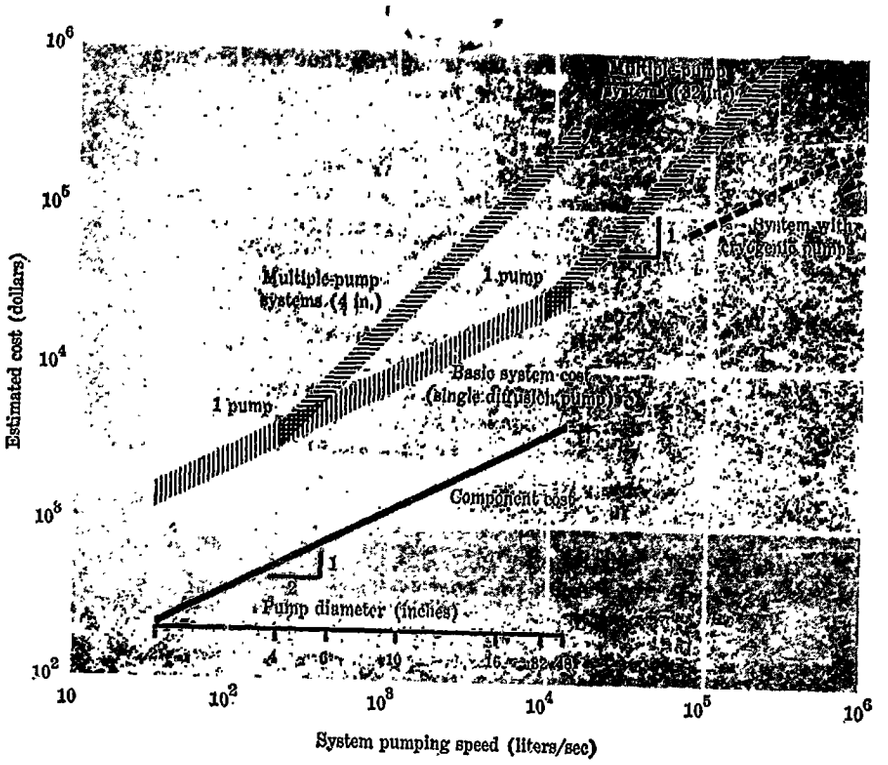

Fig. 6. Cost of basic system for evacuating a chamber can be estimated as a multiple of component costs, depending on speed desired. Multiple-pump systems give higher pumping speeds, and those with fewer pumps of larger diameter do it cheaper. Tentative costs on cryogenic pumping show it may be most economical of all for high pumping speeds.

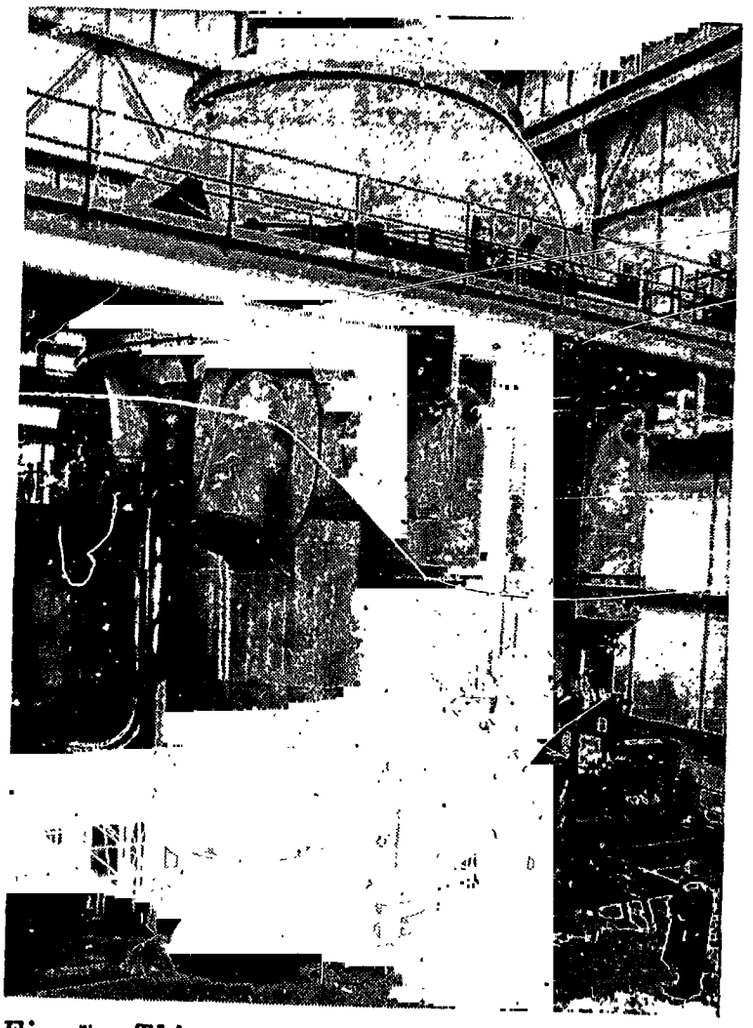

Fig. 7. This vacuum chamber simulates the hostile environment of outer space. The two diffusion pumps at right, coupled with 20°K cryogenic pumping, can hold chamber well below 10^{-8} torr. Solar radiation is mulated by xenon lamps directed through port at left center into parabolic reflectors under dome. Interior panels are cooled to 100°K to simulate thermal sink of space.

N66 28901

ELECTROMAGNETIC RADIATION IN SPACE

By

Francis J. Clauss

Lockheed Missiles and Space Company

INTRODUCTION

The purpose of this paper is to discuss the significance of the electromagnetic radiation in space to the design, testing, and operation of spacecraft.

Since this is a Conference on The Role of Simulation in Space Technology, the three types of questions which this paper is concerned with are (1) what is to be simulated, (2) why it should be simulated, and (3) how it can be simulated.

To answer the first of these questions, the first part of this paper describes the electromagnetic radiation that a spacecraft experiences in space.

Simulating electromagnetic radiation in the aerospace industry is generally done for one of three reasons:

1. To evaluate the performance of spacecraft systems that use electro-magnetic radiation either as a source of power or as an information signal. Solar cells are an example of the first of these, and horizon sensors of the second.

2. To verify the thermal design of a spacecraft or a particular spacecraft system.

3. To study photochemical effects, such as the photodegredation of spacecraft materials.

These three types of applications are discussed in some detail in succeeding sections of this paper, followed by a discussion of techniques for simulating electromagnetic radiation in order to study them.

Large amounts of time and money are being spent in simulation tests, and the test results are most important to the design and reliable operation of spacecraft. Therefore, the tests must be well planned and properly conducted. Test planning begins with test requirements, and test simulation must be adequate to meet these requirements. However, oversimulation must be avoided just as much as undersimulation, or costs will become excessive and schedules will be slipped. One is tempted to err on the safe side and try to duplicate the space environment as accurately and completely as possible in order to insure that no side effects are overlooked, but practical limitations usually force one to compromise with a tight schedule and budget. Hard thinking must be substituted for elaborate equipment, and analytical corrections must be used to correct for lack of exact duplication.

Generally, large full-scale tests are needed to verify thermal design, and small-scale laboratory tests are adequate for the other two types of studies. Photochemical effects determined in the laboratory can be taken into account in the large-scale tests, and, conversely, results on the thermal design obtained from large-scale tests are needed to establish component operating temperatures so that the small-scale tests can be conducted

at the proper temperature and the results can be applied correctly to spacecraft design.

While there appears to be common agreement on the above generalities, there is an equal amount of disagreement as to what is an adequate degree of simulation. Fortunately, a large body of basic physical and chemical data is available that can assist the simulation engineer in deciding a specific case. There is also a growing amount of experience in simulating electromagnetic radiation and conducting applied tests in the aerospace industry, as well as the growing confidence from successfully operating a host of varied satellites and space probes. A review of this information and experience is therefore most appropriate to the theme of this conference.

One final introductory remark appears in order. A one-hour paper on electro-magnetic radiation must necessarily be a survey type that presents an overall picture rather than a detailed critique in any one area. The most that can be accomplished with this type of treatment is to furnish a perspective against which to view the detailed work going on in a number of related areas.

CHARACTER OF ELECTROMAGNETIC RADIATION IN SPACE

Types of Incident Radiation

Figure 1 indicates the three types of electromagnetic radiation incident upon satellites and interplanetary space probes. These are:

1. Direct solar insolation, which is solar radiation that impinges directly on the spacecraft.
2. Albedo radiation, which is the solar radiation that is reflected or scattered by a nearby planet's atmosphere back out into space.

3. Planetary emission, which is the solar radiation that is absorbed by the atmosphere or reaches the planet and is then reradiated.

In turn, spacecraft reject heat to space as electromagnetic radiation.

Direct solar radiation is also called primary radiation, and the other two types of incident radiation are together called secondary radiation.

Although all three types of incident radiation originate ultimately from the sun, they differ in their amounts and character and in their use and significance to spacecraft. In the case of the earth, for example, albedo radiation averages about 36 to 38 percent of the direct solar insolation and, like the direct solar insolation, earth albedo lies principally in the wave length region from 3000 to 40,000 Angstroms. Earth emission accounts for the other 62 to 64 percent of the direct solar insolation. But since the earth is cooler than the sun, earth emission is of longer wave length, lying principally in the infrared. Similarly, heat energy emitted by a spacecraft also lies principally in the infrared, since spacecraft surfaces are normally around room temperature.

All three types of incident radiation are involved in the thermal balance of the spacecraft, which in turn determines the spacecraft temperature. Solar cells operate primarily on direct solar insolation, and they are often mounted on arrays that are oriented towards the sun. Horizon sensors sense the discontinuity between cold black space and planetary emission and use it to determine a spacecraft's orientation. Photodegredation of materials is caused primarily by ultraviolet radiation in both the direct solar insolation and albedo radiation.

From these brief comments one must conclude that the requirements for simulating electromagnetic radiation in the aerospace industry vary with the specific applications to be studied.

Primary Radiation

The sun is the most intense source of electromagnetic radiation in space.

Solar radiation originates in nuclear reactions deep within the interior. Energy produced in the sun's interior reaches the surface from which it is released by radiation. The surface of the sun that emits radiation is called the photosphere, and it consists of strongly ionized gases that absorb and emit a continuous spectrum of radiation.

The solar electromagnetic spectrum is a continuous band, as indicated in Figure 2. It starts at the short wave length end with γ-rays and X-rays and extends through the ultraviolet, visible, infrared, and radio waves. Visible light is only a small portion of the spectrum, extending from approximately 3800 to 7000 Angstroms (0.38 to 0.7 microns). The bulk of the solar energy lies between 3000 to 40,000 Angstroms (0.3 to 4 microns), with about 1 percent of the energy beyond each of these limits.

The energy of light varies inversely with wave length or directly with frequency according to the equation

$$E = h\ \nu = h\frac{c}{\lambda} \qquad (1)$$

where E = energy of a photon or light quantum

h = Planck's constant, 6.62×10^{-27} erg sec

c = velocity of light in vacuum, 2.99776×10^{10} cm/sec

ν = frequency

λ = wave length

By means of equation (1) and suitable conversion factors, the wavelength (lower scales, Figure 2) can be converted into energy in units of ergs, calories, electron-volts, and calories per gram-molecule (upper scales, Figure 2).

The manner in which radiation is emitted or absorbed by matter depends upon the wavelength or energy. Gamma-rays arise from changes in the energy levels of the nuclei of atoms and involve atomic transformations; X-rays from the inner electron shells of atoms; ultraviolet or visible rays from electrons in the outer shells; near infra-red rays from the vibrations of atoms bound together as molecules; and wireless waves from the oscillations of electrons set up in closed electrical circuits of comparatively large size.

Figure 3 compares the intensity and spectral distribution of sunlight at the earth's surface and in space (Refs. 1 and 2). Maximum intensity occurs at 4500 to 5000 angstroms (0.45 to 0.5 microns), in the visible range. Both curves are for the earth at a distance of 93 million miles from the sun, which is the mean solar distance, and are subject to a variation of ± 3.5 percent because of seasonal changes in the distance and fluctuations on the sun itself. The curve for solar radiation at the earth's surface is for a surface at sea level that is perpendicular to the sun's rays and with the sun directly overhead (i.e., sun at zenith, air mass = 1). It is modified from the curve in space by scattering and absorption by the air, water vapor, dust particles, and other components in the earth's atmosphere. This causes an overall attenuation, which is greatest at the short wavelengths, and strong absorption at certain wavelengths, The principal absorption occurs in the ozone bands at short wavelengths and in the water vapor bands in the near infrared. Ozone causes almost complete absorption below 3000 Angstroms (0.3 micron). Radiation at wavelengths beyond 23,000 Angstroms (2.3 microns) is so strongly absorbed by water and carbon dioxide that hardly any solar radiation is transmitted.

The absorption and attenuation of ultraviolet radiation is particularly significant, as this portion of the spectrum is primarily responsible for photochemical changes. Since radiation at these wavelengths is notably stronger in space than on earth, photochemical changes are much stronger in space than on earth.

The spectral distribution of solar radiation is approximated by the curve for radiation from a black body at 6000°K, and this temperature can be used as the effective surface temperature of the sun. In theory, solar radiation can be simulated in the laboratory by a cavity radiator maintained at 6000°K. In practice, however, even if materials were available to withstand this temperature, the cavity radiator would have to be almost infinite in size to provide the intensity required for many solar simulation requirements.

At the short wave length end of the spectrum, a number of emission lines are superimposed upon the radiation continuum. These emission lines contribute only a small amount of energy compared to the continuum above about 1400 Angstroms, but they are the major portion of the solar radiation below 1400 Angstroms. Table 1 lists the stronger lines and their intensities (Ref. 1)*. Prominent among these lines is the Lyman-Alpha line for hydrogen at 1216 Angstroms, which has an intensity of 6×10^{-4} milliwatts per square centimeter.

---

*The intensities over the spectral region below 1000A must still be regarded as rather tentative; the values shown are probably correct to better than a factor of five. The spectral lines (shown in Table 2.1) are presented with an effective line width of 10A; however, since their true widths are much less than this, their peak intensities are higher than shown, but the total energies in the lines should be the same as shown." (Ref. 1).

The energy of solar radiation at the outer boundary of the earth's atmosphere on a surface that is normal to the sun's direction and at the earth's mean distance from the sun (93 million miles) is defined as the solar constant. It is equal to the area under the curve in Figure 3 and it has a generally accepted value of 140 milliwatts per square centimeter.*

Since the intensity of light varies inversely as the square of the distance from its source, the intensity of solar radiation at various distances from the sun can be calculated. Results are shown in Figure 4, which also indicates the intensity of solar radiation incident upon the planets. This figure is based on the known distances of the planets from the sun and upon an intensity of 140 mw/cm^2 at the distance of the earth from the sun. The solar energy arriving at the mean orbital distance of Mars is slightly less than half that arriving at the mean orbit of Earth, and that arriving at the mean orbit of Venus is almost twice that for Earth. This variation is important in the thermal design of space probes, as it means a corresponding change in their absolute temperature unless steps are taken to compensate for the changes in intensity during the craft's travels.

Other important sources of electromagnetic radiation in space include the earth, moon, and other planets, which radiate principally in the infrared region, and the stars, which are responsible for radio noise.

Some geometric relations between the sun and the earth (or Venus) are shown in Figure 5 (Ref. 3). Since the diameter of the sun is on the order of 864,000 miles and the sun is about 93 million miles from the earth,

---

*Or, in other units, 0.123 Btu/ft^2/sec. = 7.38 Btu/ft^2/min. = 442.8 Btu/ft^2/hr. = 2.05 calories/cm^2/min. = 1400 watts/meter^2 = 0.140 watts/cm^2 = 140 milliwatts/cm^2 = 1.43 x 10^6 erg/cm^2-sec.

the field angle subtended by the sun at the earth is 32 minutes, and solar radiation reaching the earth or the surface of a satellite orbiting about the earth is essentially collimated to parallel rays.

The values of the essential solar radiation parameters in space at the earth's orbital distance are summarized in Table 2.

Secondary Radiation

Secondary radiation includes both albedo radiation and planetary emission.

Albedo radiation is the solar radiation that is reflected or scattered by a nearby planet's atmosphere back out into space. Its intensity varies with altitude, but is seldom more than 10 or 15 percent of the total heat load incident upon a satellite. Albedoes from the earth and other planets are estimated in Table 3.

The spectral distribution of albedo radiation is altered from the direct solar insolation due to preferential Rayleigh scattering by the atmosphere. For most calculations on the thermal balance of spacecraft, however, the spectral distribution of earth albedo is assumed equivalent to that of the sun. In the absence of data on the spectral distribution of albedo of other planets, their albedoes are also assumed to have the same spectral distribution as the sun.

Scattering and reflection diffuse the energy so that albedo radiation appears to originate from a hemisphere rather than a collimated beam as in the case of direct solar insolation. The field angle subtended by the earth is very large and depends upon the altitude or distance to other nearby planets; for a satellite in a 100-mile orbit about the earth, the field angle would be about 170 degrees.

Planetary emission (so-called "earthshine" in the case of the earth) is electromagnetic radiation emitted by a planet. This radiation represents

the solar insolation that has been absorbed by the planet and its atmosphere and is then reradiated as thermal energy. The spectral distribution of planetary emission may be assumed to be that of a black body at the temperature of the planet.

The intensities of planetary albedo and emission vary with the altitude and the orientation of a surface. Figure 6 illustrates the variation in intensity with altitude for a flat surface that is located directly between the earth and the sun and is perpendicular to the earth-sun line. Albedo radiation on the side facing the earth is more than twice the earth emission, and both decrease as the altitude increases. The direct solar radiation on the side facing the earth is zero, of course, while on the side facing the sun it is 140 mw/cm^2, or 1 solar constant. Since the distance of the plate from the sun is not significantly affected by the changes in altitude above the earth, for the range indicated, there is no change in the direct solar radiation with altitude. Note also that as the altitude increases, the percentage of secondary radiation (albedo plus emission) diminishes in comparison to the amount of primary radiation.

When the flat plate is on the opposite side of the earth, away from the sun, both the direct solar insolation and earth albedo are zero for both sides of the plate. On the other hand, earth emission incident on the side facing the earth is the same whether the plate is between the sun and the earth or in the earth's shadow, and it is always zero on the side away from the earth.

Table 4 illustrates further the manner in which the average intensities of earth albedo and earth-atmosphere emission vary with the altitude and orientation of a satellite surface.

The angle of incidence at which albedo radiation impinges upon a satellite

surface can cover the range of angles subtended by the illuminated portion of the earth. For earth-atmosphere emission, the angle of incidence covers the range of angles subtended by the earth, whether directly illuminated by the sun or not. Consequently, the angles of incidence vary with altitude and, in the case of albedo, also with the satellite's position with respect to the earth-sun line. For a satellite in a 100-mile orbit about the earth, for example, the field angle of earth emission is about 170 degrees.

Aside from the planets, the sun, and other stars, space appears as a black body whose temperature is a few degrees above absolute zero. Space is essentially a non-radiating, non-reflecting heat sink for receiving radiation from a spacecraft. It can be simulated thermally by walls of a space simulator that have an absorptance close to unity for all wavelengths at which the spacecraft radiates and that have a temperature of 100°K or lower.

THERMAL BALANCE OF SPACECRAFT

One of the most important effects of electromagnetic radiation in space is its effect on spacecraft temperature.

Requirements of Spacecraft Systems

In order for electronic equipment and power supplies to operate, as well as for human passangers to survive, spacecraft temperatures must be kept within prescribed limits despite the extremes of heating and cooling to which spacecraft are subjected. Figure 7 shows the normal operating temperatures for various types of payloads. The limits are not well defined, as efficiencies can vary with temperature even within the normally acceptable range and closer control is sometimes desirable. Outside the limits

shown, not only is the efficiency seriously reduced, but also operation can stop, sometimes with permanent damage to the system. For most payloads, one tries to maintain temperatures around room temperature with a modest swing above and velow that level.

Since space is essentially a vacuum, heat transfer to and from spacecraft is almost entirely by radiation. Radiant energy is received by earth satellites and other space vehicles by direct solar insolation, albedo, and planetary emission, as discussed in Section 2. Internal heat released from batteries or power plants is also a part of the total energy input. At the same time, energy is radiated from the surfaces of the spacecraft, and the temperature of the spacecraft is determined by a radiant energy balance between the inputs and the outputs.

Active systems for controlling temperatures can be and sometimes are used, such as shutter systems, heating and refrigerating systems, and heat switches for regulating internal conduction. However, even the simplest active controls add weight and bulk at the expense of the payload. Weight and bulk penalties are also imposed for such passive control systems as the addition of thermal capacity.

Most spacecraft have used passive controls that incorporate stable surfaces that have the proper radiation characteristics. These thermal-control surfaces are essentially tailored to the job of receiving and emitting radiant energy in balanced amounts. The principle is similar to that involved in choosing summer clothing; dark clothing absorbs sunlight and makes the wearer warmer, whereas light-colored clothing reflects the sunlight and is cooler. By using surface materials that have the proper values of absorptivity and reflectivity, the temperature of a body that is in radiative equilibrium with its surroundings can be controlled.

The importance of the surface radiative properties on temperature can be illustrated by calculating its effects on the equilibrium temperature of a body in the solar system (cf. Ref. 4). For simplicity, consider a spinning sphere far removed from any planet so that it receives heat only by solar radiation. The heat absorbed is then given by

$$Q_1 = \alpha \frac{E}{r^2} A_c \qquad (2)$$

Q_1 = heat absorbed

α = surface absorptance for solar radiation

r = distance from the sun in astronomical units, where astronomical unit is the mean distance of the earth from the sun (93 million miles)

E = solar radiation flux at the Earth's mean distance from the sun = 1.43×10^6 ergs/sec-cm^2

A_c = projected area normal to the incident solar radiation = πR^2 for a sphere of radius R.

The heat emitted is given by

$$Q_2 = \varepsilon \sigma T^4 A_s \qquad (3)$$

where

Q_2 = heat emitted

ε = surface emittance

σ = Stefan-Boltzmann constant for blackbody radiation = 5.67×10^{-5} erg/sec-cm^2-$^\circ$K^4

T = surface temperature, $^\circ$K

A_s = radiating surface = $4\pi R^2$ for a sphere of radius R.

For steady-state conditions and no internal heat generated, Q_1 and Q_2 are equal, so that

$$\alpha \frac{E}{r^2} A_c = \varepsilon \sigma T^4 A_s \qquad (4)$$

and the radiation equilibrium temperature is

$$T = \left[\frac{\alpha}{\varepsilon} \frac{1}{r^2} \frac{E}{\sigma} \frac{A_c}{A_s} \right] 1/4 \qquad (5)$$

The surface temperature at equilibrium for this case thus depends (1) on the ratio α/ε, which is the ratio of its absorptance for solar radiation to its emittance, (2) on its distance from the sun, and (3) on the ratio of its projected area to its radiating area. Temperatures of a spinning sphere ($A_c/A_s = 0.25$) calculated by means of equation (5) are shown in Figure 8 as a function of distance from the sun for $\alpha/\varepsilon = 0.10$, 1.0, and 10.0. Figure 8 also indicates the average estimated temperatures of the planets (Ref. 5). Note that planet temperatures lie slightly below the line for $\alpha/\varepsilon = 1.0$; this is because a portion of the solar radiation is reflected from the planetary atmosphere and surface (i.e., $\alpha<1.0$) and because multiple absorbing and emitting layers in planetary atmospheres results in an emittance close to unity ($\varepsilon \simeq 1.0$) (Ref. 4).

Because of their temperatures, planetary emission is mostly in the infrared region, and the α/ε ratio is the ratio of solar absorptance to infrared emittance for the surface (i.e., the ratio of absorptance for short wavelength radiation of the type present in solar radiation to the emittance in the infrared). Alpha (α) is measured for the spectral region from 2,000 to 30,000 Angstroms (0.2 to 3.0 microns), wherein over 98 percent of the sun's energy is emitted, and epsilon (ε) is measured for the spectral range beyond 30,000 Angstroms (3.0 microns), wherein over 99 percent of the energy from a spacecraft operating at normal temperatures is emitted.

As equation (5) indicates, the mean surface temperature of a satellite in orbit increases with the fourth power of the α/ε ratio. Also, for a given α/ε ratio, the orbital oscillations increase with increasing ε.

Figure 9 shows the effects of surface radiative properties on the temperature of earth orbiting of satellites. Auxiliary scales in this figure indicate the range of α/ε ratios obtainable with various surfaces.

Verifying the Thermal Design of Spacecraft

Predicting spacecraft temperatures requires sophisticated mathematical analyses of the external environment, the orbit geometry, and internal power generation, as well as the thermal radiation characteristics of exterior and interior surfaces. Surface reflections and thermal conduction through skins and joints are particularly difficult to handle analytically.

Since predicted temperatures are subject to error, the thermal design is usually verified experimentally in large chambers that can contain the entire spacecraft system.

Three different approaches are used to verify thermal design, which differ in their sophistication and cost. Thermal simulation, the first of these, is a technique whereby the spacecraft surfaces are heated or cooled in vacuum to the skin temperatures that have been calculated for them under space conditions, and the temperatures of the spacecraft components (e.g., systems, payloads, and critical areas) are measured. The spacecraft skin is forced to follow the temperature-time history that has been analytically predicted by means of heaters, heating panels, and cooling coils, for example, placed at appropriate positions either on or adjacent to the skin.

Absorbed radiation simulation (also called the absorbed heat flux technique) refers to duplicating the amount of heat flux that is calculated to be absorbed by the skin while in space. The satellite skin is made to follow

the calculated net radiant interchange with its environment.

Incident radiation simulation (also called exact simulation) refers to duplicating all of the characteristics of the radiation calculated to be incident upon the skin while in space. Intensity, spectral distribution, angle of incidence, and other characteristics of the incident radiation are provided at the levels which will be incident upon the spacecraft in space.

Viewed in another way, one might say that the common objective of all three techniques is to provide a calculated boundary condition so that the components and structural elements are caused to operate at the same temperatures that they will in space. These temperatures can then be measured and compared to their calculated values to insure that they are within safe limits. The calculated boundary conditions can be either the skin temperature, the amount of radiant energy absorbed by the skin, or the amount and character of the radiant energy that is incident on the skin.

Regardless of the technique chosen, the first step is to determine the heat balance in space. Techniques for making these calculations are discussed elsewhere (cf. refs. 6, 7, 8, and 9).

The techniques are sometimes combined. For example, the primary solar insolation that is incident on the spacecraft may be reproduced exactly, and the secondary radiation (i.e., planet and albedo reflection) may be simulated by the absorbed heat flux technique.

In at least the last two of the three techniques, a thermal sink simulates the black void of outer space, which absorbs but does not emit radiant energy.

SOLAR CELLS

Solar cells continue to be the primary source of electrical power for long-lived spacecraft. Although other types of energy conversion devices such as thermoelectric generators and thermionic devices are being improved for converting solar energy into electrical power, solar cells will apparently continue to be used on spacecraft for some time.

Figure 10 indicates the essential elements of a solar cell. Without going into the solid state theory behind its use (Refs. 10, 11, and 12), suffice it to say that the primary process in the conversion of radiant energy to electrical energy by the solar cell is the absorption of photons of radiation in such a way that the photons split off electrons from their normal positions in the crystal lattice, leaving behind a positively charged hole or vacancy. The electron and hole are then available to conduct electricity, provided they can be prevented from recombining and neutralizing each other. The p-n junction is the heart of the solar cell in the sense that it is the p-n junction that provides a built-in electric field that pulls the electrons into the n or negative side of the junction and pulls the holes into the p or positive side before many of them recombine. The electrons and holes are said to be collected by the junction. With suitable contacts and leads to the two sides of the junction, the resultant current can be used in an external circuit. Thus, the actual conversion from light to electrical energy occurs by the creation of a hole-electron pair, with the simultaneous destruction of a photon, and the ability to provide a useful electrical current to an external load becomes practical under the influence of the electric field of the p-n junction.

In a solar cell, as shown in Figure 10, the p-n junction is made very large and is oriented to face the sun. The top layer of semiconductor material above the junction (i.e. the p-layer in the p-on-n cell shown in

Figure 10) is made very thin (on the order of 0.4 to 1.0 micron) so that as many photons as possible can penetrate to the vicinity of the junction. Penetration of radiation over most of the useful spectrum is extremely shallow, so that it becomes necessary to place the p-n junction as near to the surface as possible. However, if the surface layer is too thin, power losses become excessive due to the resistance of the surface layer and the contact resistance. With silicon, the effective wave lengths of solar energy are absorbed in the outer 10^{-3} inch layer, and to be collected (i.e., to reach the p-n junction before they are lost by recombination), the electron-hole pairs must be produced within about 10^{-4} inch of the junction. In addition, the surface must have high electrical conductivity, or much of the electrical power generated is lost through the generation of heat due to the internal resistance of the cell.

While silicon solar cells remain the type most used today, the p-on-n type shown in Figure 10 is being replaced by the n-on-p type.

Figure 11 illustrates the effect of wavelength, or photon energy, on the efficiency with which photons are absorbed to create hole-electron pairs. Furthermore, the wave lengths at which a cell is most efficient can be adjusted by the choice of the semiconductor material and doping agent, by the thickness of the top layer, and by processing techniques. For example, making the top layer thinner (i.e., moving the p-n junction closer to the surface) increases the response of the cell at shorter wave lengths. For maximum efficiency, the response of the cell should be adjusted to be a maximum at the wave lengths at which photons are most numerous, which is at about 6000 Angstroms (0.6 microns) wave length. Photons with energies less than the band gap energy of silicon (1.08 electron volts, which corresponds to a wave length of 11,477 Angstroms) are completely ineffective in producing

electricity, and their energy is dissipated as heat. The rapid drop-off in response at short wave lengths is due to carrier loss mechanisms near the surface, where most of these short wave lengths are absorbed (Ref. 12).

To obtain a spectral response curve such as that in Figure 11, the output of the silicon solar cell and the incident energy are measured at each wave length, and the output is divided by the incident energy. The relative response for equal incident energy is normalized by reduction to a fraction of the maximum response. The relative response for equal numbers of incident photons can be obtained by multiplying the relative response for equal incident energy for wave length λ by $1/\lambda$, and renormalizing.

The relative spectral output of a solar cell under space solar radiation can be obtained by combining data on the solar spectrum (Figure 3) with the relative response of the cell (Figure 11). (Figure 12 shows the result). The total output of the cell is given by the area under the lower curve. For a cell having an efficiency of 10.5%, which appears typical of current practice, this area equals 14.7 milliwatts per square centimeter (i.e., 0.105 X 140 mw/cm^2, where 140 mw/cm^2 is the solar constant).

Characteristic output curves of silicon solar cells are as shown in Figure 13. With the terminals open (no current), the collected carriers accumulate until the open-circuit voltage (V_{oc}) biases the junction so that the forward current equals the collected current. When the terminals are shorted, nearly all the collected carriers provide the short-circuit current (I_{sc}). To obtain an I vs V curve such as shown in Figure 13, the cell is exposed to a constant illumination and the current and voltage are measured as the load resistance is varied between short circuit and open circuit.

The maximum power that can be extracted from a solar cell is represented by the area of the largest rectangle that can be inscribed below the I vs V curve in Figure 13. Individual cells are grouped in series and parallel arrangements so that the power drawn by the external load is matched as well as possible with the maximum power that can be supplied.

Figure 14 shows the effect of temperature upon the maximum power and other cell characteristics (Ref. 12a). As the cell temperature increases, the short-circuit current increases, due to an increase in minority carrier lifetimes with temperature which shifts the absorption edge of the cell to longer wave lengths and improves the red response of the cell, thereby allowing a large fraction of the incident photons to be absorbed usefully. This effect is more pronounced with a tungsten filament operating at 2800°K than with a 6000°K black body typical of solar radiation in space. The open-circuit voltage and the maximum power available both decrease with temperature, as do also the current and voltage at maximum power. The maximum power decreases with temperature at an approximate value of 0.534 percent of the value at 27°C per degree Centigrade rise over the interval from 27°C to 100° C.

A simplified calculation can be made to illustrate both the need to maintain solar cell temperatures at nearly constant, low values and the importance of providing correct surface radiative properties to do this. Consider the case of solar cells mounted on one side of a paddle that is oriented towards the sun and that is far enough away from nearby planets to neglect their radiation. The thermal isolation of cells mounted on paddles from the payload is much better than when the cells are mounted on the spacecraft's surface, and the energy balance of the cells can be approximated by considering heat inputs and outputs by radiation alone.

Also, the structure can be designed with sufficient thermal conductance so that the back side (away from the sun) is at approximately the same temperature as the front side (facing the sun). Setting the heat received equal to the heat emitted gives

$$\alpha_c E A_c = \varepsilon_c \sigma T^4 A_c + \varepsilon_B \sigma T^4 A_B \qquad (6)$$

where the symbols have the same meanings as before and the subscripts "C" and "B" refer to the cell-side and back-side of the paddle array, respectively. Setting $A_c = A_b$ and rearranging equation (b), one obtains

$$T = \left[\left(\frac{\alpha_c}{\varepsilon_C+\varepsilon_B}\right)\left(\frac{E}{\sigma}\right)\right]^{1/4}$$

Typical values of α_c and ε_c for bare, uncoated solar cells are 0.94 and 0.31, respectively. A typical value of ε_B is 0.90, obtained by painting the back-side. Substituting these values into equation (7), one obtains

$$T = \left[\left(\frac{0.94}{0.31+0.90}\right)\left(\frac{1.43\times10^{6}}{5.67\times10^{-5}}\right)\right]^{1/4} = 374°K\ (101°C)$$

Figure 14 indicates that the maximum power available from a solar cell at this temperature will be only 60 percent of its maximum power at 27°C.

The temperature of the solar cells can be reduced by placing over it a transparent dielectric, such as a glass cover plate, which raises the value of ε_c to about 0.90. In this case,

$$T = \left[\left(\frac{0.94}{0.90+0.90}\right)\left(\frac{1.43\times10^{6}}{5.67\times10^{-5}}\right)\right]^{1/4} = 339°K\ (66°C)$$

and the maximum available power is raised to 80 percent of its value at 27°C.

While the calculations above have been simplified,* they do demonstrate the need to use transparent dielectric coverings over solar cells. These coverings have the additional use of protecting the cells against mechanical damage, surface contamination, and beta radiation (electron) damage.

Three systems of coverings have been proposed for use on solar cells for spacecraft power systems.

1. The first and most widely used system, which is shown in Figure 15, consists of a dielectric cover plate such as glass or quartz that is cemented to the surface of the solar cell by a transparent adhesive and is provided with suitable anti-reflecting and anti-UV coatings. The advantage of this system is that it provides a thin, compact, lightweight system. The disadvantage is that the adhesive layers are subject to ultraviolet degredation, resulting in a loss of transmission, unless the anti-UV coating is 100% effective. Also, such a system is very expensive.

2. The second system, which has been used on the Telstar satellite, is similar to the first, but the cover plate is mechanically fastened over the solar cell rather than adhesively bonded to it. This eliminates any loss in transmission to the solar cell as a result of adhesive degredation, but is a bulkier and heavier construction.

3. A third system, which has so far not been effective, is the use of a coating of dielectric resin, such as an epoxy or silicone adhesive, directly on to the surface of the solar cell. This would provide a lighter and cheaper system than the first one, but its use has been restricted because of ultraviolet degradation of the resin.

It is worth emphasizing here that photodegredation of coverings is an important consideration in solar cell design. This topic is discussed later in this paper in the section titled "Photochemical Effects on Materials."

---

* Exact calculations would reduce the energy input in equation (6) by the amount of energy converted to electricity; this can be done most readily by using a "corrected" value of α_c that is obtained by multiplying the uncorrected value by (1 - cell efficiency). This correction would result in lower values for the temperatures calculated above (73°C for the bare cell and 33°C for the covered cell) giving maximum powers of 76 and 97%, respectively, of the maximum power at 27°C.

PHOTOCHEMICAL EFFECTS

General

Previous sections have considered the absorption of electromagnetic radiation and its conversion into electrical power and into heat. Another manner in which electromagnetic radiation can be absorbed by matter is to excite molecules and cause them to undergo chemical reactions or dissociation. Some of these reactions can be usefully employed by spacecraft systems, as the photochromic thermal-control surfaces, and photorigidization of polymeric structures. Others affect spacecraft performance adversely, as the photodegredation of thermal control surfaces and solar cell adhesives. In the field of simulation, photochemical reactions provide a useful means of measuring and calibrating secondary sensors for measuring the intensity of radiation, especially that at short wavelengths in visible and ultraviolet regions.

While a comprehensive treatment of photochemistry is well beyond the purpose of this paper, a few general comments on the principles involved in photochemical reactions should be helpful to understand specific cases. Two specific examples of photodegradation that are of concern in the aerospace industry are presented as illustrations and to emphasize the need for studying photochemical effects.

Some Photochemical Principles (Ref. 13 through 16)

The initial step in a photochemical reaction is the absorption of a photon of light by a molecule, which is then activated. The energy of photons varies with their wavelength in the manner discussed in Section 2.

Following absorption, molecules undergo changes in their vibrational, rotational, and electronic energy, depending upon the energy of the absorbed

photon. Transitions in the electronic energy states are most important in photochemistry, since these lead to chemical changes in the molecule.

The absorption of a photon does not guarantee that a photochemical reaction will result. In order to initiate the reaction, the energy of the excited molecule must be equal to or greater than a minimum quantity, called the activation energy of the reaction. The majority of photochemical reactions require activation energies greater than 50 kcal per mole, or 2.16 electron volts, which corresponds to a wavelength of 5710 Angstroms (0.571 microns). In other words, wavelengths shorter than 5710 Angstroms (0.571 microns) are the ones responsible for initiating most photochemical reactions. In fact, most of the photochemical reactions of interest to space technology are caused by ultraviolet radiation with wavelengths shorter than 4000 Angstroms. Also, since a good deal of the ultraviolet radiation between 3000 and 4000 Angstroms is attenuated by the atmosphere and since ultraviolet radiation below 3000 Angstroms is completely absorbed in the atmosphere, there is a great deal more radiant energy for causing photochemical reactions in space than on earth, and the sun is not an adequate simulator for studies on earth.

The extent of chemical changes in photochemical reactions depends upon the number of molecules that are activated by absorbing photons. The ratio of the number of molecules that are chemically changed to the number of photons absorbed is called the "quantum efficiency." Quantum efficiencies are commonly on the order of unity, though rarely exactly one, and they can vary from exceedingly low values, as with light stable dyes, to a million or so, as when light initiates chain reactions. Quantum efficiencies generally vary with changes in wavelength, light intensity, temperature, and other conditions.

The fact that quantum efficiencies vary with the above conditions implies that these conditions must be very accurately reproduced in any laboratory tests to evaluate the photochemical effects of electromagnetic radiation in space. The experimenter must therefore consider the necessity of simulating very short ultraviolet radiation, down to 1000 Angstroms (0.1 micron), and less, and the necessity of running very long-time tests. Sources for radiation below 2000 Angstroms (0.2 micron) are more expensive and difficult to use than sources for radiation above 2000 Angstroms, so there is a very real practical reason for desiring to limit tests to wavelengths above 2000 Angstroms. Moreover, conducting tests for the full time periods that will be encountered by spacecraft ties up equipment and slows down the production of data, so there is a very real need to accelerate tests by increasing the intensity of radiation and shortening the time of exposure by a corresponding amount.

A closer look at the solar spectrum in space reveals that the near ultraviolet radiation, with wavelengths from 2200 to 4000 Angstroms (0.22 to 0.4 microns) includes 9.01 percent of the total solar energy, whereas the far ultraviolet radiation, with wavelengths shorter than 2200 Angstroms (0.22 microns) accounts for only 0.02 percent of the total solar energy. In other words, almost 98 percent of the total energy of ultraviolet radiation is concentrated in the range from 2200 to 4000 Angstroms, which is relatively easy to simulate, and about 2 percent in the range below 2200 Angstroms, where simulation is more difficult. Although the intensity of the far ultraviolet radiation in space is small, one can argue that its effects can still be significant because of the higher energies of the photons of shorter wavelengths. Several investigators, however, have found experimentally that the effects of far ultraviolet radiation on the photodegradation

of materials are small and similar to the effects caused by near ultraviolet radiation (Refs. 17 and 18). Only the high quantum yields for photo-emission from metals were found to be unique for the far ultraviolet range. While additional verification of these findings would be most welcome, it appears that the stability of spacecraft materials under electromagnetic radiation can be adequately evaluated by laboratory tests in which the solar radiation is simulated down to 2200 Angstroms.

In many cases, the effect of the light intensity on the quantum efficiency is smaller than the experimental effects being measured, provided that no side effects are introduced, such as different temperatures, for example. Where this is true, tests can be accelerated by running at a high intensity for a short period of time so that the total incident energy is the same as for a longer period of time at lower intensity. This reciprocity between time and intensity makes it possible to obtain test results in a short time that predict the behavior of spacecraft materials over much longer periods of time in space.

The effect of interactions between the atmosphere and the other reactants of a photochemical reaction is also important. Much of the normal photodegradation of materials is not due to radiation-induced changes in the materials themselves but rather to reaction of the materials with ozone or other activated components of the atmosphere. In this respect, the vacuum of space is an advantage rather than a disadvantage, in that it can reduce the amount of photodegradation that would otherwise occur in air. It is important that a hard vacuum be provided in simulation tests to study photodegredation of materials in space.

Another factor that should not be overlooked is the reversibility of hotochemical reactions, such as the bleaching of color centers produced

in solids by ultraviolet radiation. This is important in the behavior of thermal-control surfaces. We have observed that the discoloration of some thermal-control paints caused by ultraviolet radiation bleaches out when the ultraviolet radiation is removed.

Photodegradation of Thermal-Control Surfaces

Passive techniques are invariably used either by themselves or in conjunction with active elements for controlling the temperature of spacecraft. The passive technique depends upon providing surfaces that have the proper optical characteristics for balancing the amounts of incident and emitted electromagnetic radiation, as discussed in Section 3. For spacecraft that must operate for long lifetimes in space, the stability of thermal-control surfaces under prolonged exposure to ultraviolet radiation is a prime consideration.

Figure 16 shows the effect of ultraviolet radiation on the solar absorptance of an organic-base white paint (Ref. 19). As the number of sun-hours of exposure to ultraviolet radiation increases, the solar absorptance increases. For the material shown, the initial solar absorptance can double in approximately 150 sun-hours of exposure. All other factors remaining constant, doubling the solar absorptance will raise the surface temperature 57°C (103°F).

Table 5 presents typical results of exposure to ultraviolet radiation on the solar absorptance and infrared emittance of various types of thermal-control surfaces (Ref. 20). Infrared emittance of white and black paints is not greatly affected, but the solar absorptance of organic-base white paints is substantially increased, leading to higher alpha-over-epsilon ratios and higher temperatures. Inorganic-base white paints are considerably more stable than organic-base ones.

Photodegradation of Optical Adhesives

Adhesives for optical systems must be highly transparent at the wavelengths that are to be transmitted and must have adequate strength and elasticity to resist mechanical and thermal stresses. Under intense ultraviolet radiation, adhesives discolor and lose their transparency. They can also undergo crosslinking and chain scission, particularly under penetrating particle radiation, that reduces their strength and elasticity so that the adhesive layer can rupture under thermal stresses.

One example of the above, which has been studied widely because of its importance in space technology, is the photodegradation of adhesives used to attach cover plates over solar cells. As indicated in Section 4, transparent dielectric coverings such as thin plates of glass or quartz are used over solar cells primarily (1) to provide a surface of high infrared emissivity in order to dissipate heat efficiently so that the cell temperature is kept low and its conversion efficiency is kept high; and (2) to protect the solar cell itself from penetrating radiation, such as high-energy electrons, that would otherwise reduce its conversion efficiency. Such dielectric coverings are commonly made by bonding a thin plate of glass or quartz to the face of the solar cell by a transparent adhesive.

Figure 17 shows typical data that illustrates the loss in transmission of optical adhesives as a result of exposure to ultraviolet radiation, (Ref. 20). Initially, the transmission through a thin film of the adhesives sandwiched between 80-mil thick slides of fused silica is on the order of 95 percent at most wavelengths, with a drop-off below 90 percent of wavelengths shorter than 4000 Angstroms. After exposure to ultraviolet radiation, there is a significant loss in transmission, which varies with

the wavelength and with the adhesive. The effect of using Adhesive B with fused silica cover plates would, for this condition of exposure, reduce the output of the solar cell by more than one-third!

The results in Figure 17 illustrate the need for evaluating adhesives for this application and in selecting adhesives that have good ultraviolet stability. When the adhesives are inadequate and their transmission is seriously reduced as a result of ultraviolet radiation, means must be taken to reduce the amount of ultraviolet radiation that strikes them. This can be done by means of (1) interference filters that reflect ultraviolet radiation while transmitting at other wavelengths and (2) ultraviolet absorbing cover plates. Multilayer, vacuum-deposited interference filters are very effective in reducing the amount of ultraviolet radiation that reaches the adhesive layer and have the advantage over ultraviolet absorbing cover plates of reducing the amount of heating caused by absorption of ultraviolet energy. On the other hand, interference filters are expensive, they reduce slightly the transmission at the wavelengths at which the solar cells are active, and they are themselves degraded slightly by ultraviolet radiation.

Thin vapor-deposited films of silicon monoxide, SiO, have also been considered for solar cell coverings, since they have good infrared emissivity. However, silicon monoxide has relatively poor transmission for visible light and is unstable, tending to "brown" under ultraviolet radiation and further decrease its transmission for visible light.

Higher oxides of silicon, such as silicon dioxide, are therefore used, as indicated above, since they have good ultraviolet stability when pure.

SIMULATION TECHNIQUES

Introduction

The uses and effects of electromagnetic radiation have been discussed in previous sections. Simulating this radiation is necessary for studying its uses and effects and for verifying that spacecraft have been properly designed.

Equipment for simulating electromagnetic radiation and conducting tests on its effects must include the following:

1. A source of the radiation.

2. Transfer optics, or a system for directing the radiation from the source on to the object to be irradiated. This can consist simply of a window in a chamber or an elaborate system of refractive and reflective optics.

3. A heat sink or a system for receiving heat energy from the object being irradiated. This can be simply a water-cooled mounting block, as in the case of specimens of materials whose stabilities are being measured, for example, or it can be a system of liquid nitrogen cooled shrouds that surround the object being irradiated, as in the case of large chambers for testing the thermal balance of complete vehicles. (In some material studies, it may be desirable to heat the specimen by auxiliary heaters.)

4. Instrumentation for measuring the characteristics of the radiation incident on the object being irradiated. Characteristics to be measured can include intensity, spectral distribution, uniformity, and collimation.

5. A system for maintaining the object being irradiated in a vacuum and under such other space environments as are to be studied simultaneously (e.g., nuclear radiation and micrometeoroids).

In the following sections, the first of these - the sources of radiation - are discussed.

Sources of Electromagnetic Radiation

The ideal source of solar radiation is the sun itself. But because the earth's atmosphere absorbs solar radiation unevenly, its spectral distribution on earth is decidedly different from that in space, as pointed out in Section 2, and the sun is not generally a satisfactory source for use on earth. Artificial sources are therefore required.

Many artificial sources are available. In fact, it would be impossible to describe all of them in this paper, and the following discussions are limited to three types that are commercially available and that have been found most useful in past studies.

Quartz-enclosed tungsten filament lamps

Quartz-enclosed tungsten filament lamps are the most commonly used source for high fluxes of infrared radiation. They are used for simulating radiant heating caused by solar radiation when a match of the total energy is sufficient and when a close match of spectral distribution is unnecessary.

Sources of infrared radiation are commonly used to simulate both albedo and planetary emission for verifying the thermal design of spacecraft. Although the spectral distribution of these sources does not match that of either component of secondary radiation, it represents a suitable compromise for their combination. Spectral distribution is seldom important in simulating earthshine since most spacecraft materials have a flat curve of absorptance vs wave length throughout this portion of the infrared region. They have also been used to provide high heat fluxes for simulating aerodynamic heating during spacecraft exit and reentry. Special designs of tungsten strip heaters are also used as secondary standards for spectral radiance in the near infrared (Ref. 21).

Tungsten filament lamps are essentially resistance type heating elements that are heated to an incandescent temperature below the melting point of tungsten. Figure 18 shows the spectral distribution of radiation from a tengsten filament lamp* at several power levels (Ref. 22). The radiation

---

* Type T3-16[illegible] Infrared Lamp of General Electric Co. This lamp is a 1000-watt size (100 watts per inch of lighted length) with an overall size of 11.94 inches long by 0.345 to 0.422 inch diameter. When used with a reflector, the assembly measures 12 inches long x 0.75 inches wide x 0.75 inches deep.

is principally in the infrared region, and it shifts to shorter values as the power level and filament temperature increase. Maximum filament temperature under full voltage is about 2500°K, which provides a peak spectral radiance at 11,6000 Angstroms (1.16 microns). The curves approximate blackbody radiation at the filament temperatures, except that the distribution beyond 35,000 Angstroms (3.5 microns) is modified by absorption and reemission from the quartz envelope. The total radiant energy is given by the area under the curves, and it increases as the fourth power of the absolute temperature, in accordance with Stefan's Law. Thus, a tungsten filament lamp operating at its normal filament temperature of 2500°K emits about 2.6 times as much energy as an equivalent size heating element of molybdenum disilicide operating at its highest practical temperature of 1970°K. The intensity can be increased further by doubling the voltage and raising the filament temperature as high as 3250°K, but this considerably shortens the lifetime.

The lamps consist of coils of tungsten filament in quartz envelopes, and the filaments are supported by discs at frequent intervals to avoid slumping. Reflectors are used to increase the heat flux on the object being irradiated and to reduce the amount of heat rejected to the side and rear (e.g., the heat rejected to cryogenic walls in large space simulators). Good reflectors have the lowest possible emittance. Specular aluminum and gold are used, the latter being somewhat superior in the infrared end of the spectrum and capable of higher operating temperatures.

Advantages of tungsten filament lamps include the follosing:

1. Compact size. Because of their high filament temperature, these lamps are smaller than nichrome and metal sheath heaters of the same output. Lamps with 0.375 inch diameter can be operated up to 500 watts per inch. The compact size also means minimum blockage to interfere with heat transfer and minimum weight to be supported, so that the lamps can be supported on light, open frames.

2. High radiant efficiency. Efficiency is approximately 85 percent, compared to 58 percent for lower-temperature emitters such as exposed nichrome and metal sheath heaters.

3. Fast response time. Because of their low mass, the lamps can attain 90 percent of their full operating temperature in only 3 to 4 seconds.

4. Enclosed and sealed construction. This makes them able to operate in various atmospheres in addition to vacuum.

5. Long operating lifetime.

6. Extremely low outgassing. No vapors are given off to contaminate optical surfaces or interfere with the vacuum level.

7. Variable intensity. The intensity in infinitely variable from zero to full power, although the spectral distribution shifts with the power level. Intensity has good stability.

8. Commercially available in various sizes, power ratings, and configurations.

9. Low cost.

Carbon arc lamps

Carbon arc lamps have been used for many years in movie projectors and searchlights. Their basic features are indicated in Figure 19 (Ref. 23), which also indicates some of the special features that are incorporated into arc lamps for solar simulators.

The carbon arc lamp is normally operated on direct current. During operation, electrons are emitted from the negative carbon rod and accelerated to the positive carbon rod, where their kinetic energy is converted to heat. The positive rod is thereby heated to incandescence and gradually boils off, thereby creating a plasma ball of dissociated gases within the lips of the crater formed at the end of the positive rod. Both rods are rotated to reduce preferential heating and erosion.

A secondary air injection system and exhaust flue are used for removing combustion products and reducing the loss of efficiency that otherwise occurs

due to the deposition of carbon particles and ash on the transfer optics. A magazine feed and joining system has been developed for the positive carbon rods that eliminates the need for frequent shutdowns to replace the burnt out positive rod. The negative carbon rods burn more slowly, but daily shutdowns are still necessary to replace them. Non-consumable negative electrodes of tungsten have recently been reported that make continuous operation more reliable and have estimated lives of 1000 hours (Ref. 24). These electrodes operate in an inert atmosphere of argon and are approximately 0.1875-inch diameter.

Figure 20 compares the spectral distribution of carbon arcs with that of the sun. The principal advantage of carbon arcs for simulating solar radiation in space is the close spectral match. Their radiant output is also high, providing one sun intensity with ±5 percent uniformity over a 30-inch wide hexagonal area at a distance of 30 feet and with a collimation angle of 5.4 degrees (Ref. 25)*. Efficiency is on the order of 50 to 60 percent, based on a normal power input of 19 kilowatts. Higher powered carbon arcs, using electrodes up to 35 mm in diameter (present systems use 13.6 mm diameter electrodes) are under development that have operated up to 130 kilowatts (Ref. 23).

Past disadvantages of carbon arcs as sources of solar radiation have included arc instabilities and variations in intensity as the arc burns away. Better quality control in the manufacture of the carbon rods has helped reduce this disadvantage. Automatic crater positioning devices are also used in modern equipment to maintain the tip of the burning carbon at the exact focal point of the reflector, thereby eliminating changes in

---

* Data from Ref. 25 for Type No. 75002-A System.

radiation intensity due to variations in carbon burning rates. Stability of intensity to ± 2 percent is reported by one manufacturer (Ref. 25).

High-pressure gas discharge lamps

High-pressure gas-discharge lamps produce radiation by means of an arc discharge through a gas maintained at high pressures (about 20 atmospheres). Mercury, xenon, and their mixture are the gases most commonly used. Xenon gives a higher conversion efficiency than other rare gases, such as neon, argon, and kyrpton, and it is brighter, since it has the lowest ionization potential.

When xenon gas and mercury vapor are heated in an electric arc while maintained at high pressure and density, they emit light in the form of a spectral continuum plus their characteristic line spectra. The spectrum of xenon, mercury, and mercury-xenon lamps extends from the ultraviolet, through visible light, to infrared.

The arc discharge takes place between tungsten electrodes maintained at a potential difference on the order of 15 to 60 volts, depending upon the gas filling and electrode geometry. The arc gap is about 5 mm (0.2 inch), and the most intense radiation is from the plasma that is concentrated immediately above the cathode tip.

Because the arc discharge takes place between closely-spaced electrodes, in contrast to the relatively long, narrow arcs in other types of discharge lamps, these lamps are called "short arc" or "compact arc" lamps. The gases are maintained in thick quartz bulbs.

Compact arc lamps are available for either AC or DC operation. DC lamps are preferable to AC lamps of the same wattage and gas filling for the following reasons: (1) longer life (typically, three times); (2) easier starting; (3) steadier operation (less arc wander).

Arc brightness is more concentrated near the cathode of DC lamps, whereas the arc of AC lamps is more uniformly distributed between the electrodes.

Figure 20 shows the spectral distribution from a typical xenon compact arc lamp. The distribution is seen to be heavy in the near infrared region, as compared to solar radiation in space. On the other hand, the spectral distribution within the visible range is very close to that of sunlight.

Xenon-mercury lamps are similar to xenon lamps in their operating principles, but they differ significantly in at least three respects:

1. Spectral distribution. As indicated by Figure 22, the spectral distribution of energy from xenon-mercury lamps has many strong lines in the visible, mostly in the green. There is also a great deal of ultraviolet radiation.

2. Brilliance. Energy released by excited mercury electrons returning to their normal orbits produces a much more brilliant light.

3. Warm-up. Because the mercury must be vaporized before it can emit light, the warm-up time is longer for xenon-mercury lamps than for xenon lamps. However, they have a shorter warm-up period than high-pressure mercury arc lamps.

Mercury arc lamps operate at pressures up to 70 atmospheres and emit spectra composed of characteristic mercury lines and a continuum that extends from about 2000 Angstroms (0.2 microns) to the infrared region. They are particularly useful either as a light source of high luminance in the visible range or as a source with high energy in the medium- and long-range ultraviolet region.

Simulation Systems

Although sources other than the three types discussed in Section 6.2 have been and are being used in various studies, these three types are used in the majority of both small-size laboratory systems and large-size, full-scale simulation facilities. Rather than attempt to catalogue the

various facilities,* a few general observations are made on simulation systems:

1. Among large-scale facilities used for verifying the thermal design of spacecraft, there is no general agreement as to the need of exact simulation. Advocates of the absorbed heat flux technique can claim that this technique has been satisfactory for many cases and that more exact simulation is unnecessary. A number of large companies are in fact successfully using tungsten filament lamps and are building new facilities that will use this same technique. On the other hand, the satellites and spacecraft tested by this technique have been fairly simple, and the technique may not be satisfactory for more sophisticated designs where shadowing becomes important.

2. Among the advocates of exact simulation for large-scale facilities, there is no general agreement as to the best sources for solar simulation. Carbon arcs, xenon compact arc lamps, and xenon-mercury compact arc lamps are all being used and proposed for future use.

3. There have been substantial improvements in sources of solar radiation during the past few years as a result of their use by the aerospace industry. Particularly noteworthy have been the increases in the radiant output of the sources, easier handling, and longer lifetimes. At least a part of the lack of agreement noted in item 2 above is due to the rapid advances by the source manufacturers, so that the relative merit of the different types of sources is continually changing.

4. There is a growing use of several different types of sources and filters in combination with one another in order to compensate for the deficiencies of any one source and to provide a closer spectral match where needed. Figure 23, for example, illustrates the spectral distribution obtained from combining radiation from a xenon lamp and a tungsten-filament lamp in a small size unit for testing solar cells (Ref. 27). Similarly, in one of the large space environmental chambers that uses carbon arcs for the primary solar radiation, tungsten-filament lamps are being added to make up for the deficiencies of carbon arcs in the infrared region and to provide a source of secondary radiation (i.e., planetary albedo and emission).

5. Most laboratory-size facilities for studying the photodegradation of materials use high-pressure mercury or mercury-xenon lamps. Hydorgen arc lamps have been used that provide radiation below 2000 Angstroms (0.2 micron), but the photodegradation appears

---

* Large space chambers are surveyed in Ref. 26.

> the same as when mercury or mercury-xenon compact arc lamps are used. As a result, most investigators feel it is unnecessary to go to the more elaborate systems required to provide radiation in the far ultraviolet range in order to obtain results on photodegradation of materials that correlates with behavior in space.

I am sure that these final observations will not be universally agreed to, and many of the conferees may care to express contrary opinions, add their own, or expand upon my limited comments in the light of their own experiences. Certainly, simulating space electromagnetic radiation is important in the aerospace industry, and the many workers who have been active in this field are to be congratulated on the degree of refinement to which they have advanced the state-of-the-art.

REFERENCES

1. Francis S. Johnson, "Solar Radiation," in Satellite Environment Handbook, edited by Francis S. Johnson, Stanford University Press, Stanford California, 1961, pp. 77-87.

2. Parry Moon, "Proposed Standard Solar-Radiation Curves for Engineering Use," J. Franklin Inst., 230 583-617 (Nov. 1940).

3. Halbert Fishel, "Some Thermodynamic Principles of Radiative Transfer in Optical Systems," Fifth Annual Symposium on Space Environmental Simulation, Arnold Engineering Development Center, Tullahoma, Tenn. May 21-22, 1964.

4. Carl Gaxley, Jr., W. W. Kellogg, and E. H. Vestine, "Space Vehicle Environment," Journal of the Aero-Space Sciences, December 1959, pp. 770-782, 814.

5. G. P. Kuiper, The Atmospheres of the Earth and Planets, University of Chicago Press, 2d edition, 1952, p. 308.

6. Walter G. Camack and Donald K. Edwards, "Effect of Surface Thermal-Radiation Characteristics on the Temperature-Control Problem in Satellites," Surface Effects on Spacecraft Materials, edited by F. J. Clauss, John Wiley and Sons, Inc., New York, N. Y., 1960, pp. 3-53.

7. T. O. Thostesen, A. R. Hibbs, and E. P. Buwalda, "Temperature Control of the Explorers and Pioneers," Surface Effects on Spacecraft Materials, edited by F. J. Clauss, John Wiley & Sons, Inc., New York, N. Y., 1960, pp. 55-88.

8. R. E. Gaumer, W. G. Camack, et al., "Thermal Control Materials," Space Materials Handbook, edited by C. G. Goetzel and J. B. Singletary, Lockheed Missiles and Space Company, Sunnyvale, California, First edition, 1962, pp. 81-222.

9. Walter G. Camack and Clyde A. Ellis, "A High-Vacuum Orbital Simulator," 1961 Proceedings of the Institute of Environmental Sciences, Institute of Environmental Sciences, 1961, pp. 349-357.

10. D. M. Chapin, C. S. Fuller, and G. L. Pearson, "The Bell Solar Battery," Bell Laboratories Record, 33, 241-46 (July 1955).

11. M. B. Prince and M. Wolf, "New Developments in Silicon Photovoltaic Devices J. Brit. I.R.E., 18, 583-95 (Oct. 1956).

12. Peter A. Iles, "The Present Status of Silicon Solar Cells," I.R.E. Trans. Military Electronics, 5-14 (Jan. 1962).

12a. B. Ross, "Design Criteria for Satellite Power Supplies Using Radiation Resistant Solar Cells," presented at ASME Aviation and Space Conference, Los Angeles, Calif., March 3-7, 1963.

13. E. J. Bowen, The Chemical Aspects of Light, Clarendon Press, Oxford, Second edition, 1946.

14. E. J. Bowen, "Photochemistry" in Encyclopedia of Chemical Technology, Vol. 10, edited by R. E. Kirk and D. F. Othmer, Interscience Encyclopedia, Inc., New York, 1953.

15. Sumner Levine, Howard Halter, and Fred Mannis, "Photochemical Aspects of Solar Energy Utilization," Solar Energy, 2, 11-21, (April 1958).

16. Frank A. Bovey, The Effects of Ionizing Radiation on Natural and Synthetic High Polymers (Vol. 1, Polymer Reviews), Interscience Publishers, Inc., New York, N. Y.

17. W. Versluys, N. Beecher, et al., "Ultraviolet Effects on Space Vehicle Operation in Ultrahigh Vacuum Environment," Technical Documentary Report Nos. AEDC-TDR-62-16 and AEDC-TDR-62-17, National Research Corporation to Arnold Engineering Development Center, January 1962.

18. J. E. Cowling, A. Alexander, et al., "The Effects of Ultraviolet Radiation on Organic Film-Forming Polymers," in Surface Effects on Spacecraft Materials, edited by Francis J. Clauss, John Wiley & Sons, Inc., New York, N. Y., 1960, pp. 364-376.

19. Thermophysics Design Handbook, Report 8-55-63-3, Lockheed Missiles and Space Company, Sunnyvale, California, June 1963.

20. Space Materials Handbook, edited by C. G. Goetzel, J. B. Rittenhouse, and J. B. Singletary, Lockheed Missiles and Space Co., 1964.

21. Ralph Stair, Russel G. Johnston, and E. W. Halbach, "Standard of Spectral Radiance for the Region of 0.25 to 2.6 Microns," J. Research of the National Bureau of Standards - A. Physics and Chemistry, Vol. 64A, No. 4, July-August 1960, pp. 291-296.

22. Unpublished LMSC data.

23. George MacFarland, "Review of Radiation Sources for Solar Simulation," Fifth Annual Symposium on Space Environmental Simulation, Arnold Engineering Development Center, Tullahoma, Tennessee, May 21-22, 1964.

24. P. D. Ries, "The Carbon Arc for Solar Simulation," Test Engineering, July 1964, pp. 26 and 36.

25. Anon, "Strong Arcomatic Solar Radiation Simulator," The Strong Electric Corp., Toledo, Ohio.

26. R. T. Hollingsworth, "A Survey of Large Space Chambers," NASA TN D-1673, National Aeronautics and Space Administration, Washington, D. C., April 1963.

27. D. Bickler, "The Simulation of Solar Radiation," Hoffman Electronics Corp., El Monte, Calif., Feb. 1962.

TABLE 1

Solar-Ultraviolet-Spectral-Line Intensities (Ref. 1)

Atom	Wavelength λ (A)	Mean Solar Irradiance (10^{-8} w/cm^{-2})
Si II	1817	2
Si II	1808	0.7
Al II	1671	0.1
Fe II	1663	0.3
Fe II	1660	0.4
C I	1656-1658	1.8
He II	1640	0.1
C I	1560-1561	0.7
C IV	1550	0.4
C IV	1548	0.5
Si II	1533	0.2
Si II	1527	0.2
Si IV	1403	0.1
Si IV	1394	0.2
C II	1336	0.6
C II	1135	0.5
Si II	1309	0.1
O I	1306	0.4
O I	1305	0.3
O I	1302	0.2
Si II	1265	0.2
Si II	1261	0.1
S II	1260	0.1
N v	1239	0.1
H I	1216	60
Si III	1206	0.1
C III	1175-1176	0.5
N II	1086	0.3
O VI	1038	0.8
O VI	1032	1
H I	1026	2
C III	977	2
H I[a]	<912	1.5
Mg X	625	0.2
O IV	608	0.3
He I	585	0.4
He II	304	3

*Lyman continuum.

TABLE 2

Values of Solar Radiometric Parameters in Space
at Earth Orbital Distance

Parameter	Description	Value
Intensity	Total energy or total spectrally integrated	140 milliwatts/sq. cm. 2.05 calories/sq. cm. 7.38 Btu/sq. ft/min. Variation due to Earth's changing distance from sun and solar fluctuations = ±3.5 pct.
Spectral Distribution	Distribution of energy with wave length	6000°K black body for UV, visible, and IR. 5800°K black body for UV (λ<2000A) (Also, see Fig.3)
Collimation	Parallelism of rays	Essentially parallel (sine of aperture angle = 1)
Field angle	Angle subtended by sun at earth	32 minutes of arc

TABLE 3

Planetary Albedoes (Ref. 20)

Planet	Average energy of albedo (fraction of solar constant)
Mercury	0.056
Venus	0.76
Mars	0.16
Earth	0.40
Moon	0.067

TABLE 4

VARIATION OF INTENSITY OF EARTH ALBEDO AND EARTH-ATMOSPHERE EMISSION WITH ALTITUDE AND ORIENTATION

Altitude, s. mi.	Type of Radiation	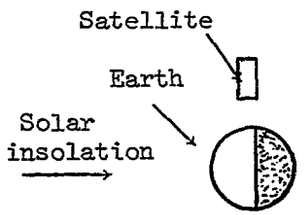		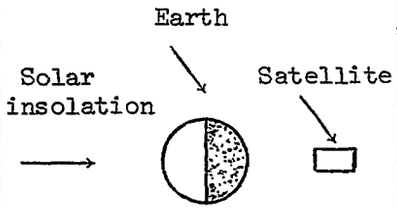		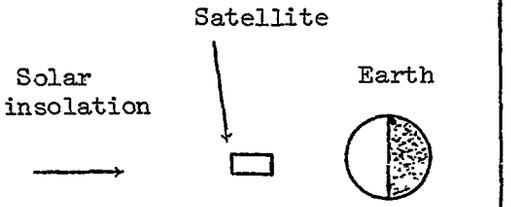	
		Sides	End	Sides	End	Sides	End
100	Albedo	<2.5	<1.25	0	0	76	160
	Emission	31	65	31	65	31	65
500	Albedo	<4.7	<2.4	0	0	54	133
	Emission	22	54	22	54	22	54
1000	Albedo	<5.1	<2.5	0	0	46.	108
	Emission	19	44	19	44	19	44
2300	Albedo	<5	<2.5	0	0	27	74
	Emission	11	30	11	30	11	30

Intensity is average intensity in Btu per hr per sq. ft. First value is for the side of the cylindrical satellite, second value is for the flat end facing the earth.

Table 5
ULTRAVIOLET EFFECTS DATA (Ref. 20)

Material Description	Exposure [a]			Optical Data [b]						Remarks
				Initial			Final			
	I	t	E	α_s	ϵ	α_s/ϵ	α_s	ϵ	α_s/ϵ	
White Paints										
Sicon 7 x 1153	6	12	72	0.25	0.89	0.283	0.33	0.88	0.38	4 coats on Dow 15 on Mg HM-21A
Sicon 7 x 1153	6	100	600	0.26	0.90	0.29	0.37	0.82	0.45	3 coats on Dow 15 on Mg HM-21A
Sicon 7 x 1153	6	100	600	0.31	0.89	0.35	0.59	0.88	0.67	4 coats on Dow 17 on Mg HM-21A
Skyspar A-423	6	25	150	0.23	0.89	0.26	0.41	0.91	0.45	4 coats on P-323-B on Dow 17 on Mg HM-21A
Skyspar A-423	6	46	276	0.26	0.93	0.28	0.45	0.92	0.49	3 coats on P-323-B on Dow 17 on Mg HM-21A
Skyspar A-423	6	12	72	0.28	0.9	0.31	0.36	0.90	0.40	5 coats on P-323-B on Dow 17 on Mg HM-21A
Kemacryl	6	25	150	0.27	0.80	0.34	0.32	0.80	0.4	3 coats on Dow 17 on Mg HM-21A
M49WC 17	6	25	150	0.26	0.79	0.33	0.32	0.80	0.41	4 coats on Dow 17 on Mg HM-21A
	6	100	600	0.26	0.79	0.33	0.37	0.82	0.45	4 coats on Dow 17 on Mg HM-21A
Fuller 517-W-1 Silicone	6	25	150	0.33	0.82	0.40	0.35	0.84	0.42	2 mils on Mg HM-21A
Fuller 517-W-1 Silicone	6	25	150	0.28	0.87	0.31	0.30	0.85	0.36	4 mils on Mg HM-21A
Fuller 517-W-1 Silicone	6	46	276	0.33	0.85	—	0.29	0.87	0.34	3 coats on Mg HM-21A
LMSC Research Paints										
Sod. Silicate "D" + Ultrox	6	91	546	0.29	0.82	0.34	0.32	0.89	0.37	
Sod. Silicate "D" + Ultrox	6	119	714	0.29	0.91	0.31	0.29	0.85	0.33	
Sod. Silicate "D" + Ultrox	6	47	282	0.27	0.87	0.31	0.47	0.86	0.55	
Black Paints										
Kemacryl M49 BC12	6	100	600	0.94	0.88	1.07	0.92	0.84	1.10	4 coats on Dow 17 on Mg HM-21A
Micobond	6	105	630	0.94	0.91	1.04	0.98	0.87	1.13	4 coats on Dow 17 on Mg HM-21A
Al Silicone, 10043										
Fuller 171-A-152	6	100	600	0.22	0.16	1.34	0.33	0.24	1.35	2 mils
Fuller 171-A-152	6	100	600	0.21	0.16	1.26	0.30	0.20	1.46	4 mils
Anodized & Misc Finishes										
Dow 15 on Mg HM-21A	6	12	72	0.23	0.05	4.47	0.28	0.05	5.22	
Dow 15 on Mg HM-21A	6	105	630	0.17	0.07	2.54	0.37	0.34	1.09	
Dow 15 on Mg HM-21A	20	12	240	0.18	0.08	2.41	0.38	0.11	3.39	
Rokide A (10546) on Aluminum	6	95	570	0.31	0.75	0.40	0.44	0.74	0.59	
Evaporated Au on 1/16" Kel-F	6	119	714	0.30	0.07	4.05	0.31	0.09	3.45	Severe discoloration of Au with surface blistering of Plastic.

(a) Exposure, E, (sun hours) is product of intensity, I, (suns) and time, t, (hours).
(b) Optical data include solar absorptance, infrared total hemispherical emittance, and post exposure data.

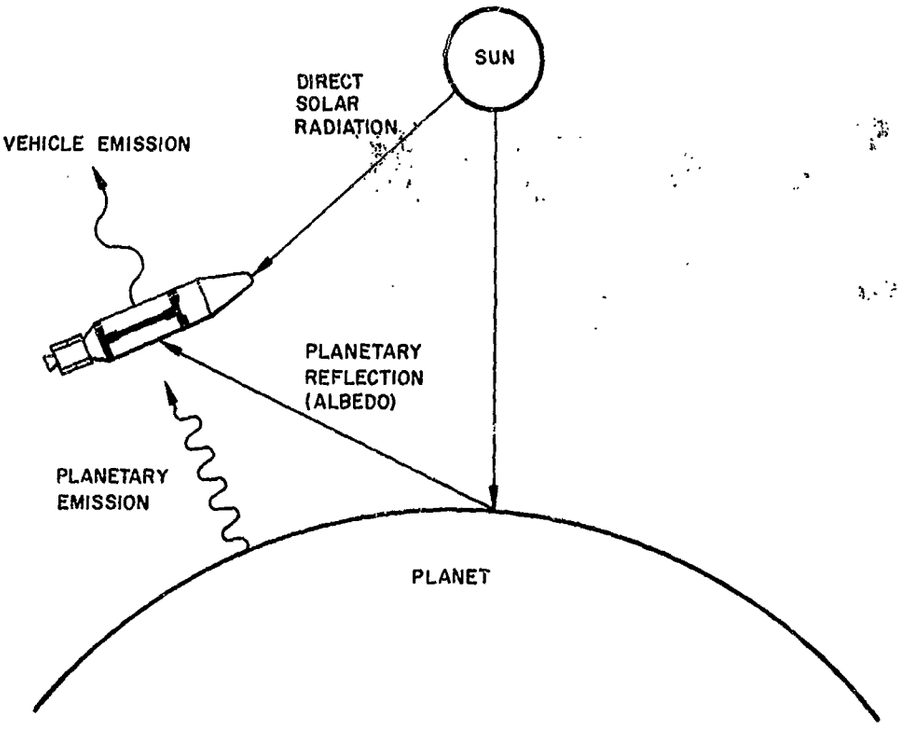

Figure 1 Types of Electromagnetic Radiation Incident on Spacecraft

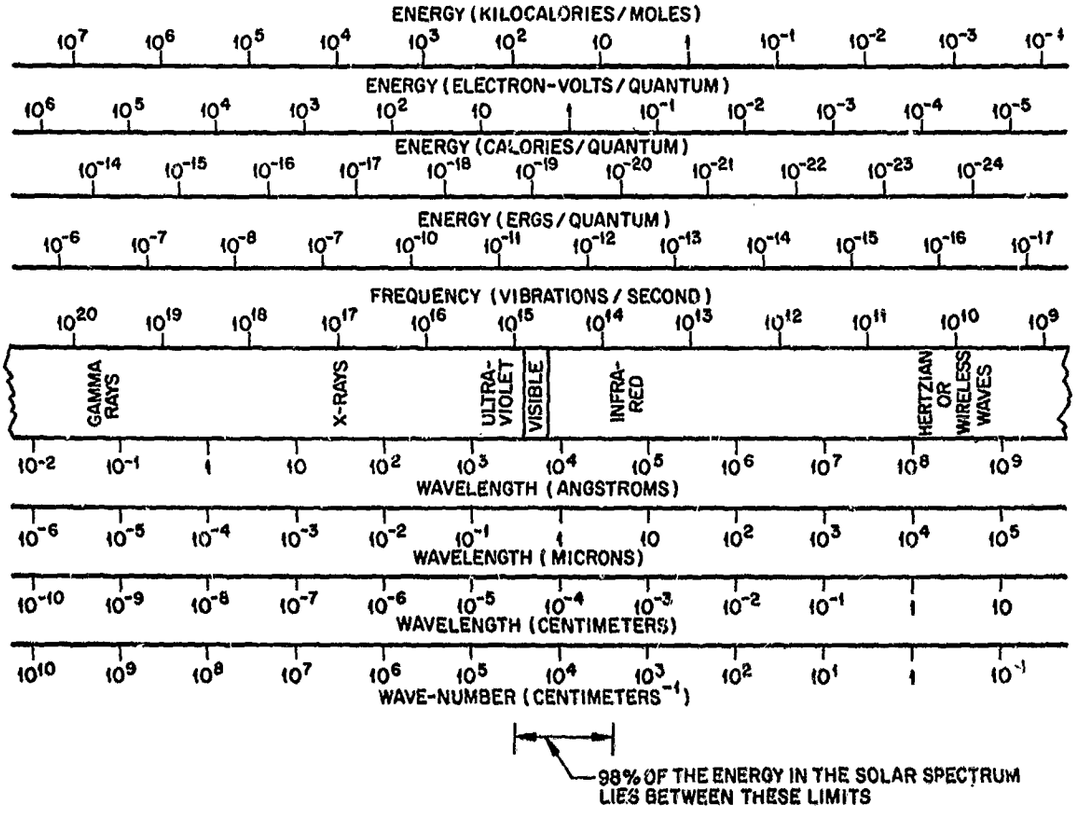

Figure 2 Electromagnetic Spectrum

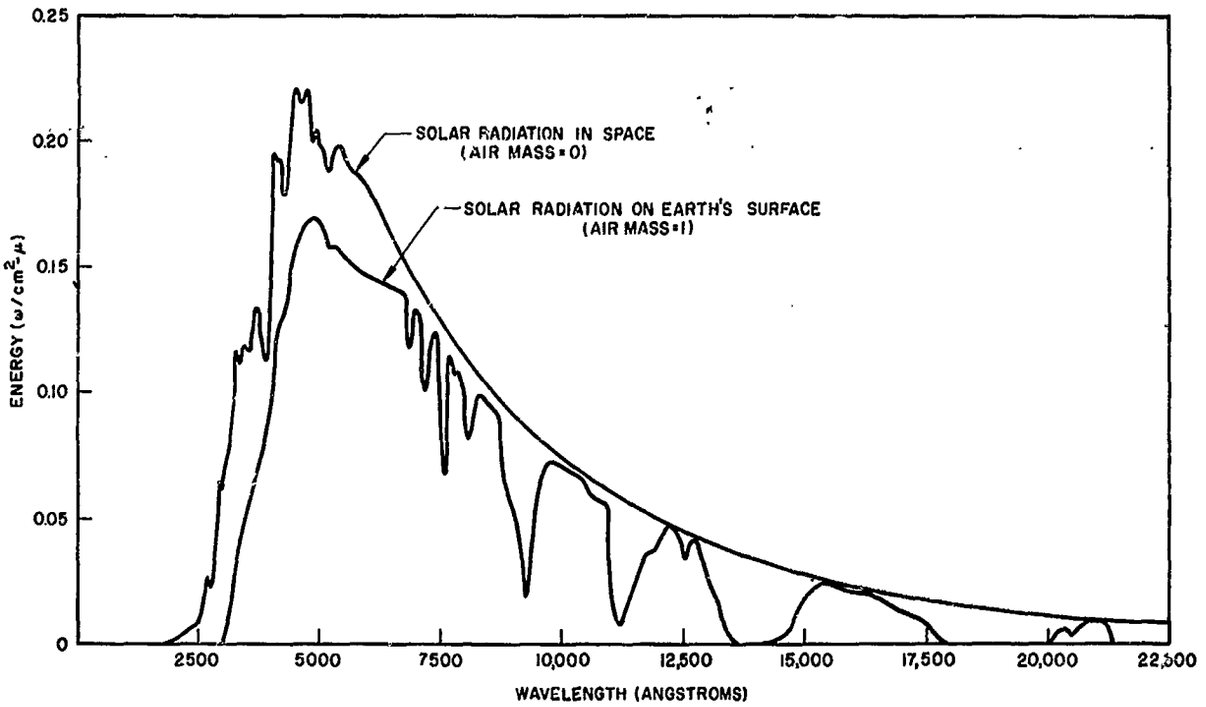

Figure 3 Spectral Distribution of Solar Radiation

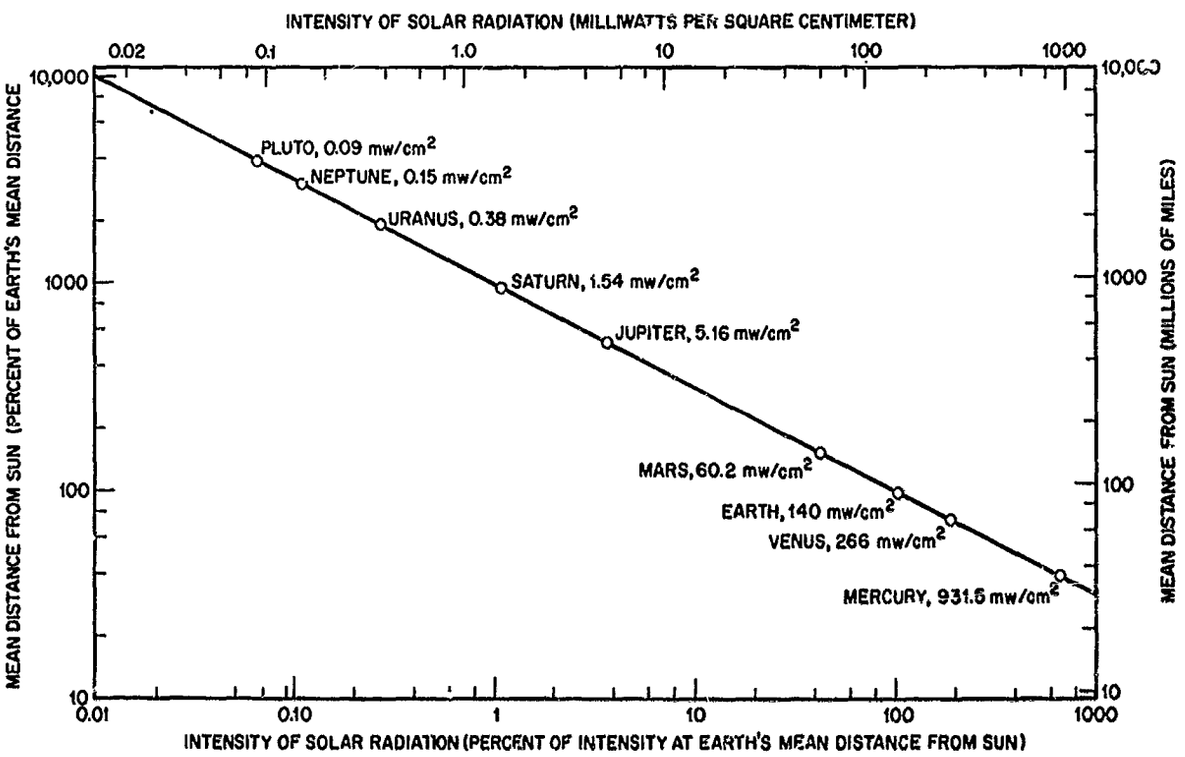

Figure 4 Intensity of Solar Radiation at Various Distances From The Sun

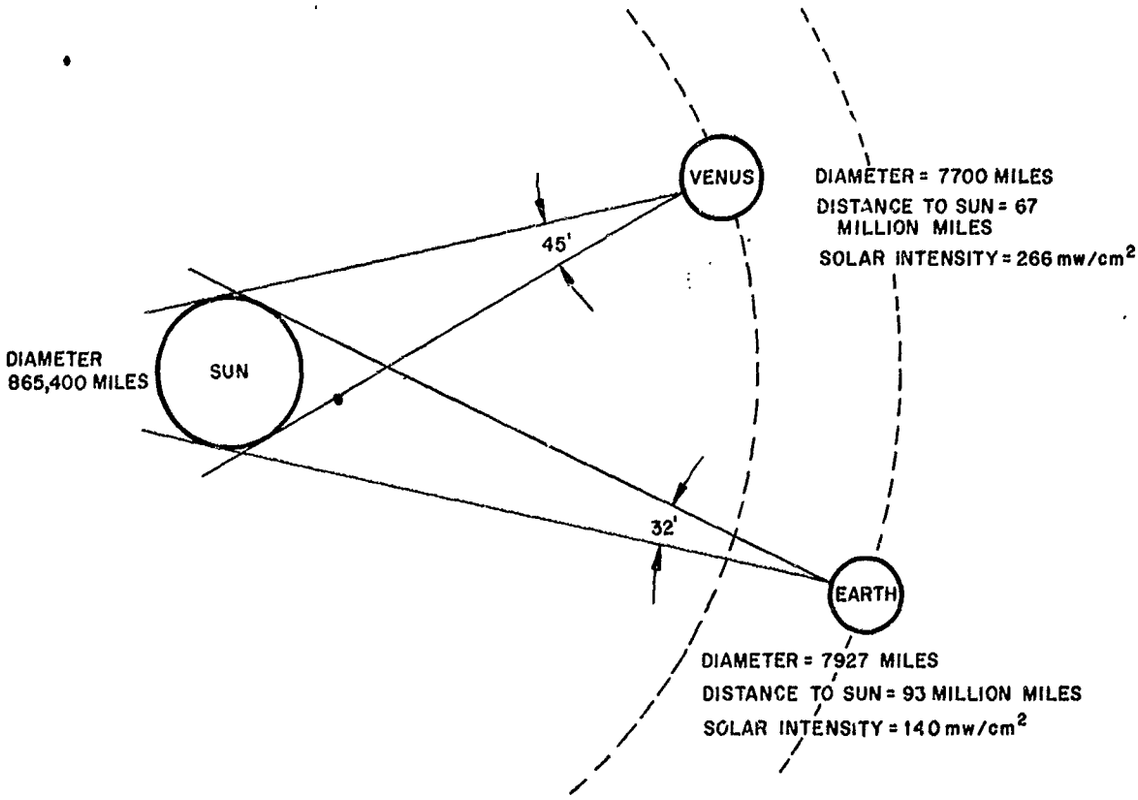

Figure 5 Field Angle Subtended by The Sun At The Mean Orbits of Earth and Venus

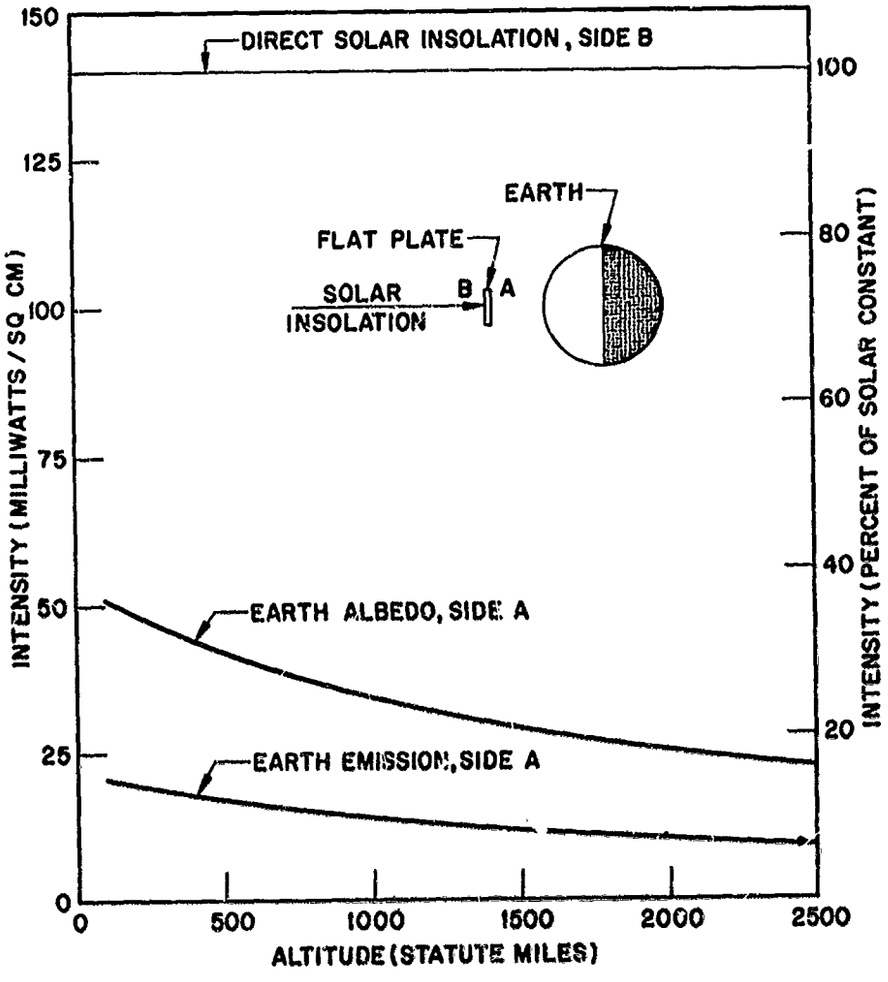

Figure 6 Effect of Altitude on Intensity of Incident Radiation

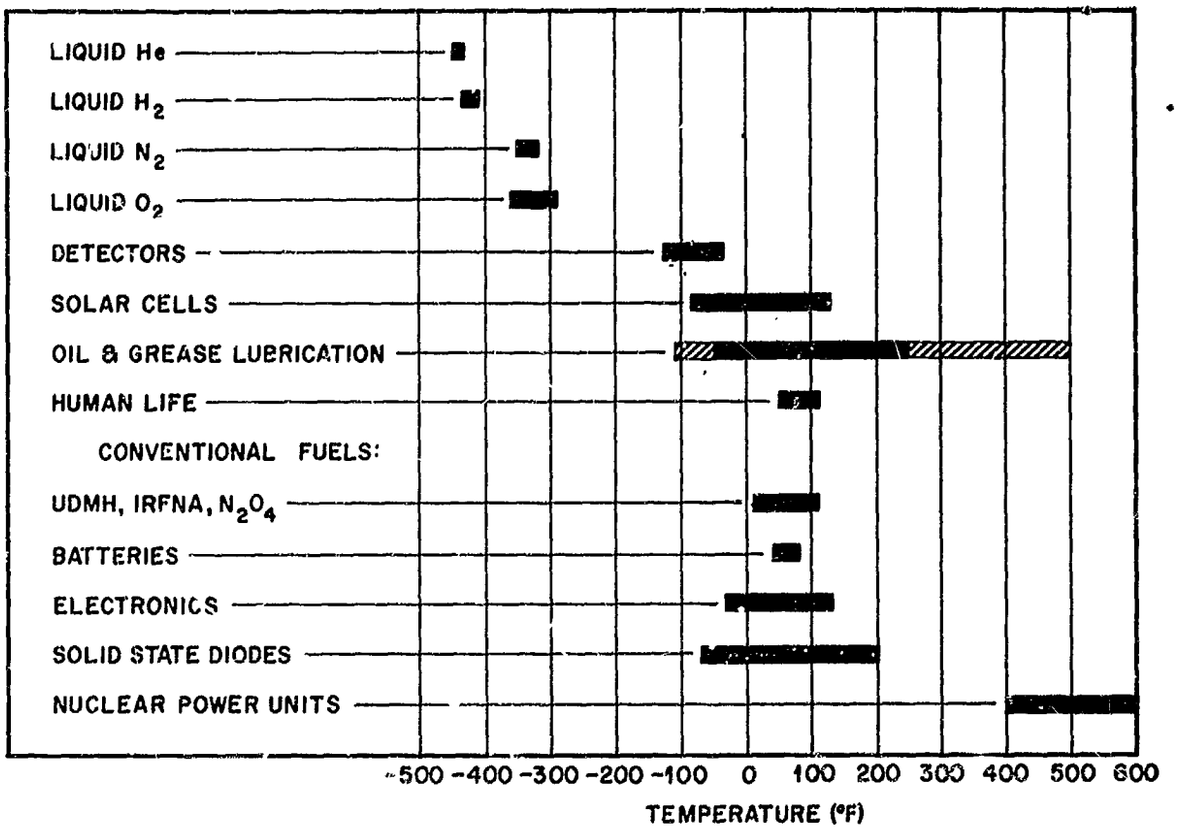

Figure 7 Payload Operating Temperature Ranges

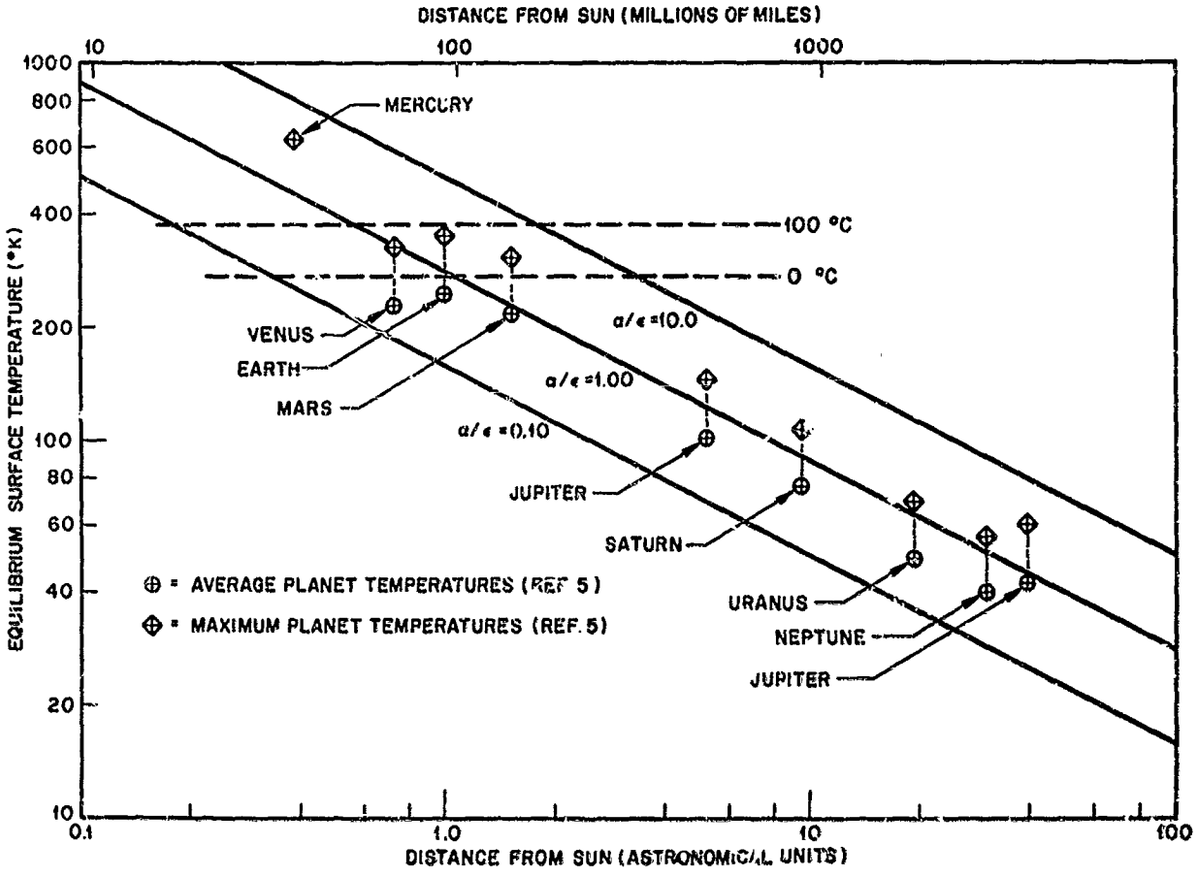

Figure 8 Effect of Distance From Sun and Surface Radiative Characteristics on Equilibrium Surface Temperature of a Spinning Sphere (After Ref.4)

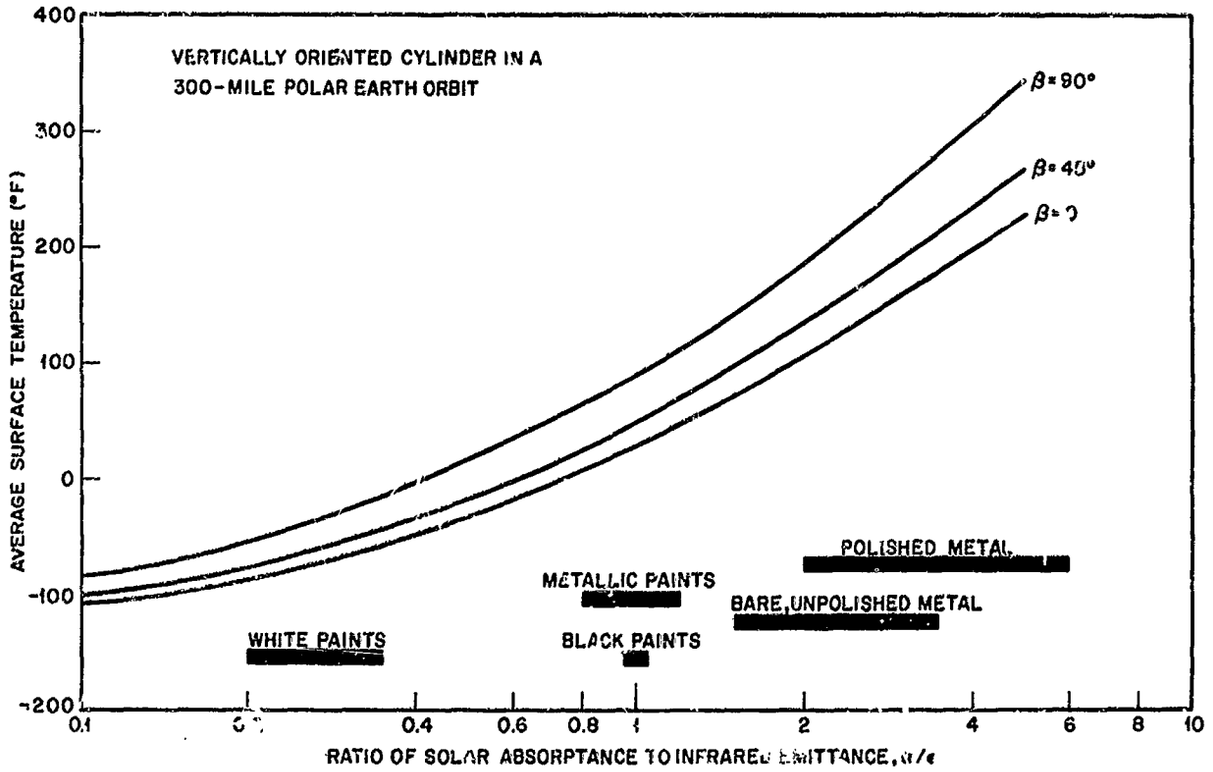

Figure 9 Effect of Surface Radiative Characteristics and Altitude on an Earth Orbitting Satellite

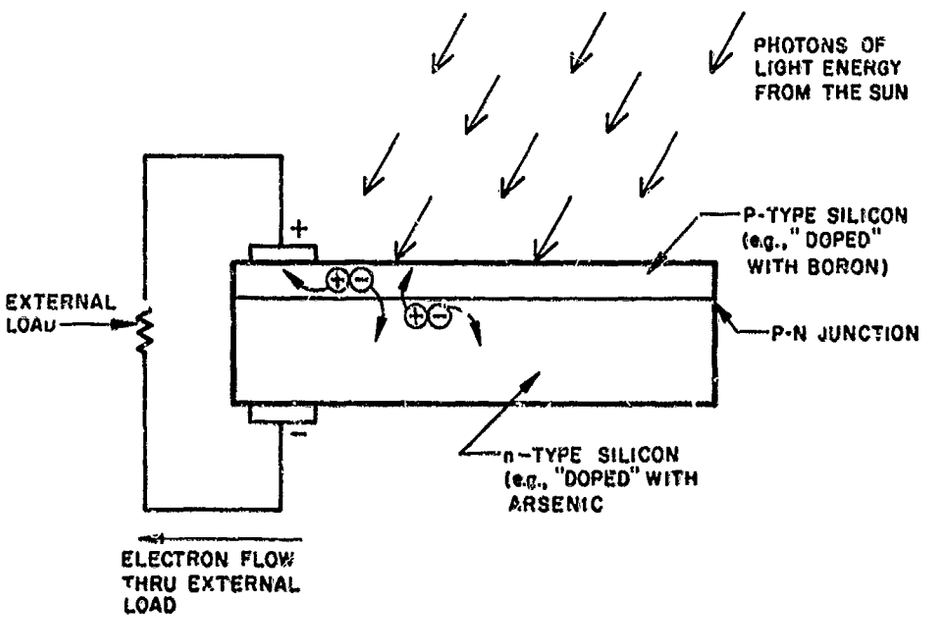
PHOTONS OF LIGHT ENERGY FROM THE SUN
P-TYPE SILICON (e.g., "DOPED" WITH BORON)
P-N JUNCTION
EXTERNAL LOAD
n-TYPE SILICON (e.g., "DOPED" WITH ARSENIC
ELECTRON FLOW THRU EXTERNAL LOAD

Figure 10 Schematic of Solar Cell

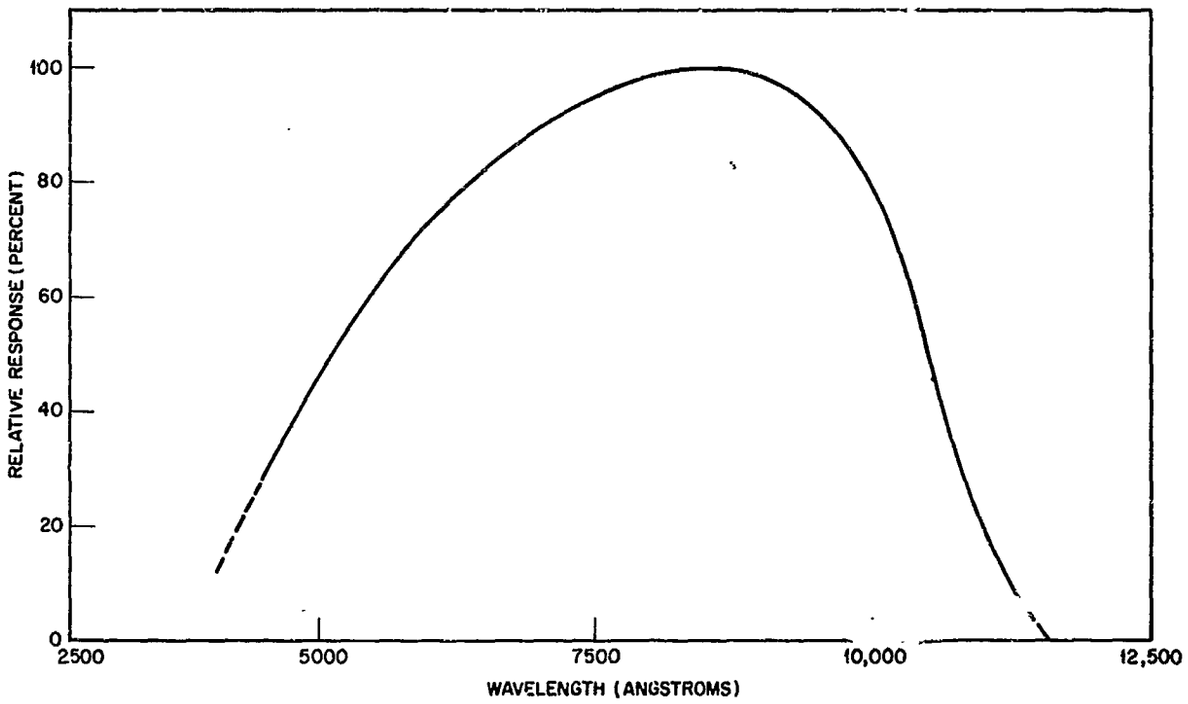

Figure 11 Effect of Wavelength on Response of a Solar Cell

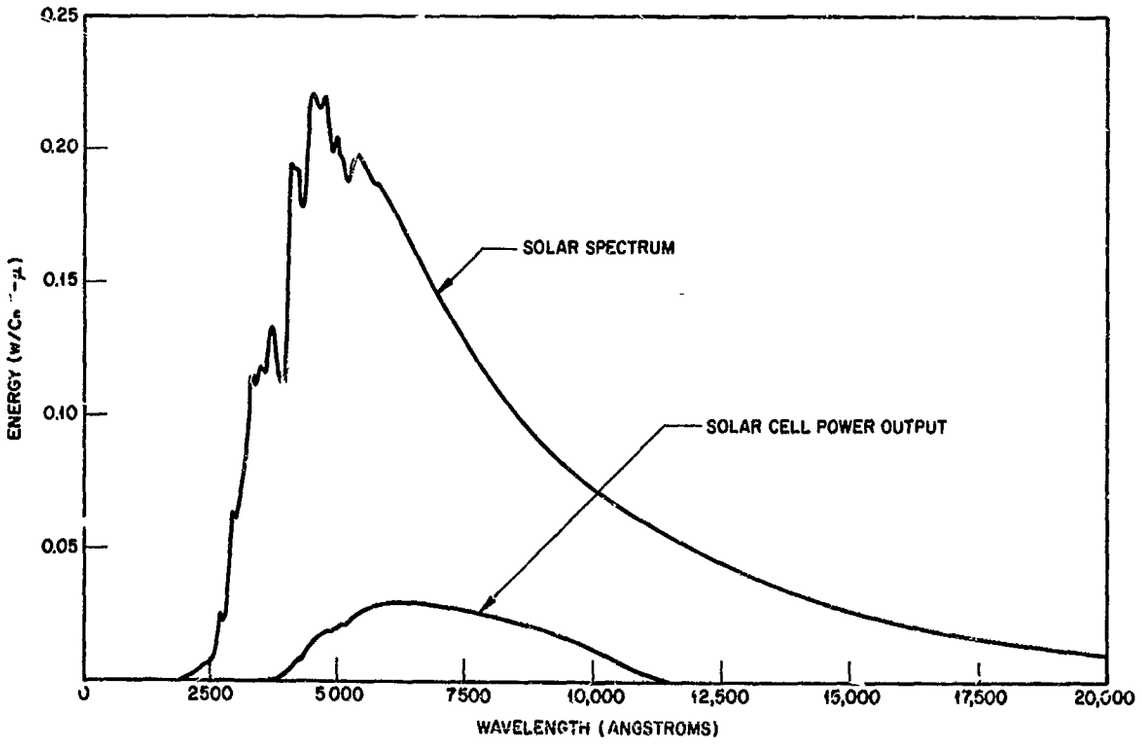

Figure 12 Response of Solar Cell Under Solar Radiation In Space

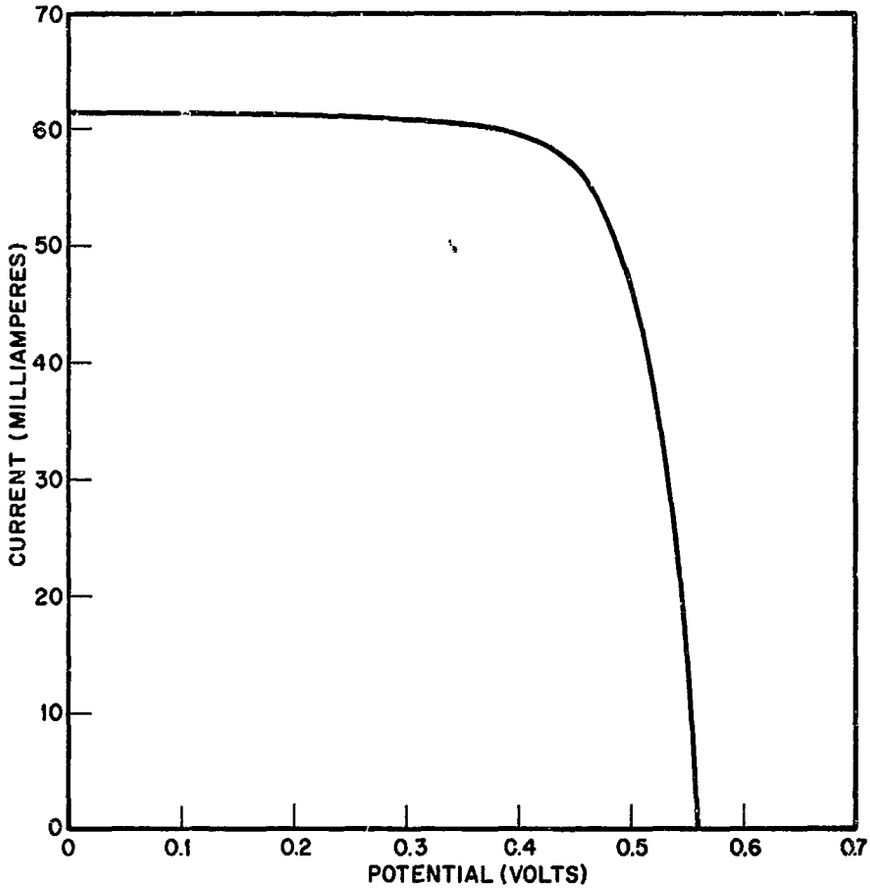

Figure 13 Characteristic Output Curve of Silicon Solar Cell

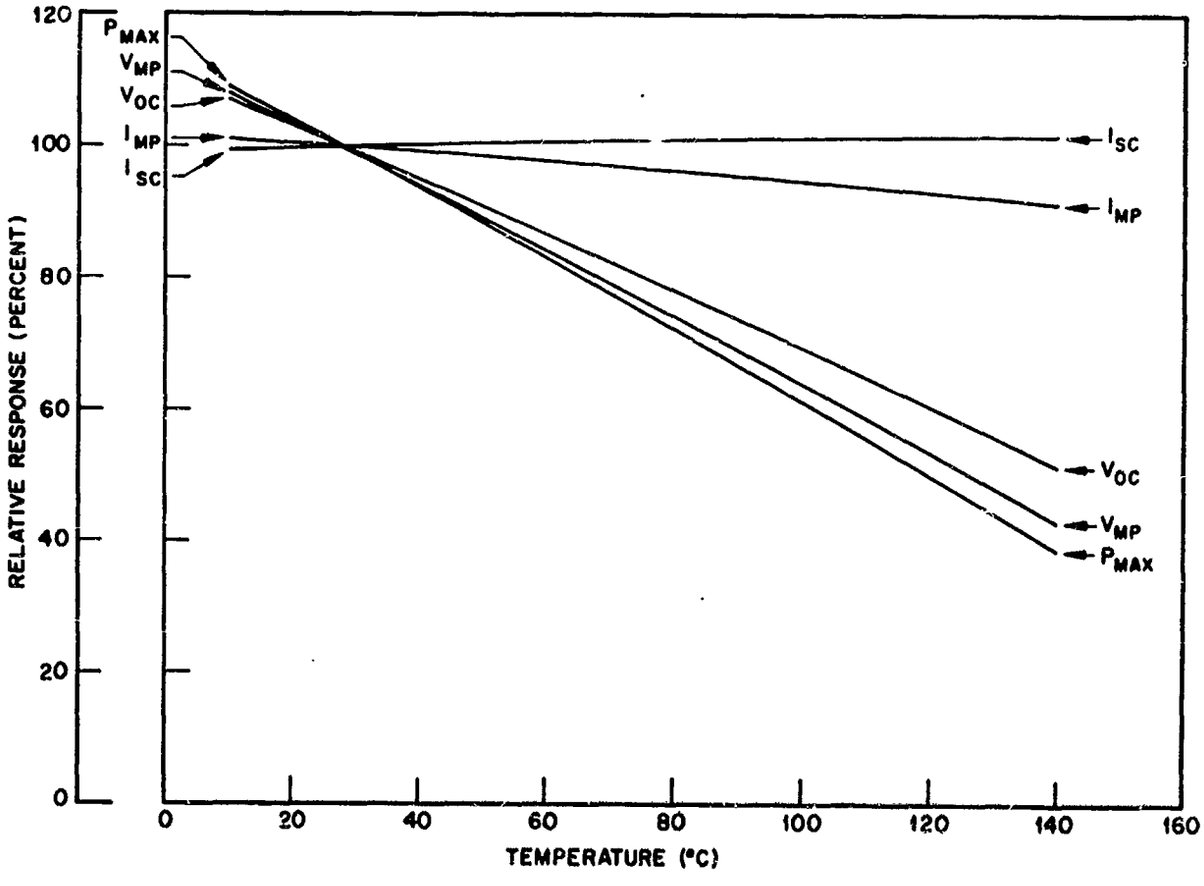

Figure 14 Effect of Temperature on Solar Cell Characteristics

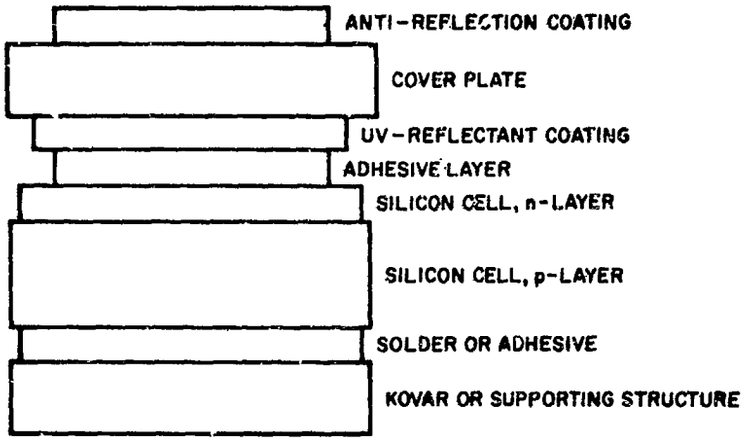

Figure 15 Cross-Section of Solar Cell Assembly

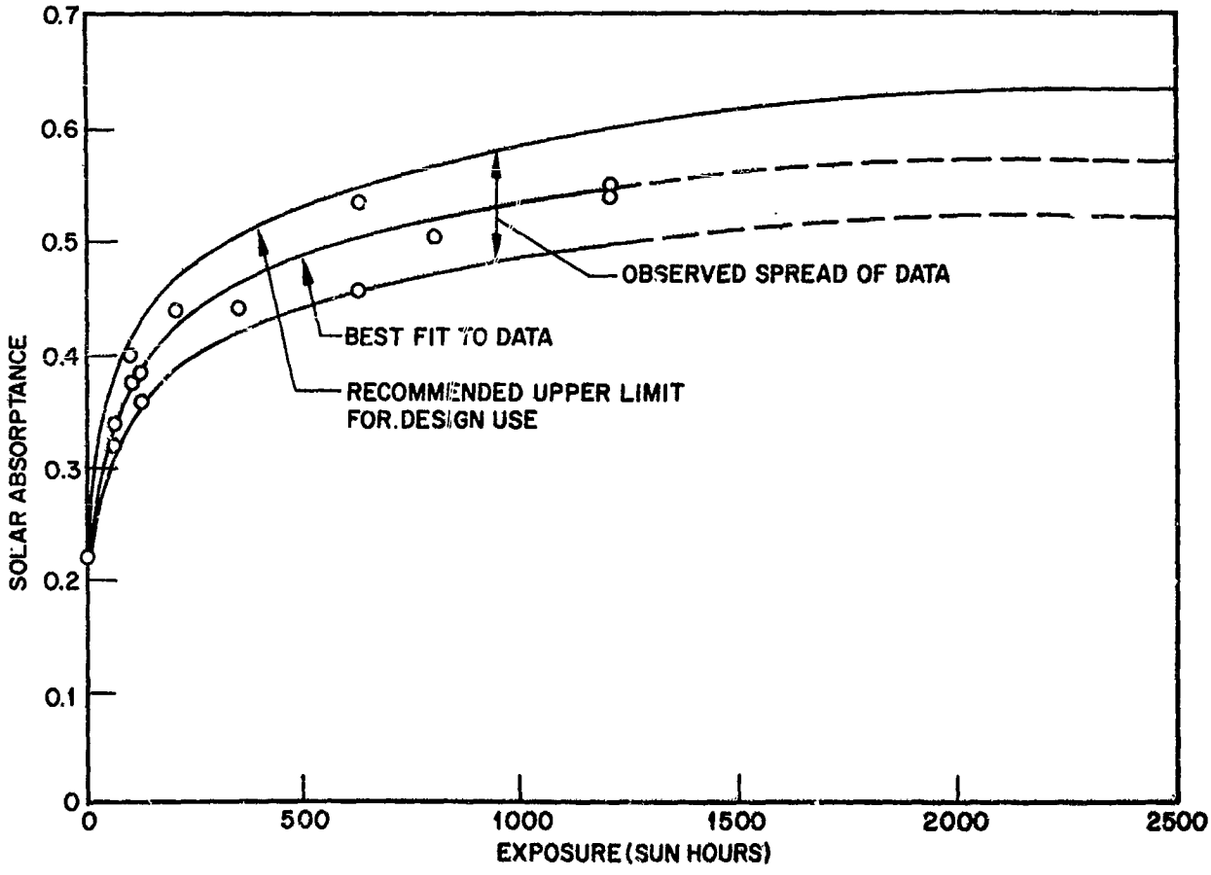

Figure 16 Photodegradation of an Organic-Base White Paint

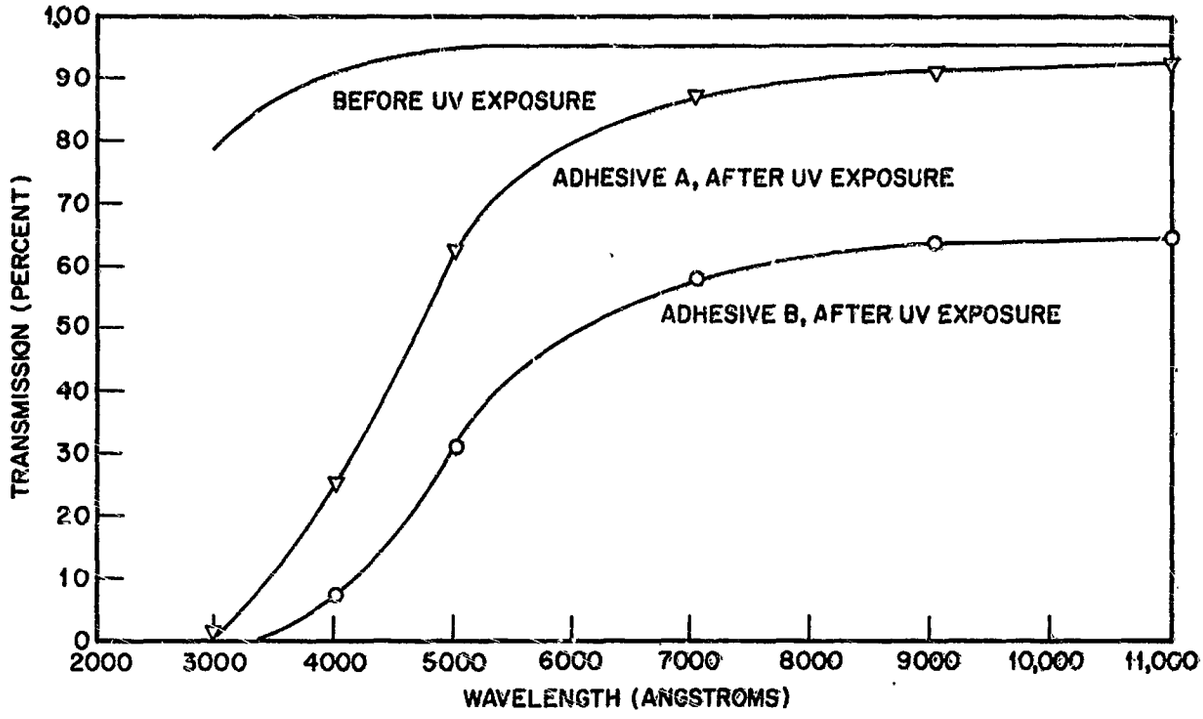

Figure 17 Photodegradation of Optical Adhesives

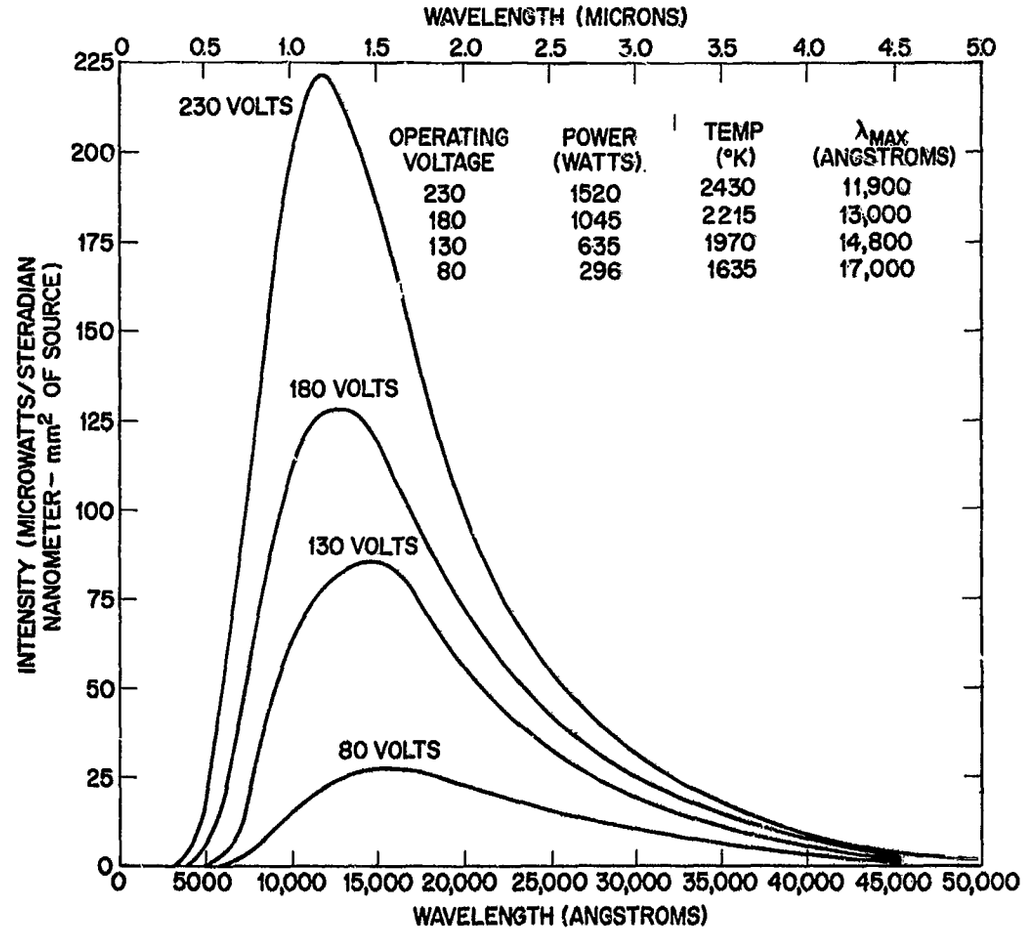

Figure 18 Spectral Distribution from a Tungsten Filament Lamp

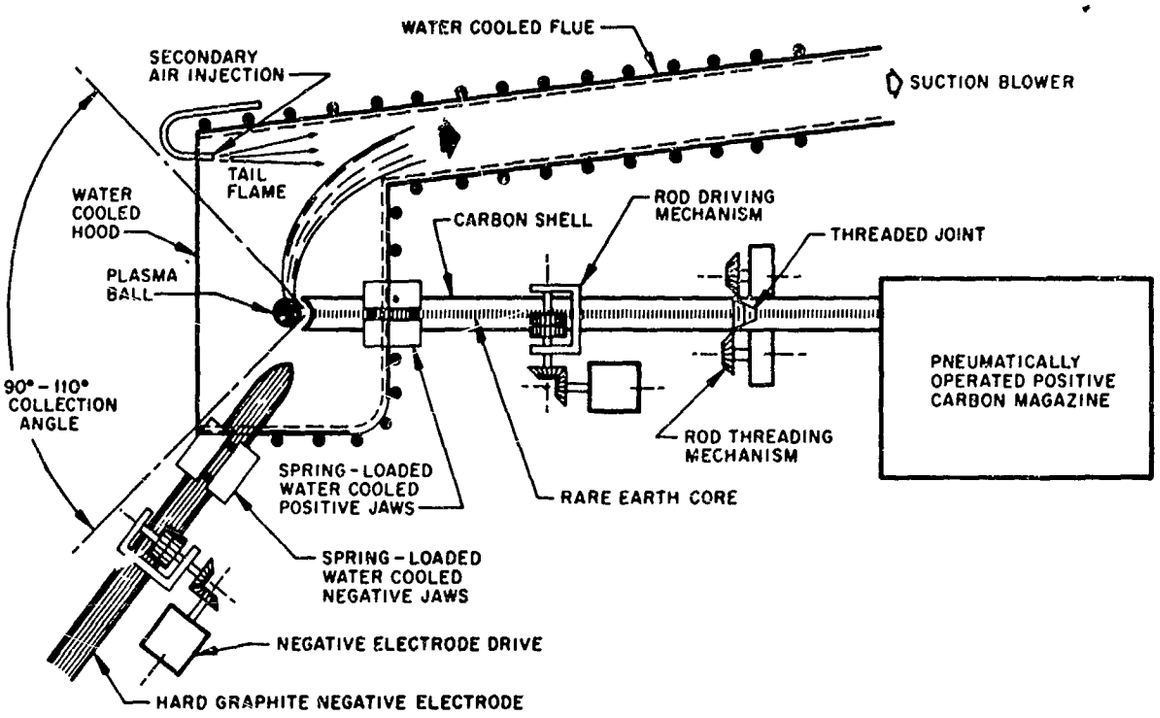

Figure 19 Basic Features of Carbon Arc Lamp (After Ref. 23)

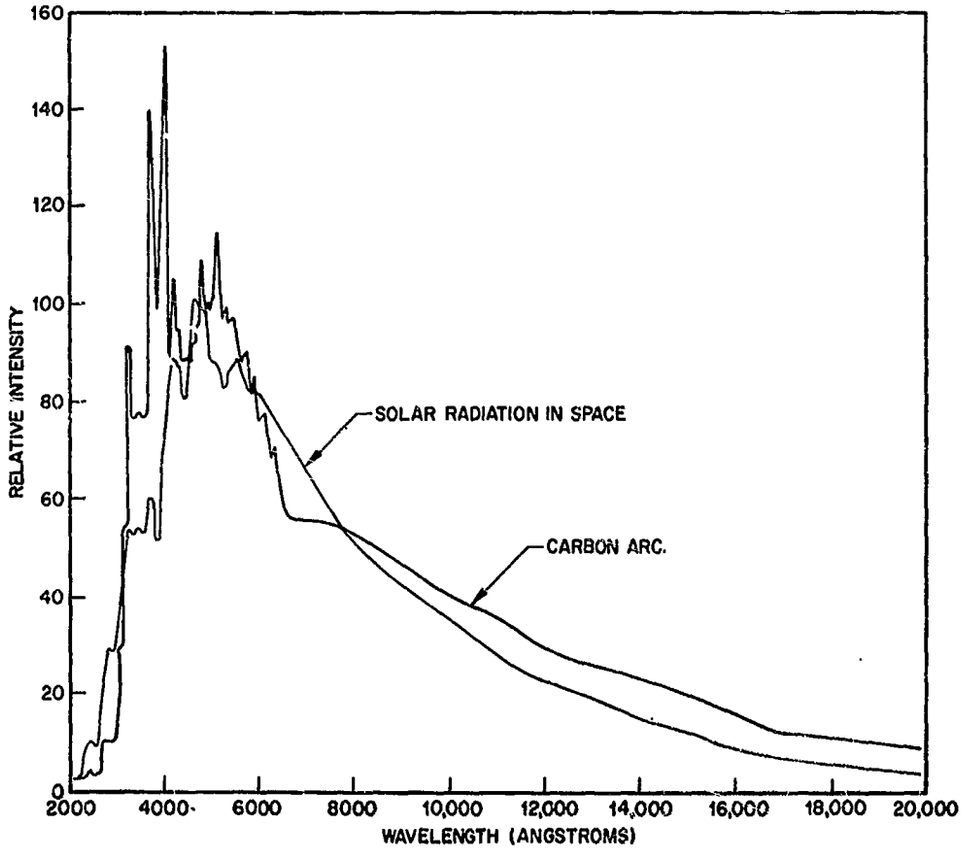

Figure 20 Spectral Distribution of Carbon Arc Lamps

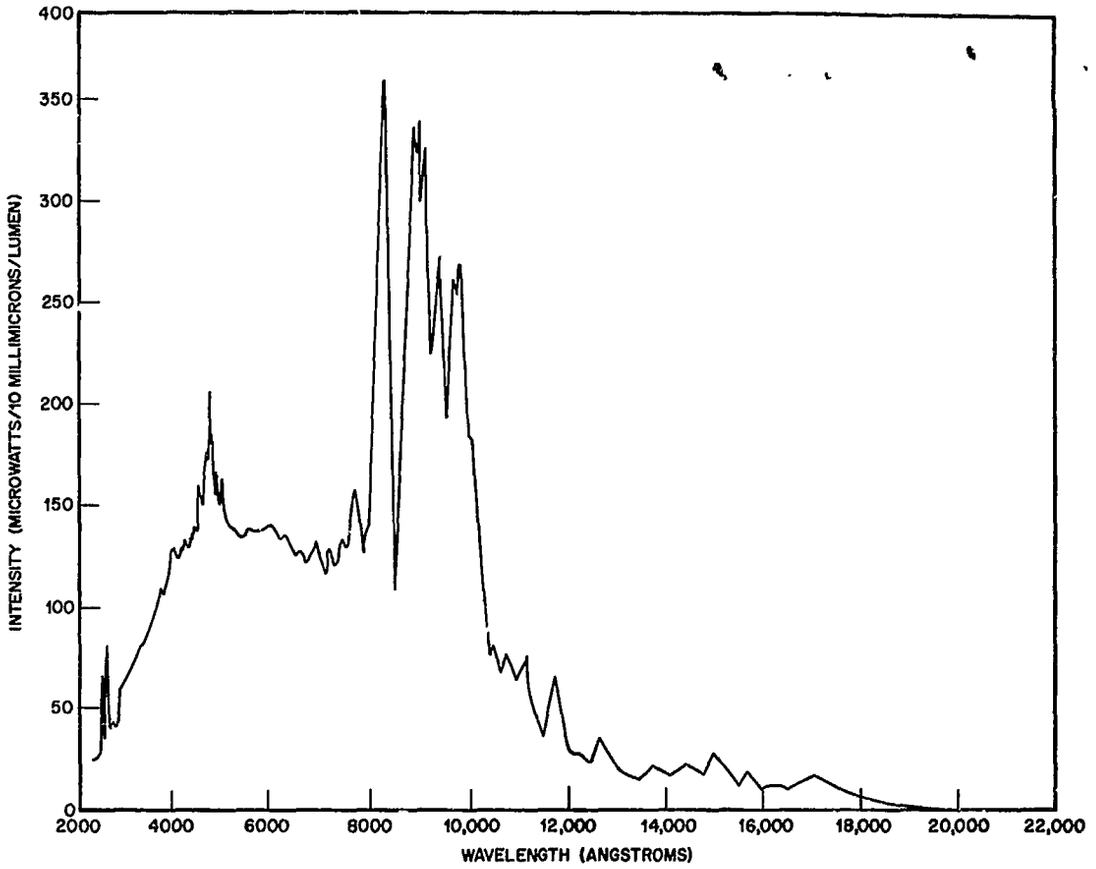

Figure 21 Spectral Distribution of Xenon Compact Arc Lamp

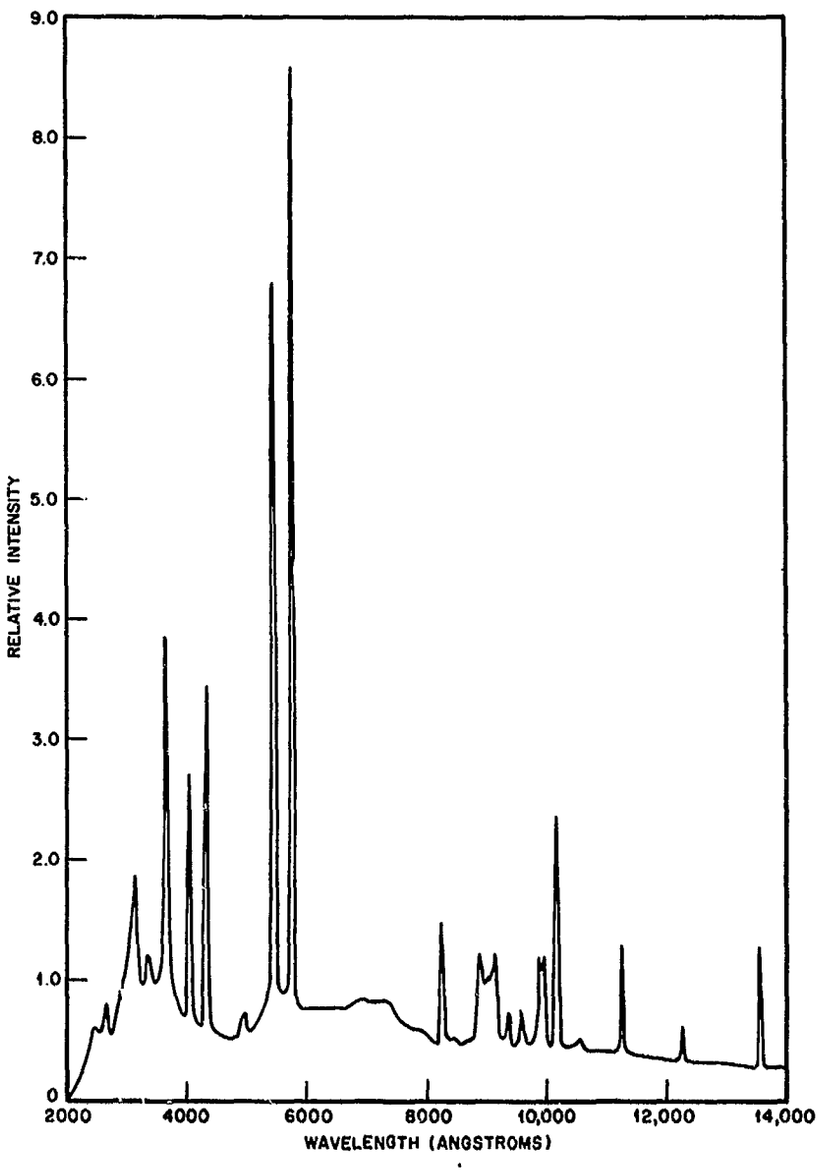

Figure 22 Spectral Distribution of Xenon-Mercury Compact Arc Lamp

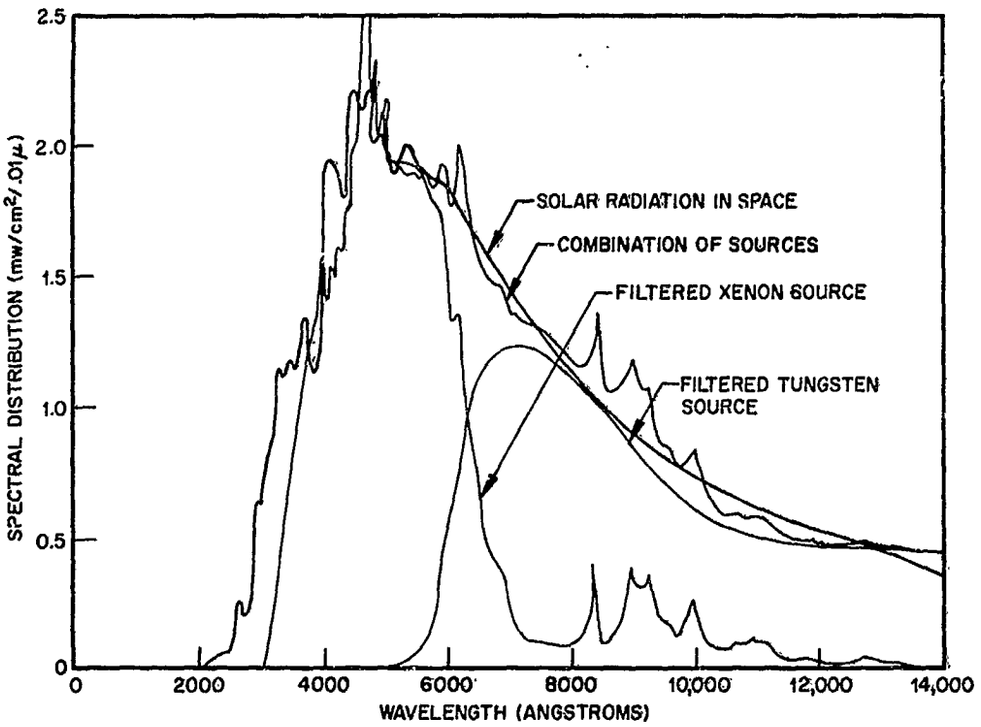

Figure 23 Spectral Distribution of Combined Source of Xenon Lamp, Tungsten-Filament Lamp, and Filters

N66 28902

IONIZING PARTICLE RADIATIONS EFFECTS AND SIMULATION CONSIDERATION

By

J. E. Duberg and W. C. Hulten

NASA - Langley Research Center

INTRODUCTION

Radiation-effects activities have developed throughout the United States because of three types of radiation environment: (1) steady-state nuclear reaction, (2) nuclear weapons - burst and pulse radiation, and (3) space radiation environment.

The prime effort in the radiation-effects field over the past decade has been concerned with the steady-state nuclear reactor environment. This effort has been to generate information needed for nuclear reactor development programs. Work in this area is continuing. Within the past few years considerable concern has been generated over the problems associated with systems operation during or after a nuclear-bomb burst. However more recently there has been an increased interest in the space environment and nuclear-propelled space vehicles.

The space radiation environment has brought about the need for additional studies of radiation effects. The useful lifetimes of earth satellite

experiments have been seriously degraded due to the damaging effects of the space radiation environment (trapped radiation fields, electrons and protons and solar flares).

The need for suitable simulation facilities for studying the effects of the space radiation environment has been a concern of NASA since the verification in 1958 of the existence of a natural trapped radiation environment in space. It has been a continuous effort to obtain more definitive information on the complex radiations by means of space probes and earth satellite systems. The environmental data obtained from space experiments on the composition, spatial distribution, and fluctuations with time are being applied constantly in the development and updating of computer codes which permits the computation of satellite exposures for planned space missions. Representative space missions for which radiation exposure information is desired are earth satellites, moon probes and satellites, and interplanetary missions. Environmental data for the representative missions are an important element in planning and carrying out programs to simulate the effects of radiation through laboratory type experiments.

SPACE ENVIRONMENT

The particular radiation environment encountered in space which offers a great threat of damage to space vehicles including both manned and unmanned systems includes; protons and electrons trapped in the earth's magnetosphere, and high-energy protons associated with solar flare events.

Protons

A brief review of our knowledge of the particular radiations in space is appropriate and, as cosmic rays are familiar, they are used as a basis of

comparison in figure 1, reference 1. The cosmic ray flux is comprised of approximately 85 percent protons, 13 percent helium nuclei, and the remainder, heavy ions, reference 2. Only the proton spectrum is shown. Although the flux is low, protons from this source attain extreme energies in the Bevs. The upper energy limit has not been determined but there is reason to believe that it is much in excess of 10^6 Bev.

The proton spectra of three solar events are shown with an indication of their time variation. The dotted portions of the curves are extrapolations. Energies of 10 Bev may be attained but flux values for these high energies are very low. Integrated, instantaneous, omnidirectional fluxes down to a few Mev may exceed 10^6 protons/cm^2/sec. The solar event of February 23, 1956, would indicate that both flux and energy decrease with time. It is more commonly believed, however, that the event of November 12, 1960, is the more likely occurrence, reference 3. For this event, the flux values of the lower energies increase, as those of the higher energies decrease with time.

The protons trapped in the earth's magnetosphere have omnidirectional fluxes ranging from over 10^4 protons/cm^2/sec at energies greater than 40 Mev to fluxes of the order of 10^3 protons/cm^2/sec at energies greater than 550 Mev.

Electrons

A high-altitude nuclear detonation in July 1962 increased the trapped radiation problem in space. The flux of these manmade electrons has been geographically located as shown in figure 2, references 4, 5, and 6, soon after the detonation and more recently after considerable decay. The

naturally trapped protons and electrons are also shown and may be used as a basis of comparison. The more recent data indicate that the manmade radiations are decaying with time and the peak intensity has shifted from approximately 1.6 earth radii to approximately 1.2 earth radii. It can be seen that the new manmade radiation contributes much of its intensity in the lower regions and thus increases the radiation damage problems of low-altitude space missions. The peak intensities of the electrons of this artificial belt, when first formed, exceeded the maxima of the natural outer region even when the latter's intensities are increased by magnetic storms.

The natural outer region is seen to be of a transient character and has variations in flux and energy due to solar activity. By far the greatest number of these electrons have energies below 1 Mev, reference 7. The manmade radiation, however, has about 45 percent of its electrons with energies between 1 and 7 Mev.

It is assumed that the electron fission energy spectrum shown in figure 3 would be obtained for manmade detonations of nuclear devices. The spectrum (ref.8) is expressed in relative differential values. If the spectrum is integrated and normalized it yields the following results: 55 percent of the electrons have energies ≤ 1 Mev and 91 percent of the electrons have energies ≤ 3 Mev. The maximum electron energy is about 7 Mev. The addition of any manmade trapped electron radiation may pose an even greater hazard than that which is already present from the natural trapped electrons.

SUMMARY

A brief summary of the particulate radiation in space is given in table I (refs. 2 and 9).

The proton data are divided into low-energy, high-energy, and solar flares. The proton data of Table I do not imply that the energy spectrum is nonexistent between 4.5 Mev and 30 Mev. This gap exists because of the limitations of the detectors which were used, and the data are therefore not available. The low-energy protons populate the region between 3.1 and 4.7 earth radii, whereas the high-energy protons are encountered at about 1.6 earth radii.

Solar flares produce protons with energies from a few Kev to 10 Bev. The maximum integral energy flux varies between 10^5 and 10^6 protons/cm^2/sec, with the largest number of these having energies below 1 Bev.

The highest intensities of the natural trapped electrons are between 10^8 and 10^9 electrons/cm^2/sec and lie between 2.5 and 4 earth radii. The manmade trapped electrons originally had peak intensities greater than 10^9 electrons/cm^2/sec occurring at about 1.6 earth radii. The energies of both the manmade and naturally occurring electrons extend from a few Kev to 7 Mev.

The complexity of the space particulate radiation environment is much greater than has been presented in this brief review. It is an active field of research in itself and would require greater emphasis than is intended at this time to provide a complete coverage.

It is felt that our present stage of knowledge of the complex radiation environment is sufficient to specify the basic facilities needed for simulation testing. Since space exploration is an important national objective and knowledge of how to cope with the radiation damage problems is limited, simulated environmental testing is imperative.

Without the aid of simulation testing facilities one cannot provide the valid data necessary for predicting the effect of radiation exposure for

planned space missions. This is true for many types of materials, electronic components, equipment, instrumentation, systems, subsystems, and humans. Radiation-effects studies are needed to develop the more radiation-resistant materials and devices and protective systems for manned and unmanned missions.

RADIATION DAMAGE MECHANISMS

To determine the simulation facilities needed to study the effects of space radiation exposure in the laboratory one must consider the different types of radiation effects. The overall spectrum of space radiation can produce effects that are transient, permanent, surface, and chemical. Although these characteristics may occur simultaneously in the actual space environment they must also be considered individually as well as concurrent to provide a basic understanding of the mechanisms of radiation effects.

Transient Radiation Effects

Transient effects are associated with the excitation or ionization of the electrons of a material by the bombarding radiation. These effects are predominately electrical in nature and generally affect the performance of the material, component, or system. The changes as a result of transient effects are short-lived, that is, the relaxation times for electronic changes in most materials are usually very short. Transient effects are a function primarily of dose rate and in most cases disappear when the bombarding radiation ceases. These effects generally do not result in permanent damage, in the sense that no difference in the material is evident after exposure. During the irradiation process, however, the entire component or

components of a system or circuit may interact and cause a complete failure.

Transient effects in a semiconductor may be described with the aid of the band structure diagram shown in figure 4, reference 10. When a semiconductor is bombarded by radiation the atomic electrons or valence electrons are excited by the bombarding particle interacting via the electrostatic Coulomb field. The electrons receive enough energy to excite them from the valence to the conduction band. This process causes an increase in the electrical conductivity of the semiconductor since the number of electrons in the conduction band and the number of holes in the valence band are increased. As mentioned before, this is a transient phenomenon since the excess electrons and holes recombine after the bombarding radiation ceases.

Examples of probable changes in materials by excited electrons are (ref. 11):

1. In semiconductors, the densities of majority and minority carriers are changed; this results in conductivity changes, a decrease in reverse impedance of rectifying junctions, and generation of photovoltages at junctions.

2. In insulators, secondary electrons are emitted from surfaces; this produces net charges on conducting elements and,in addition, induces an internal space-charge distribution.

3. In gases, free electrons and ions are produced; these conduct electric current and frequently exhibit temporary net space charge distributions.

4. Transparent materials may exhibit appreciable optical effects, such as change in transmission at certain wavelengths and emission of fluorescent radiation.

Permanent Radiation Effects

Permanent effects are commonly referred to as displacement radiation effects. These effects occur when the bombarding radiation interacts with

the displacement-type defects are shown in figure 5 (ref. 10).

The incoming particle interacts with an atom of the semiconductor being bombarded. If the bombarding particle imparts a sufficient amount of energy to the atom, it will be displaced from its normal lattice position. For example, in germanium and silicon the minimum energy transfer required for a displacement to occur is around 13 ev. Many of the displaced atoms come to rest at interstitial positions in the lattice. Thus, pairs of interstitial atoms and lattice vacancies are produced. These defects that are produced give rise to defect energy levels in the forbidden energy gap of the semiconductor.

A basic understanding of displacement-type defects is essential to the analysis of radiation damage to semiconductors. These type defects are the prime mechanism responsible for producing permanent damage in most semiconductor devices employed in space applications. The radiation-induced defects in a semi-conductor device such as a transistor serve as trapping and recombination centers for the carriers in the device. Recombination of the minority carriers in the base region of a transistor will reduce its gain.

Examples of physical evidence of displacement-type defects are (ref.11):

1. Increase in the electrical resistivity of metals, particularly at low temperatures, as the result of the enhanced concentration of electron scattering centers.

2. Changes in the minority carrier lifetime, carrier mobility, and effective doping of semiconductors, as the result of the defect states introduced in the forbidden energy gap.

3. Changes in the mechanical properties of materials, as the result of the effect of the radiation-induced defects on the lattice.

4. Changes in the mechanical properties of alloys, resulting from localized recrystallization and rearrangement.

5. Changes in the thermal conductivity of materials as the result of lattice defects which act as photon and electron scattering centers

Surface Radiation Effects

Surface effects may be a form of permanent damage effect; however, it is treated separately for simplicity reasons. Surface studies on materials include the interactions of the bombarding radiation with outer layers of atoms. Surface effects are concerned with surface films for heat balance control, erosion, sputtering, or spallation. The associated effect of other environments such as vacuum, temperature, etc., are important considerations in these studies.

Surface ionization effects on semiconductor devices such as transistors may cause appreciable changes in characteristics at doses low compared to those required for permanent bulk damage. These effects may vary considerably for different device types and even individual units of a given type. These surface effects are not well understood but involve the collection of ionized gas particles or impurities on the surface of the device, thereby producing inversion layers that can alter the shunt leakage paths around the device. This results in a significant increase in the reverse leakage currents.

Chemical Radiation Effects

In some materials and systems, irradiation may have important chemical effects. The interaction of the bombarding radiation with orbital electrons may produce free electrons and a positively charged molecule. In organic

systems, the removal of a bonding electron could disrupt the stability of the molecule, and by subsequent interaction, form new chemical systems or structures. For example, many organic systems evolve gases, mainly hydrogen when irradiated. Irradiation of water produced hydrogen peroxide and free hydrogen. The physical properties of polymers may be altered by radiation as a result of a small change in the chemical bonds.

PRESENTATION OF RECENT RADIATION-EFFECTS STUDIES

Radiation-effects research programs have been underway for some time. In most cases reactors have been used as a radiation source prior to the need for radiation effects testing simulating space conditions. Unfortunately data obtained from the reactor sources have not proven suitable for the space environment studies in regard to energy and types of radiation. Much information has been gained from the reactor work, however, and has been useful in providing relative orders of magnitude of damaging doses and provides some means for estimating the fluxes to be used for accelerated space-radiation-damage studies. Additional knowledge of the importance of experimental procedure has been gained from the review and attempts to utilize and correlate the radiation-effects data from reactor exposures. For the most part the earlier data from reactor exposures have neglected the documentation necessary for the understanding of the special experimental techniques and problems of irradiation experiments.

For the past few years the Langley Research Center has developed research facilities and experimental capabilities while pursuing its research program in experimental investigations of the effects of particulate radiation on items used in space missions. Much experience has been gained in

working with the owners of various major accelerators throughout the country. The accelerators utilized to date in carrying out the irradiation experiments include; the Oak Ridge National Laboratory's 22-Mev Cyclotron, University of Minnesota's 40-Mev linear accelerator, Harvard University's 158-Mev synchrocyclotron, University of Rochester's 240-Mev synchrocyclotron, Carnegie Institute of Technology's 440-Mev synchrocyclotron, Langley Research Center's 1-Mev Dynamitron Potential-Drop Machine, 25-Kilo-curie cobalt 60 source, and 150-Kev X-ray machine, the 2-Mev Van de Graaff of the Naval Weapons Station at Yorktown, and the Lewis Research Center's 3-Mev Dynamitron Potential-Drop Machine.

In accord with the objectives of minimizing or eliminating the effects of space radiation on all items which comprise space missions a research program has been outlined part of which is already underway in the following areas: materials, which include seals, cements, plastics, lubricants, vibration damping materials, phosphors, insulators, semiconductors, etc.; external surfaces such as coatings, transparent materials, and optical compounds; complete devices such as magnetic, electronic, and solid state; shielding which covers magnetic as well as various bulk configurations; detection encompasses design, development, testing, and calibration of new detecting devices; dosimetry including experimental studies of radiation levels and doses delivered to different areas and constituents of space vehicles; environmental contamination will deal with the ability of radiation to produce corrosive, noxious atmospheres, for example, ozone and nitrous oxides in closed ecological systems; sputtering phenomena; activation resulting from radiation; chemistry of elastomers and polymers; electrical properties for the study of radiation-induced defects in semiconductors; spectroscopy for the study of radiation-induced changes will include nuclear magnetic

resonance, electron paramagnetic resonance, infrared and visible light, electron microscopy, X-ray techniques and mass spectroscopy; thin films; experimental validation of theoretical studies; biological research including synergistic effects; health physics; and basic physics research.

Some examples of the LRC experimental radiation-effects investigations which have already been carried out utilizing the accelerator facilities mentioned earlier include: (1) the changes of electrical properties in semiconductors with proton irradiations; (2) irradiation effects on semiconductor devices, transistors, and solar cells; (3) effects of ionizing radiation on polymers; (4) irradiation-induced changes in capacitor-type detectors; and (5) effects of radiation on the optical transmission properties of transparent materials.

Semiconductor

A study has been made at the Langley Research Center by Roger A. Breckenridge and Chris Gross of the changes produced in the electrical properties of a semiconductor to provide basic information about the defects created by radiation. Changes in the electrical properties of a sample of N-type germanium irradiated with 22-Mev protons are shown in figure 6. Radiation-produced defects in the lattice of a semiconductor give rise to defect energy levels in the forbidden energy gap of the semiconductor. These levels are effective in trapping carriers from the conduction and the valence bands. The electrical properties affected are the conductivity and the Hall coefficient. In this particular sample, electrons are being trapped from the conduction band by defect energy levels as is evidenced by the decrease in the conductivity and the reciprocal Hall coefficient which

is proportional to the majority carrier concentration. Since field-effect transistors are majority carrier devices, studies of the electrical conductivity of the materials and Hall coefficient, coupled with radiation-effects studies on the devices, provides a better understanding of the total damage of devices which is complicated by the effects at the junctions.

More specific information on the location of defect energy levels may be obtained by means of temperature cycling. Figure 7 shows the location of a defect energy level in a sample of N-type germanium which has been irradiated with 22-Mev protons. The carrier concentration is measured as a function of temperature after the irradiation has been performed. As the temperature is increased, the Fermi level of the semiconductor shifts toward the middle of the forbidden gap. When the Fermi level passes over a defect energy level, it may be pinned there depending on the concentration of defects. If it is pinned, a plot of $\ln nt^{-3/2}$ versus $1/T$ gives a slope which is equal to the energy difference between the level and the nearest band edge divided by Boltzmann's constant. The particular energy level of defects in this material located is 0.20 ev from the bottom of the conduction band.

Solar cells. In view of the lack of available data on shielding effectiveness, particularly for electrons for relatively thick shields of materials other than aluminum, it has been necessary to investigate experimentally the effectiveness of shields for solar cell protection from radiation damage. An example of an earlier phase of experiments conducted at Langley by J. L. Patterson and W. E. Ellis is shown in figure 8. Degradation as a function of integrated electron flux for typical N on P solar cells both unshielded and with several thicknesses of silicon dioxide (fused silica)

shields is shown. In this case the solar cell parameter used to determine degradation is short-circuit current. The current measurements were made utilizing tungsten lamps, but were corrected to that expected in space-sun (air mass = 0). The 2.4-Mev electron has a practical range of 1.5 gms/cm^2 in fused silica or slightly over 3/16 inch. The critical flux (that required to reduce the short-circuit current by 25 percent) for cells behind the 1/8-inch-thick fused silica shows an increase by a factor of about 3. The corresponding factor for the 3/16 inch is about 60, and for the 1/4 inch thick the factor is greater than 1,000.

Additional studies on solar cells include the change in spectral response due to radiation and the effects or radiation on load and temperature characteristics.

The change in spectral response of a typical 8-percent solar cell irradiated with 22-Mev protons is shown in figure 9. The relative cell output, which is proportional to output short-circuit current per unit of wavelength, is plotted versus wavelength in microns. The irradiation causes a shift toward shorter wavelengths and toward the peak of the space solar spectrum. This shift in cell response may be explained by the fact that irradiation decreases the cell diffusion length, and because the output resulting from illumination for the longer, more penetrating wavelengths of light is more dependent on the diffusion length, as a result the total cell output is more dependent on the shorter wavelengths after irradiation. Because of their stability, tungsten lights with peak output at about 1.0 micron have been used most often to evaluate solar cell damage. Since Johnson's curve for space-sun peaks at about 0.50 micron, it is obvious that tungsten light measurements give exaggerated degradation. We have found that the spectral response of some solar cells is a function of light level. This

points out that the importance of exacting techniques to permit accurate computation of tungsten light to space-sun degradation correction factors. We are currently evaluating a recently acquired space-sun simulator which should eliminate some of the time consuming spectral response work.

Figure 10 shows experimental results from a study to determine the effect of radiation on solar cells under load and temperature conditions. Current-voltage curves have been plotted while the loading was varied from short-circuit to open-circuit conditions. Curves are plotted for four temperatures before irradiation and after radiation with 1.2-Mev electrons to an integrated flux of 10^{16} electrons/cm^2.

The drop in open-circuit voltage is relatively small (approximately 0.1 volt at room temperature); however, this can made a big difference under some load conditions. A change in the open-circuit voltages indicates a change in the junction impedance.

The percent change in short-circuit current with temperature is comparatively large after irradiation, probably caused by introduction of new recombination centers. (Change before irradiation (36° F to 160° F) ≈ 14 percent, change after irradiation (36° F to 160° F) ≈ 40 percent.) In some satellite instrument power supplies, batteries maintain the solar cell voltage very close to 0.38 volt per cell. The I-V curves indicate that at room temperature the degradation was essentially the same at the 0.38-volt as it was under short-circuit conditions. (Both before and after curves at room temperature were flat out to the 0.38-volt line.) Degradation was greater at elevated temperatures.

In some instances higher voltages per cell are used. For instance, the maximum power at room temperature for this cell is at 0.43 volt, but degradation due to radiation is worse at the higher voltages.

Solar cell damage experiments onboard satellites have been loaded with fixed resistors of 6.6 ohms. Under this load condition there is a temperature coefficient reversal. Before irradiation the power output decreased with an increase in temperature whereas after irradiation the power output increased with an increase in temperature.

It is obvious that a number of factors must be carefully considered when designing space instrument power supplies to determine predictable useful lifetimes of solar cells.

Transistors. Investigations of the effects of radiation on transistors have included many different types. For the most part we have concentrated on irradiations with high-energy protons. The transistor types investigated to date include the commonly used injection-type or bipolar units, and the most promising types such as the field effect, integrated circuits, and microcomponents. One of the most important parameters affected by radiation in the injection-type transistor is the forward-current transfer ratio h_{fe} which is the small signal current gain β. This parameter depends on the lifetime of the minority carriers in the injection-type transistor. Radiation-produced defects can reduce the lifetime of the carriers by means of trapping and recombination centers, thus reducing the gain of the transistor. Figure 11, from results obtained at Langley by F. R. Bryant and W. C. Hulten, shows typical damage curves for several 2N337 NPN silicon transistors. Changes in normalized small signal current gain is shown as a function of integrated flux in a 40-Mev proton beam. After an exposure to 0.4×10^{12} protons per cm^2 the transistor gain was reduced approximately 50 percent.

Additional findings as a result of the transistor damage studies are concerned with transistor damage as a function of base current. Figure 12 shows the actual change in gain plotted on the right ordinate and also the percent

change on the left ordinate as a function of base current before and after irradiation with 3-Mev electrons. With a base current of 2.5 microamperes the transistor showed a loss of gain of approximately 72 percent. When the base current was increased to 30 microamperes, the loss in gain was approximately 44 percent. The reason for the higher percentage loss in gain at the lower base currents is probably due to the fact that at the lower currents the carriers migrate to the surface more easily and recombine, whereas at the higher base currents the electric field is stronger and restricts the loss of carriers to the surface.

An example of radiation damage to field-effect transistors by 128-Mev protons is shown in figure 13. This type transistor is a majority carrier device and is affected less by radiation than the minority carrier devices previously discussed. The radiation-induced changes in majority carrier concentration result in damage to the field-effect transistor. The changes in common-source transfer characteristics before and after irradiation are shown, drain current is plotted versus gate voltage for a P-channel silicon and N-channel germanium field-effect transistors. In comparing the relative radiation resistance of these two types of field-effect transistors the P-channel silicon is more radiation resistant than the N-channel silicon. The change in the slope of the curves is a measure of the change in gain, where the transconductance is equal to the slope and the gain is approximately equal to the transconductance times the load, for low frequencies, where the load is constant. This difference in radiation resistance has also been indicated from the results of measurements of carrier removal rates due to irradiation of these type materials, where the removal rates are higher for the N-type germanium.

Figure 14 shows some comparative values of integrated flux to produce equal degradation (30 percent loss in gain) in a number of different types of transistors. The first three minority carrier types show that the higher the frequency or the narrower the base width the greater is the tolerance to radiation. The integrated circuit and microtransistors are equivalent to the high-frequency minority carrier types. The P-channel silicon is two orders of magnitude better than the medium frequency minority carrier types.

Polymers

Investigations of the effects of radiation on organic polymers are being carried out at Langley to determine their application in space missions. Mylar balloons, Echo I and Echo II, are two examples of the use of this material in space. More specifically, studies have been made by G. D. Sands, H. L. Price, G. F. Pezdirtz, and V. L. Bell to measure the effects of ionizing radiation experimentally, to deduce the mechanisms of the reactions involved, and to apply this information to the use of polymers to the best advantage in space and to suggest new polymer structures with improved properties.

Figure 15 shows the change in several properties of Mylar with increasing radiation dose. It should be emphasized that the threshold dose for detectable damage in Mylar is about 10 megarads, or the dose received by Echo II in 10 days at its altitude of 600 to 800 statute miles, a sizable dose; the dose range covered by the figure corresponds to a 3-year dose for Echo II. In the initial stages of irradiation, the curves depicting molecular weight, tensile strength, and elongation decrease with increased

dose in the same general way. The mechanical properties of a polymer depend upon the combined effects of the mechanical and Van der Waals interactions among the individual high molecular weight chains. As gamma radiation cleaves some of these chains, the molecular weight decreases, and this is reflected in the observed tensile strength and elongation values.

Ionizing radiation causes deterioration of physical properties through a free radical mechanism involving excitation and ionization. This deterioration of properties is a reflection of either the breaking or the cross linking of polymer chains, depending upon the structure of the polymer. Polymers with the vinyl-type structures cross link, while those with the vinylidene-type structure degrade, figure 16 If the repeating unit of the polymer has a vinyl side group (a single side group, other than hydrogen, on every other carbon atom), then the polymer will predominantly cross link. On the other hand, if the repeating unit of the polymer has vinylidene side groups (two side groups, other than hydrogen, on every other carbon atom), then the polymer will degrade when irradiated. In the case of the vinyl structure, the side groups have sufficient freedom to arrange themselves in space along the chain in such a way that there is little or no strain in the chain. In the case of the vinylidene structure, the two side groups on alternate carbon atoms are unable to find a geometric position in which they will not interact with each other. This produces an internal molecular strain along the chain and as a result when the chain is broken by ionizing radiation, this molecular strain causes the ruptured fragments to effectively fly apart and prevents "rehealing" of the broken chain.

Just as different classes of materials vary, so do different types of

polymers vary widely in their resistance to ionizing radiation, figure 17, H-film being very resistant, while Teflon is quite sensitive. Radiation stability of polymers is enhanced by several means: (1) aromatic rings, (2) high thermodynamic stability, (3) rigidity (whether imparted by inherent high modulus, or by the addition of a rigid reinforcing material or filler), and (4) lack of halogen atoms.

These effects are illustrated by the examples previously cited, H-film and Teflon, figure 18, reference 12. H-film is highly aromatic, has a small ΔH polymerization, has a high modulus of elasticity, contains no halogen atoms, and is the most resistant plastic currently available. Teflon, on the other hand, contains no aromatic rings, has a large ΔH polymerization, is not rigid, has a high proportion of fluorine atoms, and is observed to be among those polymers most sensitive to ionizing radiation.

The four principles listed above are being used as a guide by chemists as they seek to synthesize new polymers which will be even more radiation resistant for future space applications.

Dielectrics

Preliminary investigations of George M. Storti at Langley on irradiation effects in dielectrics have been directed towards the study of a particular type of transient effect that occurs during low-energy electron irradiation (35 Kev to 900 Kev) at total doses far too small to cause any significant permanent changes in the characteristics of most materials. The particular type of transient effect was observable as a voltage pulse and is apparently due to excessive charge storage in the dielectric resulting in an electric field breakdown.

Several types of capacitors were tested under varying conditions of incident electron kinetic energy, temperature, and dose rate. Results from a commercial electronic capacitor and a specially prepared flat capacitor using Mylar (Polyethylene terephthalate) as the dielectric are presented. Figure 19 shows the specially prepared flat capacitor mounted for temperature control. All pulses that were counted were greater than 1 volt in magnitude. Figure 20 shows a typical trace of a transient pulse as monitored by an oscilloscope. The vertical scale is 20 volts per division, horizontal scale 1 millisecond per division. The pulses are characterized by a very fast rise time followed by a relatively slow decay corresponding to the RC time constant of the detection circuit. The pulse dependence on electron kinetic energy and temperature is shown in figure 21. For each sample there is a characteristic dependence of the number of pulses on the incident electron kinetic energy for a given temperature. The number of pulses first increases to a maximum between 40 Kev and 80 Kev, and then, corresponding to increased transmission through and less deposition of electrons in the dielectric, the number of pulses decreases.

The effect of temperature was investigated with the commercial capacitor as the target. The dose rate was 3.2×10^{10} electrons/cm^2/sec and the total dose was 10^{14} e/cm^2. Runs were made at liquid nitrogen (-320°F) and hot water (197°F) temperatures. The incident electron kinetic energy was varied over the range where pulses were obtained. The number obtained at the higher temperature is markedly less than at the lower temperature. Also, at the higher temperature, no pulses were obtained above 80 Kev, whereas at the liquid nitrogen temperature, pulses were obtained up to 700 Kev, therefore, these results indicate an important temperature dependence,

and also show the necessity of conducting tests over the entire temperature range which a satellite is expected to experience in space.

Pulse dependence on dose rate at -320° F, 70° F, and 197° F is shown in figure 22 for the specially prepared polyethylene terephthalate capacitor. Dose rates were varied from 3.1×10^{7} e/cm^2/sec to 3.1×10^{10} e/cm^2/sec. The number of pulses shown corresponds to a total dose of 3.25×10^{13} e/cm^2. Data points were obtained at hot water (197° F), room (75° F), and liquid nitrogen (-320° F) temperatures. At liquid nitrogen temperatures there appears to be relatively little dependence on the dose rate. At the lowest dose rate the number of pulses trails off only slightly from the number obtained at the higher dose rates. However, at room temperature and elevated temperatures there appears to be some effect of dose rate on the number of pulses obtained.

Transparent Windows

The effects of radiation on the transmission characteristics of several transparent materials have been investigated to determine their suitability for protective shielding of solar cell space power supplies from space particulate radiation damage (ref. 13). Figure 23 shows the effects of 1.2-Mev electrons on the spectral transmission of synthetic annealed sapphire. The transmission in percent is plotted against wavelength, microns. Curve (a) is the spectral transmission before irradiation. Curve (b) shows a small decrease approximately 2 percent in ultraviolet transmission occurring after a dose of 10^{17} e$^-$/cm^2. The sapphire sample also showed a slight discoloration.

Figure 24 shows the effects on synthetic fused silica before and after

irradiation at several integrated doses. Curve (a) is the unirradiated sample, curve (b) shows a decrease in transmission primarily in the ultraviolet after an integrated dose of 10^{15} e^-/cm^2. As the dose increases, curves (c) and (d), the degradation extends into the visible. Associated with the visible transmission decrease is a slight bluish visible discoloration. The depth of this discoloration in the material appears to approximate the penetration depth of 1.2-Mev electrons in SiO_2.

Figure 25 represents a lightly damaged sample of fused quartz. There is a decrease in transmission in the UV, and visible regions with some changes in the infrared An absorption maximum appears to be centered at 0.55 micron. Associated with the absorption maximum in the visible is a discoloration that is proportional to the degree of absorption. It varies from a faint brownish color for lightly damaged samples to a deep purple for heavily damaged samples.

Figure 26 represents Corning No. 8363 high-density lead glass. A dose of 2.7×10^{15} e^-/cm^2 caused very little damage in the region of the spectral cut-off for the sample. The transmission decrease in the solar cell response region is minute, thus explaining the negligible wide-band transmission loss for this sample.

It is believed that the impurities in the materials are the main cause of discoloration or absorption in the visible. Damage in the UV transmission is thought to be caused by defects in the atomic structure of the material. A series of irradiation tests on quartz showed the very pure synthetic fused silica degraded relatively little while the less pure fused quartz degraded substantially.

A summary of the 1.2-Mev electron irradiation-effects investigations on transparent protective shielding for solar cells suggest that:

1. Sapphire is practically unaffected in the spectral response region of solar cells.

2. Synthetic fused silica is damaged primarily in ultraviolet transmission, thereby it is an excellent material for use as solar cell covers.

3. Although some types of fused quartz degrade rapidly in ultraviolet transmission, other types are quite radiation resistant; however, it is advisable to test fused quartz for radiation resistance before use.

4. High-density lead glass and nonbrowning lime glass are radiation resistant; however, their transmission properties are less than those for quartz, and caution must be taken in using them because cerium-doped glasses are susceptible to electron discharge patterns.

5. Results of tests yield conservative values compared to those computed from electron transmission data.

NASA SPACE RADIATION EFFECTS LABROATORY

The majority of facilities utilized for simulating space-radiation effects suc' as those located at the academic institutions have been designed for basic physics research and do not provide many of the required features for a complete radiation-effects experimental program where the major part of the program is engineering-type research. The limited programs utilizing these facilities to date have been most satisfactory since the experiments have been selected and tailored to be compatible to a specific facility.

These facilities are being used almost full time for the intended basic physics research programs and have very limited available beam time for the engineering-type research programs. To overcome this shortcoming without interference with the physics research effort, LRC, NASA, has under construction a Space Radiation Effects Laboratory.

The simulation facilities selected for the SREL are considered adequate

and necessary to meet the expanding aerospace research in radiation effects, offering the versatility and compatibility for sufficient simulation in the laboratory of the important space environmental parameters.

Proton Accelerator

The accelerator shown in figure 27 is the basis for the SREL proton accelerator, a 600-Mev frequency-modulated synchrocyclotron with a magnet weighing about 2,500 tons. It is approximately 36 feet wide, 21.3 feet deep, and 20 feet high. The magnet gap varies from 17.7 inches in the center to 14.7 inches at the outer edge, reference 14. The magnet coils are made of about 333 turns each of rectangular, hollow aluminum, are water cooled and operate at about 1.2×10^6 ampere turns.

The radio-frequency system uses a water-cooled tuning-fork modulator which modulates the RF frequency between 29 and 16.5 megacycles at 55 cps with Dee voltages varying from 6 kilovolts to 25 kilovolts, reference 15.

The vacuum system using two roughing and two 32-inch oil diffusion pumps provides a vacuum of about 10^{-6} torr.

The ion source is a cold cathode type which receives a 1,000-volt d-c pulse at the repetition frequency of the radio-frequency system and at a controllable phase.

Proton accelerator beam features. The synchrocyclotron will be capable of producing internal proton beam currents of approximately 0.5 microampere. The external proton beams will include two primary energies, 600 Mev nominal at full radius extraction, and 300 Mev at reduced radius extraction by means of a magnetic channel. The flux of the primary extracted beams will be approximately $10^{11} \cdot 10^{12}$ protons per second. The energy

spread will be less than ±1 percent. Intermediate energies will be continuously variable from 600 Mev down to at least 100 Mev. This will be accomplished by degrading the primary beams by means of absorbers. The degraded beams will have fluxes not less than 10^{10} protons per second, and the energy spread will be less than ±5 percent. The intensity distribution of the beam at the target will be less than ±5 percent. The external proton beam area at the target will be continuously variable from 15 cm^2 to 900 cm^2. With the existing external beam, a year exposure in space could be simulated in minutes to weeks over these target areas.

Internal target system. The synchrocyclotron internal target system shown in figure 28, although designed basically for high-energy physics research, lends itself readily to engineering research. There are eight internal flip targets to produce neutrons at radii corresponding to proton energies from 110 to 600 Mev, energies below 110 Mev are restricted by the physical location of the Dee. Mesons are obtained by use of a universal target, trolley mounted. The trolley can move azimuthally along the pole tip rim, and it has also provision for moving the target radially. The meson intensities will be 500,000 per second. Provision is also being made for installing vibrating targets. Also available will be beam stops, a beam clipper to absorb those parts of the internal beam that have obtained excessive vertical oscillation, and a beam chopper which will enable the operator to vary the beam from zero to a maximum.

Electron Accelerators

0.5- to 3-Mev electrons. A part of the electron capabilities will be an electron Dynamitron which is a potential-drop machine shown in figure 29. The tank, 6 feet in diameter by 20 feet long, houses the evacuated acceleration

tube; the acceleration tube power supply, which converts low-voltage a-c power to high-voltage d-c power by means of a cascade rectifier system driven in parallel from an RF oscillator.

2- to 10-Mev electrons. Additional electron capabilities includes an electron linear accelerator (Linac). The linac shown in figure 30 is a traveling wave linear accelerator which operates at L-band frequencies (1300 Mc). The injector tank is shown which includes a three-stage Cockcroft-Walton type voltage multiplier circuit as the main injector d-c power supply. Other major components of the injection system are: focus anode power supplies, electron gun, electron gun controlled grid pulser and power supply, focus anode power supplies, and RF buncher cavity.

The accelerating waveguide is a disc-loaded waveguide of uniform phase velocity. The waveguide is terminated by an output coupler which couples out excess RF power from the first waveguide section through a vacuum tight window to a dummy load. The vacuum system utilizes the ionic "getter" pumps which are fluidless, have no heated filaments, and have no moving parts. Typical life expectancies are in excess of 20,000 hours at 10^{-6} mm Hg.

Electron beam features. The low-energy electrons from the Dynamitron range from 0.5 to 3 Mev. The external beam current is variable from 1 microampere to 10 milliamperes. A magnetic scanning system will control the external beam pattern to a maximum of 2 inches wide and 24 inches high. The target scan rate is 7 to 24 cycles per second. The minimum beam diameter is approximately 1 cm. The Dynamitron also has positive ion capability.

The high-energy electrons from the Linac range from 2 to 10 Mev with provisions for eventual extension of the energy range up to 30 Mev. The beam energy is continuously adjustable over the range 2 to 10 Mev. The average d-c beam current is continuously variable from 0 to 250 microamperes at

operating energies of 3 and 10 Mev, and 1000 microamperes at an operating energy of 7 Mev, and linearly corresponding values at intermediate operating energies. The linac beam pulse length is continuously variable from 0.1 microsecond to 6 microseconds, and stepwise to 0.01 microsecond. The 0.01-microsecond-pulse rise time is 5 nanoseconds, a duration of 10 nanoseconds, and a decay time of 5 nanoseconds. The pulse repetition rate is continuously variable from 10 to 720 pulses per second. Single pulse operation capability is also available. The emerging beam diameter is less than 10 millimeters for 90 percent of the total beam current. Angular divergence is less than 3 milliradians at 7 Mev.

Beam Transport Systems

Proton system. The proton beam transport system shown in figure 31 is designed to deliver to the target areas variable energy protons from 100 to 600 Mev. The energy spread will not be greater than plus or minus 5 percent. The intensity distribution over the target will be less than plus or minus 5 percent and the beam area at the target will be variable from 15 cm^2 to 900 cm^2. The transport system will clean the beam so that particles other than protons will not reach the target. The means for doing this will be to trim the proton beam with a collimator and focus with a pair of quadrupole magnets at the cyclotron exit. The beam will then be refocused by large aperture quadrupoles at focal points along the target path. A bending magnet in the cyclotron room is used to switch the beam into the magnet hall or the proposed proton area without destroying the quality of the beam. A degrader is then used as required to reduce the energy of the beam. The energy spread of the degraded beam is reduced by a collimator and the proton

beam is deflected into a test area by a bending magnet-quadrupole- collimator set. The neutrons produced in the degrader are not deflected and are lost in the magnet room. The proton beam continues in its magnetic channel, is further degraded as needed, refocused, recollimated to reduce energy spread, and proceeds to irradiate the target. This system will be one of the most advanced beam handling systems representing the application of the latest theories and techniques available in achromatic beam transportation.

Electron system. The electron beam transport system will carry the electron beam to targets in their respective areas and also to a proton target area where a target may be irradiated with both electrons and protons. The system will accept electrons from 1 to 16 Mev with an energy spread of plus or minus 3 percent. (A magnetic energy analyzing system will produce an electron beam at the proton target with an energy spread of plus or minus 1/2 percent for all energies accepted by the system.) The beam area at the target will be continuously variable from 1 to 900 square centimeters. Capability will exist for producing neutron beams and X-rays using the electron beam. A schematic of the electron beam transport is shown in figure 32. Since the systems for the Dynamitron and the linac are almost identical, the one for the linac will be described. The electron beam is fed through a pair of quadrupole lenses, thence through a scatterer and bending magnet. All bending magnets are equipped with magnetic induction probes for monitoring the fields. If the beam is bent, it then passes through a quadrupole lens, a bending magnet, a pair of quadrupoles, a scintillation screen, secondary emission probe into the target test chamber. If the beam is not bent, it proceeds through a valve section beyond which it can be stopped by a remotely controlled beam stopper. If it is not stopped, it continues through a quadrupole pair, bending magnet, quadrupole, bending magnet, quadrupole pair,

to a scintillation screen where it can be monitored. It then passes through some of the elements of the Dynamitron beam transport which may or may not be activated for focusing. The beam is then bent, channeled through another valve section, through a pair of quadrupoles, through collimators, detectors, into a Helmholtz coil, to the proton target test chamber.

Laboratory Arrangement

The floor plan of the Space Radiation Effects Laboratory is divided into three major areas as shown in figure 33. These are the experimental test and beam handling area, the test setup area, and the support building. The experimental test and beam handling area consists of two independent target areas, the electron accelerator caves with their target areas, the proton accelerator cave, and the magnet hall which will contain the beam transport and handling for the proton accelerator. The two target areas are about 37 by 26 feet each and these dimensions may be changed by moving the movable block shielding walls. One target area is arranged for receiving a combined electron and proton beam. Sufficient space has been allowed around the accelerators to permit ready access and normal maintenance without the inconvenience of moving shielding. Very large targets may be irradiated by piping the beam directly down the magnet hall to an externally setup test area. The shielding walls are about 17 to 24 feet thick and where short particle lifetimes and space requirements dictate, heavy concrete and/or steel walls are used. Overhead shielding is provided to reduce undesired radiation effects from above. The proposed neutron meson test areas will be so isolated as to give low background radiation, thus permitting the performance of very refined experiments. The neutron-meson area will be adjacent

to the cyclotron cave separated by a relatively thin steel and heavy concrete wall. The test setup area allows setups and measurements to be made without disturbance prior to installation into the target areas. Large vertical drop doors separate the target area from the setup area. The dimensions of the experimental test and setup areas are approximately 240 feet by 143 feet covering a floor area of approximately 33,000 square feet.

The support building is located next to the setup area which separates it from the experimental test area. It consists of two floors and a basement and will contain the control room and monitoring system for the accelerators, laboratory space, shop facilities, office space, counting areas, etc. Its size is 168 by 71 feet with a total floor area of approximately 21,000 square feet.

Operation of Laboratory

The current operational plan for the SREL provides for William and Mary, the University of Virginia, and Virginia Polytechnic Institute organized as the Virginia Associated Research Center (VARC), to supply the operational personnel for SREL. The participating universities of VARC will also establish their own basic physics research program sponsored by government grant, industry grants, or self-initiated. Other institutions requiring a facility with high-energy capability for basic research can cooperate with VARC. Programs for accelerator improvement and development may also be undertaken by VARC. The Langley Research Center will conduct the engineering applications, and basic research phases associated with the space environment. Other NASA Laboratories,

government agencies, and industry under NASA contract will operate through the Langley Research Center.

CONCLUDING REMARKS

An architect's rendering of the Space Radiation Effects Laboratory is shown in figure 34. This will be located in the city of Newport News, Virginia, within 15 miles of the Langley Research Center, and will lie in a site occupying approximately 100 acres. The principal intent of the Space Radiation Effects Laboratory is to provide a facility in which investigations simulating the space environment can be performed and the results used to increase the reliability and safety of spacecraft and space missions. As the project has now evolved, the Laboratory will serve a dual function. In one capacity, it will support an engineering program aimed at increasing the reliability and safety of spacecraft and missions. In the other, it will provide our universities and colleges with the instruments by which they can conduct basic research in high-energy physics as well as expanding their graduate program in this field of radiation. Thus, by providing a facility whereby both these endeavors can be conducted concurrently, two vital needs are simultaneously fulfilled.

REFERENCES

1. Foelsche, Trutz: Current Estimates of Radiation Doses in Space, NASA TN D-1267, 1962.

2. McDonald, F. B., ed., contributed by G. E. Fichtel, D. E. Guss, H. H. Malitson, K. G. McCracken, K. W. Ogilvie, and W. R. Weber: Solar Proton Manual. NASA TR R-169, 1963.

3. Jacobs, George J., ed. (With Appendix A by J. R. Winckler): Proceedings of Conference on Radiation Problems in Manned Space Flight. NASA TN D-588, 1960.

4. Hess, W. N.; and Nakada, Paul: Artificial Radiation Belt Discussed in Symposium at Goddard Space Center. Science, vol. 138, no. 3536, Oct.5, 1962, pp. 53-54.

5. Nakada, M. P.: Synchrotron Radiation Calculations for the Artificial Radiation Belt. Jour. Geophys. Res., vol. 68, no. 13, July 1, 1963. pp. 4079-4089.

6. Van Allen, J. A.; Frank, L. A.; and O'Brien, B. J.: Satellite Observations of the Artificial Radiation Belt of July 1962. Jour. Geophys. Res., vol. 68, no. 3, February 1, 1963, pp. 619-627.

7. O'Brien, B. J.; Van Allen, J. A.; Laughlin, C. D.; and Frank, L. A.; Absolute Electron Intensities in the Heart of the Earth's Outer Radiation Zone. Jour. Geophys. Res. (Letter to the Editor), vol. 67, no. 1, Jan. 1962, pp. 397-403.

8. Carter, R. E.; Reines, F.; Wagner, J. J.; and Wyman, M. E.: Free Antineutrino Absorption Cross Section. II. Expected Cross Section From Measurements of Fission Fragment Electron Spectrum. Phys. Rev., Vol. 113, no. 1, pp. 280-286, Jan. 1, 1959.

9. Foelsche, T.: Radiation Doses in Interplanetary Flight. Paper presented at Ninth Annual American Astronautical Society Meeting of the Interplanetary Missions Conference, Los Angeles, Calif., Jan. 15-17, 1963.

10. Wertheim, G. K.: Radiation Effects on Semiconductors. Proceedings of the Symposium on High Power Accelerator Applications, New York, N. Y., October 13, 1961.

11. Van Lint, V. A. J.; and Wikner, E. G.: Correlation of Radiation Types With Radiation Effects. IEEE Transactions on Nuclear Science, January 1963.

12. Sands, George D.: Effects of A Simulated Space Environment on Polymers. Virginia Academy of Science, Charlottesville, Va., May 6-9, 1964.

13. Haynes, Gilbert A.: High-Energy Radiation and Solar Cell Shields. Paper presented at Fourth Photovoltaic Specialist's Conference, Cleveland, Ohio, June 2-3, 1964.

14. Hedin, Bengt: Design of Cern Synchro-Cyclotron Magnet. CERN 55-3 European Organ. Nuclr. Res., Jan. 14, 1955

15. Geneer, W.; Schmitter, K. H.; Kortleven, S.; Bollee, B.; and Krienen, F.: The CERN 600 Mev Synchrocyclotron at Geneva. Phillips Tech. Rev., vol. 22, no. 5, Mar. 1961, pp. 141-180.

LOW ENERGY PROTONS	HIGH ENERGY PROTONS
120 KEV < E < 4.5 MEV	30 MEV < E < 700 MEV
FLUX ≈ 10^8 P/CM^2/SEC	FLUX ≈ 2-4×10^4 P/CM^2/SEC
	INTENSITY CAN VARY BY A FACTOR OF 2-3 WITH SOLAR ACTIVITY

SOLAR FLARES

LOW ENERGY	HIGH ENERGY
E < 40 MEV	E ⟶ 10 BEV
FLUX ≈ 10^5-10^6 P/CM^2/SEC	

LOW ENERGY ELECTRONS	HIGH ENERGY ELECTRONS
110 KEV < E < 1.6 MEV	1.6 MEV < E < 5 MEV
FLUX < 10^8e/CM^2/SEC	FLUX < 10^5e/CM^2/SEC
E > 10 KEV	E > 5 MEV
FLUX ≈ 10^9e/CM^2/SEC	FLUX < 10^3e/CM^2/SEC

FLUX CAN VARY BY A FACTOR OF 50-100 WITH SOLAR ACTIVITY

Table I. Summary of The Proton and Electron Spectra in Space

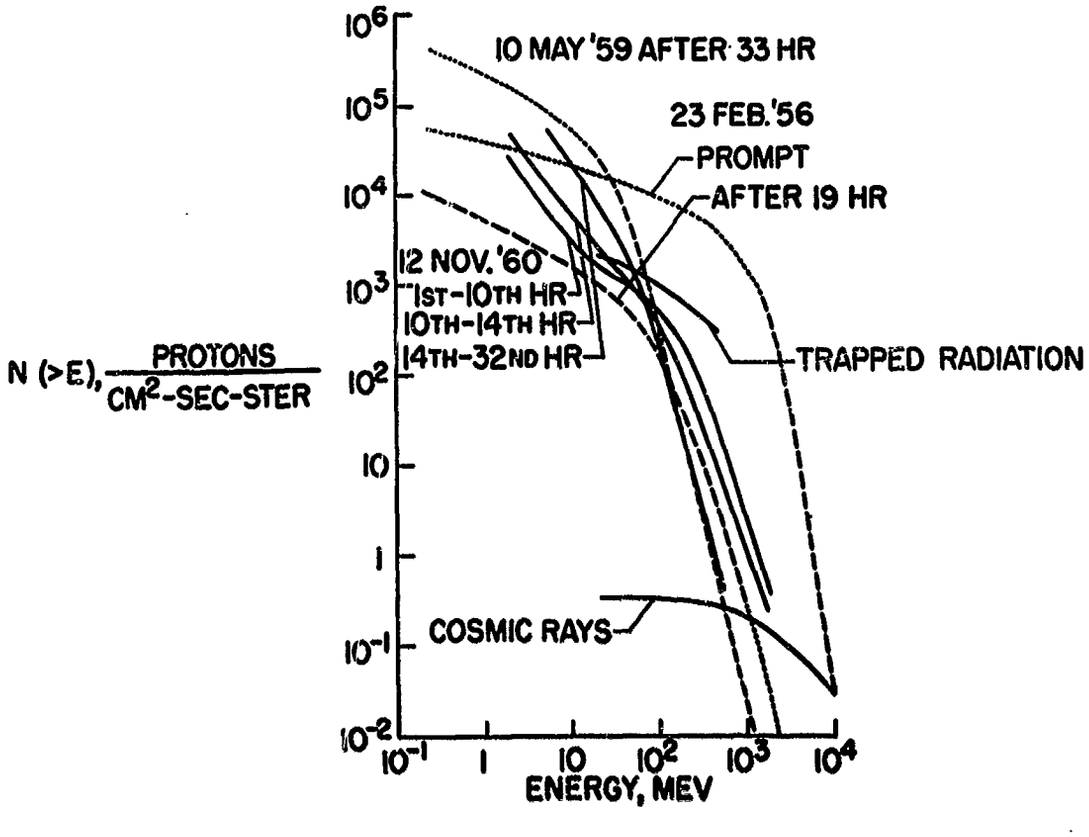

NASA

Figure 1.- The instantaneous integral energy spectra of cosmic rays, solar flare protons, and protons trapped in the earth's magnetosphere. Dotted curves indicate extrapolations of measured data (from ref. 1).

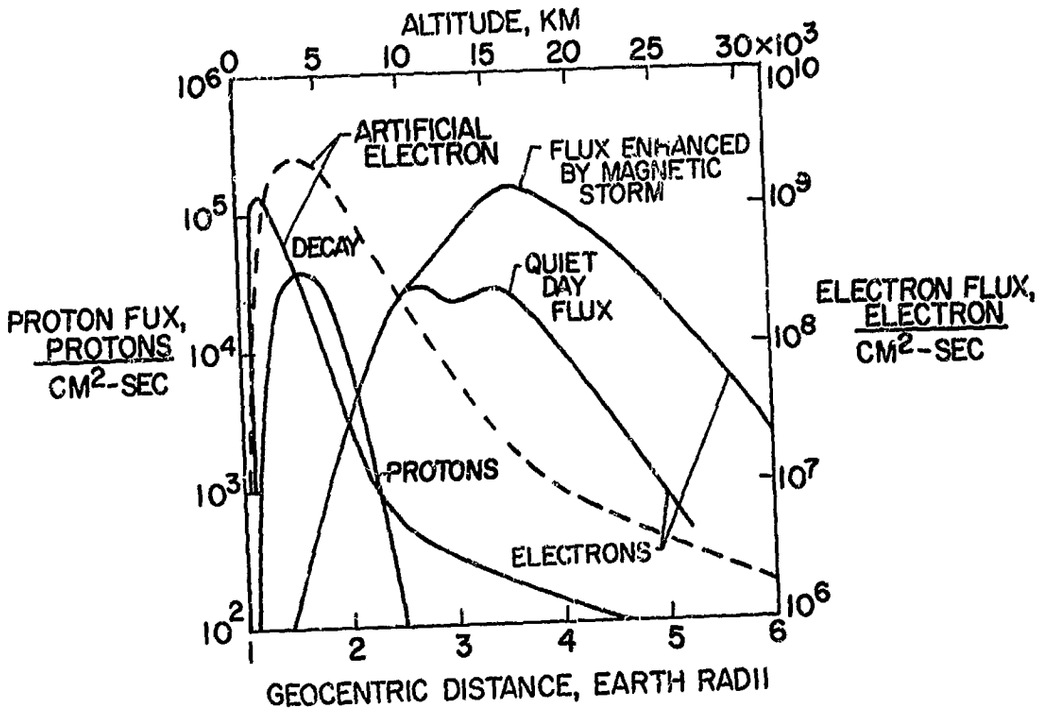

Figure 2. Manmade electron belt shown relative to the existing electron and proton distributions (from refs. 4, 5, 6, and 7). The approximate variation of flux with geocentric distance and altitude in the plane of the geomagnetic equator is depicted.

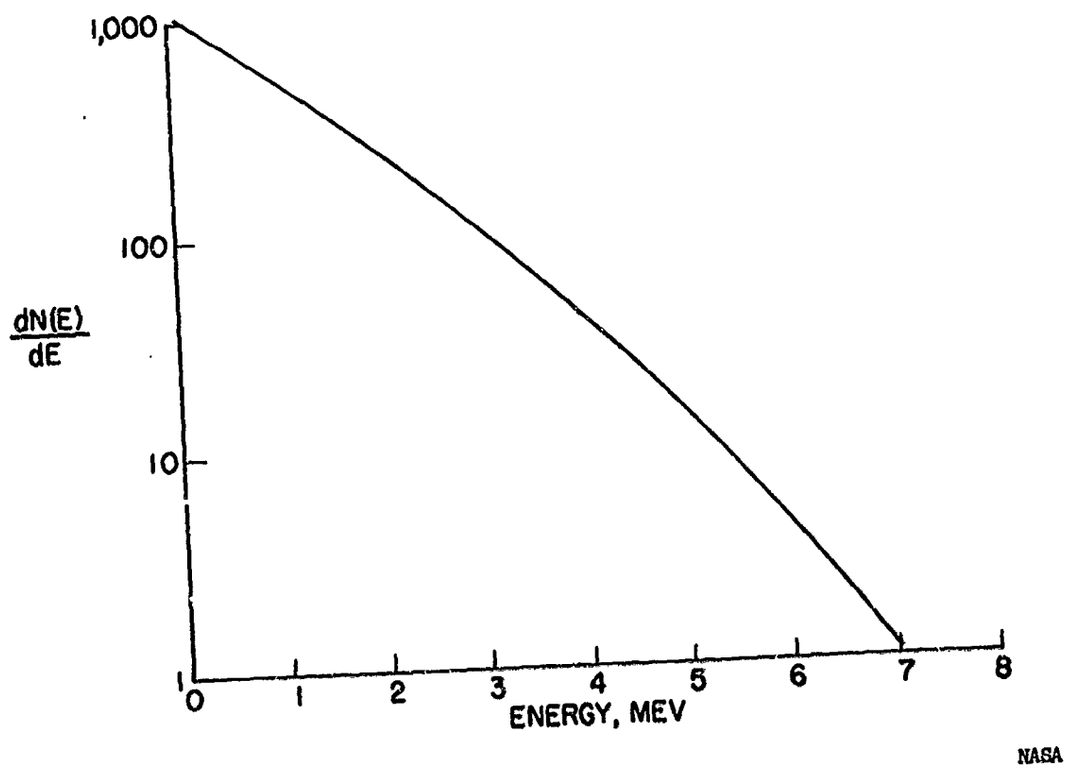

Figure 3.- Electron fission energy spectrum (from ref. 8).

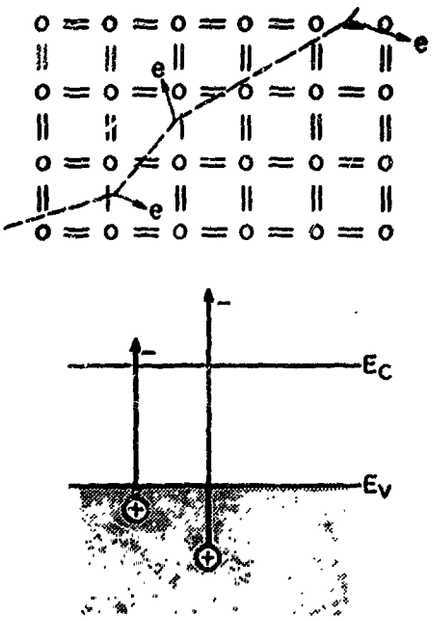

NASA

Figure 4.- Ionization of the valence electrons in a semiconductor.

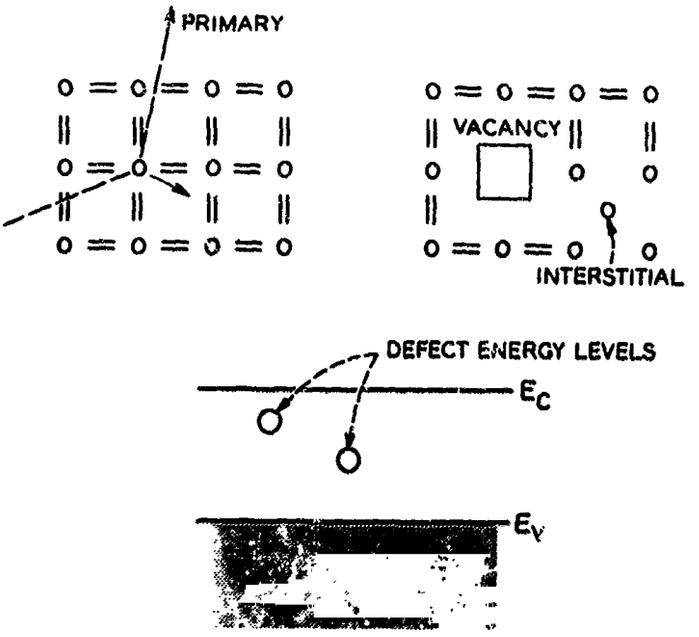

NASA

Figure 5.- Production of displacement-type defects by radiation.

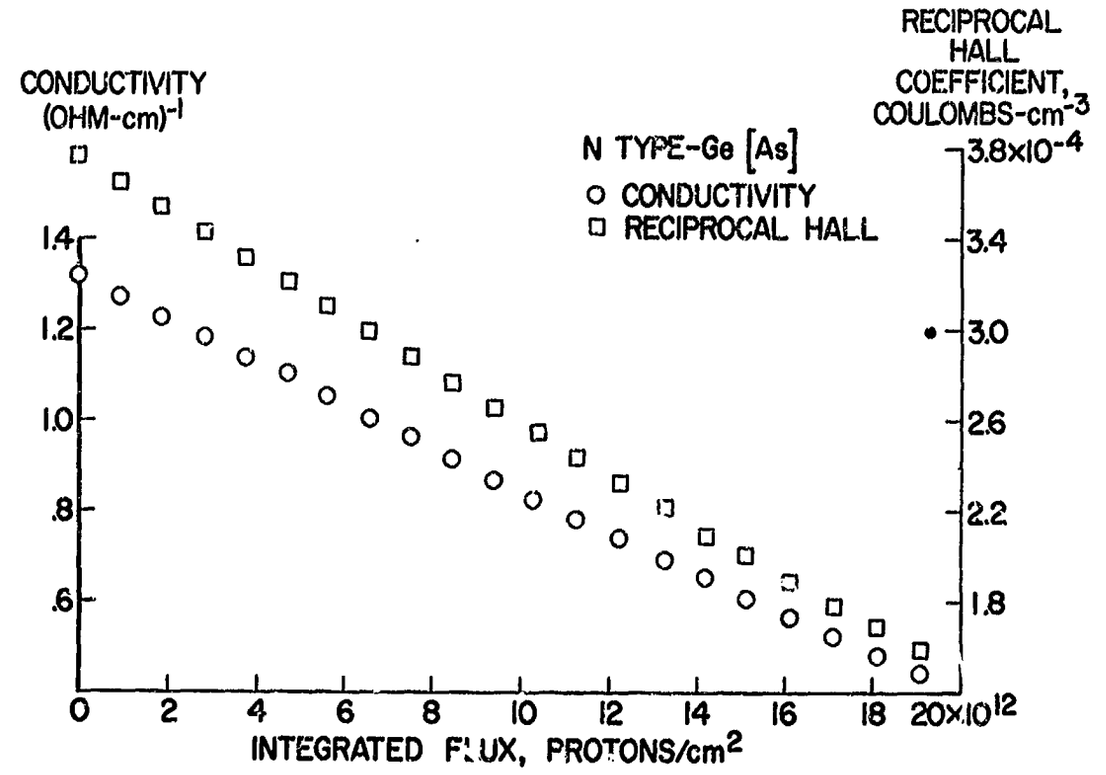

NASA

Figure 6.- Change in electrical properties of germanium due to 22 Mev proton irradiation.

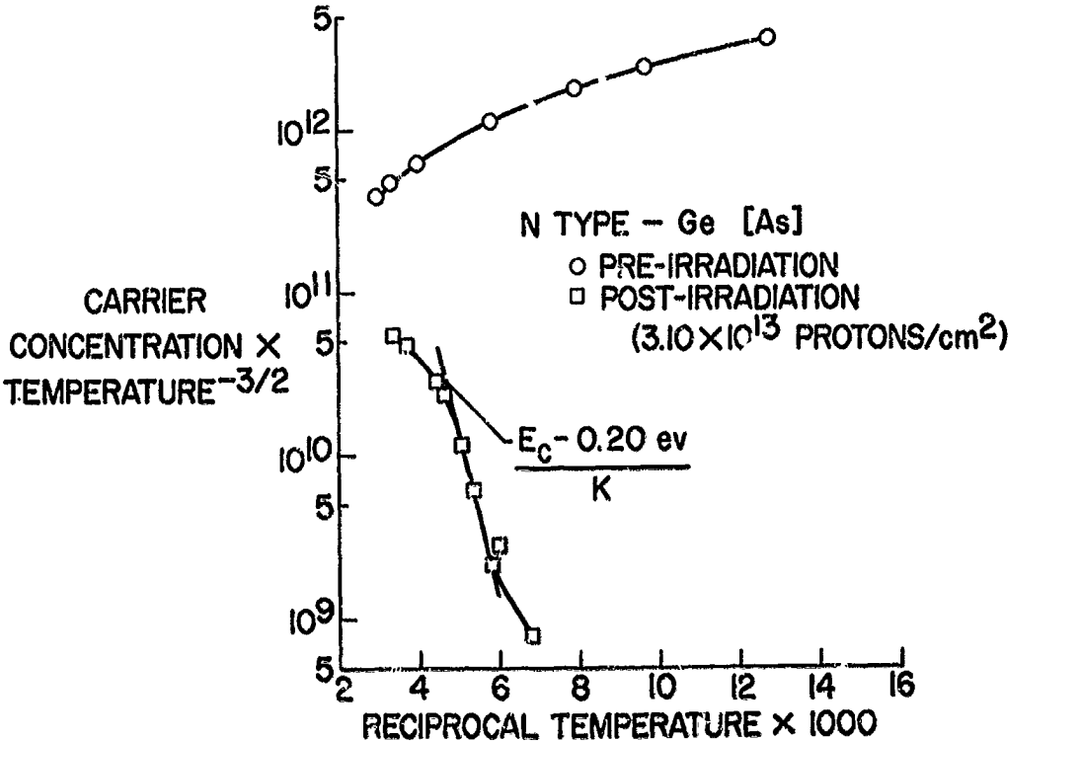

NASA

Figure 7.- Location of a defect energy level in irradiated germanium by means of temperature cycling.

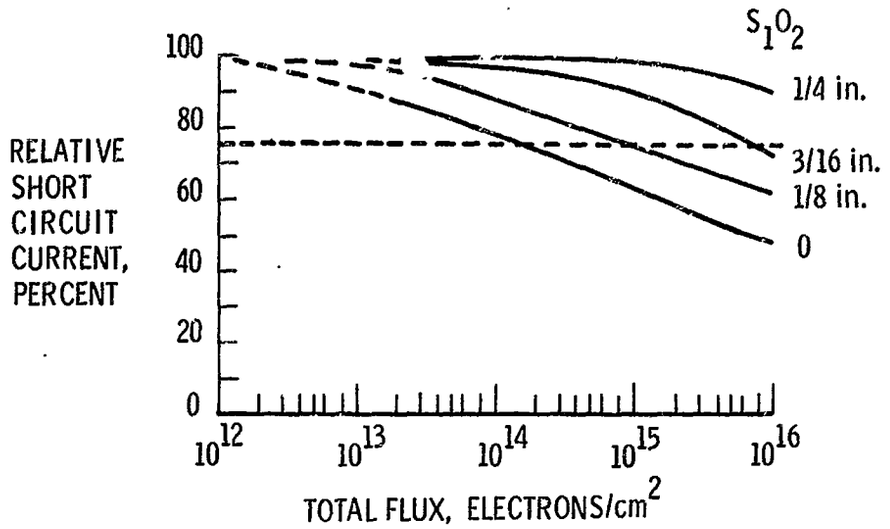

NASA

Figure 8.- Damage rates of N on P solar cells with and without shields due to 2.4 Mev electrons.

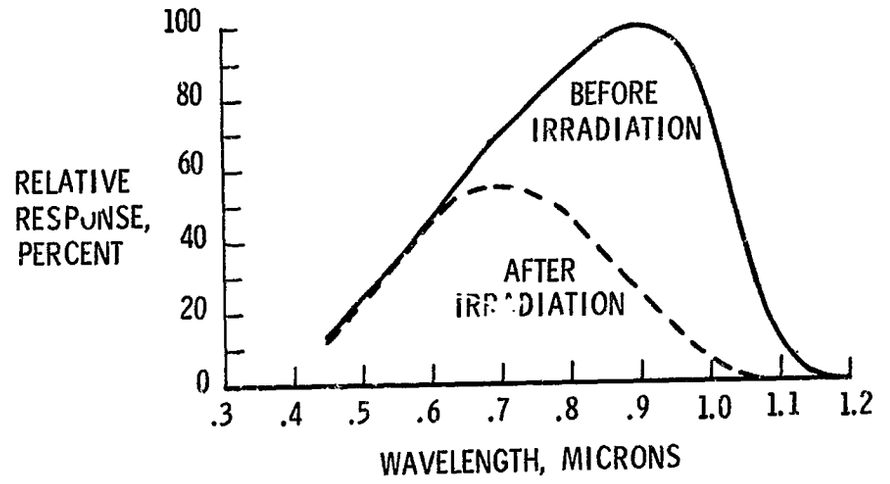

NASA

Figure 9.- Change in spectral response of a typical solar cell due to 22 Mev proton irradiation, total dose 7.2×10^{11} p/cm^2.

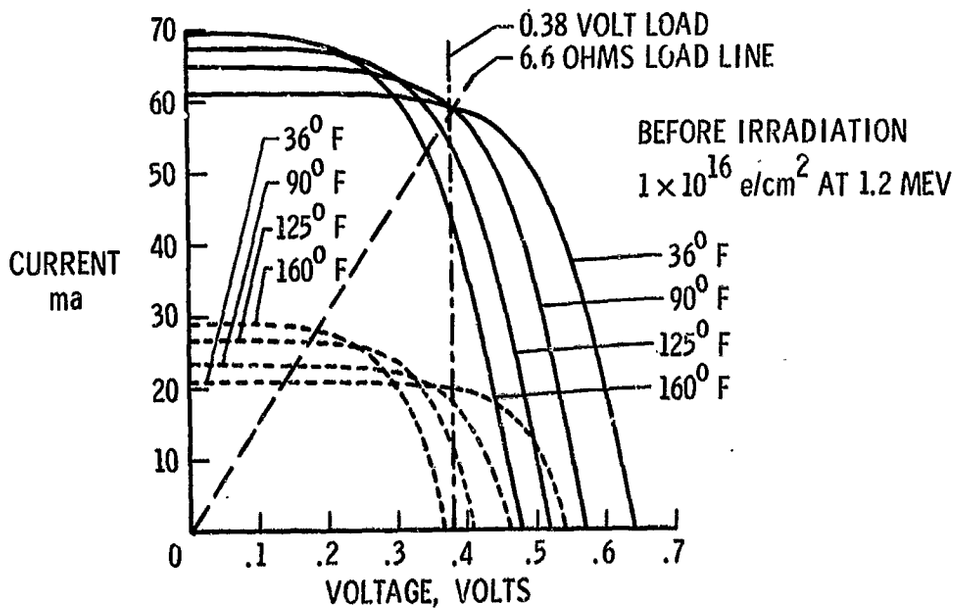

NASA

Figure 10.- Effect of electron irradiation on the load and temperature characteristics of N on P solar cell.

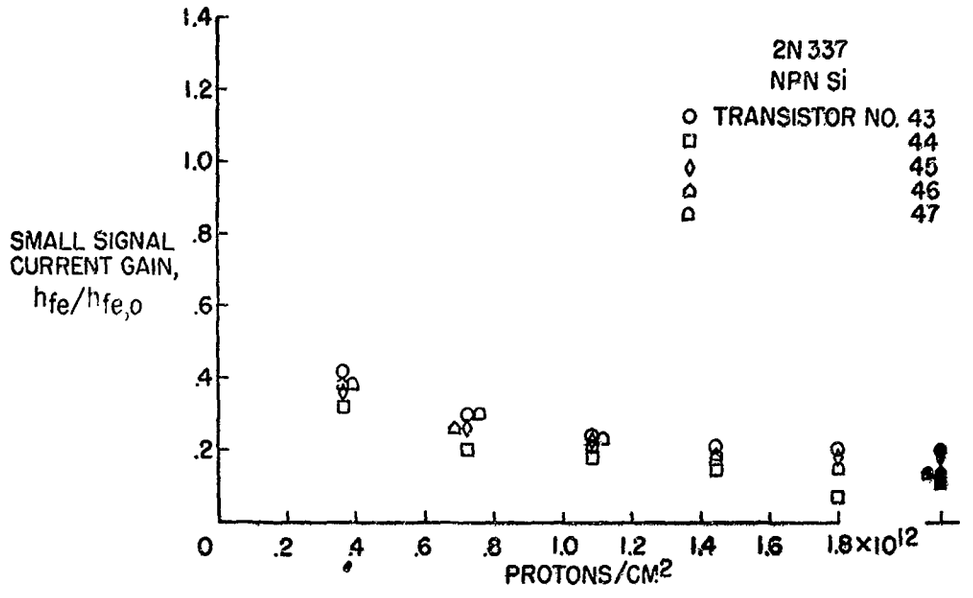

NASA

Figure 11.- Variation of small-signal current gain with integrated flux in a 40 Mev proton beam. Filled-in symbols are post check points.

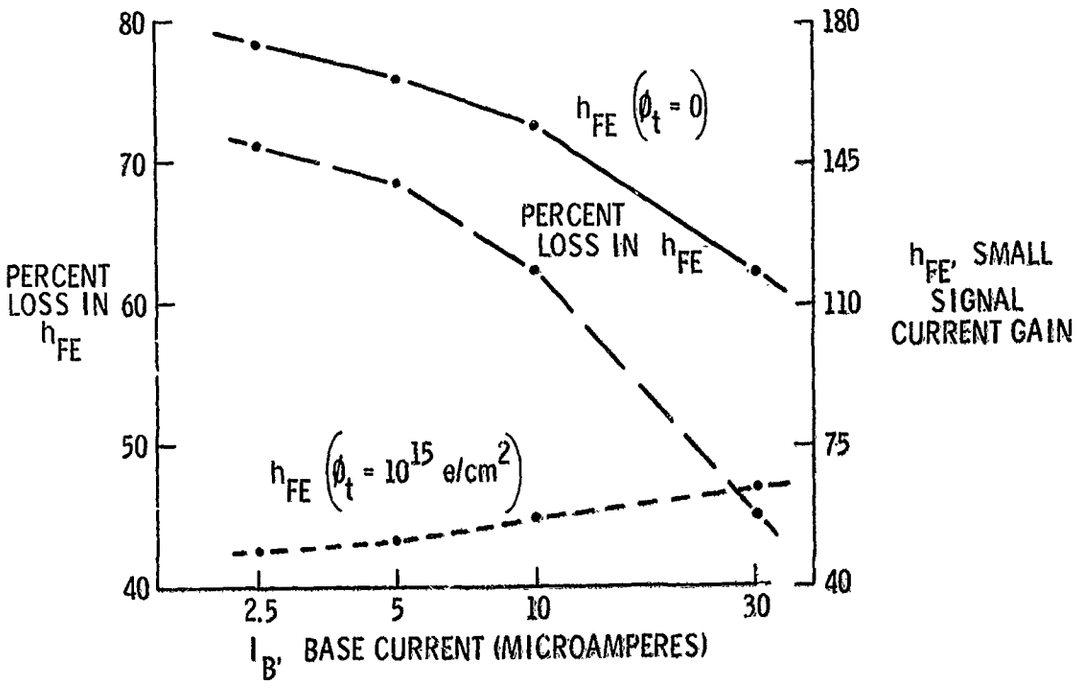

NASA

Figure 12.- Variation in gain of a 2N393, PNP-Ge transistor, as a function of base current, before and after irradiation with 3 Mev electrons.

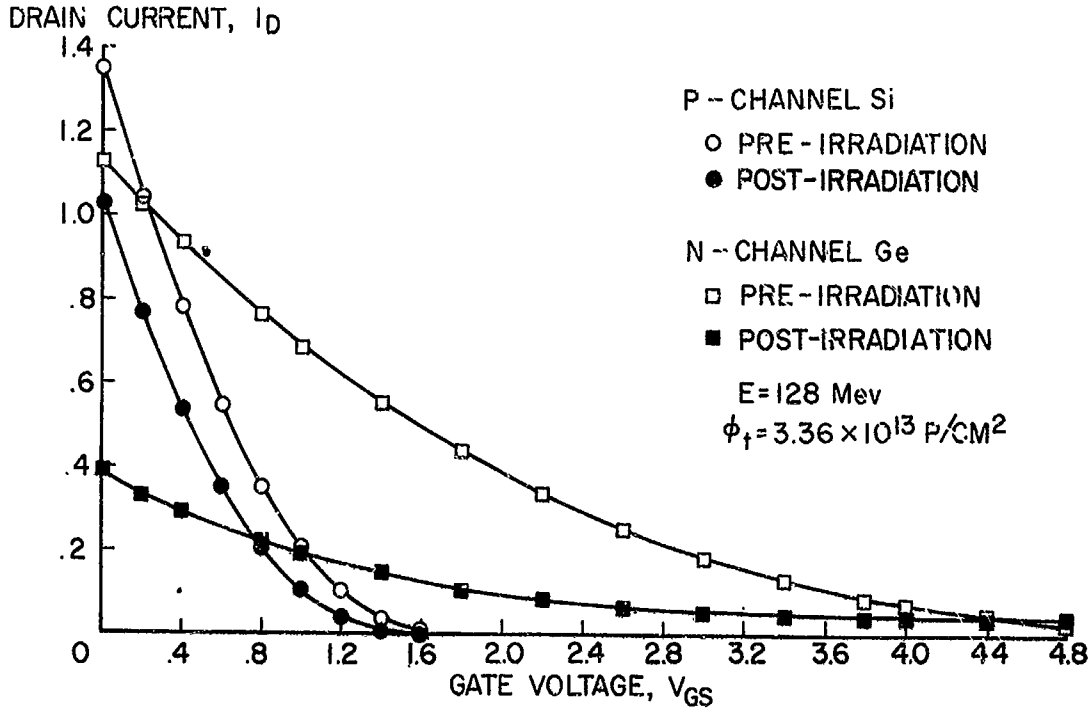

NASA

Figure 13.- Common-source transfer characteristics of field-effect transistors before and after irradiation with 128 Mev protons.

TRANSISTOR TYPE	ENERGY, Mev	MAX. TOLERANCE FLUX, PROTONS/CM^2	NOM. FREQ., mc	REMARKS
2N224 (PNP-Ge)	40	1.5×10^{11}	0.5	
2N169 (NPN-Ge)	40	7×10^{11}	9	
2N743 (NPN-Si)	40	1.8×10^{12}	400	
μET-1 (NPN-Si)	128	4.5×10^{12} ($h_{FE}/h_{FE,o} = 0.78$)	---	INTEGRATED-CIRCUIT TRANSISTOR
	22	4.1×10^{12}	---	
TMT-843 (NPN-Si)	128	1.4×10^{12} ($h_{FE}/h_{FE,o} = 0.81$)	20	MICROTRANSISTOR
MHM 1101 (NPN-Si)	128	5.6×10^{11} ($h_{FE}/h_{FE,o} = 0.27$)	60	DARLINGTON-CONNECTED
TIX-880	128	6.72×10^{12} ($A/A_o = 0.64$)	---	N-CHANNEL Ge FIELD-EFFECT TRANSISTOR
2N2497	128	3.36×10^{13} ($A/A_o = 0.87$)	---	P-CHANNEL SI FIELD-EFFECT TRANSISTOR
	22	5.34×10^{13} ($A/A_o = 0.64$)		

NASA

Figure 14.- Integrated proton flux for 30-percent loss in gain for different transistor types.

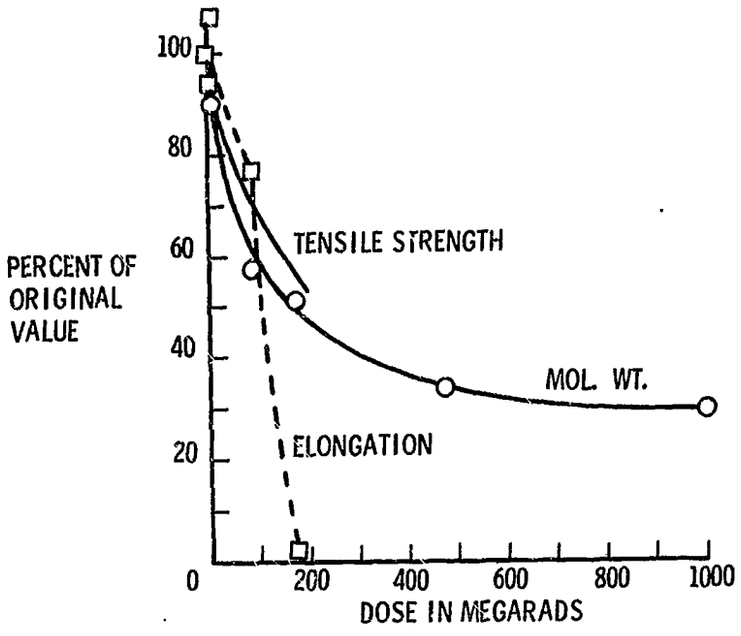

NASA

Figure 15.- Change of mechanical properties and molecular weight of mylar with gamma irradiation.

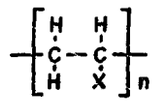

VINYL TYPE CROSS-LINK

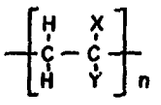

VINYLIDENE TYPE DEGRADE

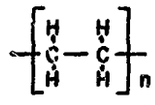

POLYETHYLENE

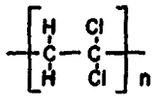

POLYVINYLIDENE CHLORIDE (SARAN)

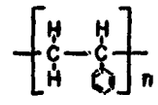

POLYSTYRENE

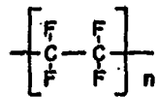

POLYTETRAFLUOROETHYLENE (TEFLON)

NASA

Figure 16.- Radiation effects on polymers.

H-FILM,

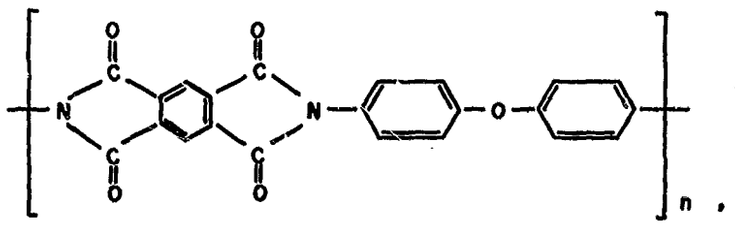

IS MUCH MORE RADIATION RESISTANT THAN TEFLON,

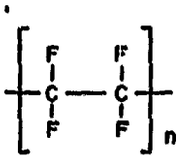

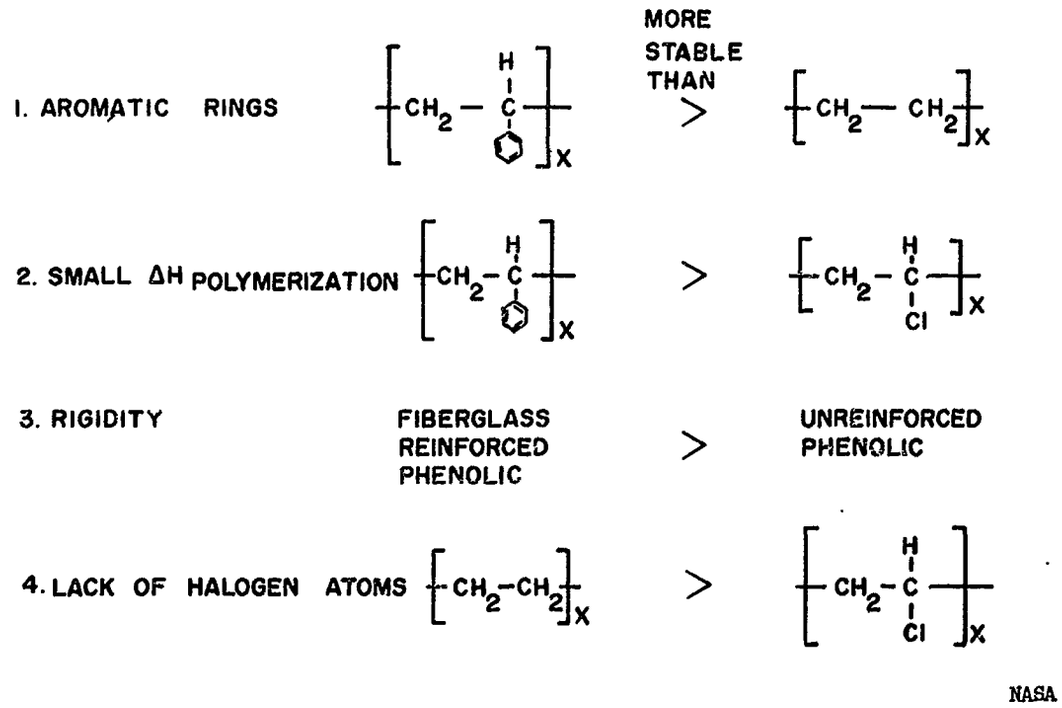

Figure 18.- Features imparting radiation stability of polymers.

SPECIALLY PREPARED FLAT CAPACITOR MOUNTED ON TEMPERATURE CONTROL BUCKET

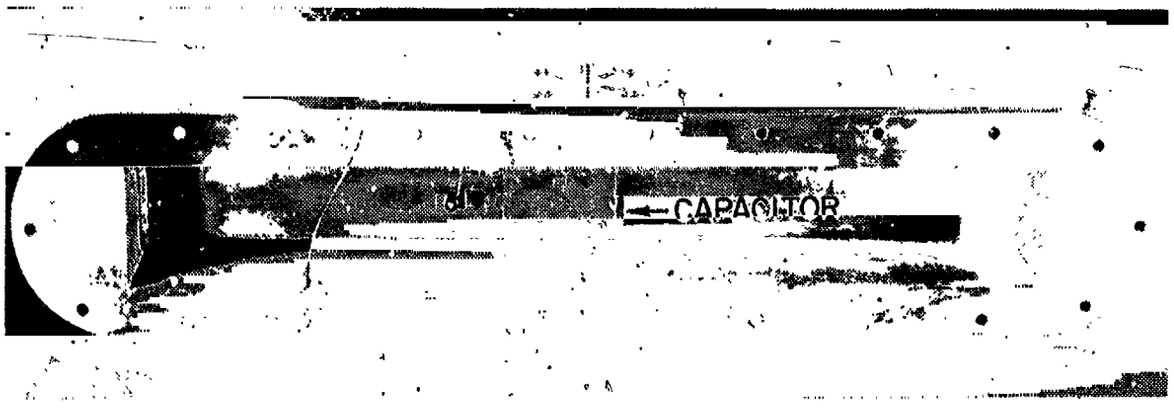

Figure 19.- Specially prepared flat capacitor mounted on temperature control bucket.

TYPICAL TRACE OF A TRANSIENT PULSE OBSERVED IN CAPACITORS UNDER ELECTRON IRRADIATION

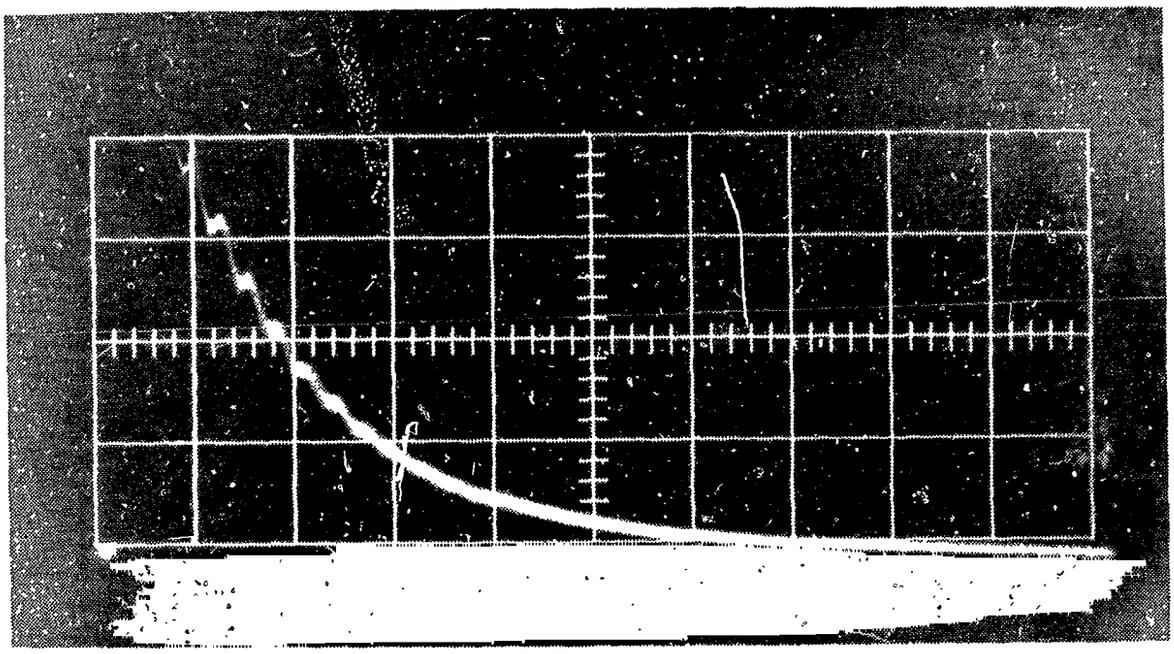

NASA

Figure 20.- Typical trace of a transient pulse observed in capacitors under electron irradiation. tion. Vertical scale is 20 volts per division, horizontal scale is 1-millisecond per division.

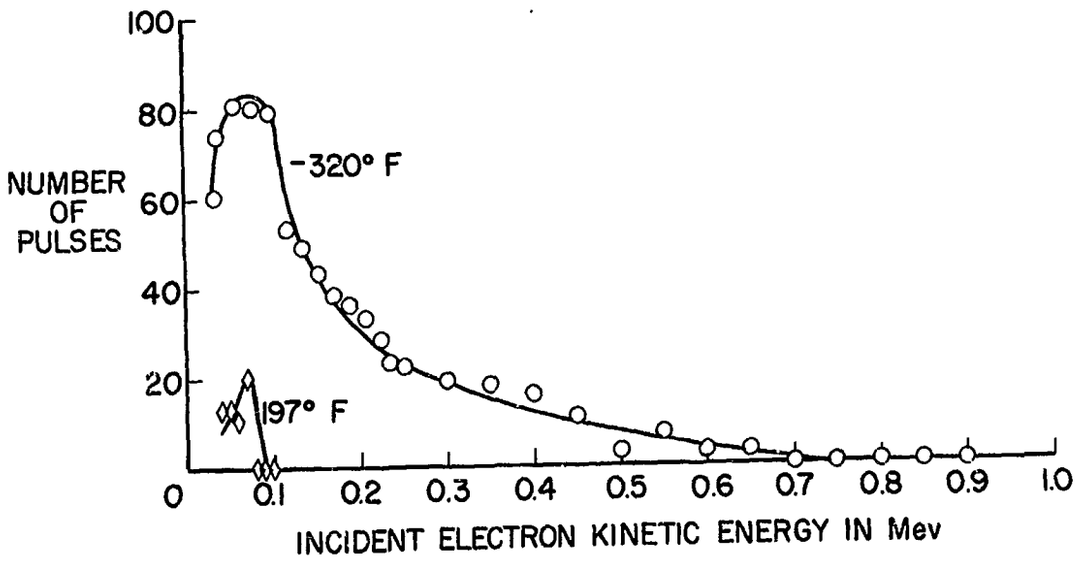

NASA

Figure 21.- Dependence of the number of pulses on incident electron kinetic energy at -320° F and 197° F in the polyethylene terephthalate commercial capacitor. Dose rate 3.2×10^{10} e/cm^2/sec.

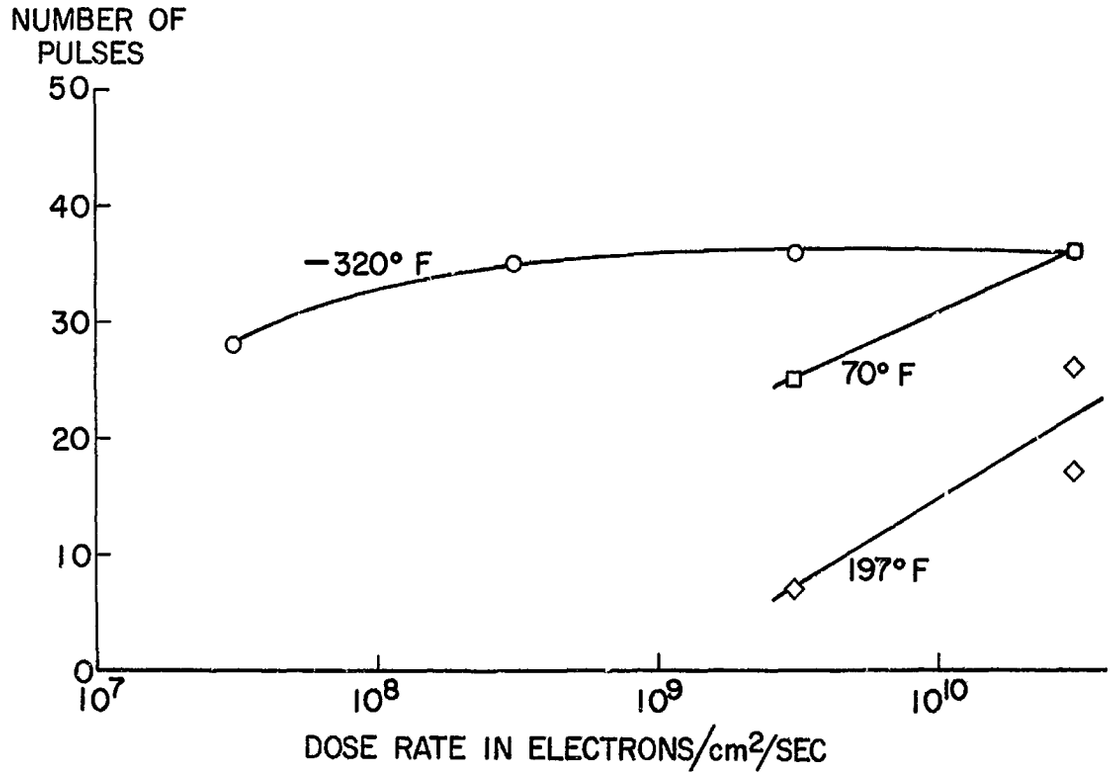

NASA

Figure 22.- Dependence of the number of pulses on electron dose rate at -320° F, 70° F, and 197° F for the specially prepared polyethylene terephthalate insulated capacitor. Total dose 3.25×10^{13} e/cm^2.

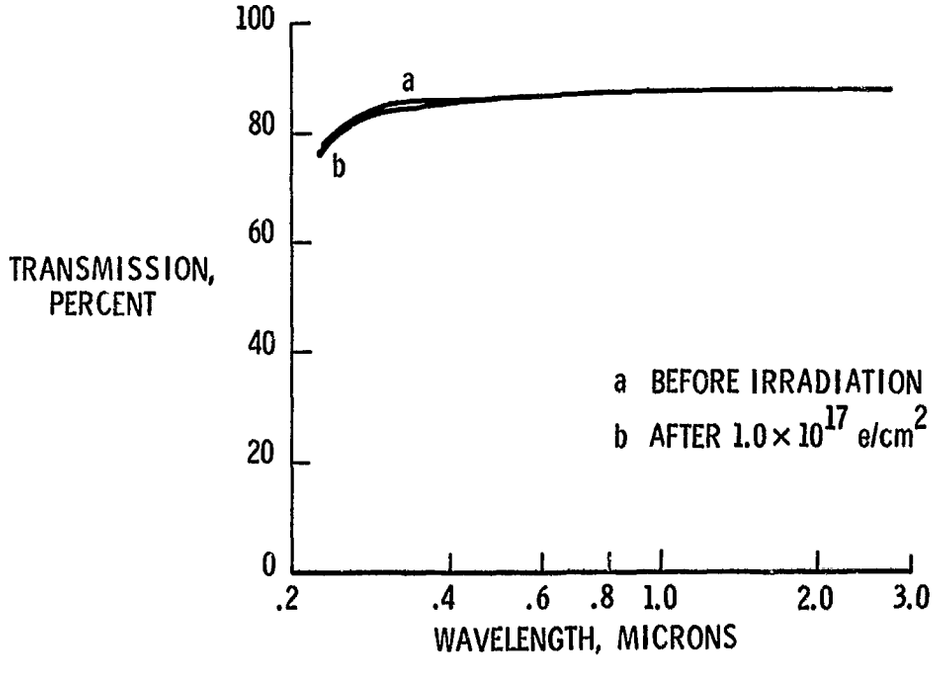

NASA

Figure 23.- Transmission of synthetic annealed sapphire before and after irradiation with 1.2 Mev electrons.

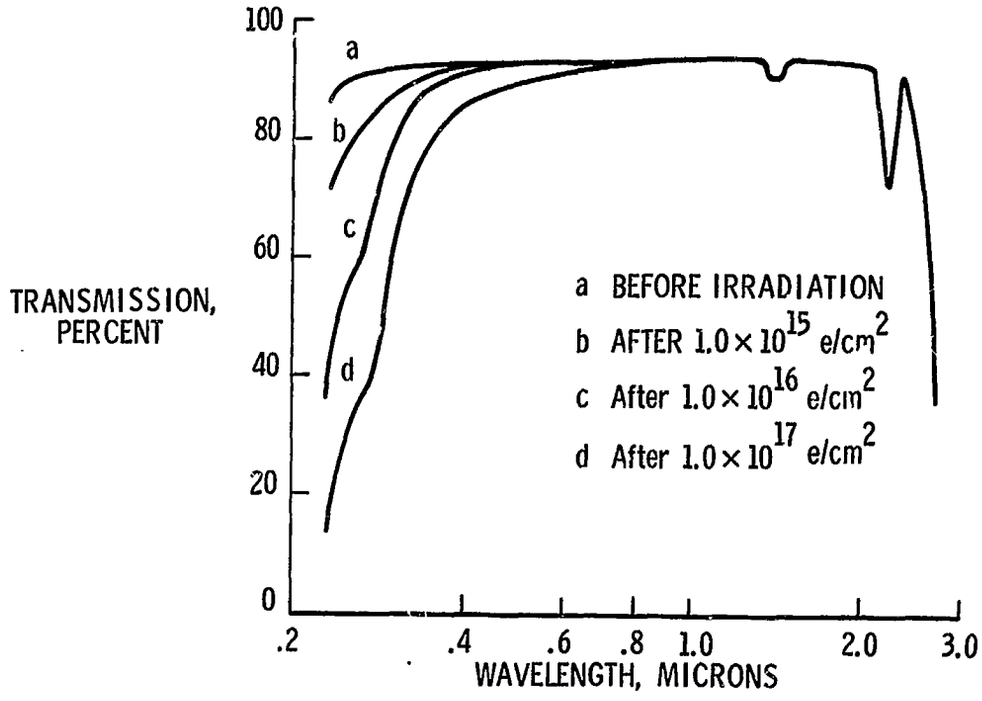

NASA

Figure 24.- Transmission of sythetic fused silica before and after irradiation with 1.2 Mev electrons.

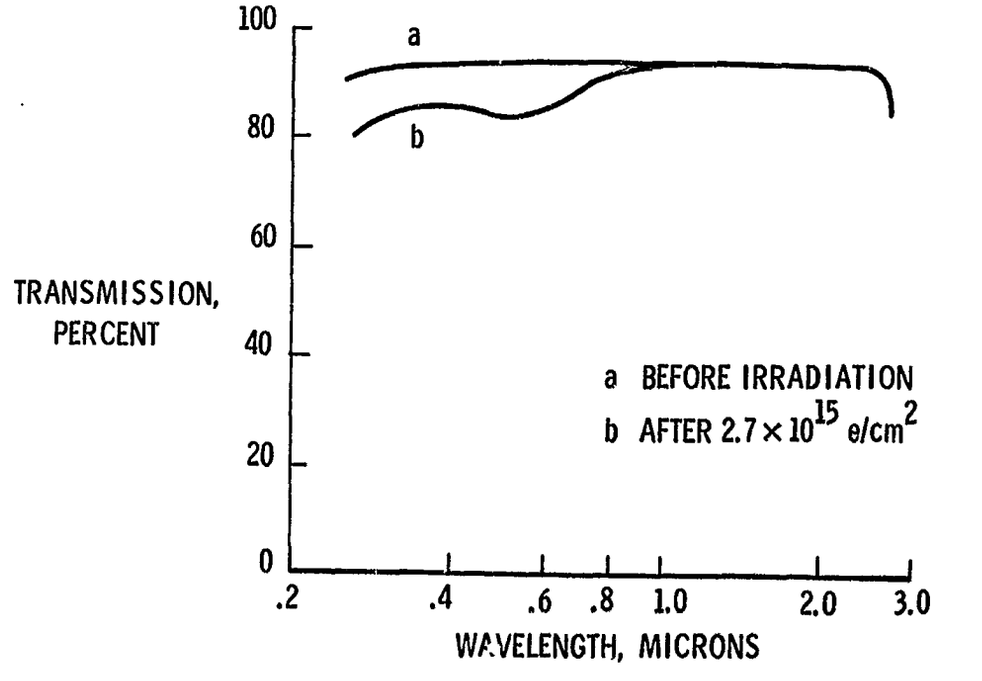

NASA

Figure 25.- Transmission of A-3 type fused quartz before and after irradiation with 1.2 Mev electrons.

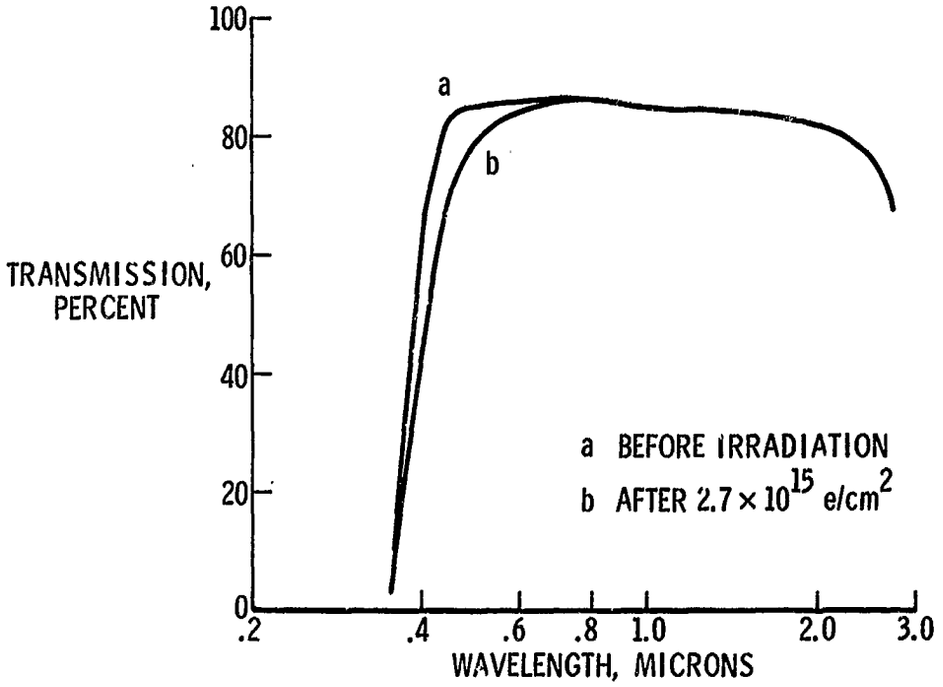

NASA

Figure 26.- Transmission of Corning #8363 before and after irradiation with 1.2 Mev electrons

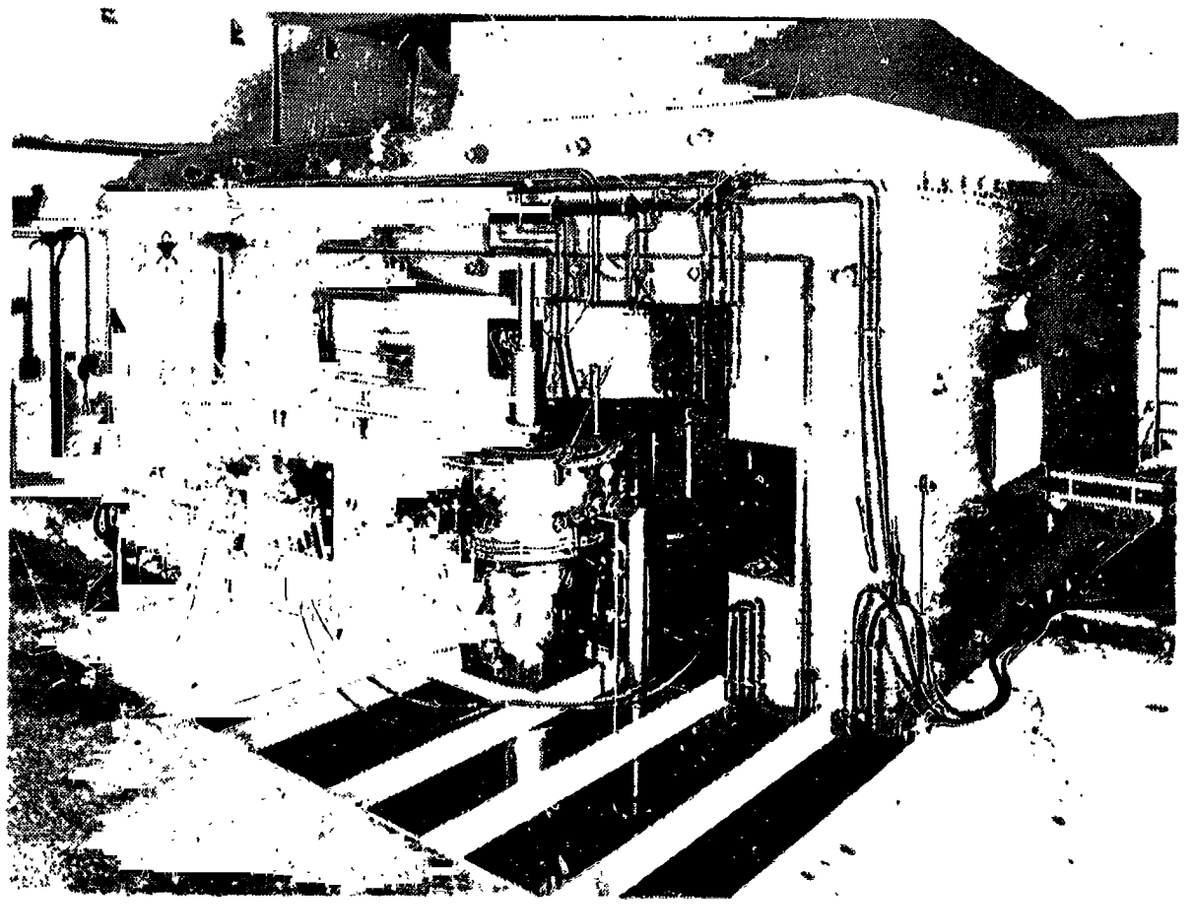

NASA

Figure 27.- CERN 600 Mev Synchrocyclotron.

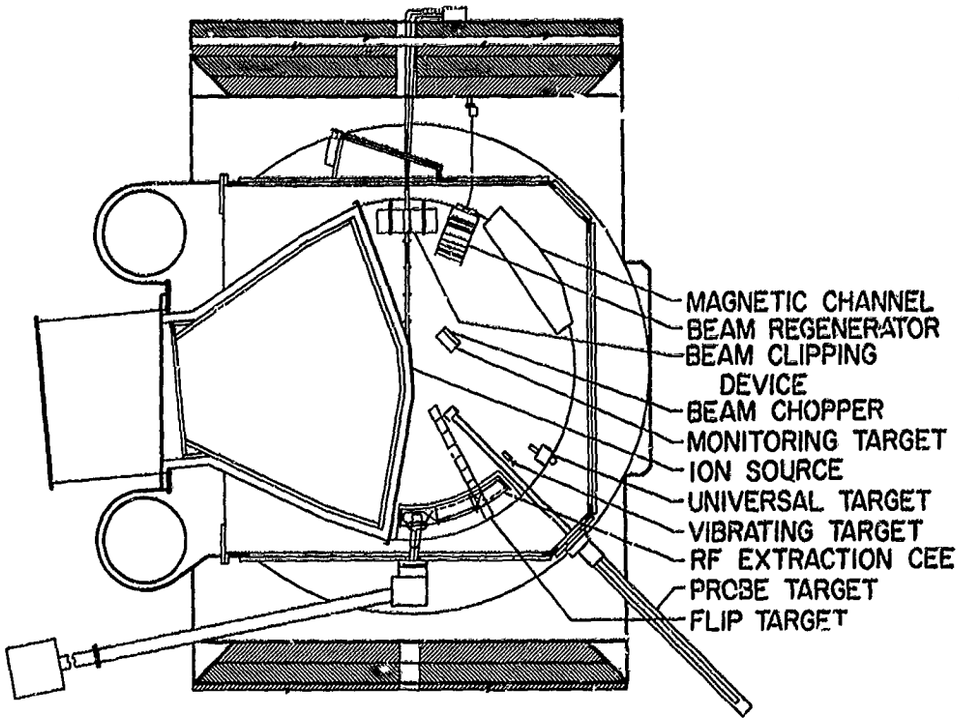

NASA

Figure 28.- Proton internal target system.

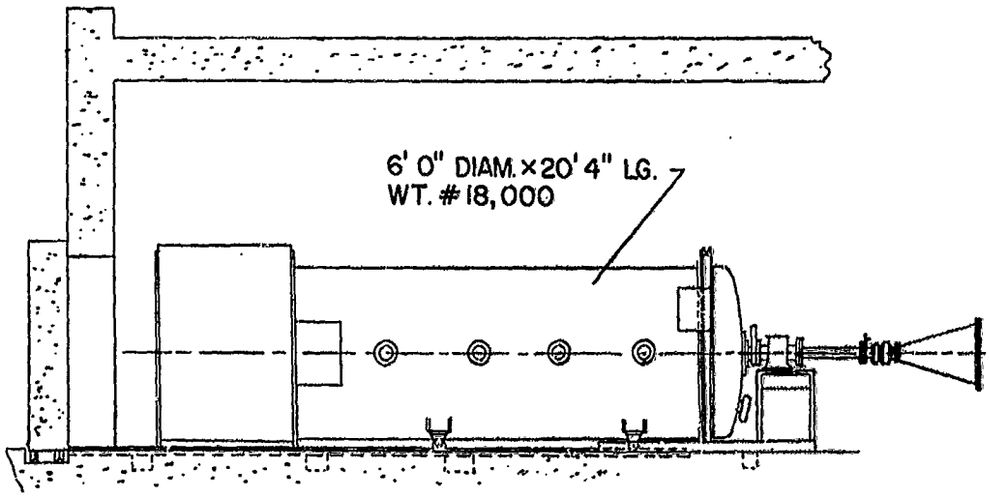

NASA

Figure 29.- Horizontal layout of the 3 Mev Dynamitron.

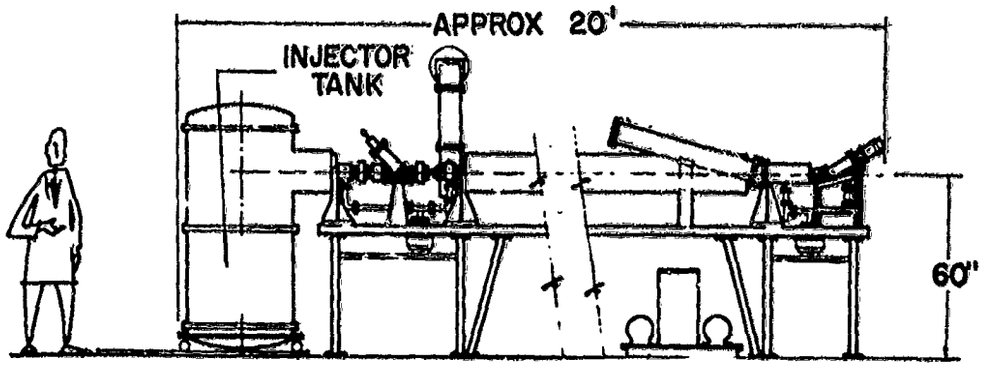

NASA

Figure 30.- Side view [illegible]

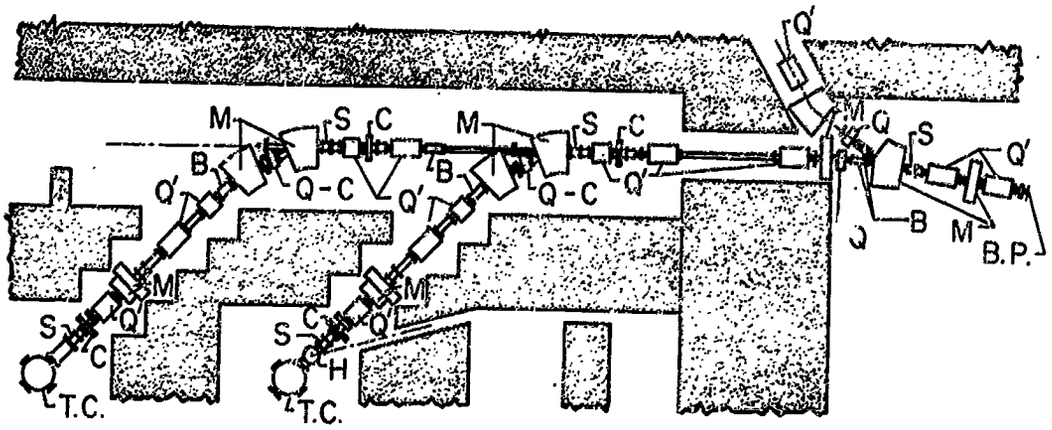

M - BENDING OR STEERING MAGNET
Q' - QUADRUPOLE MAGNET PAIR
Q - QUADRUPOLE MAGNETS
S - SCINTILLATION SCREEN
B - BEAM STOPPER
C - COLLIMATOR
H - HELMHOLTZ COIL
T.C. - TARGET CHAMBER
B.P. - BEAM PORT

NASA

Figure 31.- Schematic of proton beam transport system.

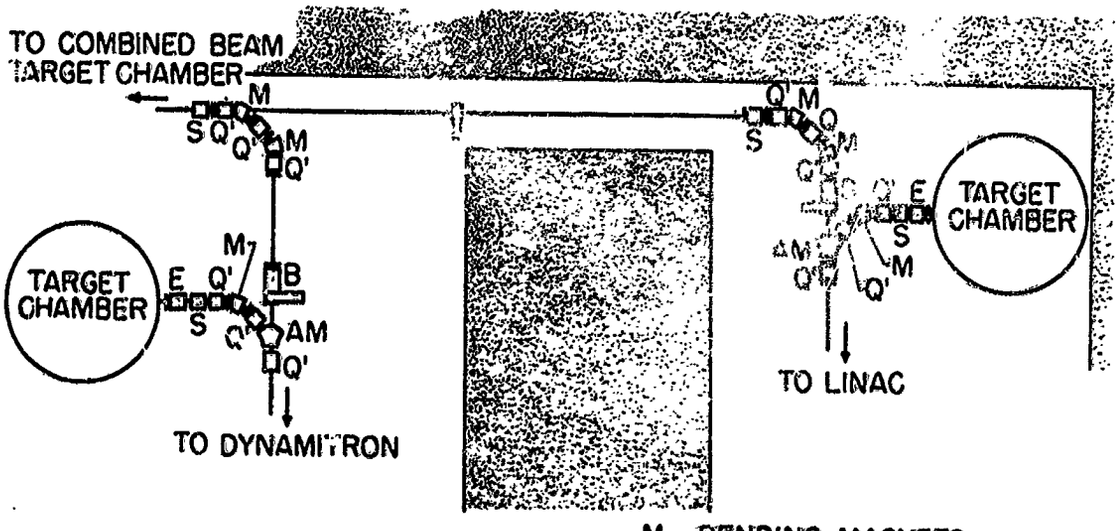

M BENDING MAGNETS
A SCATTERER
Q QUADRUPOLE MAGNET
Q' QUADRUPOLE MAGNET PAIR
S SCINTILLATION SCREEN
B BEAM STOPPER
E PROBE

NASA

Figure 32.- Schematic of the electron beam transport system.

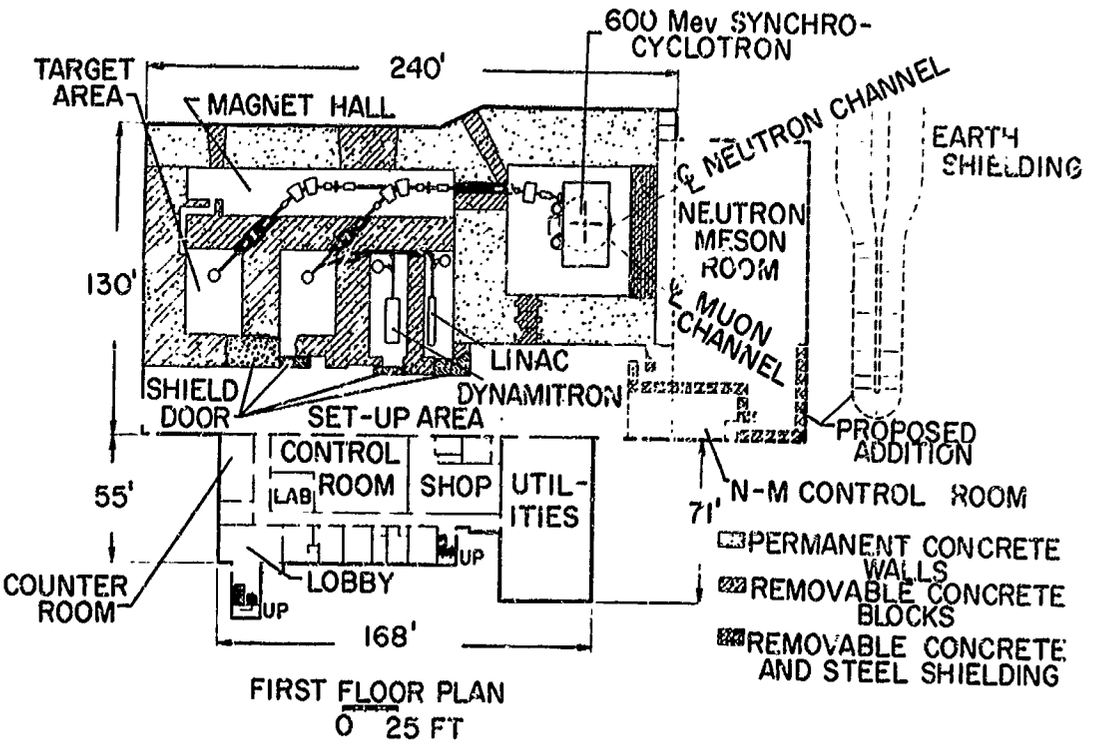

NASA

Figure 33.- Plan view of the Space Radiation Effects Laboratory.

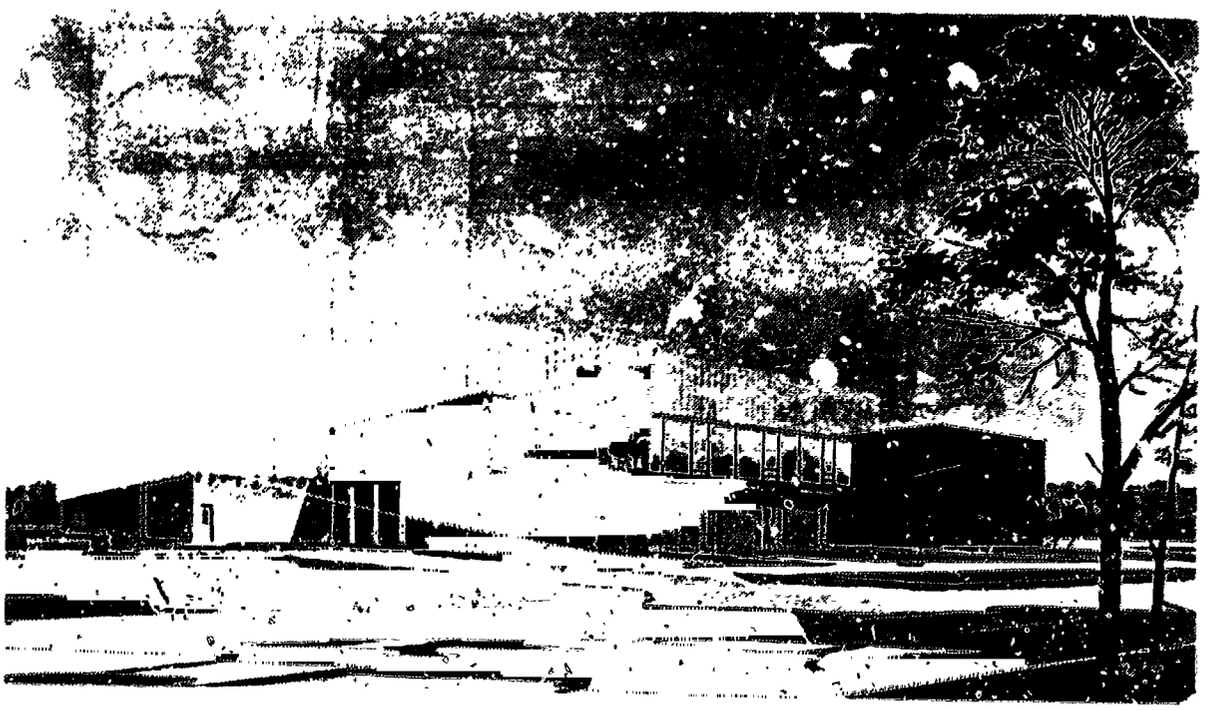

NASA

Figure 34.- Architect's perspective rendering of the Space Radiation Effects Laboratory.

N66 28903

METEOROIDS: NEEDS FOR PENETRATION SCALING LAWS AND THE POTENTIALS OF SIMULATION TECHNIQUES

by

E. T. Kruszewski

NASA - Langley Research Center

INTRODUCTION

Meteoroids are celestial bodies traveling at velocities ranging from 35,000 to 200,000 feet per second. They range in size from the smallest dust particle to large boulders. Fortunately, the larger the size the less frequent is its occurrence. The larger micrometeoroids because of their great speed could completely penetrate a space vehicle wall while the more numerous dust size particles could bombard and erode reflective surfaces, ports, lenses, and any other exposed apparatus that relies on its surface properties for proper operation.

Consequently there are two general areas that are of interest to the space technologist: Penetration by individual hypervelocity particles of the larger size that could penetrate walls of space vehicles and the erosion effects caused by the scrubbing action of the more numerous smaller particles.

LOW-VELOCITY IMPACTS

Empirical Scaling Laws

Even before space flight and its accompanying meteoroid problem there

was interest in penetration phenomena and high-velocity particle accelerators for the purpose of studying armor penetration. The bulk of these investigations, however, had to do with cratering phenomena below 15,000 feet per second and resulted in empirical formulas for penetration based on fit curves through experimental data. Some of the most widely used empirical formulas were based on correlation of experimental data with an empirical formula of the form

$$\frac{p}{l} = K\rho_p{}^m V^n \qquad (1)$$

where

p	penetration
l	some reference dimension of the projectile
ρ_p	density of the projectile
V	impact velocity
K	proportionality constant

Experiments were performed using various target and projectile materials, various shapes of projectiles, and covering different velocity ranges. Each experimentalist found the value of m and n that best fitted his experimental data usually disregarding the experimental data of others. Thus values of m from 1/3 to 1 and of n from 1/3 to 1.4 were recommended.

Other empirical relationships can be derived from the simple equation of motion shown in equation (2).

$$\frac{\pi}{6}\rho_p d^3 u \cdot du = -F dp \qquad (2)$$

where ρ_p is the density of the projectile; d, the diameter; v, the instaneous velocity; p, the penetration; and F, the resistive force. This expression equates the change in kinetic energy to the work done by the resistive force F on the projectile. Thus, the form of the penetration equation is automatically dictated by the assumption of a resistive force. Conversely, any assumed penetration formula implicitly implies a resisting force.

Shown in figure 1 are a few of the possible expressions for resistive force and the resulting penetration formula.

If the resistive force is assumed to be dependent only on the presented area of the projectile, that is, equal to some constant k, the penetration formula is of the form $\rho_p V^2$. If free surface effects are taken into account by assuming that the force is dependent on the depth of penetration (see eq. (2) of fig. 1), the penetration is of the form $\rho_p^{1/2} V$. Assuming a stronger dependence of the resistive force on the penetration (see eq. (3) of fig. 1), a formula with penetration proportional to $\rho_p^{1/3} V^{2/3}$ is obtained.

This and the next two formulas in figure 1 are of special interest as they are the most widely used and were originally obtained by relating the crater volume to either the kinetic energy or momentum of the particle.

The V to the 2/3 power penetration formula corresponds to the assumption that crater volume is proportional to kinetic energy of the projectile. The V to the 1/3 power formula corresponds to the assumption that crater volume is proportional to momentum of the projectile, while the V to the unit power states that crater volume is proportional to mementum per unit area of the projectile.

Notice from equations 4 and 5 of figure 1 that the mementum formula corresponds to a resistive force that increases with increasing impact velocity while the momentum per unit area formula results in a resistive force which decreases with increasing impact velocity.

If the resistive force is assumed proportional to the inertial forces created in the target ($\rho_t V^2$), that resultant penetration formula has a logarithmic dependence with respect to the velocity. (See eq. (6) of fig. 1.) If a term independent of velocity is added to allow for the effect of material properties such as strength, hardness, etc., the penetration formula is also of the logarithmic form.

All of these forms of the penetration equation, except the first and second, have been advocated by at least one of the numerous experimentalists in the hypervelocity penetration field.

Theoretical Scaling Laws

One of the earliest attempts to predict penetrations by a theoretical analysis occurred when E. M. Pugh and several other investigators (ref. 1) attempted to predict penetrations produced by a shaped-charge jet. The penetration model which was used is shown in figure 2.

The projectile was considered to be a jet of incompressible fluid of length l. The jet impinged on the target which was also considered to be an incompressible fluid. On the left side of the figure is shown the penetration process as viewed from the rest or laboratory frame of reference. V is the jet velocity; ρ_p and ρ_t, the jet and target densities; p, the penetration; and u is the velocity of the penetrating projectile material.

The penetration process as viewed from a moving reference frame originating at the bottom of the crater is shown on the right side of figure 2. The velocity of the material inside the jet is V-u, while the velocity of the target material is u.

In this reference frame the flow can be considered to be steady. The

stagnation pressure in both the target and projectile region can then be obtained by the Bernoulli's equation. As the stagnation pressure in both regions may be the same, a relationship between u and V can be derived and the resulting penetration at $u = 0$ can be written as

$$\frac{p}{l} = \sqrt{\frac{\rho_p}{\rho_t}} \left[\frac{1 - \sqrt{\frac{\rho_t}{\rho_p}\left[1 - \left(\frac{V_o}{V}\right)^2 \left(1 - \frac{\rho_p}{\rho_t}\right)\right]}}{\sqrt{1 - \left(\frac{V_o}{V}\right)^2 \left(1 - \frac{\rho_p}{\rho_t}\right)} - \sqrt{\frac{\rho_t}{\rho_p}}} \right] \tag{3}$$

where l is the length of the projectile and V_o is the minimum velocity that will first cause a crater. This parameter was empirically introduced into the Bernoulli's equation of target material in an attempt to introduce the effects of strength of the target material.

When the target and projectile materials are the same, the equation simplifies to the simple expression

$$\frac{p}{l} = \frac{1 - \left(\frac{V_o}{V}\right)^2}{1 + \left(\frac{V_o}{V}\right)^2} \tag{4}$$

This equation was very successful in predicting the penetration of jets and of long narrow projectiles at relatively low velocities; for higher velocities, however, this equation gave rather questionable results and for velocities much greater than V_o the penetration formula becomes independent of

the impact velocity $\left(\frac{p}{l} = 1 \right)$.

In order to remedy this fault a more refined model shown in figure 3 was suggested by Öpik.

The projectile was taken to be a circular cylinder of radius r_o and length $2r_o$. An allowance for the yield strength of the target material was made through the use of a strength parameter k, which is defined as the minimum pressure at which a penetration can occur.

As in the preceding model, both the projectile and target are considered to be incompressible fluids. The flow pattern after impact is shown in the right. As the projectile strikes the target it is decelerated by the resistance of the target in the form of the pressure p. This resistance creates a velocity gradient in the projectile material and results in a radial displacement r and radial motion of the projectile material $\dot{r}$.

By the use of the conservation of mass of the projectile, Bernoulli's equations for both the projectile and target materials, and an equation of motion, the maximum displacement was found, in terms of a complicated integral, which was indeed a function of impact velocity. A comparison of the results of Öpik's model and the jet equation by Pugh will be shown a little later in the paper.

METEOROID VELOCITY IMPACTS

Empirical Formulas

When the need for information dealing with the interaction of meteoroids and materials first became apparent, the logical step for the spacecraft designer was to turn to armor penetration analysis for his formulas. The

danger of such a procedure can be seen from an examination of figure 4.

Plotted in this figure is the nondimensional penetration p/l as a function of velocity in thousands of feet per second for four of the best known empirical penetration formulas: the momentum per unit area formula, the kinetic energy formula, the formula based on momentum, and finally the logarithmic form of the penetration formula which was based on an inertia resistive force.

To restrict comparisons to the effects of impact velocity, the projectile and target material were taken to be the same. For the sake of comparison, the constant K for all formulas was chosen so that a penetration of 0.1 was obtained at a velocity of 15,000 feet per second.

The danger of using any of these formulas to predict penetrations of particles at a high meteoroid velocity, which is one order of magnitude greater than the maximum experimental velocity, is obvious from this figure. Differences in predicted penetration of one order of magnitude can be had, depending on the formula used. This uncertainty in penetration prediction can not be tolerated.

Even if the penetration relationship at the lower velocities was known, it still would be dangerous to extrapolate to higher velocities. This is due to the fact that the mechanism of penetration is so dependent on impact velocity. This dependence is demonstrated in figure 5.

Shown in this figure are the results of an experimental investigation in which steel and tungsten carbide particles were impacted into soft lead. (See ref. 2.) The results separate into three individual regions depending on the condition of the projectile after impact. In region I the projectile remains intact and the penetration increases with velocity to the 4/3 power. The crater shape is long and narrow with about the same cross section as the

projectile. As the velocity is increased the projectile starts to deform and the crater becomes wider. In region II the penetration actually decreases with velocity, while the crater tends to become spherical. In region III the projectile reaches the fluid state and the penetration increases as V to the 2/3 power.

Hypervelocity Penetration Mechanism

A qualitative description of what happens to a semi-infinite target when impacted at meteoroid velocities can be described with the aid of figure 6.

The top sketch of figure 6 shows the projectile just before impact. The particle is assumed to be traveling at speeds well above the speed of sound in the target material (for example, the speed of sound in steel is about 17,000 feet per second). The target is considered to be a semi-infinite body.

Immediately after impact there is an intense light flash. Shock waves are propagated into the target and into the projectile. If the velocity of impact is high enough, both shock waves travel into the target. Small fragmentary particles, some of which travel at about twice the speed of impact, are ejected from the target surface.

A short time later the shock waves have propagated into both the target and projectile. The pressures and temperatures across the shocks, which depend on the impact velocity, are so great that the target material can be considered a fluid with negligible load-carrying ability. The projectile material on the other side of the shock, of course, is not as yet aware of the impact and so continues to penetrate the target. This downward motion of the projectile imparts an outward motion of the fluid particles causing

the fluid material to erupt out of the target thus forming a crater and lip. Meanwhile an expansion wave, traveling at a velocity higher than the shock velocity, originates from the corner of the projectile and is propagated into the target material. This expansion wave relieves the highly compressed material within the shocked region.

Eventually the expansion catches up with the shock. Thus the shock is weakened to the point where the temperatures across the shock are below those necessary to melt the target material and the pressures approach their allowable dynamic stresses. At this time further penetration continues through the propagation of plastic and elastic stress waves resulting in a mechanical cratering process.

Thus the energy of a hypervelocity projectile is dissipated by a variety of mechanisms: A flash or explosion, melting and vaporization of both target and projectile material, resistance of the target as a fluid mass, and plastic and elastic deformation and snapback.

A feeling for the order of magnitude of the pressures, densities, and temperatures associated with such shock phenomena can be had by examining the one-dimensional case of impact shown in figure 7.

On the left side of this figure is shown a one-dimensional body traveling at a velocity V and density ρ_o just prior to impacting a stationary one-dimensional body. The density of the target material is the same as that of the projectile (i.e., ρ_o). The two bodies after impact are shown on the right side of figure 7.

The velocity of the interface between the particle and target is equal to one-half of the impact velocity. The velocity of the shock front into the target is, of course, always greater than this, as the density of the shocked material is always increased.

The motion of the rear shock can be in either direction depending on the density ratio. If the material between the shocks is compressed to more than twice its original density ($\rho_2/\rho_0 > 2$) the shock will travel into the target. If not, the shock will travel into the projectile. The value of this density ratio and the resulting pressures are shown in figure 8.

In this figure a plot of the density ratio ρ/ρ_0 and resulting pressure in the shocked region is shown as a function of the impact velocity in feet per second plotted on a log scale. The velocity in kilometers per second is shown on the bottom scale. These results are for iron impacting on iron and were obtained from some experimental work done at Los Alamos. (See ref. 3.) Note that for iron a density ratio of 2 occurs at an impact velocity of about 70,000 feet per second. Thus at this impact velocity the rear shock wave will remain stationary at the impact surface.

The pressures resulting from these density ratios are shown by the pressure curve. Note that the pressures are plotted in megabars, where 1 megabar is approximately equal to 14.7 million psi. Notice also that even for impact velocities below 20,000 feet per second pressures in the range of 20 to 30 million psi will be generated. At 200,000 feet per second, the maximum estimated meteoroid velocity, the pressures reach over 30 megabars (450 million psi). The temperatures at these high pressures are in the thousands of degrees, which are well above the melting and even the vaporization temperature of the material.

Although the one-dimensional solution permits us to evaluate the pressures and density change across the shock, it does not contain a mechanism for dissipation of the shock nor crater production. Consequently, no estimate of penetration can be obtained through its use.

Early Theoretical Approaches

Many theoretical approaches for the prediction of high-velocity cratering phenomena have been used. The results of three of the earliest attempts to predict penetration are shown in figure 9. Each of these theoretical approaches assumes that the crater is formed by a different cratering mechanisms.

The thermal penetration theory (first suggested by Whipple) assumes that the craters are formed by removal of the target material by melting or vaporization. Consequently, the crater volume is obtained by dividing the energy of the projectile by the energy necessary to melt a unit volume of target material. The penetration equation is of the form shown at the top of figure 9 where ζ is a constant depending on the shape of the projectile and crater and Q is the energy necessary to melt a unit mass of target material. The explosive penetration theory (see ref. 4) assumes that the crater is identical to that formed by an amount of explosive whose energy is equivalent to the kinetic energy of the projectile. The explosive is assumed to generate a powerful shock wave that converts all of the target material to a strongly compressed polytropic gas. The cratering process is assumed to continue until the energy on the shock front is less than the internal energy required to disintegrate the target material. The penetration equation for this case is identical in form to the thermal penetration analogy. In this equation (see fig. 9) R represents the energy required to disintegrate the target material and K depends on the material properties of the target.

Grimminger (ref. 5) presented the first theory based on the hydrodynamic analogy which assumes that the target is a compressible fluid. This assumption

is suggested by the extremely large pressures generated in high-velocity impact. As the material strength is small in comparison to these pressures, it can be neglected. Grimminger's analyses assumed that the projectile was a rigid sphere and that the penetration occurred in two phases. In the first phase the projectile was decelerated by the drag force exerted by the compressible fluid on the projectile. This deceleration continued until the projectile reached a speed of Mach 5. The final penetration was assumed to be given by an empirical penetration formula derived from armor penetration at low velocities. The resulting penetration formula is shown at the bottom of figure 9. The first term of this formula is that due to the drag force while the second is the empirical armor penetration equation.

Hydrodynamic Approach

One of the most complete and detailed solutions of hypervelocity penetration was based on the hydrodynamic analogy. The problem solved was that of a cylindrical projectile of length equal to its diameter and made of the same material as the target. Both the target and projectile are considered to be compressible inviscid fluids. The analysis is based on a solution of the nonlinear compressible fluid equations shown below.

$$\left.\begin{aligned} &\rho \frac{\partial \vec{u}}{\partial t} + (\rho \vec{u} \cdot \nabla)\, \vec{u} + \nabla p = 0 \\ &\frac{\partial \rho}{\partial t} + \vec{u} \cdot \nabla \rho + \rho \nabla \cdot \vec{u} = 0 \\ &\rho \frac{\partial e}{\partial t} + \rho \vec{u} \cdot \nabla e + p \nabla \cdot \vec{u} = 0 \\ &P = f(\rho, e) \end{aligned}\right\} \qquad (5)$$

where u is the fluid particle velocity; p, the pressure; e, the specific internal energy; and ρ the density.

These equations represent the conservation of momentum, conservation of mass, the energy equation, and the equation of state. Note that viscosity and heat-conduction terms are neglected. The equation of state used was the so-called Los Alamos equation of state for metals. This equation was obtained by means of interpolating between results of an experimental Hugoniot in the low megabar pressure range and an analytical equation of state using the Fermi-Thomas-Dirac theory for material in the higher pressure range.

These fluid equations had to be solved numerically. The numerical method used was the one referred to as the "Particle in Cell" or PIC method and is discussed in reference 6.

In this method the region of interest is divided into a finite number of computational cells which are fixed relative to the observer. Each cell has a velocity, internal energy, and total mass associated with itself. The fluid is represented by individual particles or mass points which move through this Eulerian mesh in Lagrangian fashion. In the solution, these equations are written in finite difference form and then solved explicity.

The results of such an analysis are shown in figures 10 through 12.

In figure 10 are shown the pressure contours and velocities at 3 1/2 seconds after the impact of an iron projectile on an iron target. The projectile was assumed to have been traveling at 18,000 feet per second.

The vectors indicate the direction and magnitude of the velocity at each mesh point located at the tail of the vector. The contour lines are isobars representing equal pressures of 2. 1, and 0.2 megabars. The cylindrical projectile had a 10-centimeter diameter and a 10-centimeter height.

Note that there are two pressure pulses of more than 2 megabars and that

the pressures throughout the affected region are in the megabar range. One pulse is traveling into the target and the other into the projectile. Notice also that the numerical method used does not retain the discontinuity of the shock. Instead the shocks are smeared over a wide area.

The velocities of all target points beyond 0.2-megabar contour are zero thereby indicating that the points have not, as yet, felt the impact. Similarly the velocity of the projectile points above the 0.2-megabar contour are equal to the initial velocity and thus are not aware that the front of the projectile is being stopped. Note that the velocity vectors near the axis of symmetry are parallel to the initial projectile velocity. This is an indication that these points are still not aware that the projectile is finite. The finiteness of the projectile is indicated by the generation of an expansion wave from its outer circumferential points. Consequently, all of these points act as in the one-dimensional case.

The pressures and velocities at 8.7μ sec after impact are shown in figure 11. From this figure it can be seen that the rarefraction wave has now reached the line of symmetry and has also caught up with the shock wave. All pressures are still relatively high. The pressure at the shock, which has been weakened by the expansion wave and by the fact that it is encompassing more volume, is now only 1.0 megabar at its maximum.

In figure 12 the pressures and velocities at 81.7μ sec are shown. At this point the shock is spherical and has just about dissipated itself. Now all the pressures are relatively low. The maximum pressures are only 0.1 megabar.

Two investigators have used this method of analyses to determine dependence of penetration on velocity (R. J. Bjork ref. 3 and J. W. Walsh ref. 7). Bjork's investigation, from which the data for the preceding figures were

taken, was published in 1959 while Walsh's investigation was reported in 1963.

Both have claimed to use identical methods for calculating the pressure, velocity, and density distributions and the same equation of state. They have, however, come up with entirely different conclusions.

Bjork continued his analysis until the shock wave was dissipated, such as is shown in figure 12. He then defined his penetration by using the points of zero pressure to define the crater boundary. Using this crater criterion he made calculations for impacts with both aluminum and iron at three different velocities. The results of these calculations are shown in figure 13.

Plotted in this figure is the nondimensional penetration p/d as a function of velocity on a log-log scale. The triangles represent the results for aluminum while the circles are for iron.

The straight line drawn through these points has a slope of $V^{1/3}$. Thus Bjork concluded that the crater volume is dependent on the momentum of the particle (at least for the hypervelocity impact region).

Walsh's arguments (ref. 6) were as follows:

In the early stages of projectile-target interaction, pressures and temperatures throughout the affected region are indeed sufficiently high to neglect strength properties and the hydrodynamic approach is applicable. On the other hand, in the later states of penetration the pressures are comparable to the ultimate or yield strength of the material. Consequently, the penetration cannot be considered to totally hydrodynamic problem.

Recognizing this, Walsh did not calculate crater sizes. Instead he attempted to treat only that portion of the penetrator that is formed during the high-pressure phase of the penetration phenomena. In doing this Walsh postulated that, if at any time during the formation of craters resulting

from different impacts the pressure pulses and velocities were the same, then the subsequent reaction of the target material should be the same.

Making use of this principle, Walsh calculated the pressure and velocity distribution for a number of impacts of iron cylinders and iron targets. In all cases he varied the mass and velocity of the projectile while keeping the kinetic energy constant. From comparisons of pressure and velocity plots he concluded that the hydrodynamic portion of the penetration process varies as $V^{0.62}$. This is approximately $V^{2/3}$ which states that crater volume depends on kinetic energy.

To summarize the results of the theoretical approaches, calculations were made of the penetration of an iron projectile into an iron target using the theoretical approaches just discussed. The results are shown in figure 14.

Curves are shown for the jet penetration mode, Öpik's, Grimminger's equation, and the curves resulting from Bjork's and Walsh's investigations. The thermal and explosive analogy curves would, of course, be parallel to the $V^{2/3}$ curve. There is some experimental work at 25,000 feet per second that lies between the $V^{1/3}$ and $V^{2/3}$ work. From this we could conclude that the incompressible fluid models of Pugh and Öpik are not applicable to the hypervelocity range. Even with this, however, the spread of the predicted penetration in the high meteoroid velocity range is still too great for design pruposes.

Even the results of the two most exact analyses differ considerably in the higher impact velocity range. This is in spite of the fact that they used identical approaches, and differed only in their criteria of crater formation.

METEOROID SIMULATION TECHNIQUES

Concurrent with the development of theoretical approaches, there has

been an increasing effort to improve existing accelerators to meet the need for meteoroid simulation.

There are three requirements that must be met for the accurate simulation of the meteoroid environment:

First, the technique should be capable of obtaining impact velocities in the meteoroid velocity range (i.e., between 35,000 and 200,000 ft/sec).

Second, the technique should be such that the mass, size, and velocity of the projectile are either known or can be accurately measured.

Finally, the technique should be capable of accelerating a large number of smaller particles. This requirement is, of course, not needed for studying the penetration damage done by the large micrometeoroids. It is, however, needed to investigate the erosion damage done by the more numerous smaller micrometeoroids.

Accelerators For Armor Penetration

Two of the methods that were extensively used for armor penetration investigations are the light-gas guns and the explosive charge accelerators. The light-gas gun consists of two stages: a pump tube and a launch tube separated by a diaphragm. The pump tube consists of a light gas and a piston device to compress the gas. When the pressure becomes large the diaphragm is ruptured allowing the pressurized gas to accelerate the projectile down the launch tube.

The velocities obtained from these devices, however, were well below meteoroid velocities. Some of the methods used to increase their velocity capabilities are shown in figure 15.

The top sketch shows the basic scheme of staging. In this system the projectile of the first gun acts as a piston for the second.

The velocity of a light-gas gun is dependent on the ratio of the gas temperature to the mass of the gas. As the mass of the gas is already a minimum, higher velocities can be obtained only through raising the temperature of the gas. Three schemes have been used to augment the energy of the gas: electrical discharge into the gas, preheating the pump tube before injecting the gas, and preheating the gas outside and injecting it into the pump tank just prior to compression. Another approach to increasing the efficiency of light-gas guns has to do with proper design of the transition section. On the bottom left of figure 15 is an aerodynamic throat transition section which was designed to provide minimum resistance to gas passage. On the right is the accelerated breech transition section. In this design a piston of low mechanical strength extrudes itself into a very small angle conical transition. This extruding action creates an increase in the velocity and pressure of the front face of the piston.

A summary of the maximum capabilities of present light-gas gun facilities is shown in figure 16.

Shown in this figure is the maximum velocity in feet per second as a function of the projectile weight in grams. Equivalent velocities in kilometers per second are shown on the right-hand scale.

The circles represent the velocities of guns using the tapered throat and powder accelerated pistons. The square symbols represent the guns using aerodynamic throats. The numerals above the square symbols denote which pump tube configuration was used.

Note that the highest velocity obtained with a light-gas gun is about 34,000 ft/sec, which is still below even the minimum meteoroid velocity.

Furthermore, at this velocity only one or two shots can be obtained before the guns must be rebored.

Some of the methods developed for increasing the efficiency of the explosive charge techniques, also used initially in armor penetration, are shown in figure 17.

The top sketch is an illustration of the so-called cavity charge technique. In this technique the detonation wave propagates through the explosive until it reaches the cavity wall. At this time it generates a strong shock wave which is propagated through the cavity. The detonation wave continues through the walls of the tubular section of the explosive at a higher velocity than the original shock wave in the cavity. This detonation wave, in turn, generates other shocks from the inner sidewalls. These additional shocks interact with the original shock, progressively compressing it and creating a corresponding increase in peak pressure. Such devices have accelerated particles up to 25,000 ft/sec.

Another approach to the shaped-charge techniques are the linear charges shown in the bottom two sketches of figure 17. In this technique the projectile is formed during the launch stage.

As the detonation wave progresses forward, it collapses the metal liner material onto the axis and forms the projectile. Velocities as high as 67,000 feet per second have been measured for the cylindrical linear while a velocity of 49,000 feet per second has been obtained with the conical liner. The disadvantage of this technique is that neither the shape nor mass of the projectile is accurately known.

Accelerators For Meteoroid Simulation

Neither the light-gas gun nor shaped-charge accelerators meet the

requirements for simulation of true meteoroid environment. The velocity of the light-gas gun is too low and the particle size of the explosive charge technique is not accurately known. Consequently, in the last few years there has been an increase in effort to develop entirely new acceleration techniques. Two of the most promising are the exploding wire or foil guns and the electrostatic accelerators.

An exploding foil gun is shown schematically in figure 18. It consists of a bank of capacitors connected through a switch to a thin aluminum foil of 1/4-mil thickness. The two solid plastic blocks approximately 2 inches square and one-half inch thick act as a breech and a plastic tube acts as an expandable barrel. The barrel is then mounted into a vacuum chamber that also houses the target.

The exploding foil gun utilizes the explosive force achieved by abruptly discharging the large quantity of electrical energy stored in the capacitors through the thin metal film. When this discharge occurs the film is heated to a molten state in a relatively short time (less than a millisecond). The inertia of the film holds it in place until it becomes superheated and explodes. The explosive force punches a disk-shaped particle which forms the projectile. The projectile sizes can be altered by changing the diameter of the tube and the thickness of the diaphragm. Projectile material can be altered by using different material diaphragms. Barrels ranging from 1/8 to 1/2 inch in diameter and disk thicknesses from 0.002 inch to 0.050 inch have been successfully used.

A sequence of pictures of the firing of an exploding foil gun is shown in figure 19. The pictures were taken at 10-, 25-, 28-, and 30-second intervals after the closing of the switch.

It takes about 10 seconds for the diaphragm to shear, allowing the plasma and the projectile to be accelerated down the barrel. At 25μ sec the projectile is well down the barrel. At 28μ sec the projectile is out of the barrel and almost impacting the target. You can see the shock wave ahead of the projectile just beginning to be reflected by the target. The last picture shows the projectile impacting the target with the accompanying spray of particles. Two interesting points are brought out by these pictures: First, the plasma front is always ahead of the projectile; and, second, the barrel and breech remain intact until the particle is well on its way. As of today this technique is in its development stage. Exploding foil guns have accelerated 10-mg particles to about 35,000 feet per second with only 6000 joules of electrical energy. This indicates only a 5-percent efficiency of converting electrical energy into kinetic energy of the particle.

Analyses and experimental investigations are under way at Langley and several other organizations to improve this efficiency.

Some of the improvements needed for better efficiency are:

1. More available energy
2. Higher voltage on capacitors
3. Maximum rate of current rise
4. Lowest possible inductance
5. Better and lower induction switching

Another version of the electrical discharge accelerator is the exploding wire gun developed by Mr. Scully of North American Aviation. The facility utilizes the discharge of a large bank of capacitors of about 40,000 joules but, instead of a plastic barrel and breech and aluminum foil, it utilizes a lithium wire acr chamber shown in figure 20.

The arch chamber consists of an insulated lithium wire attached to the

are placed on a carrier membrane at the entrance to the launch tube. The membrane is in contact with the arc chamber electrode. The particles consist of thousands of small glass spheres ranging in size from 10 to 50 microns in diameter. Upon discharge of the capacitors the particles are accelerated by the lithium plasma down the launch tube which is evacuated to a pressure of 3 to 7 microns of mercury. Baffle plates are used to prevent all but a few particles from striking the target. The maximum velocity achieved with this device is about 60,000 feet per second with a 50-micron particle.

The other technique which has the potential of simulating the meteoroid environment is the electrostatic accelerator. This technique has the potential of reaching the highest meteoroid velocity, This method is applicable only to the smaller particles but allows for the acceleration of a stream of particles to meteoroid velocities thereby permitting a study not only of penetration but also of erosion effects of micrometeoroids.

The interest in this facility stems from the range of velocities that is attainable from consideration of the equations.

$$v = \sqrt{\frac{2Vq}{m}} \qquad (6a)$$

$$v = K\sqrt{\frac{VE}{r\rho}} \qquad (6b)$$

Equation (6a) shows the velocity attained by a particle of mass m with a charge q exposed to an electrical potential V. The charge on a particle can be expressed in terms of the surface field strength on the particle E. Hence the velocity of a spherical charged particle can be related to its radius r, density ρ, voltage V, and surface field strength E, as shown

in equation (6b).

This form of the equation is preferred as the maximum charge which a particle can retain can be expressed in terms of this parameter E. The maximum value of E is determined by the ability of the material to hold electrons or ions and is about one order of magnitude greater for a positive charge than for a negative charge. Consequently, only positively charged particles are considered for electrostatic acceleration.

The significance of this equation is shown in figure 21, where the attainable velocities for an iron particle, one micron in diameter, are plotted as a function of voltage in millions of volts. The curves are drawn for the maximum theoretical charge possible (which is 2.0×10^{10} volts/meter), 50 percent of maximum, and a charge corresponding to about 12 percent of the maximum or 2.5×10^{9} volts/meter.

This lower value represents the charge that can be placed on a particle by the only fully developed charging device. In this device the particles to be charged are allowed to come into contact with a small spherical charging electrode which is maintained at a high positive voltage. In the original accelerator this charging device was mounted on the accelerator tube in the dome of a two-million-volt Van de Graaff generator. Thus a micron-size particle would be accelerated to about 28,000 feet per second. Smaller particles, of course, would reach higher speeds. At the present time Langley is installing a similar device but is using a 4-million-volt Van de Graaff generator which is the largest horizontal machine made. Thus with this device we can achieve about 40,000 feet per second with a 1-micron-size particle.

As can be seen from these curves, velocities in the 100,000-foot-per-second range can be realized either by improving the particle charging device

or by providing large accelerating voltages. Both of these approaches are being investigated.

In the light of recent developments the most attractive approach to obtaining the higher velocities is through an increase in voltage. Theoretical studies have shown that voltages of the order of 20 to 30 million volts are entirely feasible by the use of a linear accelerator such as shown in figure 22. Devices similar to this have been used by nuclear physicists to accelerate electrons and protons. It consists of a linear array of cylindrical draft tubes of which the length and gap separation progressively increase. Alternating tubes are connected to opposite terminals of an alternating-current source. The frequency of this source is adjusted so that each time the particle enters a gap it sees an accelerating voltage. Consequently, the total accelerating voltage is equal to the sum of all the accelerations received at each gap.

Studies are also under way to improve the charging devices. One promising new method is one that charges the particles by exposing them to a concentrated ion beam. One such method (see ref. 9) has successfully imposed a large charge on carbon particles. However, it takes from 4 to 8 hours to charge just one small particle. In addition, the charging device requires constant visual observation of the particle precluding its intergration into a Van de Graaff accelerator.

A summary of the meteoroid simulation capabilities is shown in figure 23 where the attainable velocity in both feet per second and kilometers per second is plotted against the size of the projectile in meters. The solid lines indicate present capabilities of these devices while the dotted lines are realistic potentials for the near future. The shaded area represents the estimated meteoroid velocity range. As the figure illustrates, the existing

devices are capable of simulating the meteoroid impacts only in the lower meteoroid velocity region. In the near future, however, velocities in the higher meteoroid velocity region will be possible with the electrostatic accelerator. This, of course, will be with the smaller, dust size particles. Larger particles can be accelerated only to about 60,000 feet per second even with the anticipated improvement in the exploding foil gun.

Of all these devices the electrostatic accelerator is the only one that can accelerate the high fluxes of particles needed (10/sec) for erosion studies.

CONCLUDING REMARKS

A summary of the state of the art of predicting the penetration of simi-infinite targets by particles traveling at meteoroid velocities has been presented. From this summary it was concluded that uncertainties in predicted penetration of one order magnitude exist in the high meteoroid velocity range. Although several accurate analytical solutions of the penetration problem, treated as a hydrodynamic phenomena, have been made, uncertainties in the equation of state and the cratering criteria have caused large differences in the resulting scaling laws.

From a summary of simulating techniques it was concluded that existing devices are capable of simulating meteoroid impacts only in the lower meteoroid velocity range.

REFERENCES

1. Berkhoff, G.; MacDougall, D. P.; Pugh, E. M.; and Taylor, G. I.: Explosives With Lined Cavities. J. Appl. Phys., vol. 19, 1948.

2. Charters, A. C.: High Speed Impact. Sci. Am., vol. 203, no. 4, Oct. 1960.

3. Bjork, R. L.: Effects of a Meteoroid Impact on Steel and Aluminum in Space. Paper P-1662, The RAND Corp., Dec. 16, 1958.

4. Stanyukovich, K. P.: Concerning the Impact of Solids at High Velocities. Soviet Physics - JETP (Letters to the Editor), vol. 36(9), no. 5, Nov. 1959, p. 1141.

5. Grimminger, G.: Probability That a Meteorite Will Hit or Penetrate a Body Situated in the Vicinity of the Earth. J. Appl Phys., Vol. 19, 1948.

6. Harlow, F. H.: Particle-in-Cell Method for Numerical Solution of Problems in Fluid Dynamics. Proceedings of Symposia in Applied Mathematics, vol XV, 1963.

7. Walsh, J. M.; and Tillotson, J. H.: Hydrodynamics of Hypervelocity Impact. General Atomic Division of General Dynamics - GA-3827, Jan. 1963.

8. Vedder, James F.: Charging and Acceleration of Microparticles. The Review of Scientific Instruments, Vol. 34, no. 11, Nov. 1963.

	RESISTIVE FORCE F	PENETRATION p/d
1	k	$K\left(\frac{\rho_p}{\rho_t}\right)V^2$
2	kp	$K\left(\frac{\rho_p}{\rho_t}\right)^{1/2}V$
3	kp^2	$K\left(\frac{\rho_p}{\rho_t}\right)^{1/3}V^{2/3}$
4	kp^2V	$K\left(\frac{\rho_p}{\rho_t}\right)^{1/3}V^{1/3}$
5	kp^2/V	$K\left(\frac{\rho_p}{\rho_t}\right)^{1/3}V$
6	$k\rho_t V^2$	$K_1\left(\frac{\rho_p}{\rho_t}\right)\log V + K_2$
7	$k_1\rho_t V^2 + C_2H$	$K_i\left(\frac{\rho_p}{\rho_t}\right)\log\left[1+\frac{\rho_t V^2}{C_2H}\right]$

NASA

Figure 1 Empirical penetration formulas.

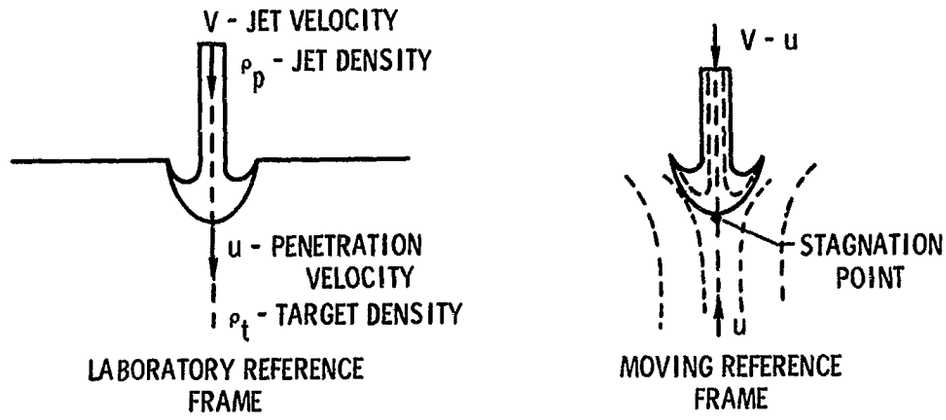

NASA

Figure 2.- Penetration by jet action.

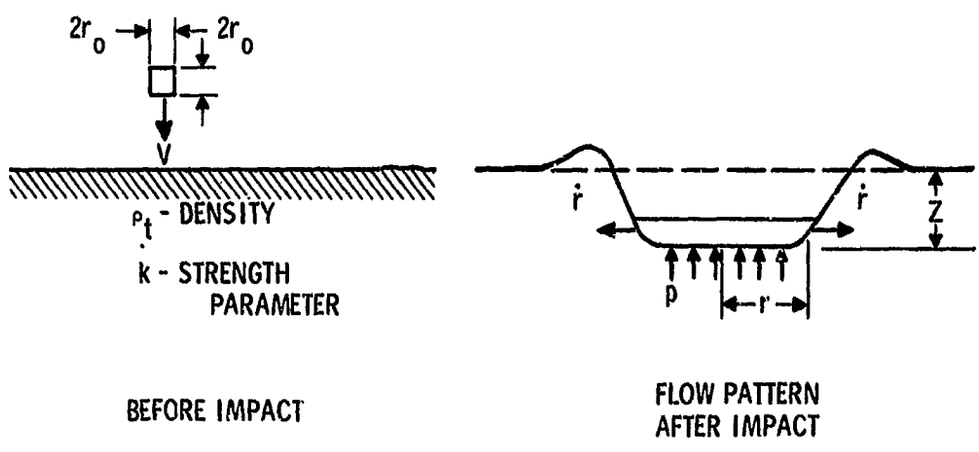

NASA

Figure 3.- Öpik's description of crater formation.

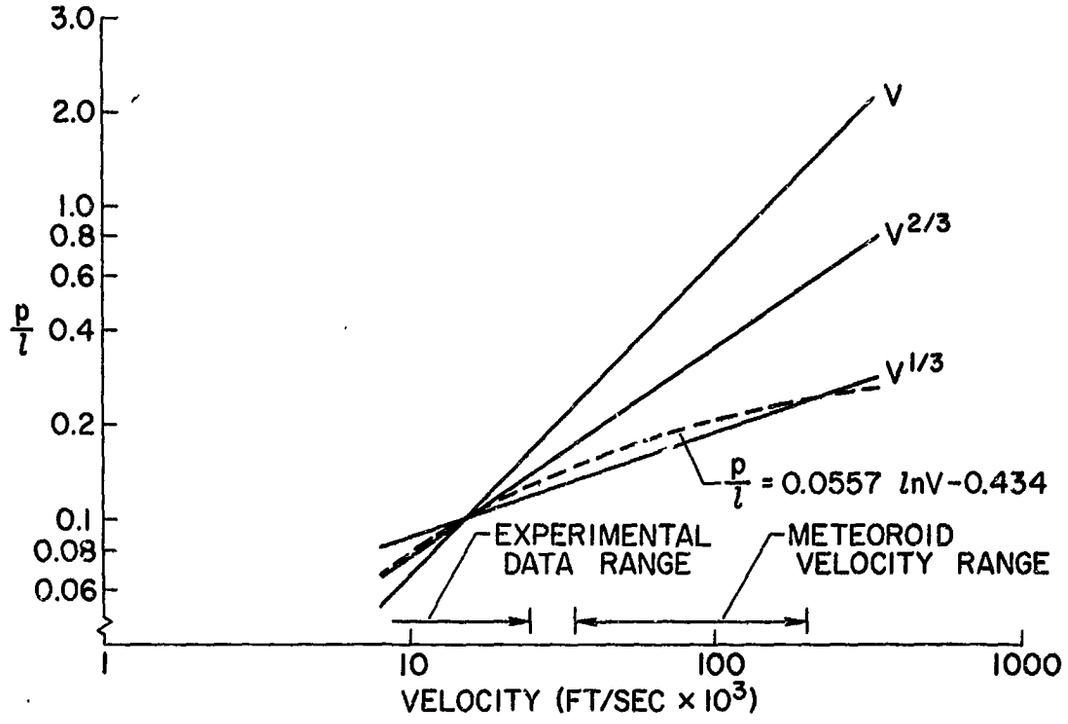

NASA

Figure 4.- Empirical penetration curves.

REGION I - PROJECTILE REMAINS INTACT $(P \sim V^{4/3})$

REGION II - PROJECTILE DEFORMS AND SHATTERS

REGION III - FLUID IMPACT $(P \sim V^{2/3})$

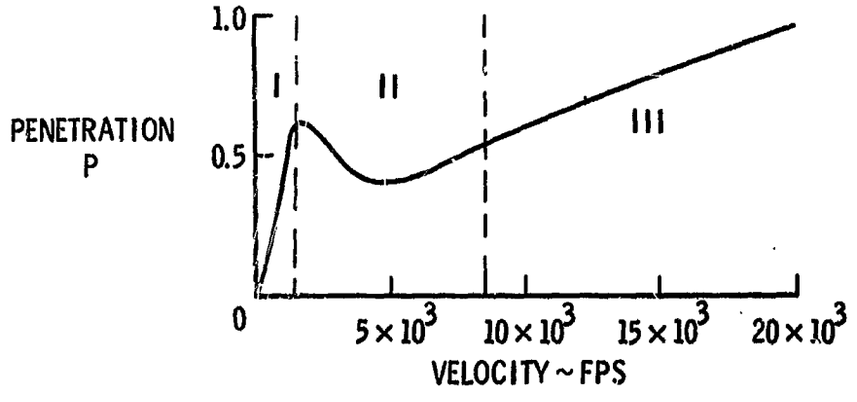

NASA

Figure 5.- Impact of steel and tungsten carbide into soft lead.

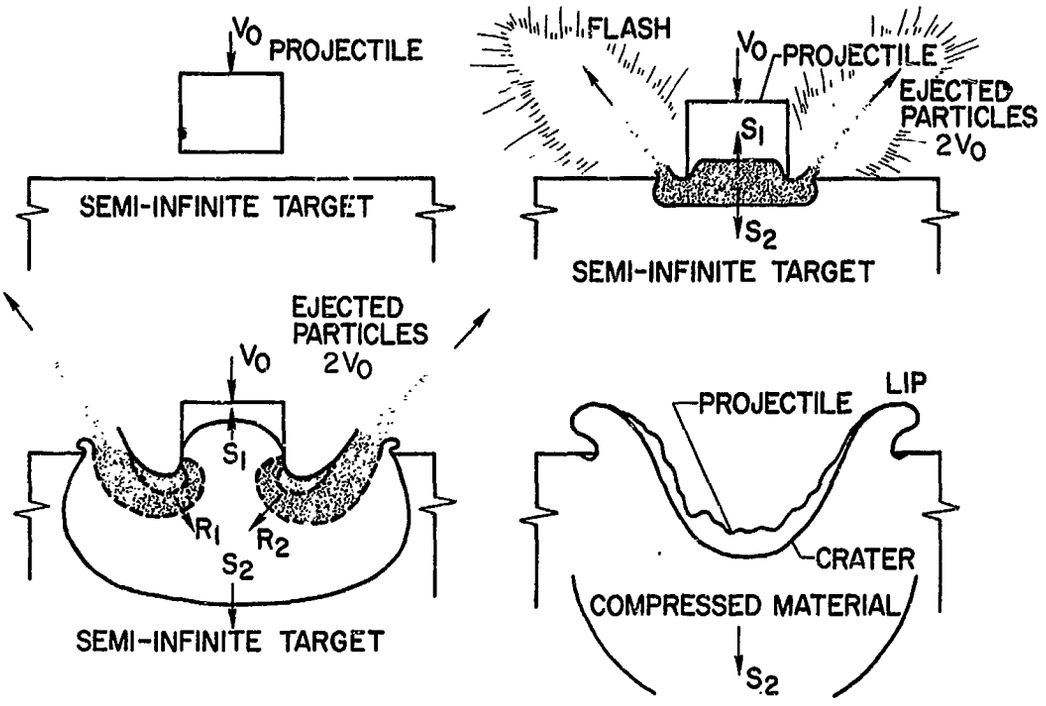

NASA

Figure 6.- Impact mechanism.

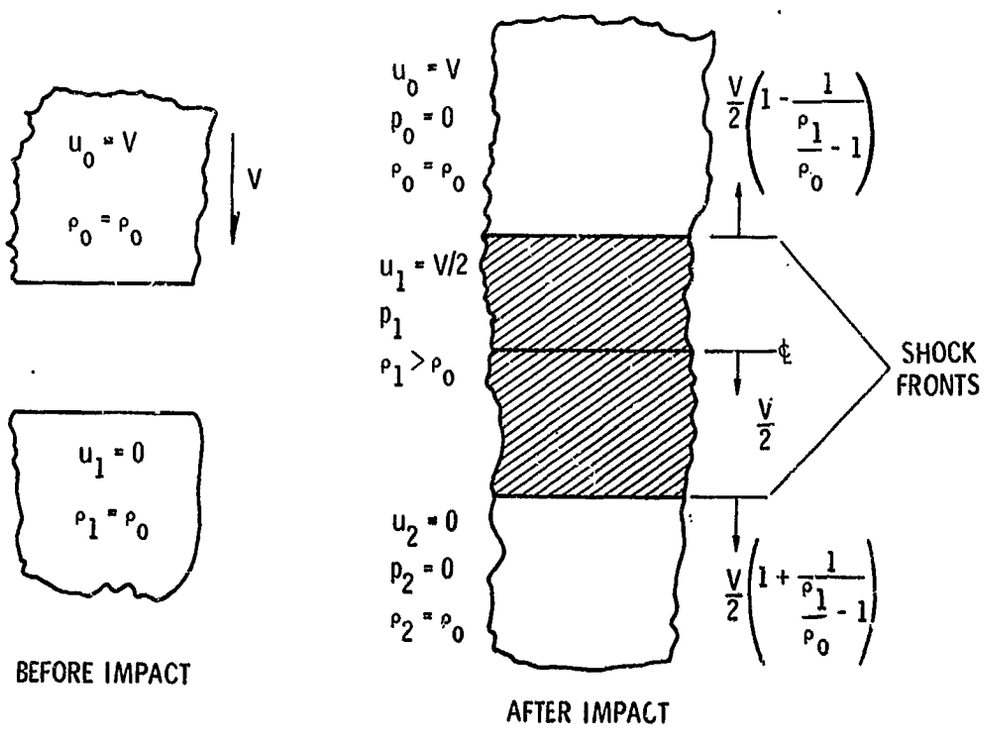

NASA

Figure 7.- One-dimensional impact.

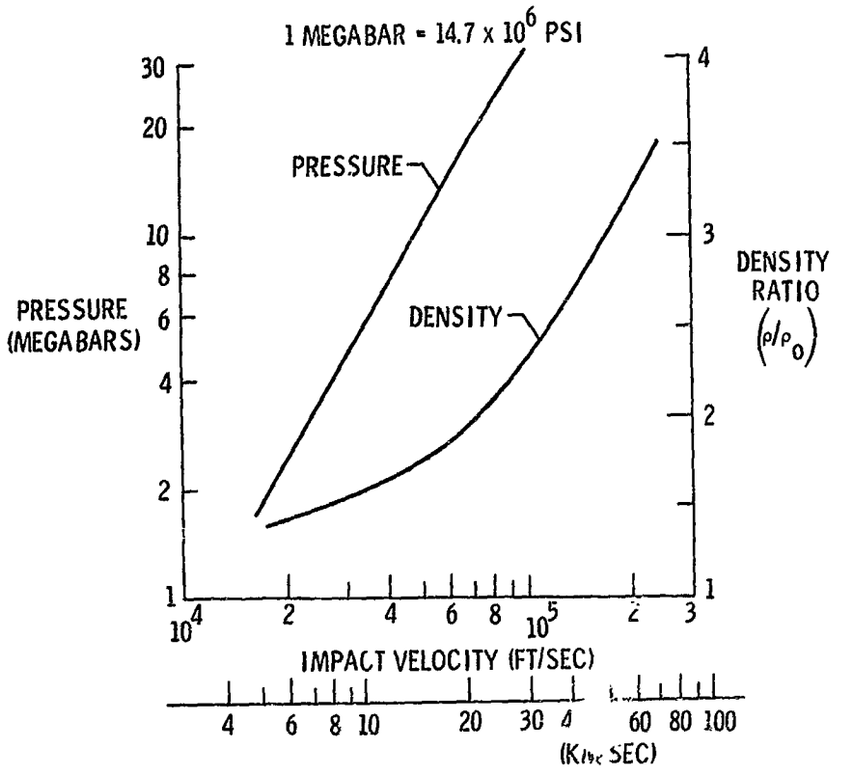

NASA

Figure 8.- One-dimensional shock conditions for iron.

THERMAL PENETRATION

$$\frac{p}{d} = K\left(\frac{\rho_p}{\rho_t}\right)^{1/3} \frac{V^{2/3}}{Q^{1/3}}$$

EXPLOSIVE PENETRATION

$$\frac{p}{d} = K\left(\frac{\rho_p}{\rho_t}\right)^{1/3} \frac{V^{2/3}}{R^{1/3}}$$

GRIMMINGER'S HYDRODYNAMIC PENETRATION

$$\frac{p}{d} = \frac{4}{3}\frac{\rho_p}{\rho_t} \ln \frac{V}{5C} + \frac{25C^2}{3}\frac{\rho_p}{K}$$

$$K = 5.03 \frac{\sigma_t}{\sigma_{CU}} \times 10^7$$

C - PLASTIC WAVE VELOCITY

NASA

Figure 9.- Theoretical penetration equations.

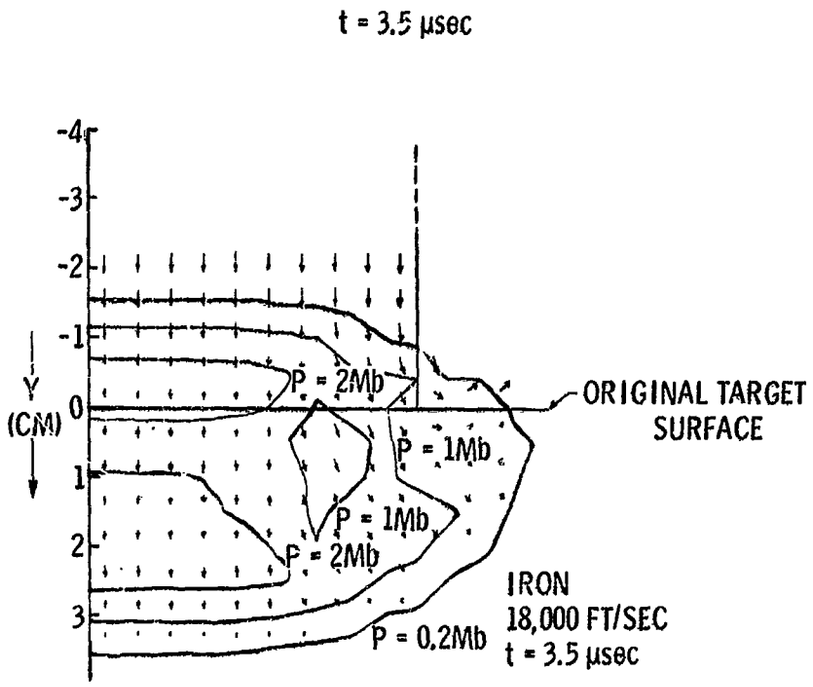

NASA

Figure 10.- Pressure contours and velocity field.

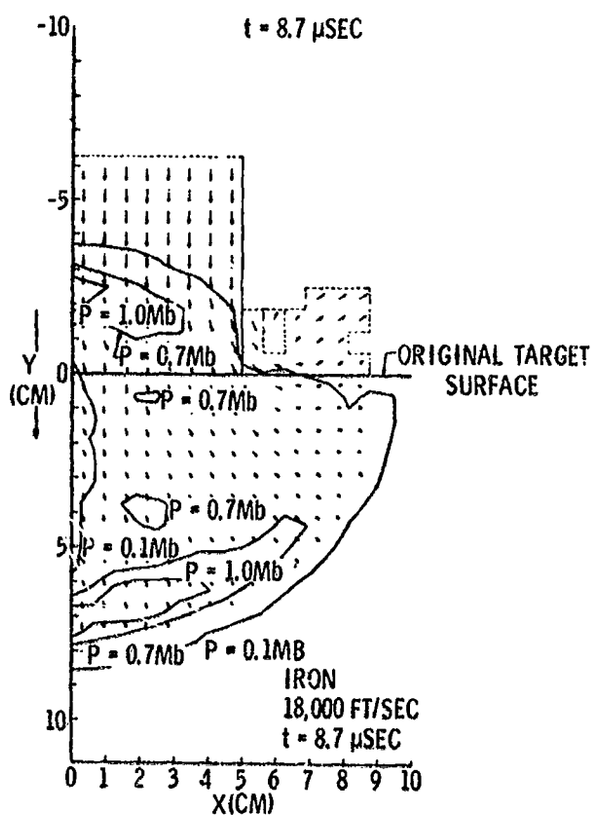

NASA

Figure 11.- Pressure contours and velocity field.

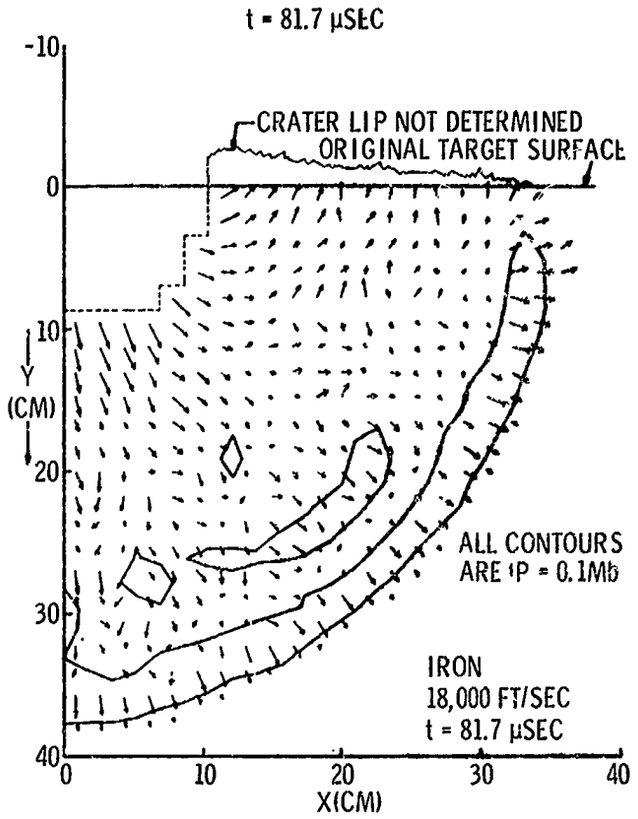

NASA

Figure 12.- Pressure contours and velocity field.

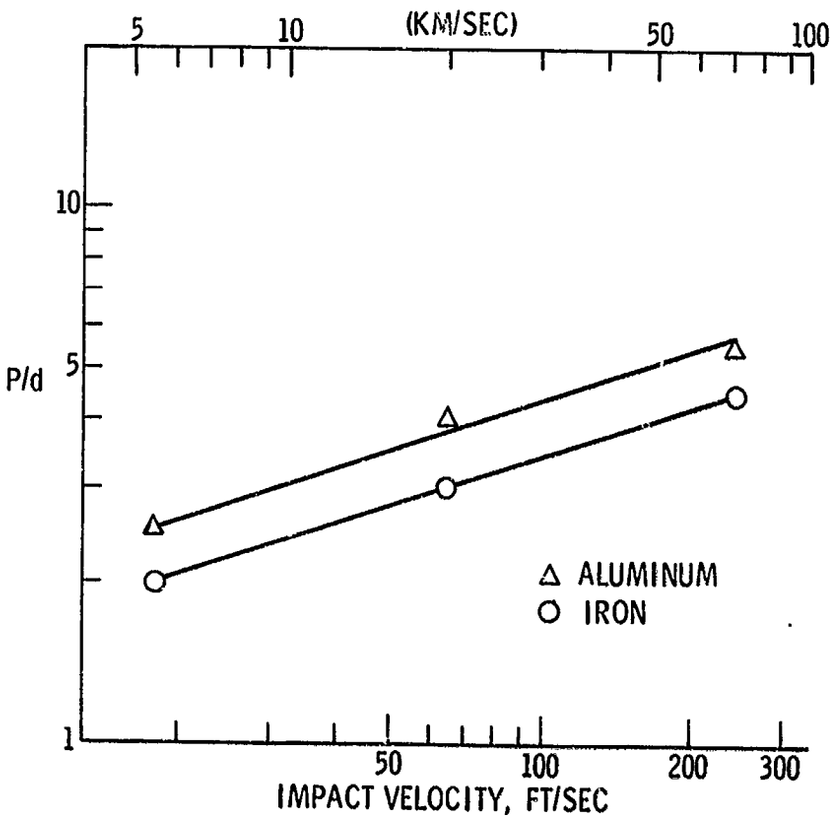

NASA

Figure 13.- Bjork's penetration results.

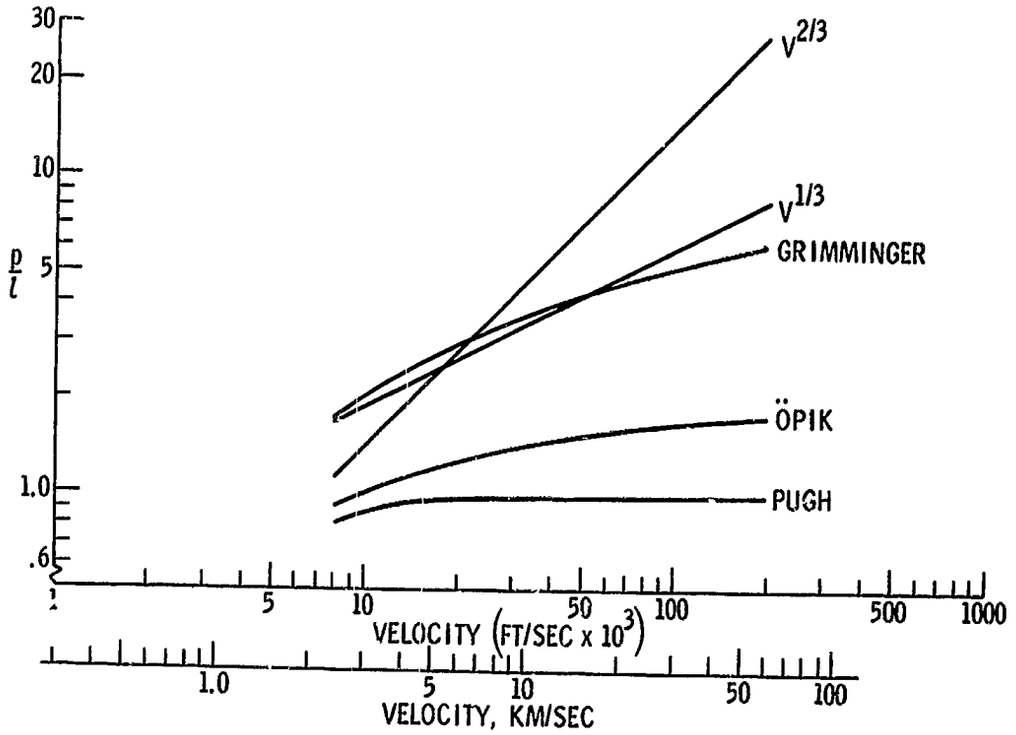

NASA

Figure 14.- Theoretical penetration curves.

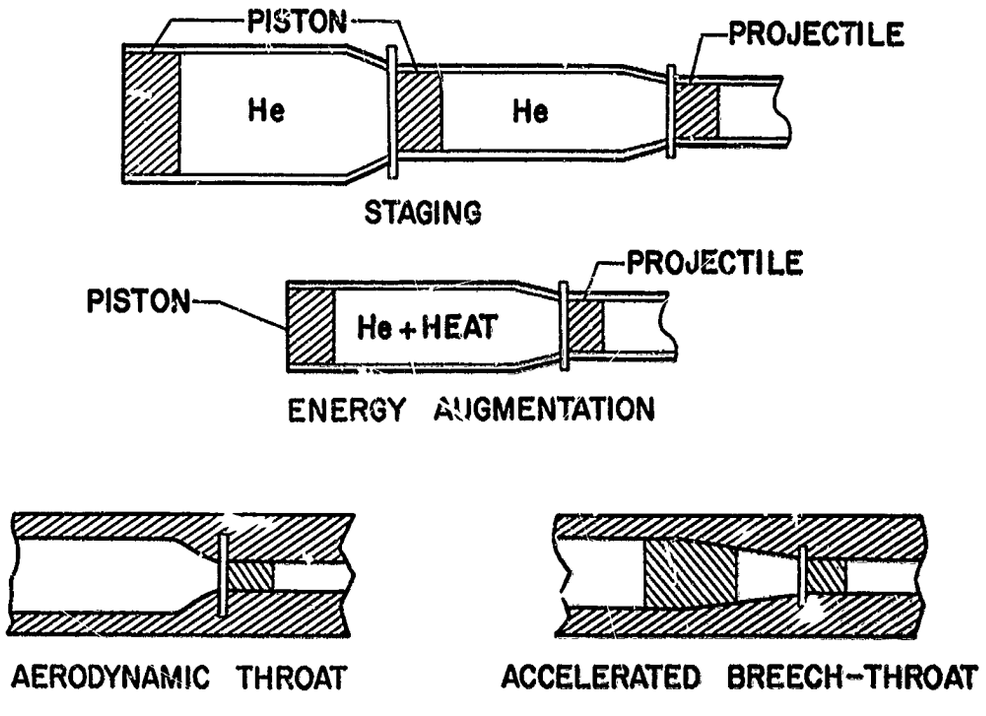

NASA

Figure 15.- Modified light-gas gun techniques.

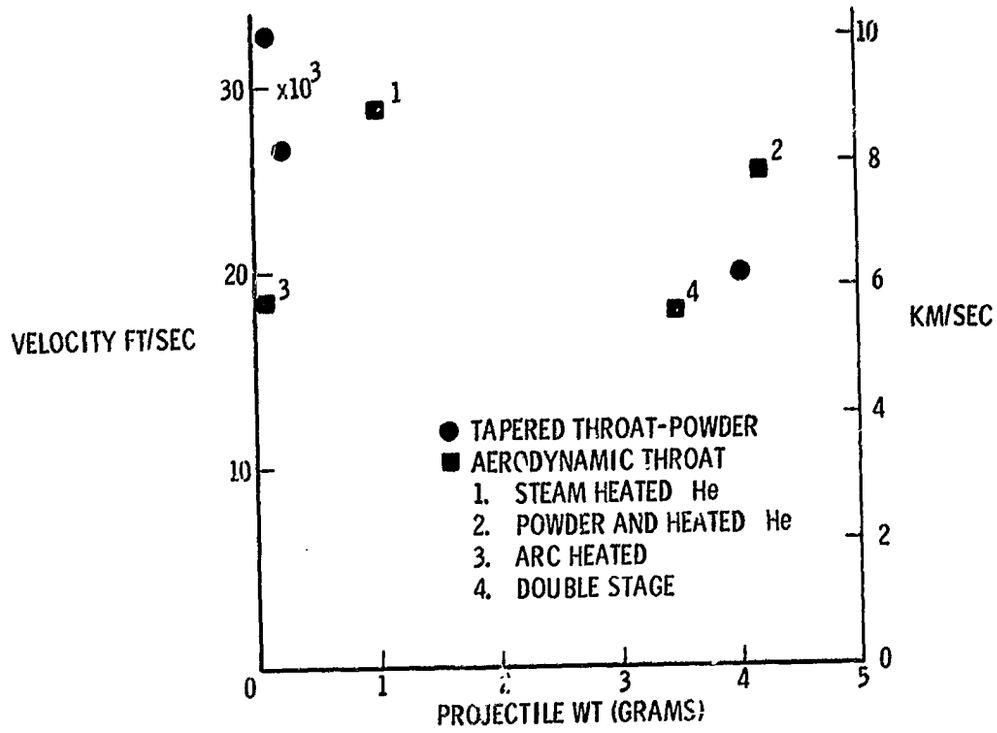

NASA

Figure 16.- Light-gas gun capabilities.

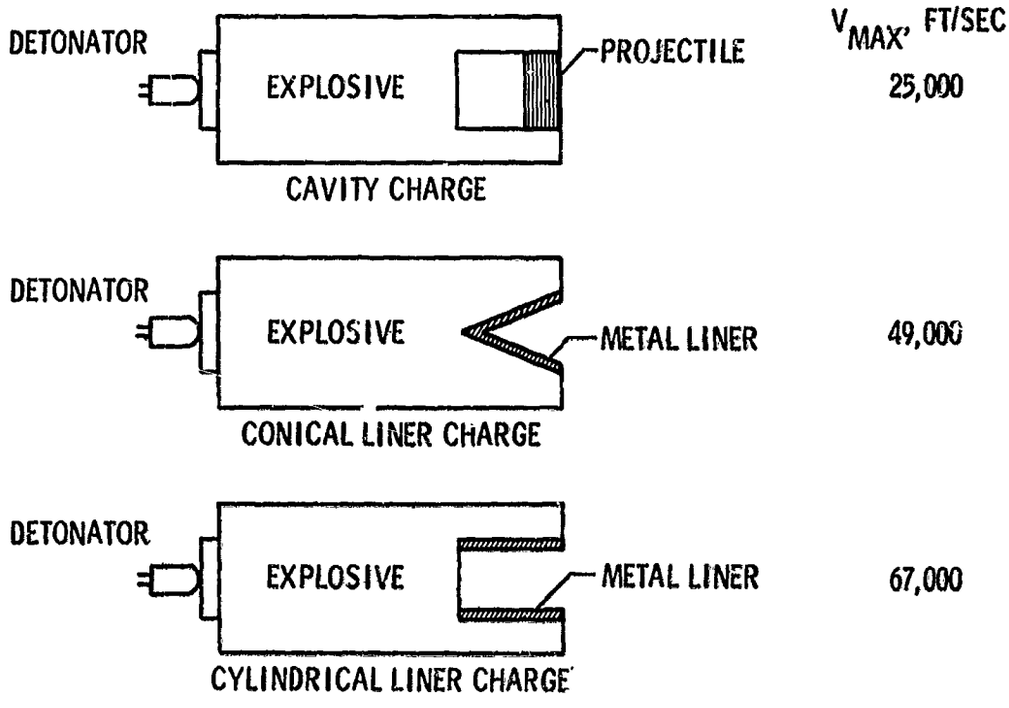

NASA

Figure 17.- Modified shaped charge techniques.

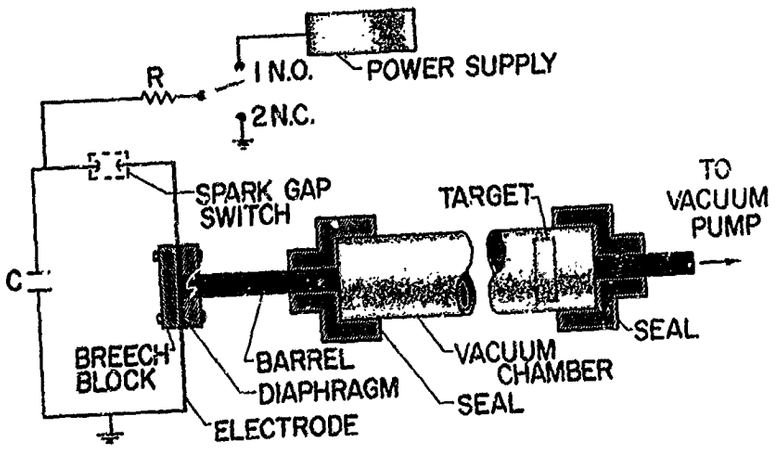

Figure 18.- Exploding foil gun facility schematic.

Figure 19.- The exploding foil gun firing sequence.

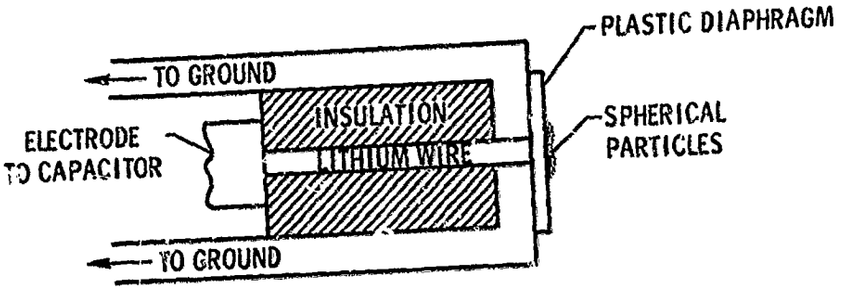

Figure 20.- N.A. exploding wire gun.

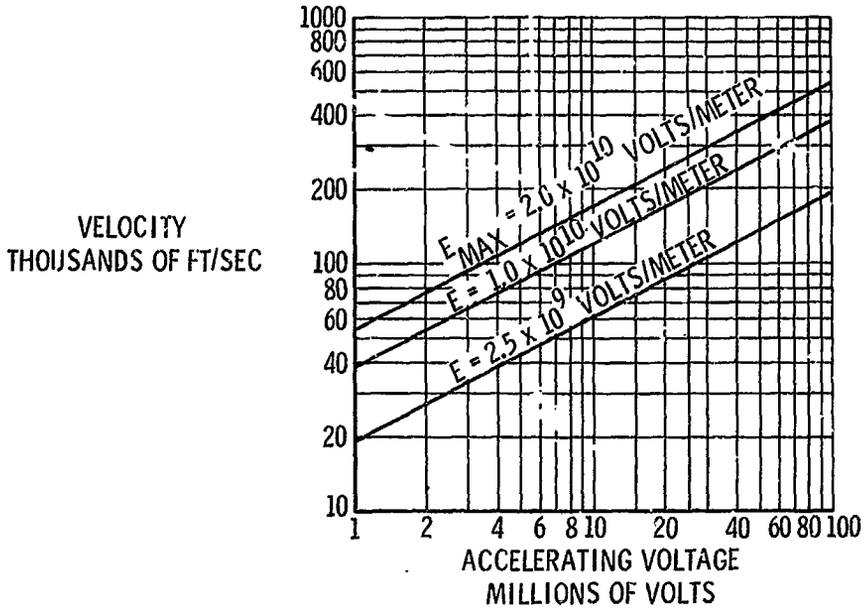

NASA

Figure 21.- Velocity vs. voltage for 1-micron iron particles.

(SLOAN-LAWRENCE)

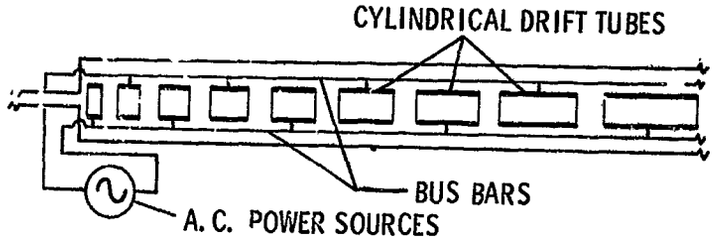

NASA

Figure 22.- Linear accelerator.

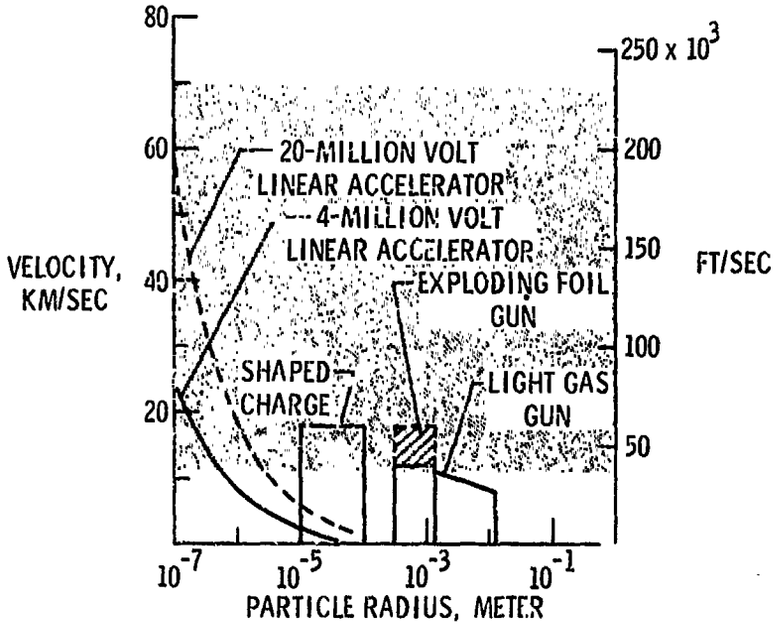

NASA

Figure 23.- Summary of [illegible]

N66 28904

MAGNETIC FIELDS:

REASONS FOR SIMULATION AND METHODS AVAILABLE

by

Norman F. Ness

NASA - Goddard Space Flight Center

INTRODUCTION

Magnetic fields are among the most ubiquitous of physical phenomenon scudied by man. They are important on an atomic level in which magnetic field strengths of thousands of gauss are employed in the study of atomic structure. In cosmic physics stellar magnetic fields of tens and hundreds of gauss are important factors controlling the physical phenomenon observed. In interstellar and in interplanetary space magnetic fields of less than 10^{-4} gauss are important in determining the motion of charged particles and in the dynamics of the interstellar and interplanetary medium. The major portion of this talk is to be directed towards a description of the present spatial environment of the Earth with respect to magnetic fields. Following the descriptive aspects of the magnetic field, as observed by satellite and space probes, the quantitative representation of these fields will be given. A description of the presently available systems to simulate the magnetic fields in space will be reviewed and the most recent large scale facility for such work discussed.

The last section of the paper deals with engineering applications of our knowledge of the Earth's magnetic field in various satellite programs. Certain of these applications are quite unique and represent some of the reasons for necessitating simulation of magnetic fields as observed in space. The unit of magnetic field force as commonly used in geomagnetism is the gamma (equal to 10^{-5} Gauss). On this scale a current of one milliampere flowing in an infinitely long wire creates a magnetic field whose strength is 20 gammas at a distance of one centimeter.

There are a number of scientific reasons for mapping the magnetic field environment of the Earth. These include:

1. Investigation of secular changes and the present state so as to determine the sources of the geomagnetic field and the interplanetary magnetic field structure;
2. To study and analyse charged particle motion, which requires a knowledge of the geomagnetic and interplanetary magnetic field and
3. To determine the time variations of these fields and their correlation with auroral phenomenon and solar activity.

In order to successfully map the magnetic fields in space it is necessary to perform direct measurements of the magnetic field from satellites and space probes. Thus they represent portable laboratory platforms upon which instruments sensitive to magnetic fields are placed.

One of the primary engineering reasons for simulating magnetic fields in space is to test and calibrate the magnetometer sensors which will be used to directly measure magnetic fields in space. A second objective is to allow a measurement of the magnetic properties of satellites and space probes to determine:

1. Their contaminating or noise effects on magnetic field measurements made by magnetometers on board the same spacecraft,
2. To determine the dynamic interaction of the moving and possibly spinning spacecraft with magnetic fields, principally the earth's field and
3. To allow the testing of specific orientation and attitude control and spin producing subsystems which employ the geomagnetic field for magnetic torque interactions and/or directional information.

As more is learned about the magnetic fields in space more sophisticated use in an engineering sense can be made of this valuable information. The principal techniques of simulating terrestrially the weak magnetic fields which exist in space employ large current carrying coil systems which generate steady magnetic fields canceling the earth's field over a small volume.

Results of Magnetic Field Measurements in Space

A number of satellites carrying magnetometers have been launched by both this country and the USSR. A summary of those satellites measuring principally the earth's magnetic field is shown in Figure 1. In general the life time of these satellites has been individually limited as shown in Figure 2, summarizing trajectory characteristics pertinent to mapping of the earth's magnetic field. A very limited number of space probes have investigated the interplanetary magnetic field. In order to measure the properties of the interplanetary medium, undisturbed by the presence of the Earth, it is necessary to perform measurements at a considerable distance from the surface of the Earth. The interaction of the solar plasma resulting from the expanding solar corona[1] requires that these measurements

be performed at least 80,000 Km from the Earth near the subsolar point and at a considerably larger distance away from this region. As shown in Figure 3 most satellites which have performed measurements of the interplanetary field were limited either in accuracy or in measuring only a limited characteristic of the field and not the complete vector magnetic field.

A representative sample of the results of measurements in space confirming the general characteristics of the dipolar geomagnetic field is shown in Figure 4. The Explorer X satellite[2] carried a rubidium vapor magnetometer and performed successful measurements of the Earth's magnetic field from 2 to 7 R_e (Earth radii) in March 1961. In Figure 4 are summarized both the direct measurements and the difference between the observations and the theoretical field values predicted by extrapolation using spherical harmonic analysis of the surface terrestrial field. It is seen that the deviations are quite small and represent less than 5 percent of the ambient field. However, these small deviations of the Earth's magnetic field are extremely important in this region of space. It is precisely within this radial distance range that the trapped charged particle fluxes are observed to reach their peak intensities.[3] The deviations observed, as illustrated in Figure 4, are consistant with the magnetic effects of charged particle spiral and drift motion in the Earth's magnetic field. At the present time detailed models of the particle belts are being developed as more refined instrumentation permits investigation of the spectral and pitch angle distributions of the energetic particles within the belts.[4]

A substantially different result in measuring the Earth's magnetic field occurs when one considers Figure 5. The magnetic field data as obtained on the IMP-1 satellite[5] are shown near the subsolar point. It is

seen that the Earth's magnetic field agrees reasonably well with that predicted by spherical harmonic analysis until a distance of 7 or 8 R_e is reached. Beyond this point the observed field becomes increasingly stronger until a distance of 10.7 R_e is reached. At this point the measured magnitude of the field is approximately twice that predicted by theoretical analysis. Subsequent to this point on the trajectory the field abruptly drops to low and fluctuating values. This characteristic abrupt decrease of the Earth's magnetic field following a gradual but significant increase in magnitude is identified as a boundary of the Earth's magnetic field. It is due to the flow of solar plasma much in the fashion suggested by Chapman-Ferraro[6] more than 30 years ago to explain transient variations of terrestrial fields following solar activity.

A naive and simplified approximation to the very complex interaction of the solar plasma impacting the Earth's magnetic field is shown in Figure 6. Here specular reflection from the boundary of the Earth's magnetic field is assumed for the individual particle trajectories. Within this bounding region the dominant magnetic field is that of the Earth's and the distortion of the geomagnetic field by currents on the confining boundary. This region of space has been referred to as the magnetosphere by Gold[7] since the motion of charged particles is completely dominated by the Earth's magnetic field. On the assumption of direct impact of the solar plasma on the Earth's magnetic field, the stand off distance of the boundary, depending upon the solar plasma momentum flux and geomagnetic field strength, can be predicted. Figure 7 summarizes a parameter distribution of stand-off distances as a function of particle densities and energies. In order to convert from these values to fluxes one multiplies particle density by the equivalent proton velocity. The fluxes being discussed have been measured by space probes and satellites, but

this paper does not intend to review this material. Interested readers are referenced to the papers by Snyder and Neugebauer, 1963;[8] Bonetti et al. 1963;[9] and Bridge et al. 1964.[10] The observed distance of 10.7 R_e and estimated plasma velocities of 300 to 700 Km/sec leads to plasma densities of of 1 to 10 protons per cubic centimeter. A general summary of the present field environment illustrating the relative position of the radiation belts in the magnetosphere is shown in figure 8. This illustration also shows the position in which the Explorer X satellite probe mapped the magnetic field of the Earth and detected only small differences between theoretical and observed magnetic fields.

The results of the IMP-I magnetic field experiment for out bound orbit number 15 is shown in Figure 9. The similar characteristic of a gradual increase in the strength of the observed field, over and above that predicted, is clearly seen. Beyond this, a region of rapidly fluctuating and low magnetic field strength is observed to extend to a distance of 23.1 R_e. Beyond this distance the magnetic field is reasonably steady and stable in orientation. We identify this abrupt termination of the fluctuating or tubulent region as a collisionless magnetohydrodynamic shock wave[11] associated with the interaction of the solar plasma with the Earth's magnetic field. Our present understanding of this phenomenon is principally based upon an analogy with high speed gas dynamics.[12] In a fluid, disturbances can be propagated at a sensible velocity characteristic of the medium. In gas dynamics it is the acoustic velocity while in magnetohydrodynamics where ionized gases are in motion the appropriate velocity is the Alfvén speed. This is shown in figure 10 as a function of particle density and magnetic field strength.

The average magnetic field strength in interplanetary space has been measured to be approximately 5 gammas [13] with extreme values between 1γ and

10γ. Particle densities between 1 and 10 protons per cm^3 lead to an Alfvén velocity in general less than 100 Km/sec. Direct measurements of the plasma velocities in interplanetary space indicate velocities on the order of 400 Km/sec. or more, and thus the flow of solar plasma is super Alfvénic with respect to the propagation of characteristic disturbances in the medium. On this basis the interaction of the Earth's magnetic field with the solar plasma becomes much like that of a blunt object in supersonic gas flow in which a detached shock wave precedes the body. It is separated from the obstructing article, which in this case is the magnetosphere boundary and not the Earth's surface. A summary of the magnetic field environment of the earth in cis-lunar space is shown in figure 11. This is based upon the first 19 orbits of the IMP-I satellite, which is the first satellite to have performed detailed and accurate measurements of both the magnetospheric boundary and the collionless shock boundary.

Three regions of space,

1. Magnetosphere
2. Turbulent Boundary layer and
3. Interplanetary medium

are representative of the characteristic types of magnetic fields which must be simulated on the surface of the Earth. The important conclusion deduced from these data is that very weak magnetic fields are observed in space and must be simulated on the surface of the Earth. In addition it also implies that the "portable laboratory bench" upon which magnetometer sensors are placed must be very clean in the magnetic sense so that accurate measurements will be performed.

Geomagnetic Field Representation

In a region of space containing no sources of magnetic flux the magnetic vector $\vec{F}$ is derivable from a potential V which is a solution of Laplace's equation. In a spherical coordinate system (R, θ, ϕ) represent geocentric distance, colatitude and longitude east of Greenwich. The potential V can be represented in terms of a series of spherical harmonic functions as

$$V = R_e \sum_{n=1}^{\infty} \sum_{m=o}^{n} P_n^m (\cos\theta) \left\{ \left[G_n^m \cos m\phi + H_n^m \sin m\phi \right] \left(\frac{R_e}{R} \right)^{n+1} \right.$$

$$\left. + \left[\bar{G}_n^m \cos m\phi + \bar{H}_n^m \sin m\phi \right] \left(\frac{R}{R_e} \right)^{n} \right\} \qquad (1)$$

in which

R_e = 6371.2 kilometers, equivalent radius of a spherical Earth

P_n^m = the partially normalized associated Legendre polynomials introduced by Schmidt and utilized in classical geomagnetism.[14]

G_n^m, H_n^m = harmonic coefficients for sources internal to the spherical surface $(R = R_e)$ with the dimensions of magnetic force. (gauss)

$\bar{G}_n^m$, $\bar{H}_n^m$ = the harmonic coefficients for sources external to the spherical surface $(R = R_e)$ with the dimensions of magnetic force. (gauss)

From the potential representation the magnetic field $\vec{F}$ is derivable as the negative gradient, $\vec{F} = -\text{grad } V$, which straight forwardly yields the X, Y and Z or southward, eastward and radially outward components of the Earth's magnetic field. Other elements common in geomagnetic field analyses are the horizonal and vertical components and declination of the magnetic field. There exist at present 10 sets of spherical

harmonic coefficients for this analytic representation, all differing slightly.[15] In general $\overline{G}$ and $\overline{H}$ are small (of the order less than 3% of G and H) but become very important at satellite altitudes greater than 5 R_e.

The familiar approximation to the Earth's magnetic field utilizing a centered dipole is based on the following values of harmonic coefficients:

$$G_1^0 = 30470 \text{ gammas}$$

$$G_1^1 = 3030 \text{ gammas and } H_1^1 = 45770$$

Using only these terms the observed magnetic field can be predicted within an accuracy of 87 to 91 per cent at geocentric distances of up to several radii. These values of coefficients correspond to a centered dipole tilted 12^0 with respect to the Earth's rotational axes and at a longitude 297.7° east of Greenwich with an equivalent surface magnetic field at the equator of 31,159 gammas. This is obtained from Vestine's model A for 1955 which is the best of all simple dipole coefficients.

It is possible to represent the Earth's magnetic field by an eccentric dipole which improves upon the accuracy and utilizes the first eight coefficients in a spherical harmonic expansion. In this representation the centered dipole is replaced by a dipole displaced from the center of the by 436 kilometers and intersecting the surface of the Earth at

$\theta_n = 8.1°$ $\qquad$ $\theta_s = 165.6°$

$\Phi_n = 275.4°E$ $\qquad$ $\Phi_s = 120.4°E$

Use of this representation yields accuracies of the order of 90-96% for altitudes less than several R_e. At present most current students of the

geomagnetic field have used coefficient sets with less than or equal to 63 elements corresponding to n and m being less than 6 (one exception utilized 512 coefficients).

However, the impact of the solar wind leads to a distortion of the Earth's field which at geocentric distances greater than 5 R_e contributes a significant portion to the observed magnetic field. This has been studied by Beard and Mead[16] to determine the contribution of the external sources to the magnetic field interior to the magnetopause. They used a centered dipole approximation with an equatorial field strength of 31,000 gammas and assumed impact of the solar plasma normal to the dipole axis. Satisfying the boundary condition of zero normal component of the net magnetic field and assuming a curl free magnetic region interior to the magnetosphere leads to the following values for the external sources:

$G_1^0 = -0.277\ (R_e/R_b)^3$ gauss equals 27.7 gammas at $R_b = 10\ R_e$

$G_2^1 = 0.108\ (R_e/R_b)^4$ gauss equals -1.1 gamma at $R_b = 10\ R_e$

At altitudes greater than 5 R_e the contribution is large. For example at 10 R_e the external field contributes 46 gammas while the internal field contributes only 31 gammas. At 5 R_e the contribution of the external field is reduced to 37 gammas while the internal field is increased to 248 gammas. We see that in the noon meridian the distortion is large, approximately 15% at a distance of 5 R_e but on the midnight meridian the situation is vastly different. Satellites are presently investigation this particular region of space and theoretical predictions and experimental evidence indicate that the Earth's magnetic field may trail out far into interplanetary space well beyond the orbit of the moon in a fashion analogous to the structure of cometary tails in interplanetary space. In conclusion, for

accuracies of the geomagnetic field representation of several percent one must restrict altitudes at present to less than about 4 R_e and include external sources for greater altitudes.

Interplanetary Field Representation

On the assumption that

(1) the efflux of solar plasma from the sun is radially outward at velocity V_s

(2) the rate of solar rotation is 2.9×10^{-6} radians per second ($= \Omega$)

(3) assuming a photospheric magnetic field strength given by B_o it is possible, following Parker[17], to predict the strength of the interplanetary magnetic field as

$$B = B_o \left(\frac{a}{r}\right)^2 \sqrt{1+\left(\frac{r\Omega}{V_s}\right)^2}$$

where a = radius of sun

r = heliocentric distance

This theoretical model of the interplanetary field shows a characteristic geometrical configuration in interplanetary space which resembles the classical Archimedean spiral in the ecliptic plane. A representation of this spiral structure in the interplanetary field is shown in Figure 12. The fixed rotation rate of the sun and high plasma velocity combine to drag out the lines of magnetic force by the highly ionized gases and leads to this characteristic structures. In Figure 13 the theoretical angle ϕ, as measured in the plane of the ecliptic, which the field makes with a radial line to

the sun is shown as a function of plasma velocity. It should be noted that the particle density has no bearing on the direction of the interplanetary magnetic field strength nor its magnitude. It is seen that the angle ϕ is approximately 135° near the orbit of the earth.

Direct measurements of the interplanetary magnetic field have been performed from the IMP-I satellite. These measurements indicate agreement with the theoretical model just discussed. A sample of the magnetic field measured in interplanetary space, obtained on the IMP-I satellite, is shown in Figure 14. It is seen that the magnitude is approximately 5 gammas and that the field is reasonably near the plane of the ecliptic and approximately at the azimuthal angle theoretically predicted. This indicates, by extrapolation to the surface of the sun, that field magnitudes on the order of several gauss at least are present. It also means that for space probes going inward toward the sun a general increase in the magnitude field strength should be observed. Unfortunately the one satellite carrying magnetometers to date which has investigated the region of space towards the sun, Mariner II, was contaminated by spacecraft magnetic fields and did not allow accurate measurements to be performed.[18]

Simulation of Magnetic Fields in Space

The preceding discussion has summarized our present knowledge of magnetic fields in space and presented a foundation upon which we can base our requirements for simulation of such magnetic fields. The most common method employed in the past has been to utilize circular coils of wire carrying electrical currents to create a magnetic field whose magnitude and direction can be controlled. The first coil system developed was due to Ampere and consisted

of a single coil of radius A as illustrated in Figure 15. In this case the axial component of the magnetic field is given by (mks units)

$$H_z(0,0,Z) = \frac{i}{2} \frac{A^2}{[(Z-Z_o)^2 + A^2]^{3/2}} \qquad (3)$$

Two such coil systems placed symmetrically with respect to the origin at $\pm$ B give

$$H_z(0,0,Z) = \frac{iA^2}{A} \left\{ \frac{1}{[(Z-B)^2 + A^2]^{3/2}} + \frac{1}{[(Z+B)^2 + A^2]^{3/2}} \right\} \qquad (4)$$

In order to optimize the two coil configuration it is desirable to have a maximum field on the Z axis for a minimum current. This is obtained analytically by differentiating the above formulation, setting it equal to 0 and solving for the various values permitted:

$$\left. \frac{\partial H_z}{\partial z} \right|_{o,o,z} = 0 \qquad (5)$$

In addition, in order to provide a maximally homogeneous magnetic field one would require a minimum gradient of the actual component of the magnetic field. This is determined by setting the second derivative of the field with respect to Z equal to 0 as shown below

$$\left. \frac{\partial^2 H_z}{\partial z^2} \right|_{o,o,z} = 0 \qquad (6)$$

Now clearly at Z equals 0 the field is a maximum regardless of the value of B as long as the location of the two coils is chosen to be symmetric. However, in order that the gradient be a minimum then the final result of formula (6) is that $4B^2 = A^2$ or that $A = 2B$. This optimum coil configuration utilizing two coils was developed by Helmholtz many years ago and

has become a standard reference in the simulation of magnetic fields in space.

Maximally uniform magnetic fields utilizing multiple sets of coil pairs rely on these two principles:

1. That pairs of coil symmetrically located with respect to the origin give maximum fields and
2. Minimum gradients if appropriately positioned (which can be determined by analytical investigations).

One can introduce four coils with different numbers of windings on each pair of coils or vary the distances and/or size of radii. In general the homogeneity of the magnetic field is the most important goal since symmetry quite easily achieves the maximum field. Indeed a figure of merit can be defined which measures the degree of homogeneity as the deviation of the field at any point, x, y, z from the field at the center:

$$100\left[1 - \frac{H(x,y,z)}{H(0,0,0)}\right] = \% \text{ Homogeneity} \qquad (7)$$

The Helmholtz coil provides a homogeneity of $\pm$ 1% along the axis if the absolute value of Z is less than .32 A. It has a maximum error of $\pm$ 1% off the axis if the $\sqrt{X^2 + Y^2}$ is less than .38 A. It is seen that the region of space homogenous in magnitude to 1% is roughly an oblate spheroid whose dimensions of principal axes are given by .32A, .38A, .38A.

Now the Earth's magnetic field is approximately 50,000 gammas and one percent of this is 500 gammas thus for interplanetary work one needs a uniformity much better than one percent. In order to provide a homogeneity of one gamma over a working region of space implies a requirement of homogeneity of .001%. For a Helmholtz coil this implies a very small region of

space and a large coil radius. Indeed, for an homogeneity of 0.1% the dimensions of the region of space are approximately one half the dimensions for 1% accuracy, being .16A, .2A and .2A. For values of .001% the dimensions are .04A, .05A and .05A, so that if the radius of the coils is 25 feet then one has a sphere of approximately 1 foot radius in which the field is homogeneous to 1 gamma. Clearly the practical limitations of constructing such large coil systems requires a re-evaluation of the utility of the very simple Helmholtz configuration. It is found that by adding more coils but using the same principles governing the development of the Helmholtz system one can rapidly imporve upon the situation for the practical development of coil systems.

An intriguing possibility but one which has not proven successful in practical applications is available in what is referred to as the "sine winding" coil system. In this geometry the density of turns per unit length actually is held constant while the coil is continuously wound on the surface of a sphere. This provides a completely uniform magnetic field interior to the spherical surface. Unfortunately such a configuration is not reasonably practical when consideration of access to the coil system is made.

The general approach is to develop hybrid coil systems utilizing multiple pairs of coils and employ analytical procedures to determine optimum coil constants and configurations. One begins by using circular coordinates and expressing the potential V in cylindrical harmonics and then determining the appropriate turns and current values.[19] The important considerations in the development of such coil systems are:

1. The difficulty in implementing the coil manufacture, which has lead to consideration in some instances of square coil systems,
2. Current stability and current ratios required, which has lead

to constant current but separate turns ratios for coil pairs rather than attempting to develop precise current dividers;

3. The accessibility for various geometries, which has lead to the development of cubic and square coil systems and
4. The analytical difficulties in developing optimum coil systems, which have lead students of coil geometries to consider mainly equal amp turns or sets of coils which lie on the surface of a sphere but at different distances along the axis of the system.

A summary of some existing coil systems and their figure of merits is shown in Table I.

Presently the Goddard Space Flight Center is fabricating a 25 foot Braunbek coil system in which three separate sets of such coils are employed for three axis cancellation of the Earth's magnetic field. The specific parameters of the GSFC facility are;

1. the diameter of the smaller coil is .76388 of the larger,
2. the separation of the smaller is .84565 of the larger diameter, and
3. the separation of the larger coils is .27803 of the larger diameter, and
4. The real diameter of the coil systems are:
   (a) the vertical is 22 feet,
   (b) the horizontal east-west magnetically oriented is 18 feet and
   (c) the horizonal north-south magnetic is 16 feet.

The orientation of the geomagnetic field at the Goddard facility is such that a large coil system is required for the vertical component since

Summary of Some Existing Optimum Coil Systems

Name	Dimensions	Volume of Homogeneity (0.1%)	Turns ratio
Circular Helmholtz	b = 0.5a	0.9%	1:1
Fanselau[20]		14%	equal amp turns
Braunbek[21]		22%	" "
McKeehan[22]		22%	on surface of sphere
Square Helmholtz[19]	b = 0.55a	1%	1:1
4 Coil Cubic[19]	b = $\pm$ .33a, $\pm$a	0.8%	46:43:43:46
5 Coil Cubic[19]	b = 0, $\pm$ .5a, $\pm$a	2.2%	134:44:66:44:134

TABLE I

it is the largest in magnitude, while the remaining coil systems are chosen to be compatible with practical implemeniation of an inter laced set of such coils.

In Figure 16 is shown a picture of a model of the GSFC coil system. The coil constant is 15.4 gammas per milliamp and there are 36 turns of number 6 aluminum wire on each coil. The performance of the Braunbek coil system is seen, by review of the characteristics of Table I, to be equivalent to a McKeehan and to have the additional merit that equal amp turns on each coil system are required, whereas the other requires different currents in each of the coils. The measured performance of the Goddard facility provides a homogeneity of .001% in a 1 meter diameter sphere with an accuracy of $\pm$ 0.5 gamma and a resolution of 0.1 gamma.

An important aspect of such coil systems is that they be capable of being servo controlled to simulate a stationary weak magnetic field in spite of the fact that the Earth's magnetic field varies as a function of time. A secondary set of coils is associated with this coil facility and is used to monitor the variations of the geomagnetic field. The stability of the coil system is approximately 1/2 to 1 gamma and the cancellation of the Earth's magnetic field can thus be automatically controlled. The Goddard facility is not yet completely operational although sensible measurements have been made utilizing the coil systems. The completed system is scheduled for March 1965. As such it will be the largest and most accurate facility in the world.

Spacecraft Applications

The most important application of any coil system is its ability to simulate magnetic fields which represent those to be measured in space for

calibration of magnetometer sensors. A secondary objective is to permit the mapping magnetically of the inherent magnetic properties of spacecraft and spacecraft subsystems whose magnetic fields may yield adverse effects on the data collected. The following paragraphs summarize briefly the specific applications of the knowledge of the Earth's magnetic field and its interaction with satellites which have developed over the past several years.

Vanguard I - Spin Decay

The Vanguard I satellite provided a unique example for investigation of the electro magnetic interaction of a spin stabilized satellite with the earth's magnetic field over a long time scale. The basic physics involved is based upon the fact that a rotating sphere in a magnetic field will induce eddy currents in a fashion such as to generate currents who magnetic fields not only oppose the spin, but whose currents lead to dissipation of kinetic energy. On the assumption that the electro magnetic readjustments, as the spin axis changes inclination with respect to the magnetic field, occur at a rate much greater than the mechanical readjustments, the theoretical development and explanation of the Vanguard I spin rate decay can be understood. The first investigation was conducted by J. P. Vinti[23] assuming a spherical shell of uniform conductivity and non-magnetic material. The characteristic summary of the results is that the induced eddy currents create a torque on the spinning satellite proportional to the inertial moment of the satellite, and the angular spin rate and the magnetic field strength squared as shown in the formulae below:

$$\overrightarrow{\text{Torque}} \alpha I (\vec{\omega} x \vec{B}) x \vec{s}$$

where I is the angular moment of inertia

$\vec{\omega}$ is the angular velocity

$\vec{B}$ is the magnetic field vector

The net result of the torque can be separated into a spin decay which is proportional to the angular spin rate and its product with the magnetic field perpendicular to the spin axis as shown in the following formula:

$$L(\text{decay}) \alpha \omega B_{\perp}^{2}$$

Similarly the precession torque is given proportional to B and B

$$L(\text{precession}) \alpha \omega B_{\perp} B_{||}$$

The Vanguard I satellite was launched March 17, 1958 into an orbit with elevations between 650 to 3,900 Km at which the Earth's magnetic field was approximately 40 to 30 thousand gammas. The spin decay studies indicated the satellite slowed down from an initial rate of 3.0 rps to 0.05 rps in 2.5 years.[24] These measurements were performed by investigation of the periodic fading of radio signals associated with the antenna pattern of the satellite. The first anomaly was detected in December 1958 and a rapid evaluation of theoretical models (which go back to Hans Hertz in 1896) indicated that classical EM theory could explain the observed anomaly.

Injun III Passive Magnetic Orientation

The motions of charged particles trapped in the Earth's magnetic field

are generally helical spirals about field lines with associated drift of electrons east and protons west due to the spatial gradient of the earth's magnetic field. The particles "bounce" back and forth along a line of force between their "mirror" points. The angle that the spiral makes with the field lines is called the pitch angle and is an important parameter to be measured in charged particle investigations in space. Since it is known that the first adiabatic invariant of particle motion is preserved then measuring the pitch angle distribution of the particles at a point in space predicts the particle flux characteristics along the line of force. The variation in pitch angle is shown by the following formula in which B_o is the field strength when $\alpha = 0°$ and B_m is the field strength at the mirror point when $\alpha = 90°$.

$$B_o = B_m \sin^2 \alpha_{90°}$$

and in general (10)

$$\sin^2 \alpha = \frac{B_o}{B}$$

In order to separate by direct detector analysis the pitch angle distribution requires unique instrumentation. An ingeneous suggestion has resolved this difficulty by placing a bar magnet in the spin stabilizated spacecraft Injun III [25] so that the satellite spin axis becomes parallel to the local magnetic field. Recalling the results of the previous discussion on Vanguard I, it is found that both the decay and the precession torques are zero for perfect alignment of the magnetic vector and spin vector of the satellite. In the Injun III satellite an Alnico-V magnet 22 inches long and 1 inch square was employed and permalloy rods perpendicular to the spin axes were employed to damp the periodic motion induced by the

variable aspect to the Earth's magnetic field. The Injun III satellite was launched December 13, 1962 and achieved an apogee of 2787 Km. and a perigee of 237 Km. The natural period of this satellite was approximately two minutes and the satellite damped to being almost perfectly aligned with the Earth's magnetic field in approximately three days. The success of this particular passive orientation device was checked by onboard magnetometers measuring the magnetic field perpendicular to the spin axis of the satellite.

Tiros-Active Attitude Control System

The Tiros wheel satellite, number 9, will be launched into a circular orbit of 640 Km. with a unique active attitude control system utilizing the principles already discussed. It will be placed into a near polar orbit with the spin axis perpendicular to the orbital plane which is sun synchronized. The precession of the orbital plane due to the Earth's equatorial bulge will maintain the satellite in a solar orientation so that a constant illumination of the observed Earth's surface is maintained. The magnetic aspect control system (MASC) will keep the spin within its proper limits and the quarter orbit magnetic attitude control system (QOMAC) will keep the spin axis perpendicular to the orbital plane. These systems are illustrated in figure 17 with respect to orientation to the satellite spin axis.

The need for such current carrying coil systems was not recognized until after Tiros I.[26] On successive Tiros, numbers II through VIII, the magnetic attitude control system was utilized mainly to provide proper cancellation of the satellites magnetic field so that spin torques on the

satellite were negligible. It is possible to alter the polarity of the spacecraft dipole moment by these coil systems and indeed the magnetic properties of the satellite are planned to be cancelled continuously by these attitude systems.

Summary

The above discussion has been very brief but illustrates the utilization of the Earth's magnetic field in attitude control systems going from strictly interaction to highly sophisticated computer programmed active attitude systems. The necessity for verifying the operation of such systems is clear and the utilization of large coil facilities for attitude studies such as that being fabricated at GSFC is clearly indicated.

REFERENCES

1. Beard, D. B., The interaction of the terrestrial magnetic field with the solar corpuscular radiation, J. Geophys. Res., 65, 3559-3568, 1960.

2. Heppner, J. P., N. S. Ness, T. L. Skillman, and C. S. Scearce, Explorer X magnetic field measurements, J. Geophys. Res., 68, 1-46, 1963.

3. Van Allen, J. A., Dynamics, composition and origin of the geo-trapped radiation, in Space Science edited by D. P. Legalley, John Wiley and Sons, New York-London, 1963.

4. O'Brien, B. J., Review of Studies of Trapped Radiation with Satellite-Borne Apparatus, Space Science Revs., 1, 415-484, 1963.

5. Ness, N. F., C. S. Scearce, J. B. Seek, Initial Results of the IMP-Magnetic Field Experiment, J. Geophys. Res., 69, 3531-3569, 1964.

6. Chapman, S. and Ferraro, V. C. A., A new theory on magnetic storms, Terr. Mag. and Atmos. Elec., 36, 77-97, 171-186, 1931; 37, 147-156, 421-429, 1932; 38, 79-97, 1933.

7. Gold, T., The Motions in the Magnetosphere of the Earth, J. Geophys. Res., 64, 1219-1224, 1959.

8. Snyder, C. W. and M. Neugebauer, Interplanetary Solar wind measurements by Mariner II, Space Res., IV, to appear 1964.

9. Bonetti, A., H. S. Bridge, A. J. Lazarus, B. Rossi, and F. Scherb, Explorer X Plasma measurements, J. Geophys. Res., 68, 4017-4063, 1963.

10. Bridge, H., A. Egidi, A. Lazarus, E. Lyon and L. Jacobson, Preliminary results of plasma measurements on IMP-A COSPAR presentation, Florence, Italy, 1964.

11. Kellogg, P. J., Flow of plasma around the earth, J. Geophys. Res., 67, 3805-3811, 1962.

Axford, W. I., The interaction between the solar wind and the earth's magnetosphere, J. Geophys. Res., 67, 3791-3796, 1962.

12. Lees, L., Interaction between the solar plasma wind and the geomagnetic cavity, N. Y. meeting of AIAA, January, 1964, Preprint 64-88.

13. Ness, N. F. and J. M. Wilcox, Solar Origin of the Interplanetary Magnetic Field, Phys. Rev. Letters 13 (15), 461-464, 1964.

14. Chapman, S. and J. Bartels, Geomagnetism, Oxford, 1940

15. Heuring, F. T., The Analytic Description of the Geomagnetic Field at Satellite Altitudes, J. Geophys. Res., 69, 4959-4968, 1964.

16. Mead, C. D. and D. B. Beard, Shape of the geomagnetic field solar wind boundary, J. Geophys. Res., 69, 1169-1180, 1964.

Mead, G. D. Deformation of the geomagnetic field by the solar wind, J. Geophys. Res., 69, 1181-1195, 1964.

17. Parker, E. N., Dynamics of the interplanetary gas and magnetic fields, Astrophys. J., 128, 667-676, 1958.

18. Smith, E. J., P. J. Coleman, and L. Davis, Interplanetary magnetic field measurements with Mariner 2, paper presented at JPL Symp. Solar Wind, Calif. Inst. Tech., Pasadena, Calif., April 1-4, 1964, to be published, 1964.

19. Warburton, F. W., Design of Coil Systems for Magnetic Field Control at the Naval Ordnance Laboratory, NAVORD Report 3768, 1955.

20. Fanselan, G. Die Erzengung Weitgehend Homogener Magnetfelder durch Kreisstrome, Zeits. Phys., 54, 260-269, 1929.

21. Braunbek, W., Die Erzeugung Weitgehend Homogener Magneticfelder durch Kresstrome, Zeits., Phys., 88, 399-402, 1934.

22. McKeehan, L. W., Combinations of circular currents for producing uniform magnetic fields, Rev. Sci. Instr., 7, 150-153, 1936.

23. Vinti, J. P., Theory of the Spin of a Conducting Satellite in the Magnetic Field of the Earth, Aberdeen Ballistic Research Laboratory Report 1020, 1957.

24. Arendt, P. R., Anomalies of the Geomagnetic Retardation of the Spin of Satellite Vanguard I (1958 Beta), ARS Journal 31-3, 286-289, 1961.

25. O'Brien, B. J., C. D. Laughlin and D. A. Gurnett, High-Latitude Geophysical Studies with Satellite Injun 3, 1. Description of the Satellite, J. Geophys. Res., 69, 1-12, 1964.

26. Grasshoff, L. H., Eddy Current Torque Compensation in a Spin Stabilized Earth Satellite, ARS Journal 31-3, 290-293, 1961.

SATELLITE	INSTRUMENT	RANGE	SENSITIVITY	DISTANCE
SPUTNIK III	TRIAXIAL FLUXGATE	$<6\times10^4$	5%	<1.3
PIONEER I	SEARCH COIL	$<10^3$	1%	3.7–7.0 12.3–14.6
LUNIK I	TRIAXIAL FLUXGATE	<6000	200 γ	3–6
EXPLORER VI	SEARCH COIL SOLAR ASPECT	$<2\times10^4$	3%	2–7.5
LUNIK II	TRIAXIAL FLUXGATE	<1500	50 γ	3–6
VANGUARD III	PROTON PRECESSION	10^4–6×10^4	4 γ	<1.8
PIONEER V	SEARCH COIL	$<10^3$	0.05–5 γ	5–9
EXPLORER X	RB VAPOR FLUXGATES	$30-5\times10^3$ ±30	3 γ 0.3 γ	1.8–7 6–42.6
EXPLORER XII	TRIAXIAL FLUXGATE	±500	10 γ	4–13.5
EXPLORER XIV	TRIAXIAL FLUXGATE	±250	5 γ	5–16.5
ALOUETTE	IONOSPHERIC SOUNDING	$<6\times10^4$	0.3%	1.17
EXPLORER XV	TRIAXIAL FLUXGATE	±4000	40 γ	1.7–4.0

Figure 1. Tabular summary of US and USSR earth satellites launched to date which have provided measurements of the geomagnetic field. Included are a brief description of the type of instrumentation employed and the associated dynamic range as measured in gammas. The sensitivity is normally determined as a percentage of the maximum range (frequently 1%) except in the cases of those satellites for which large spacecraft magnetic fields were present such as on the Russian spacecraft Lunik I and II. The distance over which sensible magnetic field measurements were performed is indicated in units of earth radii. (see Figure 2)

SATELLITE	LAUNCH	INCLINATION	LIFETIME(d)
SPUTNIK III	5-15-58	65°	30
PIONEER I	10-11-58	EARTH IMPACT	1
LUNIK I	1-2-59	SOLAR ORBIT	1
EXPLORER VI	8-7-59	47°	61
LUNIK II	9-12-59	LUNAR IMPACT	33.5 HRS.
VANGUARD III	9-18-59	33°	85
PIONEER V	3-11-60	SOLAR ORBIT	50
EXPLORER X	3-25-61	33°	2.2
EXPLORER XII	8-16-61	33°	112
EXPLORER XIV	10-3-62	33°	300
ALOUETTE	9-29-62	80°	STILL TRANS.
EXPLORER XV	10-27-62	18°	90

Figure 2. Tabular summary of earth satellites launched to date measuring the geomagnetic field. Indicated are the launch dates, the inclination of the orbital plane to the earth's equator (when this parameter is significant) and the life time of the satellite as measured in days. Note that some spacecraft clearly traversed the indicated region only once.

STUDIES OF THE INTERPLANETARY MAGNETIC FIELD

SPACECRAFT (LAUNCH)	LIFETIME (DAYS)	REGION	INSTRUMENT	SENSITIVITY	ACCURACY	COMMENTS
PIONEER V (3-11-60)	50	.9-1.0 AU	SEARCH COIL	$\angle 0.1^{\gamma}$	?	COMPONENT ⊥ TO SPIN AXIS ONLY
EXPLORER X (3-25-61)	2.2	$\angle 47$ R_e	RUBIDIUM, FLUXGATES	$\pm 0.25^{\gamma}$	$\pm 1.0^{\gamma}$	NEVER OUTSIDE EARTHS INFLUENCE
MARINER II (8-26-62)	104	.7-1.0 AU	FLUXGATES	$\pm 0.7^{\gamma}$	?	SPACECRAFT FIELDS, ZEROS UNKNOWN
IMP-A (11-27-63)	STILL OPERATING	$\angle 32$ R_e	RUBIDIUM, FLUXGATES	$\pm .25^{\gamma}$	$\pm .25^{\gamma}$	INITIAL APOGEE TOWARDS SUN

Figure 3. Tabular summary of US space probes launched to date which have provided measurements of the interplanetary magnetic field. Prior to the launch of the IMP-I spacecraft no accurate and precise measurements of the interplanetary field had been performed due to various limitations as indicated in the tabular summary under the heading "comments".

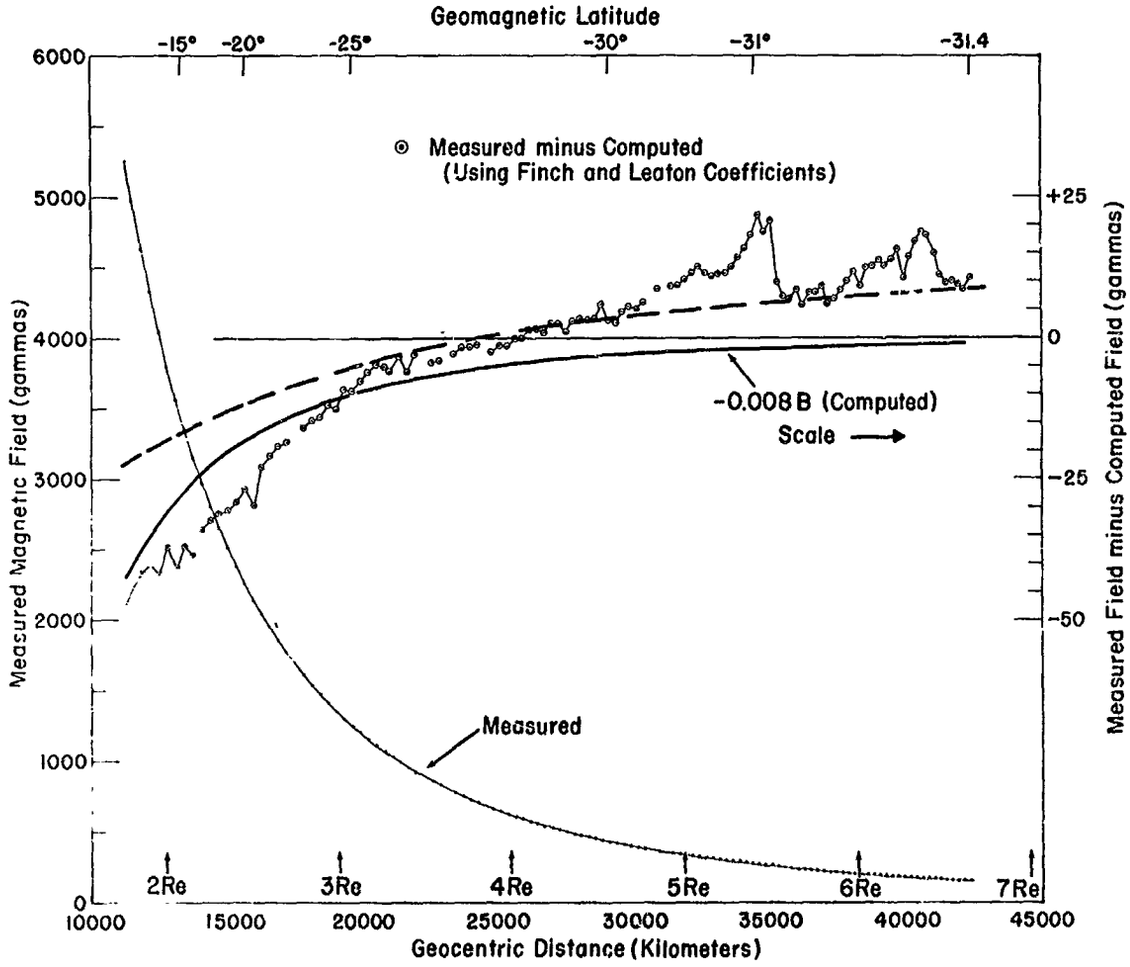

Figure 4. Results of the Explorer X measurements of the geomagnetic field from 4 to 12.5 R_e. The observations are indicated by solid dots connected by straight line segments, the theoretical values indicated by solid lines and interpreted fit assuming a constant field indicated by the dashed line.

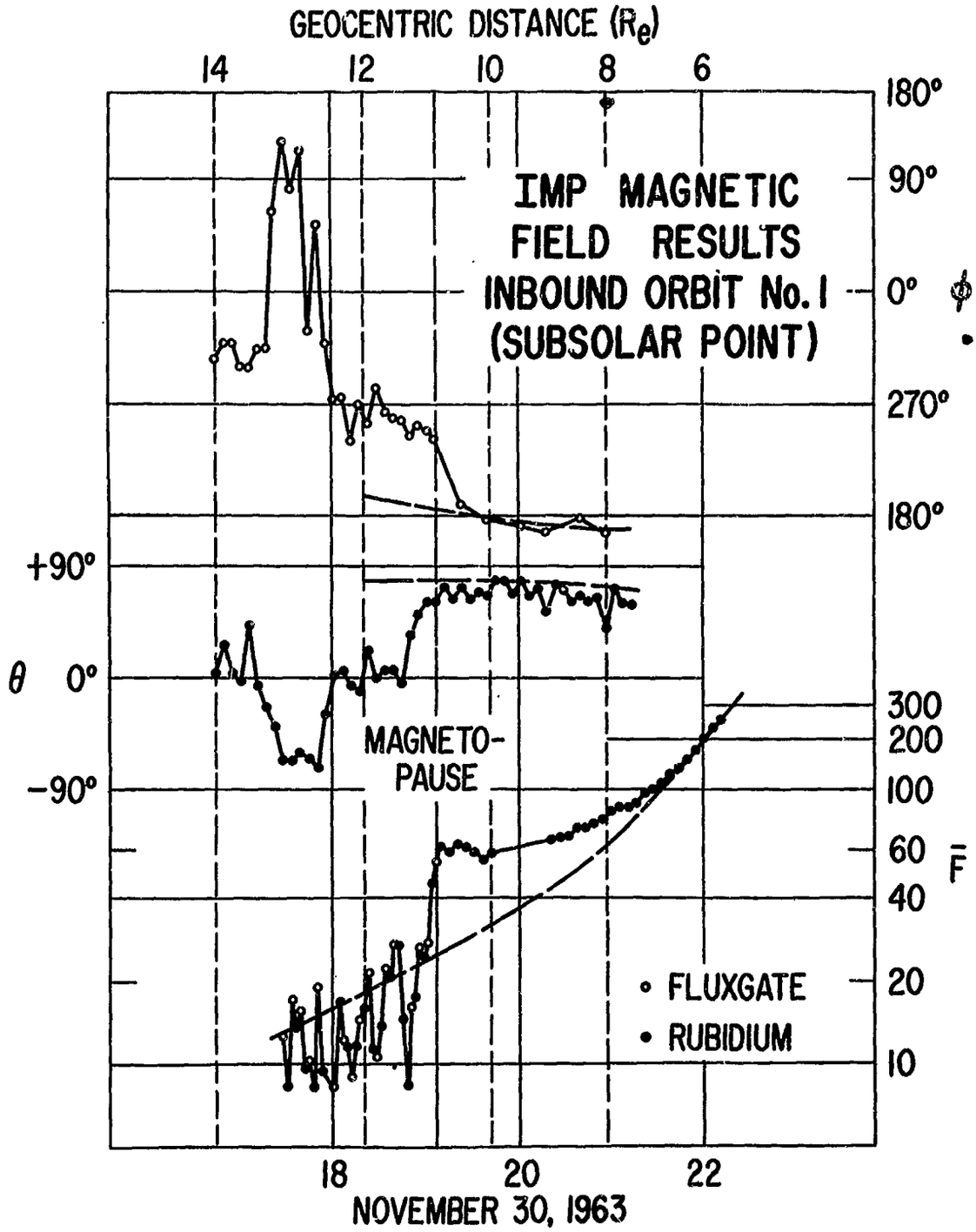

Figure 5. Results of the traversal of the magnetosphere boundary by IMP-I on inbound orbit pass No. 1. Observed values are indicated by open and closed circles connected by straight line segments as provided by both the tubidium vapor magnetometer and the fluxgate magnetometers carried onboard the satellite. The dashed curves represent the theoretical magnetic field extrapolated from terrestrial surface measurements. At these distances the only contributing factor in the multipole expansion of the earth's field is the dipole moment of the earth. The abrupt transition at 10.7 R_e identified as the boundary of the magnetosphere, the magnetopause.

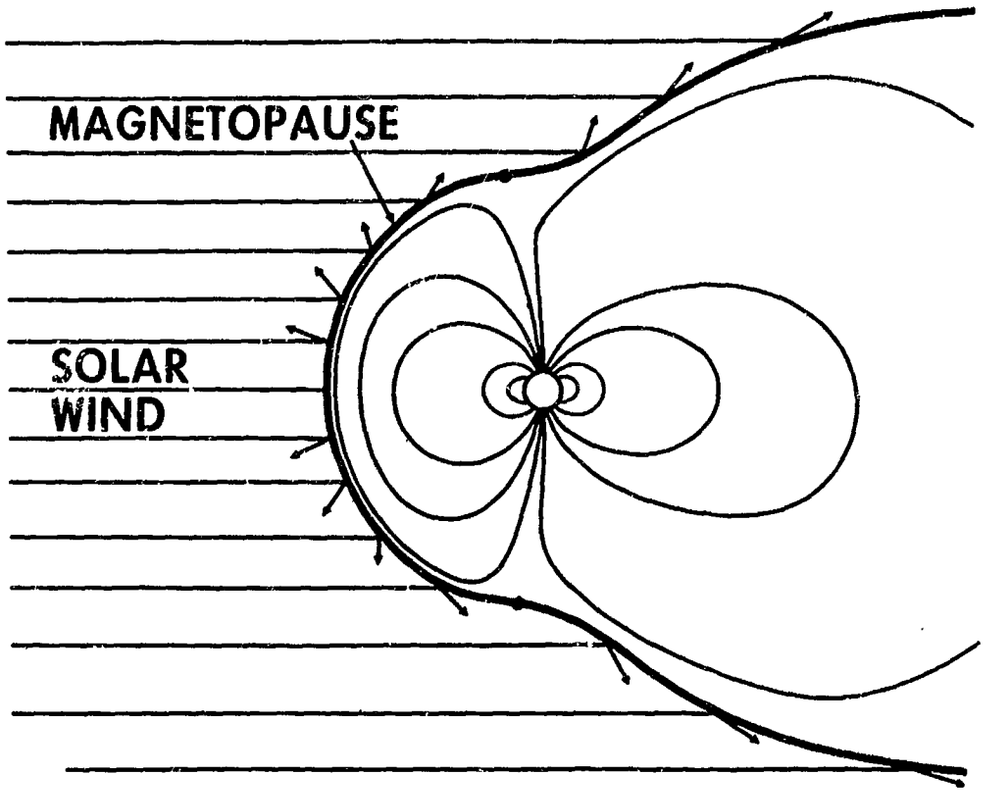

Figure 6. Naive representation of the interaction of the solar plasma with the geomagnetic field. Direct impact of the plasma with the magnetic field is shown as being specularly reflected from the geomagnetic boundary. The distance to the boundary at the subsolar point is given by:

$$R_m = R_e \left[\frac{B_o^2}{4\pi\, mn\, V_s^2} \right]^{1/6}$$

where R_e is the radius of the earth, B_o is the equatorial magnetic field strength and V_s the velocity of the solar plasma with density n p/cm^3.

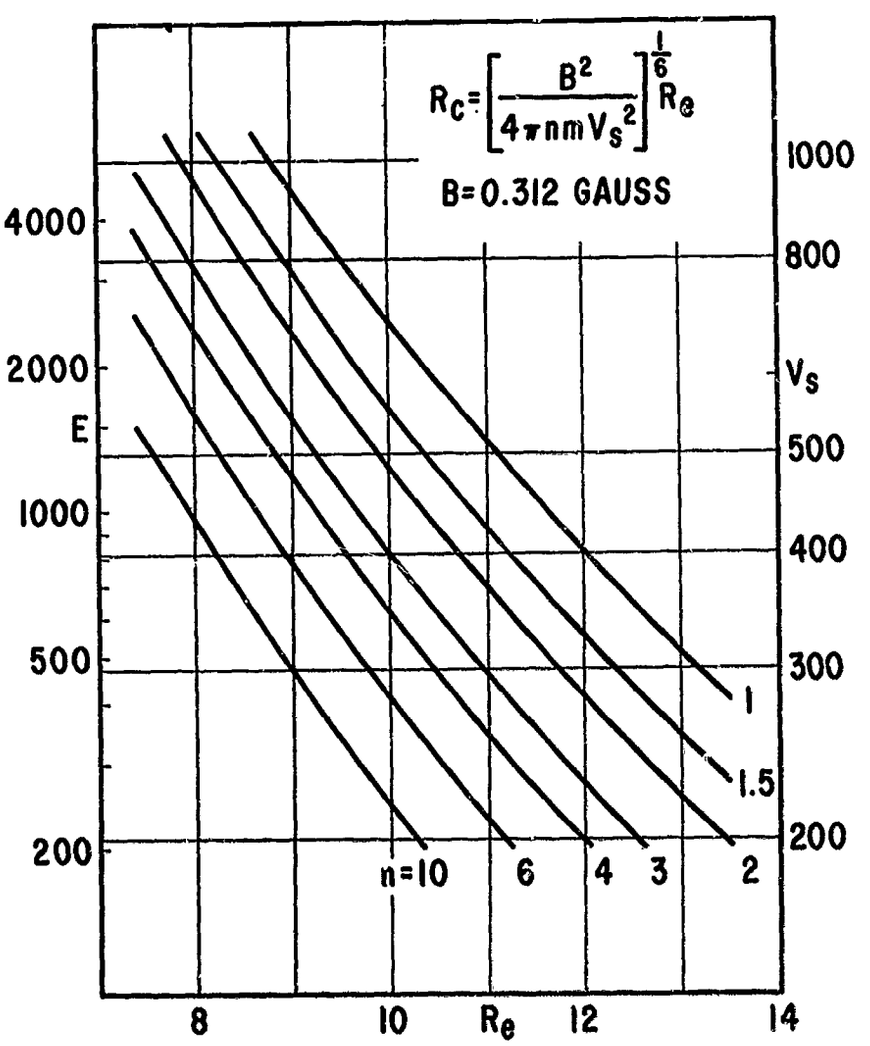

Figure 7. Theoretical size of the magnetosphere at the subsolar point assuming

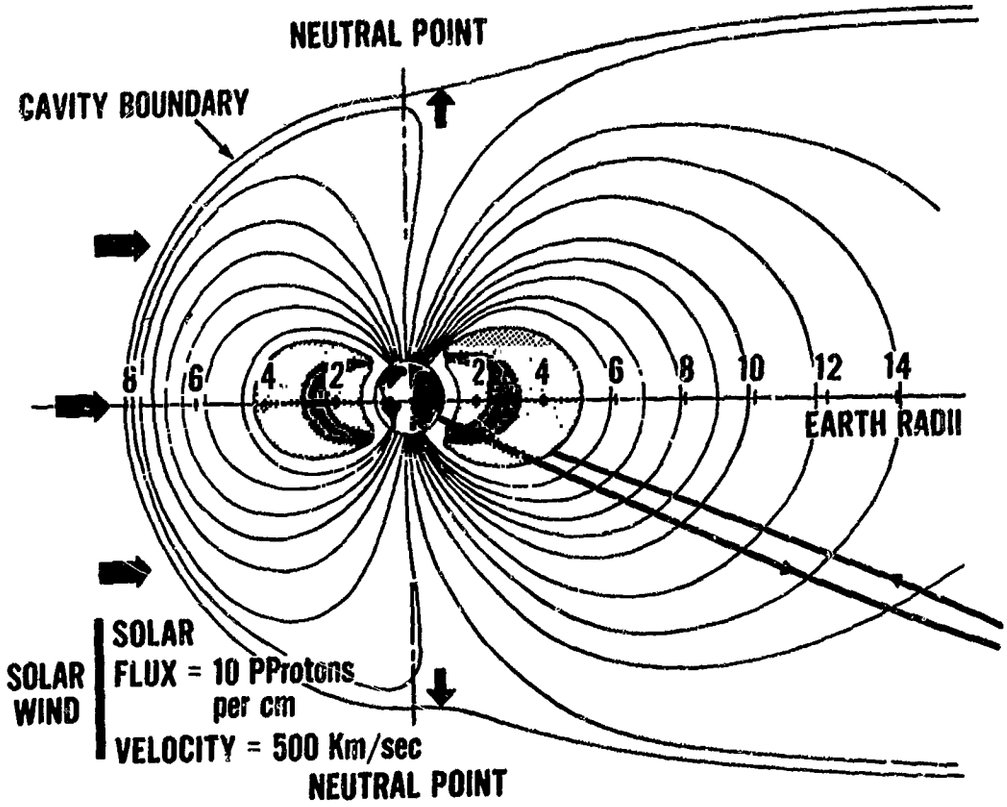

Figure 8. Summary pre-IMP-I illustration of the confined geomagnetic field of the earth and the location of the radiation belts. The flow of solar plasma is taken to be directly from the sun and the trace of the Explorer X trajectory is shown on the magnetic meridian plane.

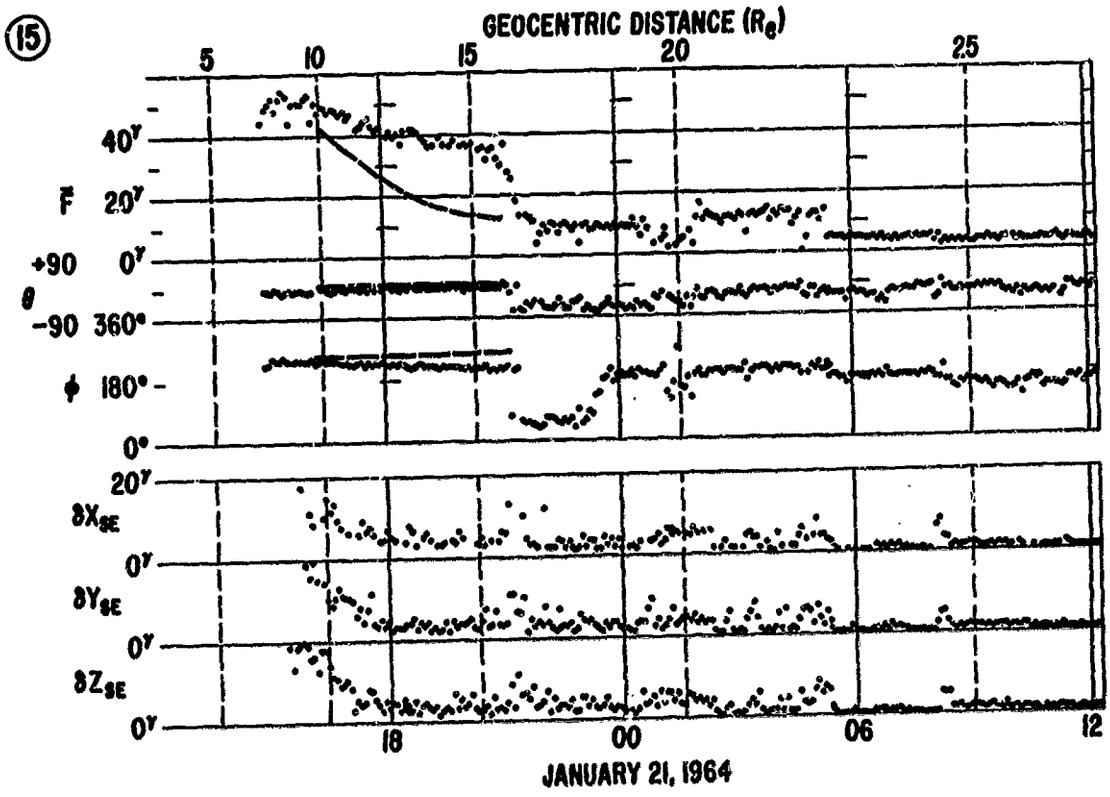

Figure 9. The results of the magnetic field experiment carried on the IMP-I spacecraft from orbit No. 15, January 21, 1964. These data illustrate the outbound traversal of the magnetosphere boundary at 15.7 R_e and the collisionless magnetohydrodynamic shock wave at 22.7 R_e, with a possible precurser occurring at 24.5 R_e.

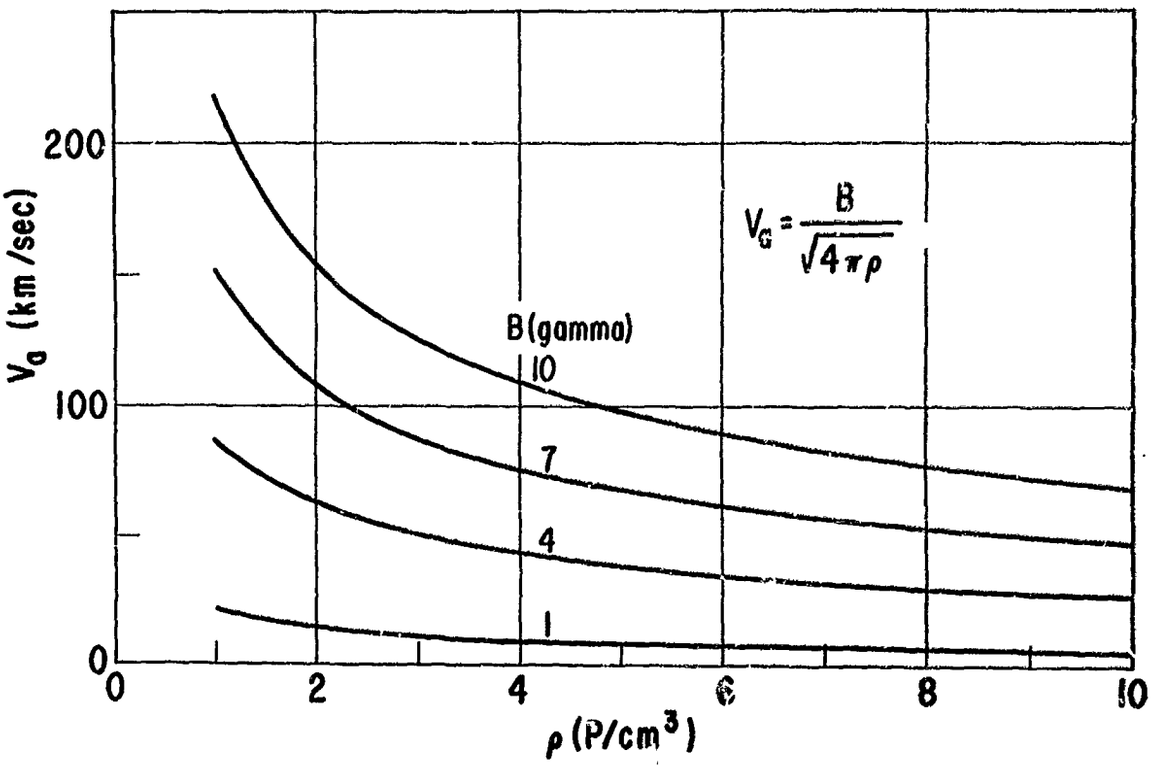

Figure 10. Alfvén magnetohydrodynamic phase velocity of wave propagation as a function of magnetic field strength and plasma density. Representative values for the interplanetary medium are chosen in this diagram.

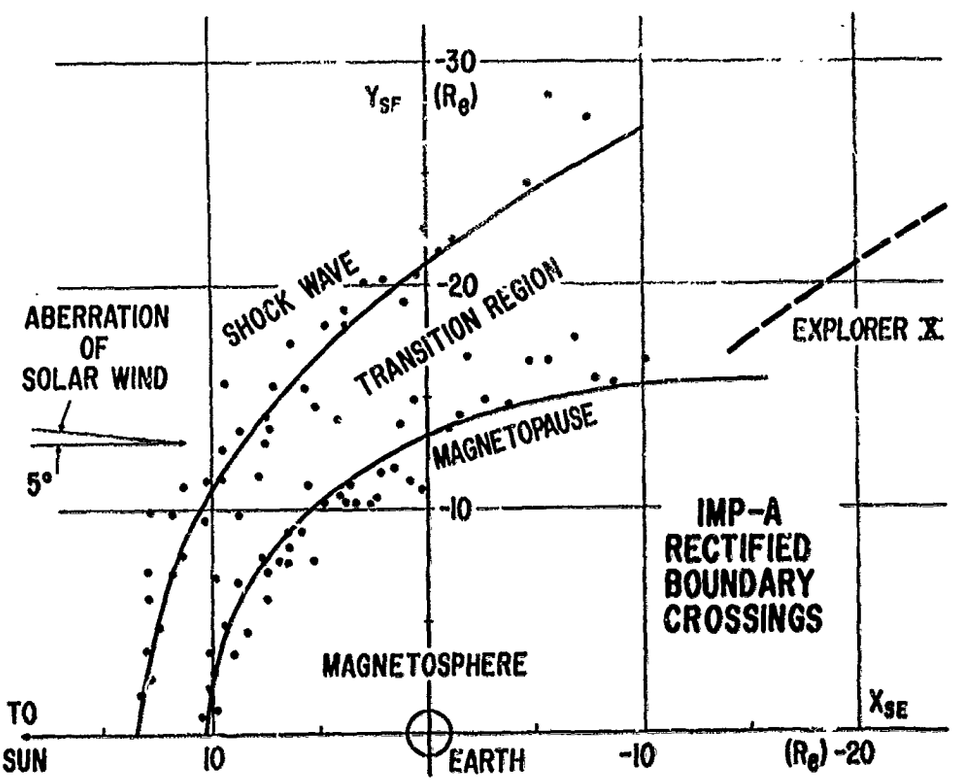

Figure 11. Comparison of the observed positions of the boundary of the magnetosphere and shock wave as shown by solid dots with the theoretical positions according to the computations of Spreiter and Jones (1963) adjusted for a different gas dynamic specific heat capacity ratio. Very good agreement is obtained with this modification of their treatment and an aberration by 5° to accommodate the heliocentric orbital motion of the earth around the sun. The distance to the magnetosphere boundary at the subsolar point is 10.25 R_e and the distance to the shock wave boundary is 13.4 R_e.

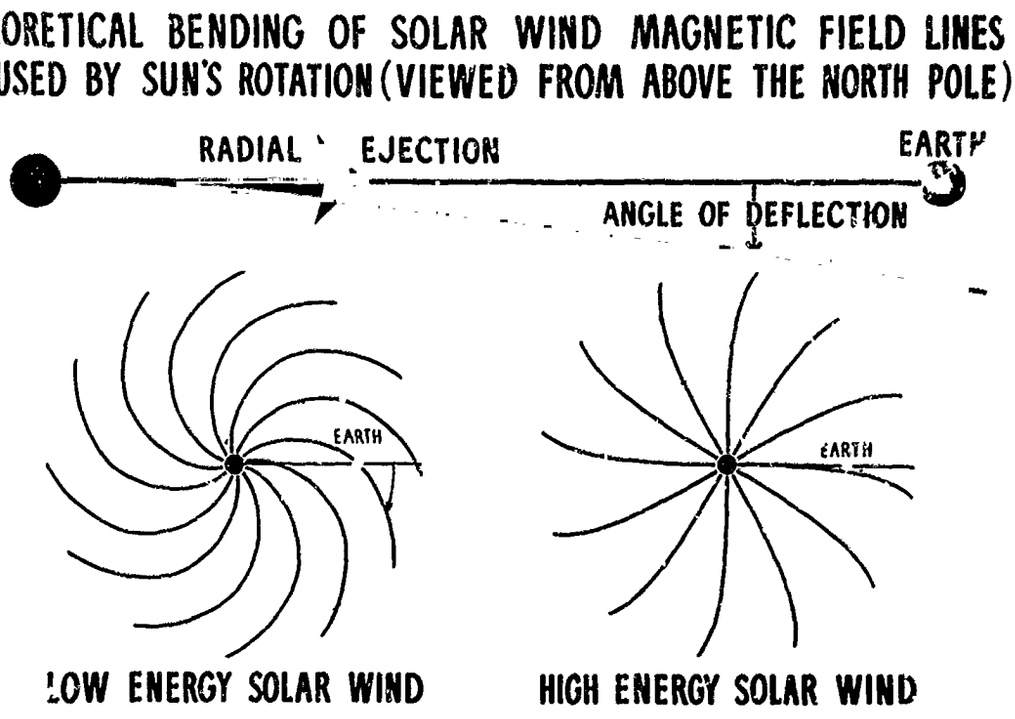

Figure 12. Schematic illustration of the spiral interplanetary magnetic field as obtained by assuming a uniformly expanding, infinitely conducting solar corona. The topology of the interplanetary magnetic field changes significantly as the velocity of the plasma increases. At high velocities the field lines are radially directed, paralleling the flow field from the sun, while for very low velocities and field lines are tightly wound in a Archemedian spiral configuration as shown on the left hand side.

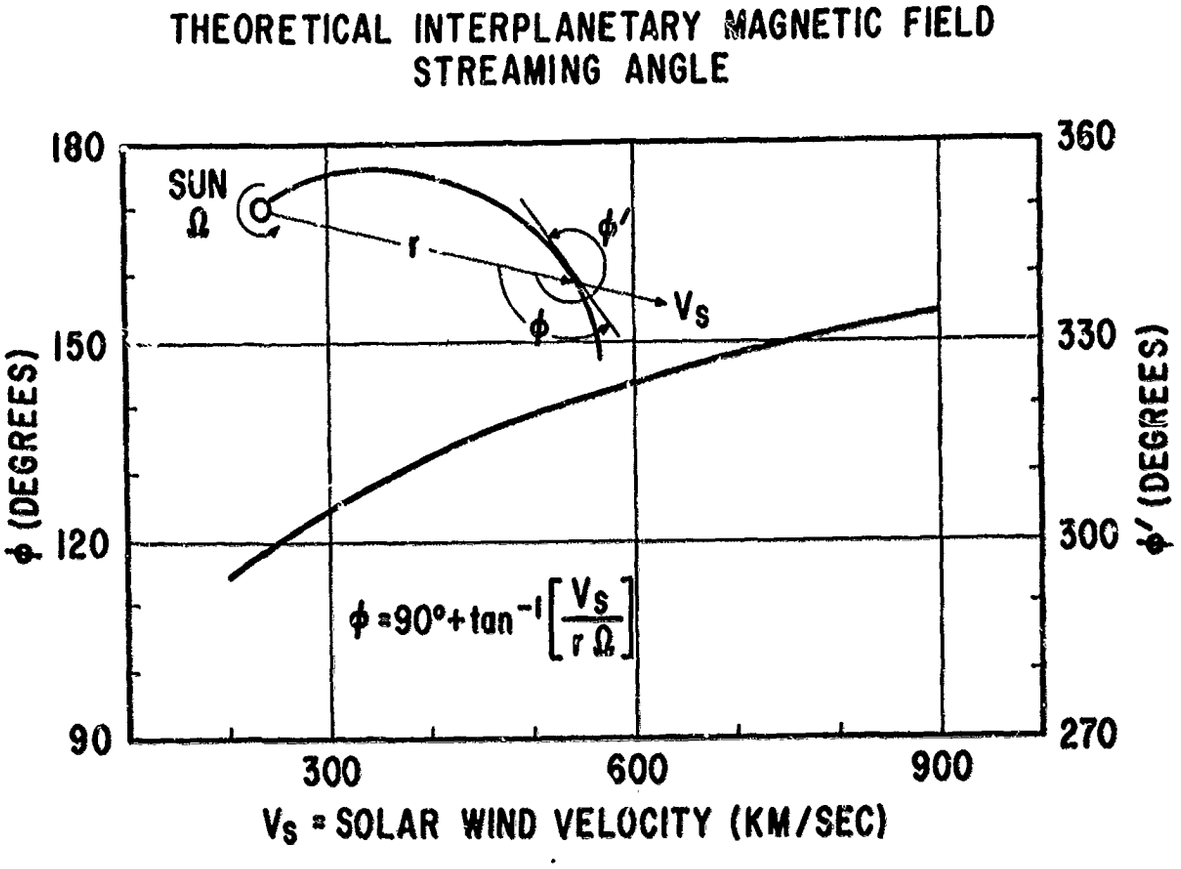

Figure 13. Theoretical direction of the interplanetary magnetic field as measured by the azimuthal angle ϕ in the plane of the ecliptic as a function of the solar wind velocity V_s.

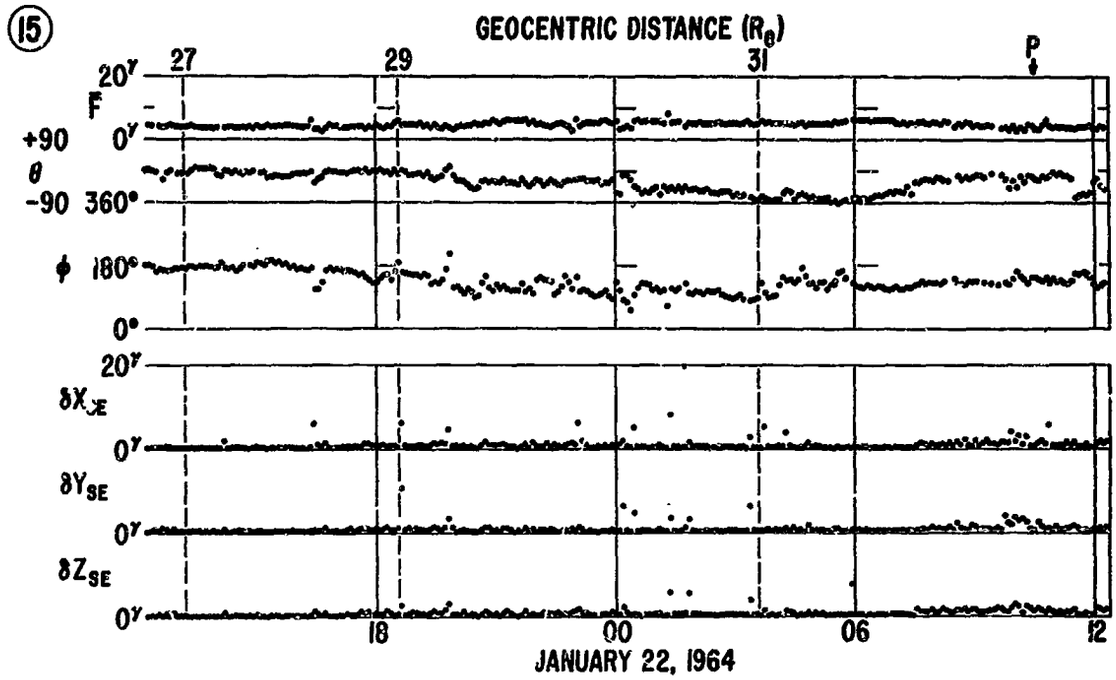

Figure 14. Representative measurements of the interplanetary magnetic field from IMP-I during orbit 15, January 22, 1964. These data follow immediately after those of Figure 9 and indicate the characteristic of the interplanetary magnetic field magnitude and variability of the direction.

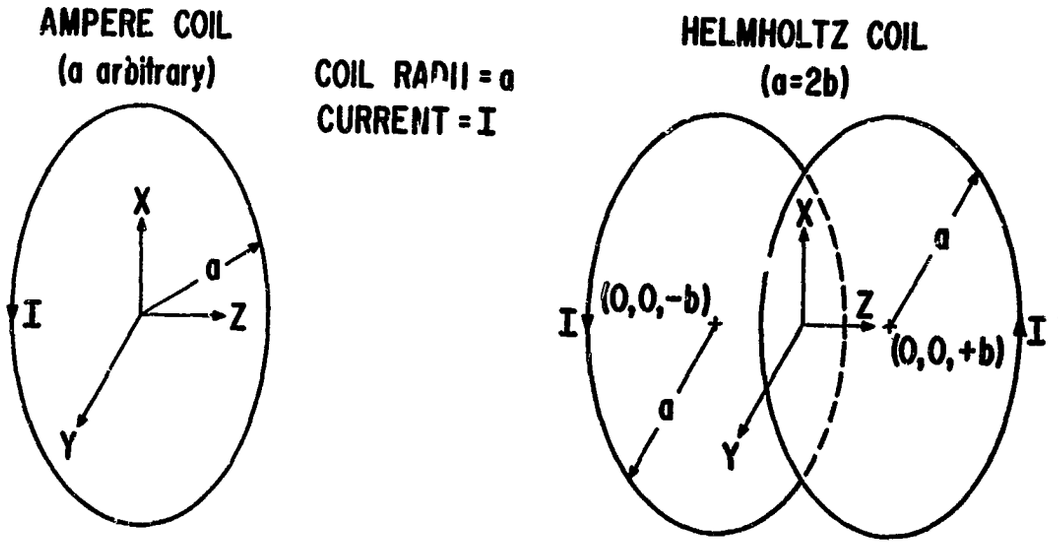

ELEMENTARY COIL SYSTEM GEOMETRIES

Figure 15. Geometry and relative scale of the Ampere coil and Helmholtz coil configurations utilized to nullify the earth's magnetic field in space simulation. The Z axis of the coil system is normal to the plane of the coils.

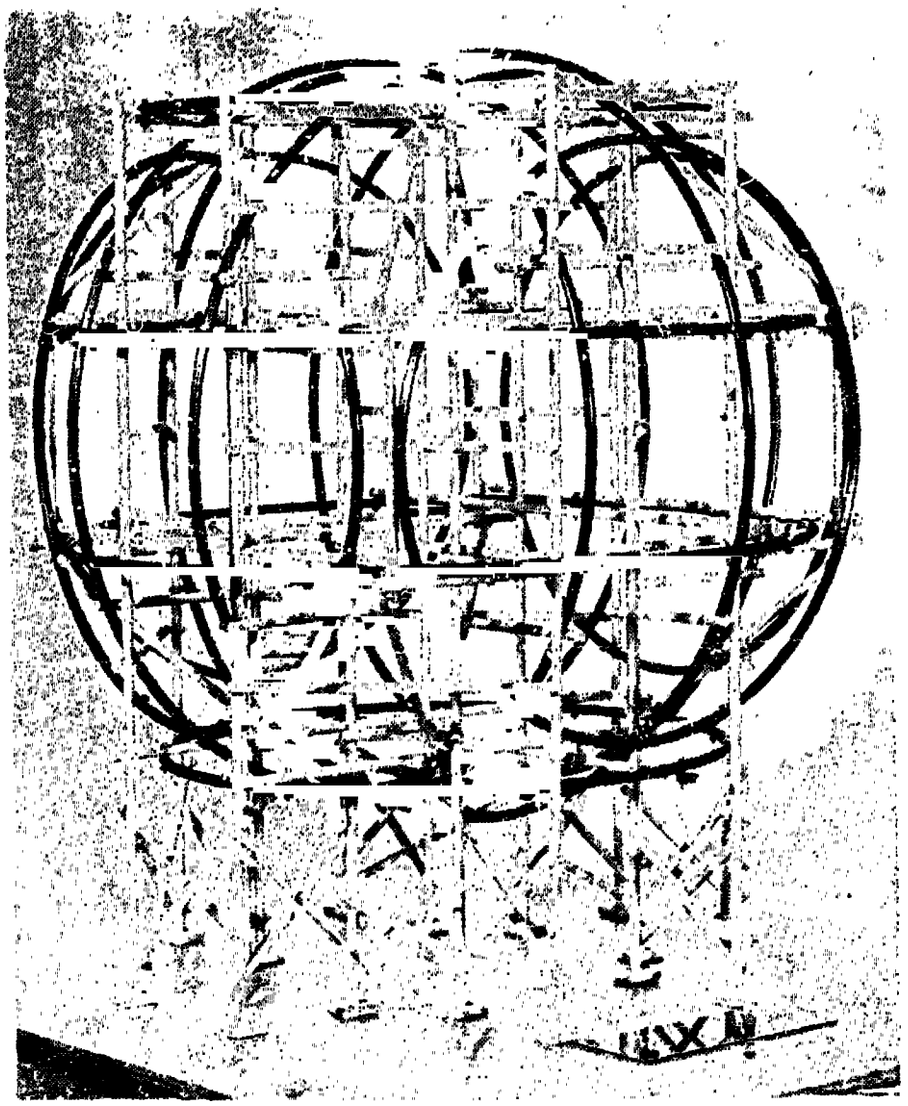

Figure 16. Model of the Goddard Space Flight Center, Magnetic Fields component test facility located adjacent to the laboratory in Greenbelt, MD. This large scale coil facility will be utilized for calibration of magnetometer sensors and mapping of magnetic field properties of spacecraft and subsystems.

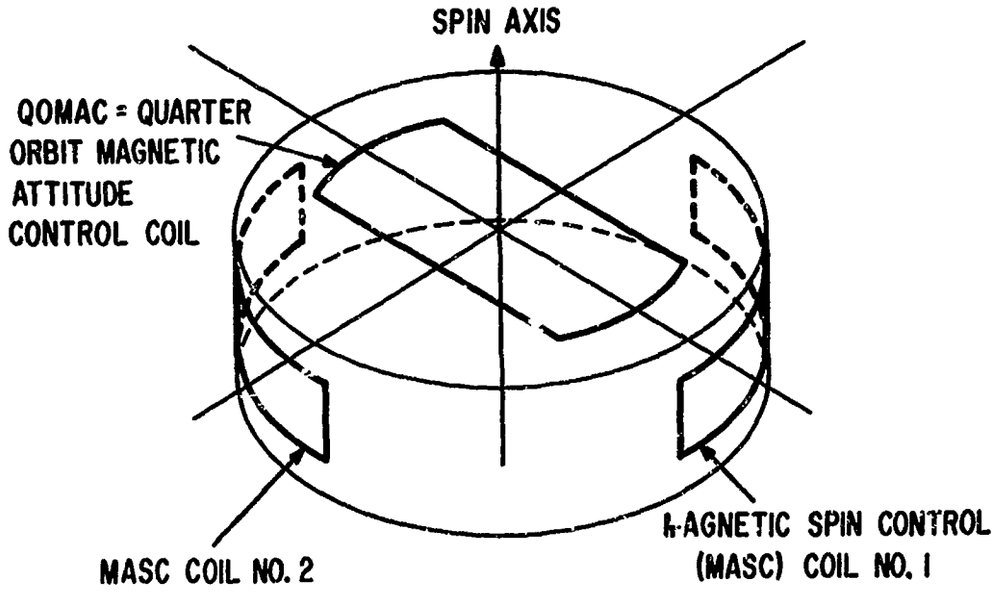

TIROS ACTIVE ATTITUDE CONTROL SYSTEM

Figure 17. Schematic illustration of the Tiros wheel satellite geometical configuration of coil systems employed to control the aspect and attitude of the satellite. Electrical currents can flow in either polarity on the coils as indicated under ground computer control.